POLITECNICO
MILANO 1863

DIPARTIMENTO DI ENERGIA

Modelling of boundary plasmas in linear devices and tokamaks

PhD Programme in Energy and Nuclear Science and Technology

Doctoral Dissertation of
Elena Tonello
Student ID: 929748

Advisor: **Prof. Matteo Passoni**
Co-advisors: **Dr. Andrea Uccello**
Tutor: **Prof. Carlo Spartaco Casari**
Chair of the Doctoral Programme: **Prof. Vincenzo Dossena**

Year 2023 - PhD cycle XXXIV

Abstract

The control and mitigation of plasma and power exhaust are crucial to ensure a stable and economically viable operation of a magnetic confinement nuclear fusion power plant. A fusion reactor is made of a toroidal vacuum chamber in which a magnetic field confines the thermonuclear burning plasma at hundreds of millions of Celsius degrees. In the periphery of a tokamak reactor, the edge plasma is the narrow transition region between the hot plasma core and the wall of the vacuum chamber. This is characterised by the presence of steep gradients, turbulence and multi-species plasma, including also atoms, molecules and impurities.

The possibility of correctly predicting the heat loads resulting from the plasma-wall interaction (PWI) is an essential prerequisite for developing strategies to mitigate exhaust fluxes. This requires having models capable of describing the physics of the edge plasma, including plasma transport, interaction with neutral atoms and molecules and interaction with the solid wall.

This doctoral thesis aims to further improve the available modelling tools expanding their exploitability in connection to the modelling of plasma-material interaction experiments in linear plasma devices, helium plasmas and negative triangularity tokamaks. These are extremely topical subjects in the context of preparing the operational phases for the ITER experiment and developing the first DEMO reactor.

The linear plasma device GyM of Istituto per la Scienza e la Tecnologia dei Plasmi (ISTP-CNR) is modelled using the SOLPS-ITER boundary plasma package. This thesis has provided an improved tool for the analysis of plasma-material interaction (PMI) in GyM to compare and complement the experimental activities. Specifically, the analysis focused on the investigation of helium plasma experiments, expanding the database for plasma-neutral interactions with the inclusion of charge exchange and collisional excitation of He atoms. These reactions proved to be especially important in low-temperature mildly ionised plasmas as in GyM.

The operation of tokamaks in helium plasma is also important to prepare ITER Pre-Fusion operation. An L-mode helium discharge in ASDEX-Upgrade tokamak is modelled using SOLPS-ITER. In particular, the work estimates the relative fraction of He^{+} and He^{2+} contributing to the ion flux onto different plasma-facing components, an im-

portant parameter to address PMI and erosion properties, however, difficult to estimate directly from experimental measurements.
Finally, this thesis addresses for the first time the investigation of plasma detachment in negative triangularity (NT) with SOLPS-ITER, by comparison to a standard positive triangularity (PT) case. The results of this work indicate that some of the differences observed experimentally between NT and PT can be justified only by considering the different shapes of the magnetic flux tubes. However, to reproduce the detachment suppression observed in NT density ramp experiments, a reduction of cross-field transport could be assumed in the model.

Keywords: nuclear fusion, edge plasma, linear plasma device, tokamak, helium, plasma exhaust, modelling

Estratto

Il controllo e la mitigazione dei carichi termici indotti dall'interazione tra il plasma che sfugge al confinamento e la prima-parete della macchina sono fondamentali per garantire un funzionamento stabile ed economicamente sostenibile di un impianto a fusione nucleare. Un reattore basato sulla fusione nucleare a confinamento magnetico è composto da una camera da vuoto di forma toroidale, all'interno della quale il plasma termonucleare viene confinato grazie a campi magnetici e raggiunge temperature di centinaia di milioni di gradi Celsius. La regione periferica del tokamak è chiamata "plasma di bordo" ed è la regione di transizione tra il core plasma e la parete della camera. Questa è caratterizzata da forti variazioni dei parametri di plasma, turbolenza e dalla presenza di un plasma multi-componente, che include atomi, molecole e impurezze.
Questa tesi di dottorato ha lo scopo di approfondire ed ampliare lo studio di questi argomenti mediante strumenti modellistici, con particolare riferimento alla modellizzazione di macchine lineari, plasmi di elio e tokamak a triangolarità negativa. Questa analisi è di estrema attualità nel contesto della ricerca volta a preparare il funzionamento di ITER e per la progettazione del primo reattore DEMO.
La macchina lineare GyM dell'Istituto per la Scienza e la Tecnologia dei Plasmi (ISTP-CNR) è stata modellizzata utilizzando il codice SOLPS-ITER. Questa tesi ha reso disponibile uno strumento ottimizzato per lo studio dell'interazione plasma-parete in GyM, a complemento e supporto delle attività di natura sperimentale. Nello specifico, l'analisi presentata è legata allo studio di plasmi di elio, proponendo l'ampliamento del database di reazioni di interazione tra plasma e neutri. Nelle condizioni del plasma di GyM, caratterizzato da bassa temperatura ionica e grado di ionizzazione, le reazioni di scambio di carica ed eccitazione collisionale degli atomi di He sono risultate particolarmente importanti.
Il funzionamento di tokamak con plasmi di elio è un altro argomento rilevante in virtù della preparazione della Pre-Fusion Operation Phase di ITER. In questa tesi si è analizzata una scarica di puro elio in modo-L in ASDEX-Upgrade utilizzando il codice SOLPS-ITER. In particolare, l'analisi ha portato alla stima della frazione di ioni He^{+} ed He^{2+} nel plasma. Questo parametro è importante per stimare le caratteristiche di erosione dei materiali della prima parete e, tuttavia, non è facilmente ricavabile da dati

sperimentali.
Infine, per la prima volta si è condotto uno studio di plasma detachment in un tokamak con triangolarità negativa usando SOLPS-ITER. All'interno dell'analisi è stato fatto un confronto tra triangolarità positiva e negativa che ha mostrato come alcune delle differenze osservate sperimentalmente possano essere spiegate considerando la diversa forma delle superfici di flusso magnetico. Tuttavia, la soppressione del detachment in triangolarità negativa osservato sperimentalmente potrebbe essere spiegato con una riduzione del trasporto perpendicolare.

Parole chiave: fusione nucleare, plasma di bordo, macchine lineari, tokamak, elio, analisi modellistica

Contents

Summary

Thermonuclear fusion is one of the key technology that could play a role in sustaining an energy system with net-zero emissions in the next centuries. This process is based on the fusion of two light nuclei to form a heavier, more stable product, releasing energy. Among the various nuclear fusion reactions, the one between deuterium and tritium nuclei, yielding helium and a fast neutron, has the highest reaction probability at the lower energy and it is thus considered the most feasible. Fusing together two nuclei, however, requires overcoming the Coulomb barrier. Nuclei have to be supplied with tens of keV of thermal energy, corresponding brings the system to hundreds of millions of degrees Celsius. At these temperatures, the atoms dissociate in electrons and ions, forming the so-called plasma state. Today most of the fusion power-plant-oriented research is based on the tokamak concept, which exploits a magnetic field to confine the plasma in a toroidal chamber. The ITER tokamak, under construction in France, is the most ambitious international project on fusion and aims at operating the first experimental fusion reactor capable of producing a 10-fold fusion energy gain.

Among the various challenges that the design and operation of a magnetic nuclear fusion power plant face, this thesis focuses on power exhaust and plasma-wall interaction (PWI). Indeed, plasma confinement by the $\vec{B}$ field is imperfect. Particles diffuse radially across the magnetic flux surfaces ultimately reaching the wall of the torus. The mitigation of the particles and power loads onto the plasma-facing components (PFCs) is crucial to operating a tokamak ensuring steady-state output power while avoiding excessive degradation of the first wall material and impurity contamination of the main plasma.
Presently, there are several tokamaks in operation worldwide which have many relevant plasma parameters close to reactor conditions. However, concerning the PWI properties, there are still significant gaps in some crucial parameters, like ion fluxes and fluences at the strike point and temperature of the PFCs. *Linear plasma devices* (LPDs) offer the possibility of closing these research gaps by emulating the conditions of plasma-material interaction (PMI) in fusion plasmas which can not be reached in today's tokamaks. LPDs are thus ideal to test material erosion and other plasma-wall interaction processes under well-defined and controlled conditions.

A relevant concern of PMI is dealing with helium plasma in a tungsten environment. Under specific conditions of material temperatures, fluxes and fluences, He ions lead to the formation of nanostructures on the surface of tungsten. This phenomenon is known as *tungsten fuzz (W-fuzz)*. The nanostructures modify the erosion properties of tungsten PFCs, thus being of particular concern for the working condition of the ITER W-divertor. In ITER, indeed, helium ash will be present in the plasma mixture during the D-T active phase and, more importantly, He will be used as the main plasma species during the Pre-Fusion Operation Phases. Controlled experiments investigating the formation conditions for W-fuzz are performed in linear plasma devices. Moreover, very recently experimental campaigns with helium plasmas were performed in ASDEX-Upgrade and JET tokamaks to answer whether W-fuzz can be observed in present-day experiments, if it is expected under ITER operational conditions and how its presence affects the plasma operation.
Finally, alternative magnetic configurations for tokamak scenarios with improved confinement and reduced PWI impact are of great interest for the design of next-generation fusion reactors. Among these, negative triangularity (NT) is considered very promising, besides only a few tokamaks can operate with NT equilibria. Experimental observations on TCV and DIII-D tokamaks showed that this configuration may exhibit increased plasma confinement with respect to analogous positive triangularity (PT) discharges. Concerning the edge plasma behaviour and the PWI properties, however, NT configurations are still understudied if compared to standard PT scenarios.

Motivations and goals of this thesis

Understanding, predicting and mitigating plasma-wall interaction and the resulting particle and heat loads on the divertor and first wall is a crucial requirement for a fusion reactor. To investigate a complex system such as the edge plasma of a magnetically confined plasma numerical tools are also essential. Sophisticated numerical codes describing plasma transport within the boundary region of a tokamak are indeed needed for interpreting experimental results and for making predictions in the design phase of new machines.
To further the understanding of the theoretical framework of boundary plasma and plasma-material interaction modelling, this thesis work aims to extend the applicability of standard boundary plasma codes to non-standard conditions. In particular, the work focused on improving the available modelling tools to describe linear plasma devices, which constitute an asset for the research on material for the PFCs of future fusion reactors. In light of the ITER Pre-Fusion Operation Phases, the investigation of helium

plasma properties is crucial, especially concerning the behaviour of the edge plasma and its interaction with PFC materials, tungsten in particular. In this thesis, these aspects are investigated through modelling both in linear device and tokamak geometries. Finally, following the recent interest in negative triangularity as a promising configuration for the development of reactor-relevant scenarios, this thesis presents a study of plasma detachment in negative triangularity, in comparison with standard positive triangularity scenarios.

Structure of the thesis

The PhD thesis is organized as follows:

Part I: Introduction and thesis goals introduces the general framework connected to the edge plasma of magnetic confinement devices and its modelling and summarises the goals of this thesis work. **Chapter 1** gives a general overview of the current research status on magnetic confinement fusion, with particular emphasis on boundary plasma and plasma-wall interaction. **Chapter 2** summarises the status of the available physical models to describe the edge plasma in a tokamak, addressing the aspects of plasma transport, plasma-neutrals interactions and plasma-wall interactions. **Chapter 3** highlights the goals and the methods used to develop this thesis work. This includes a general description of the two numerical tools exploited within this work, namely the SOLPS-ITER and GBS boundary plasma packages, as well as some original methodological aspects developed within the thesis.

Part II: Plasma dynamics and plasma-wall interaction in LPDs collects the achievements in developing an extended modelling framework to describe linear plasma devices. Specifically, **Chapter 4** investigates the possibility of successfully applying SOLPS-ITER to linear geometry. It presents a benchmark of the simulation results with the available experimental data of the GyM linear machine and with a newly developed global 0D model to describe He plasma in linear geometry. This simplified model helped share light on the relevant plasma-neutral interaction processes of relevance for low-temperature helium plasmas. Finally, the first global erosion and impurity migration study in a linear device is presented. **Chapter 5** discusses the benchmark of the SOLPS-ITER and GBS cross-field transport models in a linear geometry. The benchmark includes the comparison of the equations solved by the SOLPS-ITER and GBS plasma transport models in linear geometry and a benchmark of results obtained simulating the same system with the two codes.

Part III: Modelling edge plasma in tokamaks extends many of the competencies acquired by modelling LPDs to tokamaks. In particular, the SOLPS-ITER boundary code package is used to investigate helium plasma in the ASDEX-Upgrade **Chapter 6** presents our strategy to produce an L-mode helium plasma background with SOLPS-ITER to be used for the modelling of a global PMI experiment in ASDEX-Upgrade. The chapter includes the benchmark with the available AUG experimental data and a discussion of the importance of He^{+} and He^{2+} fluxes onto the PFCs. **Chapter 7** is devoted to the first numerical study of plasma detachment in a TCV negative triangularity configuration performed with SOLPS-ITER. The study includes the benchmark of the simulations with TCV experimental data of a negative triangularity discharge, the comparison with a positive triangularity discharge with similar parameters and the investigation of detachment properties through the modelling of a density ramp experiment.

Publications and research activities

The contents of this PhD thesis are published in the following peer-reviewed articles:

- M. Sala, **E. Tonello**, A. Uccello, X. Bonnin, D. Ricci, D. Dellasega, G. Granucci, M. Passoni, "Simulations of Argon plasmas in the linear plasma device GyM with the SOLPS-ITER code", Plasma Physics and Controlled Fusion, 62 055005 (2020). Personal contribution: derivation of the theoretical model, development of SOLPS-ITER numerical simulations and post-processing, contribution to manuscript writing and figure production.
- **E. Tonello**, A. Formenti, G. Alberti, A. Uccello, M. Passoni, "A point plasma model for linear plasma devices based on SOLPS-ITER equations: application to helium plasma", Nuclear Fusion, 61 066036 (2021) Personal contribution: derivation of the theoretical model, implementation of the numerical solution of the model in Matlab, development of SOLPS-ITER numerical simulations and post-processing, contribution to manuscript writing and figure production.
- G. Alberti, **E. Tonello**, P. Carminati, A. Uccello, X. Bonnin, J. Romazanov, S. Brezinsek, M. Passoni, "Global SOLPS-ITER and ERO2.0 coupling in linear devices: study plasma-wall interaction in helium plasma", Nuclear Fusion, 63 026020 (2023). Personal contribution: development of SOLPS-ITER numerical simulations and post-processing, implementation of the coupling strategy between SOLPS-ITER and ERO2.0 in Matlab, contribution to manuscript writing and figure production.

and in the following conference proceeding:

- M. Sala, **E. Tonello**, A. Uccello, X. Bonnin, D. Ricci, D. Dellasega, G. Granucci, M. Passoni, “SOLPS-ITER simulations of the GyM linear plasma device”, 46 EPS Conference on Plasma Physics (2019)

Other contributions were presented to the following international conferences and workshops:

- 46th Conference on Plasma Physics, EPS 2019 (8-12 July 2019, Milano). **Poster contribution** entitled “SOLPS-ITER simulations of the GyM linear plasma device”
- FuseNet PhD Event 2020 (23-24 November 2020, Online event). **Oral contribution** entitled “Modelling of Plasma-Wall Interaction in magnetic Nuclear Fusion System”. The presentation took part in the competition for best presentation and it has been nominated among the 4 finalists.
- PSI-24 International Conference on Plasma Surface Interactions in Controlled Fusion Devices (25-29 January 2021 - Online event). **Poster contribution** entitled “ERO2.0 and SOLPS-ITER modelling of rough W coatings exposures to He plasmas in the linear machine GyM”
- Workshop on Atomic and Molecular Data Needs for Plasma Applications (13-15 April 2021, Online event). **Poster contribution** entitled “A global plasma model for linear plasma devices based on SOLPS-ITER equations”
- PSI-25 International Conference on Plasma Surface Interactions in Controlled Fusion Devices (13-17 June 2022 - Online event). **Poster contribution** entitled “Modelling plasma dynamics in linear plasma devices using the SOLPS-ITER and GBS codes”
- FuseNet PhD Event 2022 (4-6 July 2022, Padova). **Oral contribution** entitled "Modelling plasma dynamics in LPDs with 0D, 2D and 3D approaches”.
- 32nd Meeting of the ITPA - Divertor and Scrape-off layer Topical Group (Cadarache, 24-28 October 2022). **Oral contribution** entitles "SOLPS-ITER modelling of pure helium plasma background for PMI experiments in ASDEX-Upgrade "
- SOLPS-ITER Workshop (14-18 November 2022, Leuven).

and Summer Schools:

- LaPlaSS2020 - 3rd Laser-Plasma Summer School (14-18 September 2020, Online event)

- 9th Summer School Plasma in super-intense laser fields (1-11 July 2022, Erice), **Poster contribution** entitled "Modelling plasma dynamics with 0D, 2D and 3D approaches".

This thesis work was funded by the European Union via the Euratom Research and Training Programme. A consistent part of the work was developed to support experimental activities in the context of the EUROfusion Work Packages Tokamak Exploitation (WP-TE) and Plasma-Wall Interaction and Exhaust (WP-PWIE). Additionally, part of the outcomes of this thesis was carried out during a 4-month research stay at École Polytechnique Fédérale de Lausanne - EPFL (1st November 2021 - 5th March 2022 Lausanne, Switzerland).

PART I:

Introduction and thesis goals

1 | Nuclear fusion research

This chapter introduces the framework under which this doctoral thesis is developed.

Nuclear fusion is one of the low-carbon energy-producing technology that could play a role in sustaining a net-zero emission energy system in the next centuries.
Research on nuclear fusion is particularly active in these years. ITER, the first experiment designed to sustain and control a nuclear fusion reaction, is in its assembly phase and the first plasma is due in 3 to 5 years. To support ITER preparation, several experimental and computational facilities are in operation in Europe and around the world. In the latest years, moreover, many nuclear fusion startups are also being developed, driving the first private investments into the sector.
Among the various challenges of designing and operating a nuclear fusion power plant based on magnetic confinement of the plasma, this thesis focuses on the power exhaust and plasma wall interaction. This introductory chapter aims to present the basic concepts related to these topics, which will be needed for the following discussion.

1.1. Why nuclear fusion?

The world needs low-carbon energy sources to replace fossil fuels which today represent around 80% of the world's primary energy supply [1]. According to the latest report of the International Energy Agency (IEA) [2], the goal of reaching net-zero emissions by 2050 will be achieved by a massive deployment of renewable energy sources to decarbonise the electricity sector. Electrification and H_2-based fuels shell be implied for transportation and industry, together with the widespread use of the Carbon Capture, Utilisation and Storage (CCUS) technologies to tackle emissions from existing assets that could not be decarbonised. Among the low-carbon nuclear technologies, nuclear fission will have a role in the next three decades. In the same period, however, nuclear fusion is on track to be proven a feasible energy source, with the finalisation of the ITER experiment [3]. Many features indeed make this technology desirable to play a role in a net-zero emission energy system in the next centuries.

Nuclear fusion is a nuclear reaction in which two light nuclei are fused together to produce a heavier and more stable product. The mass defect between the sum of the original nuclei and the products is released as kinetic energy of the latter. Similarly to nuclear fission, the typical energy gain per reaction is of the order of several MeV, around a million times higher than the energy gain of chemical combustion reactions. This energy is extracted from the system by recovering part of the kinetic energy of the fusion products and transforming it into heat and/or electricity.
Among the various fusion reactions, the one between deuterium and tritium nuclei, yielding helium and a fast neutron, has the highest reaction cross-section at the lower energy and it is thus considered the most feasible. Indeed, to overcome the Coulomb barrier nuclei have to be supplied with tens of keV of thermal energy. At these temperatures, the atoms dissociate in electrons and ions, forming the so-called plasma state. Plasma confinement is the first challenge to be faced in designing a fusion reactor. In the last six decades, two confinement strategies have been investigated: inertial and magnetic confinement. Presently, the latter is the most power-plant-oriented.

The main features that make nuclear fusion attractive as an energy source are the availability of fuel, the high energy density typical of nuclear technologies and the absence of long-living radioactive waste. A D-T nuclear fusion power plant is fueled with deuterium, a stable hydrogen isotope which can be extracted from water. Tritium, on the other hand, is radioactive with a short decay time and needs to be bred inside the reactor. The development of a tritium breeding system based on Li-n reactions is thus part of a D-T fusion reactor concept.
Radioactive waste produced by nuclear fusion is related to neutron-induced materials activation and tritium permeation and it is thus limited to short to medium-living radioactive elements.

1.2. Magnetic confinement of plasmas

Magnetic confinement fusion (MCF) aims at producing a thermonuclear burning plasma by confining the fuel in high external magnetic fields. Starting from the Sixties, several magnetic topologies were investigated. Today, most of the MCF research is based on two toroidal confinement configurations: the tokamak and the stellarator. This thesis will only focus on the first one.

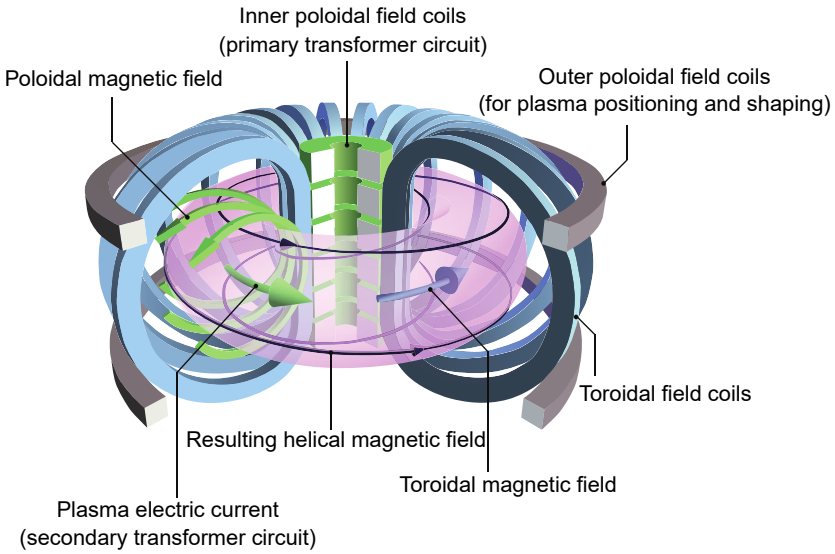

Figure 1.1: Structure of a tokamak and its key components from [5].

Tokamaks

The tokamak is the most developed concept of magnetic confinement device aiming at achieving controlled nuclear fusion [4]. The main elements of a tokamak are shown in figure 1.1: a toroidal vacuum chamber with inner (central solenoid) and outer poloidal field coils (PF-coils) and a set of toroidal field coils (TF-coils), poloidally wrapped around the vacuum chamber. The TF-coils generate the toroidal magnetic field B_ϕ ($\sim$T range). The inner poloidal coils drive the toroidal plasma current I_p ($\sim$MA range), which in turn induces the poloidal magnetic field component B_θ. The outer PF-coils also contribute to B_θ but their main purpose is to control the plasma shaping. The total tokamak magnetic field is:

$$\vec{\mathbf{B}} = \vec{\mathbf{B}}_\phi + \vec{\mathbf{B}}_\theta \qquad \text{with } B_\phi \gtrsim 10 B_\theta \tag{1.1}$$

The induction mechanism exploited to drive the plasma current makes the tokamak intrinsically a pulsed device. Presently, tokamak discharge times are in the range of $\approx 1 - 1000$ s, depending on the device's capabilities and the magnetic coil technology. The pulse duration in future power plant reactors will have to be extended to ≈ 1 hour.

Plasma heating

Besides being confined, the plasma needs to be heated to temperatures of the order of $\sim$ 10 keV to study fusion-relevant conditions. The tokamak heating systems are usually divided into *Ohmic heating* and *additional heating systems*.

Ohmic heating is the power absorbed by the plasma due to Joule dissipation of the toroidal current and it is thus associated with a finite plasma resistivity. Plasma electrical resistivity η, however, decreases with increasing plasma temperature $\propto T_e^{-3/2}$, hence making Joule dissipation less effective at high temperatures.
For this reason, plasma temperatures that can be reached with Ohmic heating alone are limited. Tokamak discharges in which only Ohmic heating is used are referred to as *Ohmic discharges*.
To reach fusion-relevant conditions, other heating systems are required. Additional heating power can be provided by injecting high-energy neutral particles into the plasma or by shining electromagnetic waves in the frequency range of radio or microwaves.
Neutral beam injection (NBI) heating is based on the acceleration of ions (H isotopes or He, typically) to energies of $\sim$ 100 keV - 1 MeV and their injection into the plasma, after being neutralised. The resulting neutral beams are not deflected by the magnetic field and can reach the region where plasma is confined. Collisions between energetic neutrals and plasma ions result in an efficient energy transfer in favour of the latter.
Besides being a heating mechanism, NBI also contributes to plasma fueling and can be used to diagnose plasma properties.
Radio and microwave heating exploit different resonant mechanisms between the electromagnetic wave and the plasma. The two most important ones are:
Electron cyclotron resonance heating (ECRH) uses microwaves in the range 30-170GHz, that resonate with the electron-cyclotron frequency $\omega_{L,e}$.
Ion cyclotron resonance heating (ICRH) uses radio-frequency in the range 20-100MHz that can resonate with the ion cyclotron motion $\omega_{L,i}$.

High confinement mode (H-mode)

Providing additional power to the plasma is desirable not only to increase its temperature but also to enter the *high-confinement* (H-mode) plasma regime. The transition from *low-to-high confinement regimes* (L-H transition) was first observed in ASDEX tokamak [6] at the end of the Eighties. When the heating power raises above the *L-H transition power threshold* $P_{\mathrm{L-H}}$ [7], the energy confinement time τ_E almost suddenly doubles and the core plasma density and temperature increase. The rise in n_e and T_e, hence the improved particle and energy confinement, is localised in the very edge of the tokamak. Steep density and temperature gradients arise, which are ascribed to the formation of an edge transport barrier. The qualitative behaviour of radial plasma pressure profiles in L-mode and H-mode is shown in figure 1.2.

Improved confinement is desirable for the operation of a fusion reactor. However, H-mode plasmas are also characterised by magnetic-hydro dynamics (MHD) instabilities, known as *edge localised modes* (ELMs) [8, 9]. ELMs are fast and periodic relaxations of the transport barrier, which cause the ejection of particles and power from the core to the edge plasma and ultimately to the tokamak wall. The investigation of alternative configurations with H-mode grade confinement and which exhibit the partial or total suppression of ELMs is appealing for the operation of fusion reactors [10, 11]. A possibility in this direction seems to be the operation of tokamaks with negative triangularity magnetic configuration [12]. This topic will be the focus of the analysis presented in chapter 7 of this thesis.

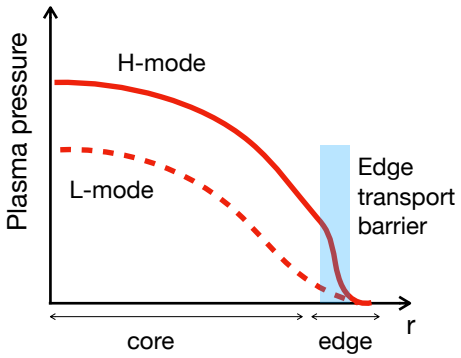

Figure 1.2: Radial plasma profiles in L-mode and H-mode.

1.2.1. Overview of the European tokamaks

Part of the work of this thesis project was done in the context of the EUROfusion Programme. EUROfusion is a consortium among the European Union member states[1] and Switzerland to support and fund fusion research activities on behalf of the European Commission's Euratom programme.
A consistent part of the work performed in this thesis aimed at supporting the activities of the EUROfusion Work Package Tokamak Exploitation (WP-TE) and Plasma-Wall Interaction and Exhaust (WP-PWIE). In particular, the main objective of WP-TE is to provide the physics basis for fusion reactor operational scenarios, exploiting machines of different capabilities, sizes and parameters available in different European facilities. Five tokamaks are presently part of WP-TE:

JET (Culham, United Kingdom)

The *Joint European Torus* (JET) is the largest experimental tokamak in the world and it is one of the only two devices that has operated with a deuterium/tritium mix plasma. Between 2009 and 2011 JET has been the object of a major upgrade to substitute its graphite wall with a tungsten/beryllium *ITER-like wall* to test plasma-wall interaction in ITER-like conditions [13–16]. The results of the latest D-T campaign in 2021 detain the

[1] At the time EUROfusion was founded (2014) EU included also the United Kingdom.

record of fusion power ever produced by a controlled fusion experiment [17]: 59 MJ of energy with a pulse duration of 5 s, overcoming the 1997 record obtained with the C-wall.

ASDEX-Upgrade (Garching, Germany)

The *Axially Symmetric Divertor Experiment* (ASDEX-Upgrade or AUG) [18] was first designed to study plasma boundary and first wall problems in diverted reactor-relevant configurations. AUG is presently equipped with a full-tungsten wall and can investigate ITER-like high power loads at the reactor wall. In 2013, an upgraded divertor structure was installed in AUG together with a large divertor manipulator [19] which allows retracting and exchanging two adjacent divertor tiles without breaking the vessel vacuum. This tool makes AUG a crucial asset for plasma-material interaction experiments in reactor-relevant conditions.

TCV (Lausanne, Switzerland)

The *Tokamak à configuration variable* (TCV) is characterized by a highly elongated and rectangular vacuum vessel which can accommodate a large variety of plasma shapes. The most classical single null (SN) magnetic topology can be investigated in a wide range of different parameters, including lower and upper single null with negative and positive triangularities. Other reactor-relevant plasma shapes that can be investigated are double null (DN), snowflakes (SF) and Super-X (SX) configurations.
To allow high magnetic flexibility, the machine is not provided with an actual divertor structure. However, a major upgrade of TCV in 2019 concerned the installation of removable gas baffles that partially separate the vessel into main and divertor chambers [20, 21].

MAST Upgrade (Culham, United Kingdom)

The *Mega Ampere Spherical Tokamak* (MAST) is a pioneer of the research into spherical tokamaks (STs) [22]. STs are tokamaks with a very narrow aspect ratio and an almost spherical plasma volume. They are an appealing alternative to conventional tokamaks for building compact machines and hence smaller and cheaper fusion power plants in the future. Starting in 2013, MAST underwent a major upgrade to allow the investigation of *alternative divertor configurations*. This results in MAST Upgrade, the first tokamak installing a divertor tailored for the *Super-X configuration* [23, 24].

Table 1.1: The European tokamaks of the Tokamak Exploitation Work Package (WP-TE) and their main characteristics: major radius R_0, maximum toroidal field B_ϕ, maximum plasma current I_p, total power that can be supplied to the plasma, pulse duration and first-wall materials. Data are taken form [25]. TCV and AUG tokamaks are considered in the context of this thesis and the corresponding features are highlighted in light blue.

	TCV	**ASDEX-Upgrade**	**MAST-U***	**WEST**	**JET**
R_0 (m)	0.89	1.65	0.85	2.50	2.96
B_ϕ (T)	1.54	3.2	0.8 (0.65)	3.7	3.4
I_p (MA)	1.2	1.4	2 (0.75)	1	5
Additional power (MW)	6.5	34	11 (8.7)	15	51
Pulse duration (s)	2.5 (max. 4)	10	2 (max. 5)	up to 1000	up to 60
Superconducting magnets	-	-	-	✓	-
First wall materials	C	W	C	W	ITER-like (W - Be)

* Data refer to design values from [25], while the 2022 campaign status is in brackets.

WEST (Cadarache, France)

The *W-Environment in Steady-state Tokamak* (WEST) is the upgrade of the Tore Supra tokamak [26], with a full-tungsten wall and a divertor configuration. It is the only EUROfusion WP-TE tokamak equipped with superconducting coils, that allows for long pulse (steady-state) operation. The main aim of this facility is the investigation of steady-state tokamak operation with actively cooled plasma-facing components [27].

A summary of the main parameters of the different machines is reported in table 1.1. WP-TE will also include the Divertor Tokamak test (DTT) facility, under construction in Frascati (Italy) [28, 29].

1.2.2. ITER

At present, all the tokamaks operating worldwide are not designed to produce fusion power. The first machine with this purpose is ITER, presently under construction in Cadarache (France). ITER (*"The Way"* in Latin) is considered one of the most ambitious energy projects around the world today. It is a collaboration of the seven ITER

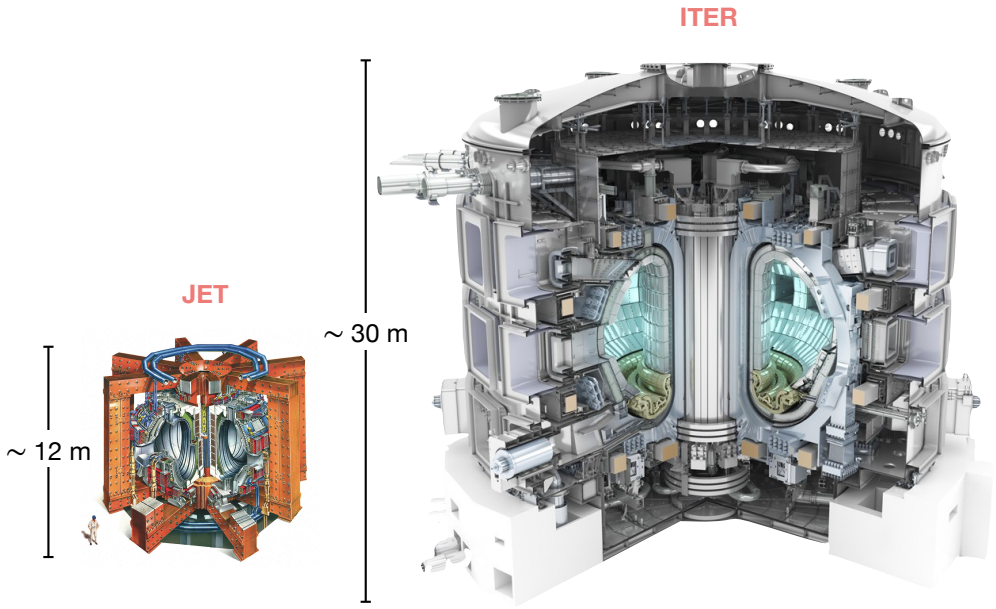

Figure 1.3: The JET (Joint European Torus) tokamak, which is the world's largest operating tokamak, compared to ITER, under construction at Cadarache, France.

Members: EU[2], India, China, Japan, Russia, South Korea and the United States.
ITER is designed to provide the first self-sustained thermonuclear burning plasma, exploiting the D − T fusion reaction. Its main goal is to demonstrate a ten-fold fusion energy gain (Q = 10) with a total output thermal power of $P_{\text{fus}}^{th} \simeq 500\,\text{MW}$. The success of the ITER project would be a milestone in fusion energy research, proving the feasibility of nuclear fusion as an energy source and leading the way to the first demonstrative power plant (DEMO) and, ultimately, the commercialization of fusion power.

If compared to existing ones, ITER will be by far the largest and more powerful tokamak in the world. In figure 1.3, ITER size is compared to JET, which is the present world's largest operating tokamak. The ITER baseline scenario with Q = 10 and a total output power of $P_{th} = 500$ MW is designed with a plasma current of $I_p = 15$ MA and a maximum magnetic field of $B_\phi = 5.3$ T, sustained by fully super-conducting coils. To obtain the desired gain and P_{th}, a total additional power ≈ 50 MW will be provided to the plasma. Total external input power installed in ITER, however, will be ≈ 73 MW, including two

[2]EU-27 + Switzerland and the United Kingdom. Non-Member technical cooperation agreements are also in place with other Countries - Australia, Canada, Kazakhstan and Thailand - international organizations, national laboratories, universities and schools.

neutral beam injectors (16.5 MW each), two ion cyclotron resonant heating antennas (10 MW each) and 24 gyrotrons for electron cyclotron heating (approximately 20 MW in total). In terms of pulse duration, the baseline Q = 10 inductive scenario has $\tau \simeq 300-500$ s. A second non-inductive scenario is also foreseen, with $Q \approx 5$ and a longer pulse duration ($\tau \simeq 1000 - 3000$ s).

ITER research plan, as presented in 2018, is divided into four Operational Phases [3]:

- *First Plasma:* plasma breakdown in hydrogen or helium with at least 100 kA of plasma current for at least 100 ms.
- *Pre-Fusion Power Operation 1 (PFPO-1):* diverted plasma operation in hydrogen or helium up to at least I_p = 7.5 MA and B_ϕ = 2.65 T. Additional heating systems available during this phase: ECRH (up to full power) and ICRH (up to half power).
- *Pre-Fusion Power Operation 2 (PFPO-2):* commissioning of the NBI system, both for heating and diagnostic purposes, and full power ICRF system. Development of H-mode operation in hydrogen or helium and systematic studies of plasma-wall interaction issues, including erosion of the plasma-facing components, redeposition, dust production, fuel retention and fuel removal.
- *Fusion Power Operation (FPO):* demonstrate the operation of high-power H-modes in deuterium to prepare plasma scenarios for DT operation. Gradually transition from D-only to trace-T to full DT operation.

From this research plan, it is clear that helium plasma will have a central role in ITER operation, not only as ash from D-T fusion reactions but also, presumably, as the main plasma species in PFPO-1 and PFPO-2. For this reason, investigation of plasma-wall interaction and operation in helium plasmas of existing tokamaks is one of the priorities of the fusion community these years. The work presented in chapters 4 and 6 is done within this context.

1.3. Plasma exhaust and plasma-wall interaction

One of the technical challenges to the development of a nuclear fusion reactor is the *plasma and power exhaust* issue [30]. Indeed, operating a fusion reactor must ensure long pulse and steady-state operation while avoiding excessive degradation of the first wall material and without large impurity contamination of the main plasma.

1.3.1. The divertor

Since plasma confinement is imperfect, particles diffuse radially across the magnetic flux surfaces ultimately reaching the wall of the torus. Instead of letting cross-field transport distribute the power and particle fluxes all over the vessel chamber, most tokamaks today operate in the *diverted magnetic field configuration*, shown in figure 1.4. This configuration is characterised by the presence of at least one *X-point*, where $B_\theta = 0$. The magnetic flux surface that contains the X-point is called *separatrix*. Fluxes escaping the confined region, eventually cross the separatrix and enter the *scrape-off layer* (SOL), a narrow plasma layer that controls power deposition onto the *divertor*. The divertor is a crucial element in a tokamak which is designed to exhaust the particles and thermal loads coming from the main plasma.
Developing physical models able to describe the plasma behaviour across the separatrix and in the SOL and predicting the expected power deposited onto the wall and divertor is one of the great challenges that plasma boundary research aims to solve.

1.3.2. Plasma detachment

In typical reactor conditions, the power diffusing across the separatrix and flowing along the SOL results in peak-heat loads onto the divertor target that easily exceeds the tens of $\mathrm{MW\,m^{-2}}$. In general, the narrow the SOL, the higher the peak power load. Since a narrow scrape-off layer is however desirable in terms of core confinement, to avoid failure of the divertor materials, in reactor conditions almost the entire exhaust power has to be dissipated before reaching the divertor target. ITER's first design required $80\% - 90\%$ of the power dissipated upstream of the divertor and in DEMO the fraction grows to $\gtrsim 90\%$ [31, 32]. To do so, the reactor must operate in *detached conditions*.

Operationally, *plasma detachment* [33–35] from the divertor targets is achieved by a controlled increase of gas puffing, typically done from a valve in the divertor region. In today's tokamaks, this can be achieved either by puffing additional gas of the main plasma species or by adding extrinsic impurities ("seeding") [36]. Both strategy results in an increase of the average plasma density $\langle n_e \rangle$. In ITER, operation with N_2, Ne and Ar seeding is foreseen [3].
According to the puffing intensity and characteristics, qualitatively different profiles of plasma density and temperature at the strike points are observed and three plasma regimes can be identified: a) attached, or sheath limited, b) partially detached and c) detached. The qualitative radial profiles of electron density and temperature at the

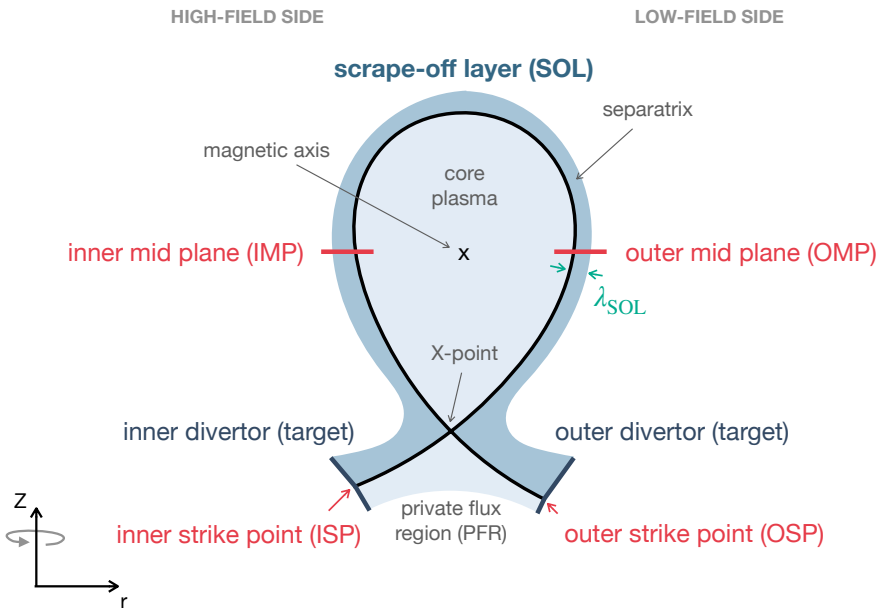

Figure 1.4: Poloidal cross-section of a diverted tokamak. This figure defines the scrape-off layer (SOL) and most of the plasma-edge and divertertor elements (and their acronyms), which will be largely used in the following of this thesis.

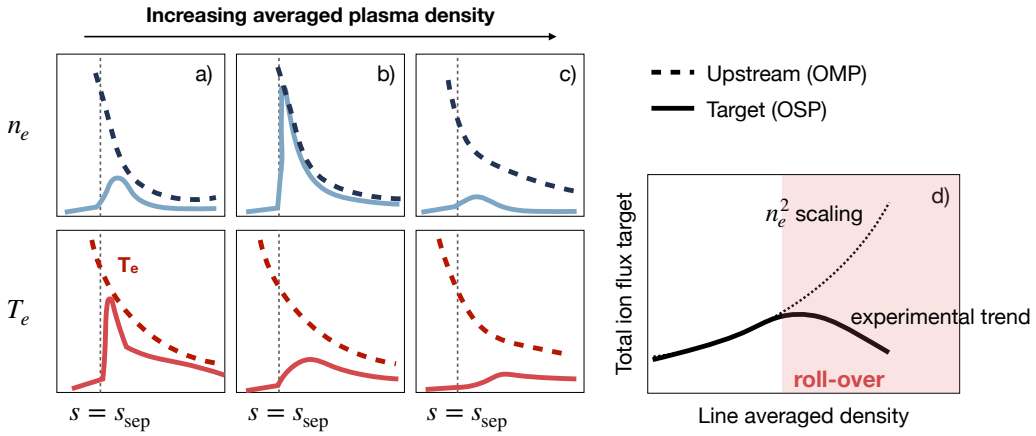

Figure 1.5: Qualitative electron density and electron temperature radial profiles upstream (dashed) and at the divertor target (solid) in **a)** sheath-limited, **b)** partially detached and **c)** detached regimes. **d)** Particle flux roll-over, is often used to identify detachment onset. The scaling $\propto n_e^2$ is derived from the Two-Point model (2PM) [30].

outer midplane (OMP) and outer divertor target are shown in figure 1.5 for each regime. *The attached regime*, which is also identified as a sheath-limited regime, is characterized by relatively low plasma density and constant temperature along a flux tube, which results in high peak temperature values $T_{e,\max}$ at the strike points. At increasing the gas puff, the *partially-detached* or high-recycling regime is entered. This is characterised by a decrease of $T_{e,\max}$ and an increase of the maximum electron (and ion) density at the strike points $n_{e,\max}$. Finally, when $T_{e,\max}$ drops below $\lesssim 5$ eV, plasma becomes *fully detached* and the ionization front moves further upstream the divertor target, resulting in the drop of $n_{e,\max}$.
The full-detachment onset is often identified by looking at the total ion flux profile at the target as a function of the line-averaged plasma density. The qualitative behaviour of this profile is shown in figure 1.5.d. Transition from partial to full detachment is attained in correspondence of the *flux roll-over*.

Further information on detachment physics and how the related phenomena are modelled is given in section 2.2.1.

1.3.3. Plasma recycling and erosion of the plasma-facing components

Strictly connected to the plasma exhaust is the plasma-wall interaction (PWI) problem [37]. When ions or neutrals strike a solid surface they may (i) be absorbed and trapped by the surface; (ii) be reflected; (iii) be adsorbed by the surface and released as a thermal particle with a velocity dependent on the surface temperature; (iv) release surface material through chemical or physical sputtering, producing intrinsic impurities; (v) induce secondary electron emission.

The balance of processes (i), (ii) and (iii) regulates the *fuel recycling process*. The main factors that influence fuel recycling are surface saturation, energy and incident angle of the plasma particles and the chemical species of both the ion and the wall material [38].
Erosion of the plasma-facing components (PFCs), process (iv), produces the release of impurities into the plasma. Transport of these intrinsic impurities upstream of the divertor, their ionization and trapping in the confined plasma is a concern since they cause radiative core cooling and fuel dilution that can prevent fusion conditions to be reached. The two processes that determine the erosion of the PFCs are physical and chemical sputtering [38]. The latter is relevant for hydrogenic plasmas in a carbon-wall environment [39]. After being transported within the plasma, eroded impurities will

eventually redeposit on the wall, changing the chemical and physical properties of the surface. If impurities can chemically react with the fuel, the latter is more likely to remain trapped and co-deposited on the PFCs together with the sputtered material [40]. In a D-T fusion reactor, fuel retention is an important concern since, besides reducing fuel availability, it leads to the accumulation of radioactive tritium in the wall [41].
The choice of the first-wall materials in a fusion reactor is thus crucial [42]. Low-Z materials would be preferable to reduce radiative losses and fuel dilution in case of impurities migration in the confined regions, while high-Z materials have usually a higher sputtering threshold [43]. Among the European tokamaks described in section 1.2.1, two of them have a full-metal (tungsten, W) high-Z wall (AUG and WEST), two have graphite (C) wall (TCV and MAST-U) and JET has an ITER-like wall, with a tungsten divertor and a beryllium (Be) first wall.

Further information on the PWI processes and their modelling is given in section 2.3.

1.4. The role of linear plasma devices (LPDs)

The discussion on PWI in section 1.3.3 highlights the importance of understanding phenomena related to plasma-material interaction (PMI) and testing materials to be used as PFCs in future fusion reactors [44]. Although most tokamaks in operation today have many relevant discharge parameters close to reactor conditions, there are still significant gaps in some crucial PWI parameters, like ion fluxes and fluences at the strike point and temperature of the PFCs. *Linear plasma devices* (LPDs) offer the possibility of closing these research gaps at moderate costs and with existing technologies. Emulating the conditions of fusion plasmas both at the first wall and in the divertor, LPDs are ideal to test material erosion, fuel recycling and plasma detachment. Unlike in complex tokamak experiments, indeed, each parameter influencing plasma-material interaction and sample erosion can be independently tailored in LPD experiments providing a reproducible and controlled environment for PMI experiments [45–47].

The structure of a linear device is simple if compared to tokamaks. A cylindrical vacuum chamber is surrounded by magnetic coils and the external current flowing in the azimuthal direction ($I_{\phi,\text{coils}}$) produces a magnetic field directed in the axial direction (B_Z). Samples of different materials, morphologies and compositions are exposed to the plasma column by using manipulators. These tools are usually flexible to change the pinch angle between the surface and the magnetic field and can control the sample surface temperature, using external heaters or cooling systems. One of the major

drawbacks of studying PMI in LPDs is that typical ion and electron temperatures are relatively low (few eV at maximum). To increase the incident ion energies at the target surface in a range for erosion studies to be performed, a negative bias voltage is applied to the sample. This leads to the acceleration of ions towards the material surface, which is reached with an almost mono-energetic distribution. In addition, many LPDs can also expose liquid samples to test the liquid-metal divertor concept [48, 49].

Two of the most advanced project in the context of LPD facilities for nuclear fusion research are the Magnum-PSI device at the PSI-Lab of the Dutch Institute for Fundamental Energy Research (DIFFER) [50, 51] and the Material Plasma Exposure eXperiment (MPEX) at the Oakridge National Laboratory [46]. The main goal of these facilities is to provide experimental conditions for testing PFC materials under regimes that are not achievable in present-day tokamak experiments. In terms of particles ($\gtrsim 10^{23}\,\mathrm{m^{-2}\,s^{-1}}$) and power fluxes ($\gtrsim 10\,\mathrm{MW\,m^{-2}}$) and fluences ($\gtrsim 10^{30}\,\mathrm{m^{-2}}$), they are designed to cover the exposure conditions expected for the divertor materials of ITER and next-generation fusion power machines. The MPEX device, moreover, allows the possibility of exposing previously neutron-irradiated materials to test PMI under neutron-induced damage.
A third LPD facility largely used for plasma-material interaction experiments within the EUROfusion programme is the PSI-2 device of the Forschungszentrum Jülich [52]. This is the pilot experiment for the JULE-PSI project [53], a LPD installed in the nuclear environment for the operation with neutron-irradiated and toxic materials. In PSI-2, the plasma source is based on arc discharge, which generates a plasma column of approximately ~ 6 cm of diameter and ~ 3 m long with density $\lesssim 10^{19}\,\mathrm{m^{-3}}$ and electron temperature $\lesssim 20\,\mathrm{eV}$. The ion flux on the samples ranges between $10^{20} - 10^{23}\,\mathrm{m^{-2}\,s^{-1}}$ and it is compatible with the values expected on ITER divertor. The PWI experiments considered in chapter 6 make use of samples that were pre-exposed in PSI-2.

1.4.1. GyM linear plasma device

The linear plasma device GyM is the object of the analyses presented in chapters 4 and 5 of this thesis. GyM is a medium-flux linear plasma device operating at Istituto per la Scienza e Tecnologia dei Plasmi (ISTP) of the Italian National Research Council (CNR) in Milano. The device was originally thought to investigate basic plasma physics and plasma turbulence [54–56]. Since 2014, however, it has been mainly used to study plasma-material interaction for nuclear fusion applications [57–68].

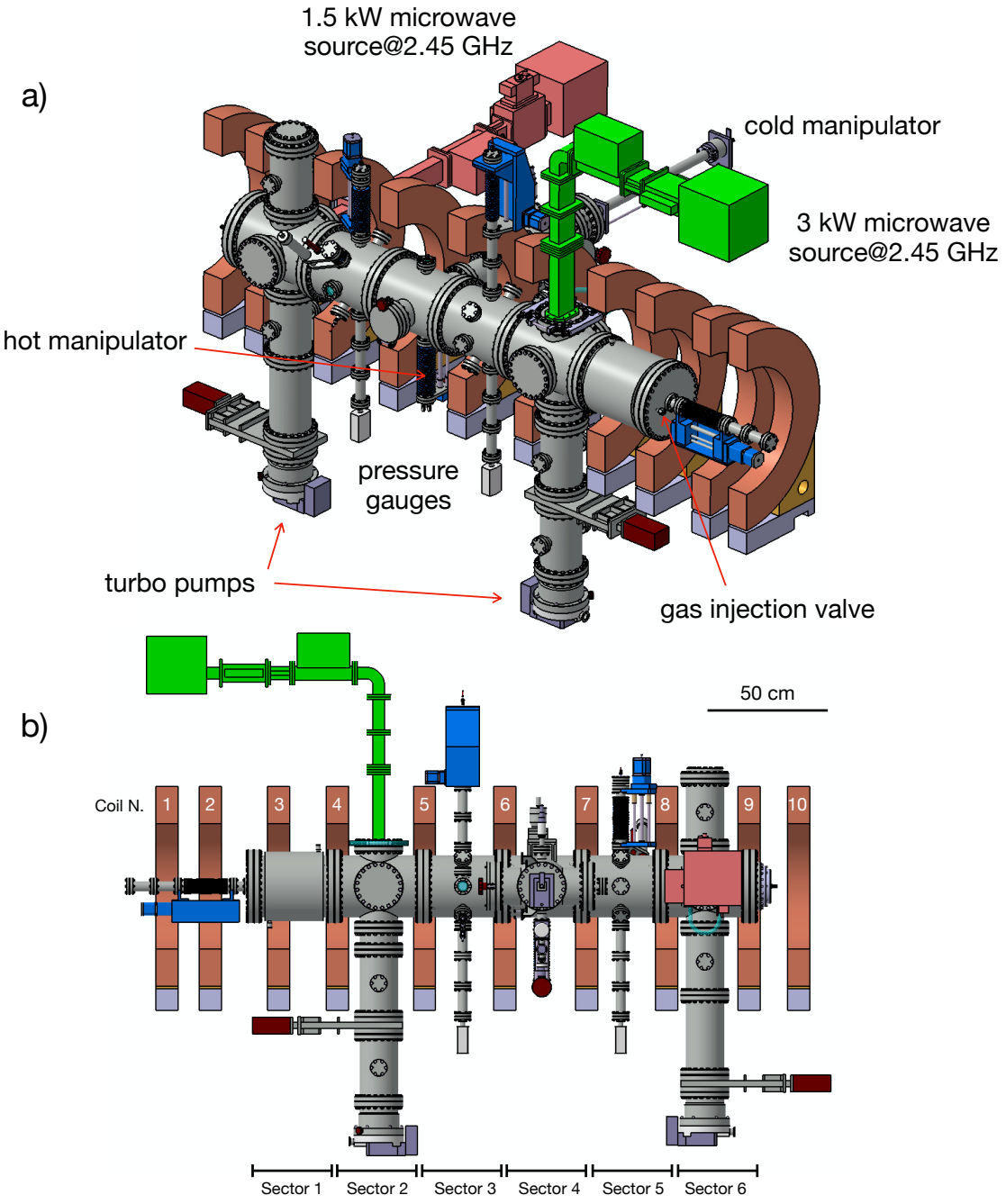

Figure 1.6: **a)** 3D rendering of the GyM linear plasma device (ISTP-CNR, Milano), showing the location of the ECRH sources, turbo-molecular pumps, gas injection valve, pressure gauges and manipulators for PMI experiments. **b)** Lateral view of GyM. The chamber sectors are indicated at the bottom of the figure. The LPs manipulators used to acquire experimental data discussed in section 4.2.3 were mounted on three CF40 in sectors 3, 4 and 5.

Table 1.2: Summary of the main operational and plasma parameters of GyM linear device located at ISTP-CNR, Milano.

Operational parameters	
Power sources	2 Magnetrons @2.45 GHz with P_{ext} = 1.5 kW and 3 kW
Magnetic field B_0 (T)	$\leq$0.13
Plasma diameter r_0 (m)	0.25
Base pressure (Pa)	5.0×10^{-6}
Working pressure p_0 (Pa)	$1.0 \times 10^{-3} - 1.0 \times 10^{-1}$
Puffing strength Γ_{puff} (particles/s)	$1.0 \times 10^{18} - 1.0 \times 10^{19}$
Plasma parameters	
Electron density n_e (m^{-3})	$\sim 1.0 \times 10^{17}$
Electron temperature T_e (eV)	≤ 15.0
Ion temperature T_i (eV)	$\lesssim 0.1$
Ion flux Γ_n ($m^{-2}s^{-1}$)	$\lesssim 1.0 \times 10^{21}$
Fluence* Φ_n (m^{-2})	$\lesssim 1.0 \times 10^{25}$

* Fluence after 7 hours of steady-state operation.

The machine consists of stainless steel (AISI 304L) cylindrical vacuum chamber, a pumping system with two turbo-molecular pumps, a gas injection system, 10 magnetic field coils, two magnetron sources at 2.45 GHz, a set of diagnostics and two manipulator systems for PMI experiments. The layout of GyM is shown in figure 1.6 and the main operational and plasma parameters are summarised in table 1.2.

GyM stainless steel vessel is divided into 6 sectors and it has a total length of $L \simeq 2.11$ m and a diameter of $2r_0 \simeq 0.25$ m. The nominal velocity of the two turbo-pumps is S = 500 L/s for helium gas and a baseline pressure of $p_{base} \simeq 5 \times 10^{-6}$ Pa can be reached. The working pressure is usually around $p_0 \simeq 10^{-3} - 10^{-1}$ Pa, depending on the puffing strength. The gas injection system can be fed with hydrogen, deuterium, helium, argon and nitrogen. Nitrogen-seeded deuterium (or hydrogen) plasmas were also investigated.

The two magnetron sources heat the plasma exploiting ECRH. At 2.45 GHz, the resonant magnetic field is B_{ECRH} = 0.0875 T. In standard operation, GyM works with $I_{\phi,coils}$ = 600 A and the resonant magnetic field B_{ECRH} is reached in sector 2 by modulating the axial distance between the coils.

The main diagnostic systems for monitoring the plasma background in GyM are a set of single Langmuir probes (LPs) with cylindrical tips of length 15 mm and diameter 1.5 mm, a high-resolution spectrometer and an ultra-fast camera. The monitoring of neutral gas impurities, e.g. NH_3 formed within nitrogen-seeded plasmas in presence

of W PFCs [68], can be investigated using a quadrupole mass spectrometer. The LPs can be installed on three CF40 linear shifts with remote-controlled stepper motors to collect measures at different radial positions and estimate the radial plasma profiles. In section 4.2.3, SOLPS-ITER simulations will be compared with experimental plasma profiles acquired using the three linear shifts systems mounted on ports 3U, 4U and 5U respectively on the upper part of sectors 3, 4 and 5 shown in figure 1.6.b.
If compared to other LPDs used for plasma-material interaction experiments, the peculiarity of the GyM LPD is given by its microwave plasma sources. These produce a fairly homogeneous plasma distribution within the cylindrical volume and in the radial direction, the plasma extends up to the lateral wall of the device $r_0 \simeq 0.125$ m. Plasma sources based on electromagnetic waves, like the GyM ECRH or MPEX helicon sources, guarantee a purer plasma with respect to arc source devices. In the latter, indeed, the plasma is contaminated by impurities produced at the electrodes of the source. This contamination characterises the plasma in high-density/high-flux arc devices, like the Magnum-PSI and PSI-2 described in section 1.4, and makes the interpretation of PMI experiments harder. However, the present 2.45 GHz ECRH source installed in GyM is able to produce only limited plasma densities $\sim 1.0 \times 10^{17}\,\mathrm{m}^{-3}$ and thus fluxes onto the sample $\lesssim 1.0 \times 10^{21}\,\mathrm{m}^{-2}\mathrm{s}^{-1}$. From the quantitative point of view, thus, GyM is able to reproduce PWI conditions expected on remote regions of the first wall of tokamak reactors but not close to the strike point. To increase the machine's performance in terms of plasma density and ion flux, an upgrade of the device is currently under study. This includes the installation of a 28 GHz gyrotron source and an additional plasma source based on helicon waves.

2 | Edge plasma modelling in tokamaks

Chapter 1 globally introduces many relevant aspects of magnetic confinement nuclear fusion, particularly related to the boundary plasma and PWI. This second chapter focuses instead on how those phenomena are modelled. The extremely wide problem of describing the complexity of the edge plasma in a magnetic confinement device is here divided into three main sub-problems: the modelling of *plasma transport* is described in section 2.1, *plasma-neutrals interaction* is the focus of section 2.2 and *plasma-wall interaction* is discussed in section 2.3.

2.1. Plasma transport

Plasma transport in the edge of magnetically confined plasmas is strongly anisotropic with respect to the magnetic field direction. As introduced in section 1.3.1, in a tokamak we can distinguish between a well-confined core region and the scrape-off layer, a narrow layer outside the separatrix characterised by magnetic field lines which terminate onto the divertor targets. This thesis focuses on the *edge plasma*, the region extending from the outermost part of the core radially outward in the scrape-off layer up to the first wall and downstream to the divertor targets.
When modelling the edge plasma, we are interested in describing the transport of particles, momentum and heat across the magnetic flux surfaces into the SOL and the flow towards the divertor and non-divertor materials. This description should likely include the dissipative mechanisms that contribute to the plasma heat loss towards the divertor and that are thus responsible for the detachment onset, as discussed in section 1.3.2.
Plasma transport along the SOL, in the direction parallel to $\vec{\mathbf{B}}$, is usually well described by a laminar fluid approximation driven by the sink action of the plasma-divertor interface. The description of cross-field transport, on the contrary, is one of the key missing points to provide a comprehensive and effective understanding of the problem.

2.1.1. Braginskii fluid model

The *fluid closure problem* is a well-known problem in fluid dynamics [69]. In plasma physics, one of the most adopted closures when dealing with the description of SOL plasma regimes is the one proposed by S. I. Braginskii in 1965 [70].
Braginskii fluid model describes a fully-ionized two-fluids plasma in an external magnetic field. The two plasma populations considered by Braginskii are electrons ($a = e$) and a single ion species ($a = i$). Conservation equations of density, momentum and total energy for the generic plasma species a are

$$\frac{\partial n_a}{\partial t} + \nabla \cdot (n_a \mathbf{u}_a) = 0 \tag{2.1}$$

$$\begin{aligned} \frac{\partial}{\partial t}(m_a n_a \mathbf{u}_a) + \nabla \cdot (m_a n_a \mathbf{u}_a \mathbf{u}_a) = \\ - \nabla p_a - \nabla \cdot \underline{\underline{\mathbf{\Pi}_a}} + q_a n_a (\mathbf{E} + \frac{\mathbf{v}}{c} \times \vec{\mathbf{B}}) + \sum_{a \neq a'} \mathbf{R}_{aa'} \end{aligned} \tag{2.2}$$

$$\begin{aligned} \frac{\partial}{\partial t}\left(\frac{3}{2} n_a T_a\right) + \nabla \cdot \left(\mathbf{q}_a + \frac{3}{2} n_a \mathbf{u}_a T_a\right) + p_a \nabla \cdot \mathbf{u}_a = \\ - \underline{\underline{\mathbf{\Pi}_a}} : \nabla \mathbf{u}_a + \sum_{a \neq a'} \left(Q_{aa'} - \vec{\mathbf{R}}_{aa'} \cdot \vec{\mathbf{v}}\right) \end{aligned} \tag{2.3}$$

The closure model is derived assuming that binary Coulomb collisions between electrons and ions happen frequently enough to relax the electron and ion distribution functions to *quasi-Maxwellian* distributions:

$$f_a = f_{Max,a} + f_a^1 \quad \text{with} \quad |f_a^1| \ll f_{Max,a} \tag{2.4}$$

where f_a^1 is a small-first order correction to the Maxwellian distribution $f_{Max,a}$ for the species a. In terms of collisional mean free paths λ_{coll}, consition (2.4) reads $\lambda_{\text{coll}} \ll L$, where L is the characteristic dimension of the system. As concerns the magnetic field strength, it is assumed that $\omega_a \tau_a \ll 1$, where ω_a is the gyro-frequency of species a and $1/\tau_a$ is its collisional frequency. With this hypothesis, Braginskii derived the following expressions to close the system of equations.

Friction force and heat exchange due to friction

Considering particle, momentum and energy conservation within collisions, the friction force experienced by electrons due to collisions with ions $\mathbf{R}_{ei}$ and the associated heat

transfer Q_{ei} are:

$$\mathbf{R}_{ei} = -\mathbf{R}_{ie} \tag{2.5}$$

$$Q_{ei} = -Q_{ie} - \mathbf{R}_{ei}\,(\mathbf{u}_e - \mathbf{u}_i) \tag{2.6}$$

The expression of the friction force on electrons $\mathbf{R}_{ei}$ is given by two contributions: $\mathbf{R}_u$, due to the existence of a relative velocity between electrons and ions $\mathbf{u} = \mathbf{u}_e - \mathbf{u}_i$, and $\mathbf{R}_T$, also referred to as *thermal friction force*, due to the gradient of the electron temperature T_e. Each force contribution can be decomposed into a component parallel to the magnetic field, denoted with $\|$, and one orthogonal to the magnetic field denoted with $\perp$. The unit vector along the magnetic field is indicated with $\vec{\mathbf{B}} = \vec{\mathbf{B}}/B$.

$$\mathbf{R}_u = -\frac{m_e n_e}{\tau_e}\left(0.51\mathbf{u}_\parallel + \mathbf{u}_\perp\right) = e n_e \left(\frac{\mathbf{j}_\parallel}{\sigma_\parallel} + \frac{\mathbf{j}_\perp}{\sigma_\perp}\right) \tag{2.7}$$

$$\mathbf{R}_T = -0.71 n_e\,(\mathbf{b}\cdot\nabla T_e) - \frac{3}{2}\frac{n_e}{\omega_e \tau_e}\,(\mathbf{b}\times\nabla T_e) \tag{2.8}$$

where the *current density* is defined as $\mathbf{j} \equiv -e n_e \mathbf{u}$, $\omega_e = eB/m_e$ is the electron gyro-frequency, τ_e is the electron-electron collision time and σ is the electrical conductivity. Heat transferred in collisions from electrons to ions is:

$$Q_{ie} = \frac{3 m_e}{m_i}\frac{n_e}{\tau_{ei}}(T_e - T_i) \tag{2.9}$$

Electron and ion heat fluxes

For electrons, the expression for the heat flux is given by $\mathbf{q}_e = \mathbf{q}_{e,u} + \mathbf{q}_{e,T}$, where:

$$\mathbf{q}_{e,u} = 0.71 n_e T_e \mathbf{u}_\parallel + \frac{3}{2}\frac{n_e T_e}{\omega_e \tau_e}\,(\mathbf{b}\times\mathbf{u}) \tag{2.10}$$

$$\mathbf{q}_{e,T} = -\kappa_\parallel^e \nabla_\parallel T_e - \kappa_\perp^e \nabla_\perp T_e - \frac{5}{2}\frac{n_e T_e}{m_e \omega_e}\,(\mathbf{b}\times\nabla T_e) \tag{2.11}$$

with *electron thermal conductivities* $\kappa_\parallel^e$ and $\kappa_\perp^e$ given by

$$\kappa_\parallel^e = \frac{3.16 n_e T_e \tau_e}{m_e} \qquad \kappa_\perp^e = \frac{4.66 n_e T_e}{m_e \omega_e^2 \tau_e} \tag{2.12}$$

While for ions, the heat flux is:

$$\mathbf{q}_i = -\kappa_\parallel^i \nabla_\parallel T_i - \kappa_\perp^i \nabla_\perp T_i + \frac{5}{2}\frac{n_i T_i}{m_i \omega_i}\,(\mathbf{b}\times\nabla T_i) \tag{2.13}$$

with *ion thermal conductivities* $\kappa_{\parallel}^{i}$ and $\kappa_{\perp}^{i}$ given by

$$\kappa_{\parallel}^{i} = \frac{3.9 n_i T_i \tau_i}{m_i} \qquad \kappa_{\perp}^{i} = \frac{2 n_i T_i}{m_i \omega_i^2 \tau_i} \tag{2.14}$$

Viscous stress tensor

The viscous stress tensor in absence of magnetic field $\underline{\underline{\mathbf{W}}}$ is

$$\underline{\underline{\mathbf{W}}} = \left(\nabla \mathbf{u}_i + \nabla \mathbf{u}_i^{\top}\right) - \frac{2}{3}\left(\nabla \cdot \mathbf{u}_i\right) \underline{\underline{\mathbf{I}}} \tag{2.15}$$

Considering a strong magnetic field, $\omega_a \tau_a \ll 1$, and a reference frame with z parallel to the magnetic field $\mathbf{B}$, the viscous stress tensor becomes:

$$\begin{aligned}
\Pi_{zz} &= -\eta_0 W_{zz} \\
\Pi_{xx} &= -\frac{\eta_0}{2}\left(W_{xx} + W_{yy}\right) - \frac{\eta_1}{2}\left(W_{xx} - W_{yy}\right) - \eta_3 W_{xy} \\
\Pi_{yy} &= -\frac{\eta_0}{2}\left(W_{xx} + W_{yy}\right) - \frac{\eta_1}{2}\left(W_{xx} - W_{yy}\right) + \eta_3 W_{xy} \\
\Pi_{xy} = \Pi_{yx} &= -\eta_1 W_{xy} + \frac{\eta_3}{2}\left(W_{xx} - W_{yy}\right) \\
\Pi_{xz} = \Pi_{zx} &= -\eta_2 W_{xz} - \eta_4 W_{yz} \\
\Pi_{yz} = \Pi_{zy} &= -\eta_2 W_{yz} + \eta_4 W_{xz}
\end{aligned} \tag{2.16}$$

where the η are different for electrons and ions:

$$\begin{aligned}
\eta_{e,0} &= 0.73 n_e T_e \tau_e & \eta_{i,0} &= 0.96 n_i T_i \tau_i \\
\eta_{e,1} &= 0.51 \frac{n_e T_e}{\tau_e \omega_e^2} = \frac{1}{4}\eta_{e,2} & \eta_{i,1} &= \frac{3}{10}\frac{n_i T_i}{\tau_i \omega_i^2} = \frac{1}{4}\eta_{i,2} \\
\eta_{e,3} &= -\frac{1}{2}\frac{n_e T_e}{\omega_e} = \frac{1}{2}\eta_{e,4} & \eta_{i,3} &= \frac{1}{2}\frac{n_i T_i}{\omega_i} = \frac{1}{2}\eta_{i,4}
\end{aligned} \tag{2.17}$$

Equations (2.1), (2.2) and (2.3) are written using the form which in standard computational fluid dynamics is called *conservative formulation*. However, the *advective formulation* of the conservation questions is sometimes preferred to write Braginkii equations. To avoid confusion and start from a common basis, plasma conservation equations written using both formulations are reported in appendix A. In addition to the total energy equation, appendix A also reports the internal energy equation.

2.1.2. Beyond the Braginskii model

Section 2.1.1 presents the classical Braginskii formulations for a fully ionized two-fluid plasma. However, additional aspects should be considered if one wants to describe specific issues of boundary plasmas.

Partially-ionized plasmas

Boundary plasmas are not fully ionized. They include neutral atoms and molecules originating from the recycling process at the wall or added by seeding. Neutral species and their interaction with ions and electrons in the plasma play a paramount role in the power exhaust issue, as already mentioned in section 1.3.2 and will be further discussed in section 2.2.
Boundary plasma models typically assume that neutrals do not directly affect Braginskii closure, so that equations from (2.5) to (2.17) are not modified by the presence of charge-less particles. This assumption allows the decoupling of the transport of charged particles from the transport of neutrals. However, to account for the effect of plasma-neutral interaction in plasma fluid equations, source terms of particles S_n, momentum $\vec{\mathbf{S}}_m$ and energy S_T are added on the RHS of equations (2.1), (2.2) and (2.3), respectively. Additional information on how these sources are calculated is given in section 2.2.2.
Differently from electron and ion populations, neutral self-collisionality in the SOL is low and the transport model for neutral particles usually can not rely on the fluid approximation. Fully kinetic models based on the solution of the Boltzmann equation [71–73] or hybrid models [74] are instead used. Sections 3.2.1 and 3.2.2 include a brief description of the two approaches used to solve the neutral transport problem in SOLPS-ITER and GBS, respectively.

Multi-component plasmas

Boundary plasmas are not two-fluids but include many different ion species. The differences are related to the presence of several chemical elements, each one identified by its atomic number Z_n, but also for each element, many charge states can coexist. The ion charge is usually identified with Z_a with a spanning over the ion populations.
The multi-species nature of boundary plasmas is true in present-day tokamak experiments, where impurities are added to the main plasma by erosion of the PFCs or seeding. It will be also true in future reactors, where even the main plasma will be a mixture of deuterium, tritium and helium ash. To take this aspect into account, equa-

tions (2.5) to (2.17) of the Braginskii closure should be replaced with the expressions proposed by V. M. Zhdanov for multi-component plasmas [75, 76].
Zhdanov closure is based on the hypothesis that the plasma is made of a single main ion species $n_{main} \gg n_{imp}$ and that all the impurities are much heavier than the main species $m_{imp} \gg m_{main}$. Zhdanov closure was implemented in SOLPS-ITER model, first assuming *trace-impurity approximation* $Z_{eff} \sim 1$ [77] and subsequently relaxing the approximation, allowing higher Z_{eff} [78]. These hypotheses are consistent with the modelling of present-day deuterium experiments but present limits to modelling a D-T thermonuclear burning plasma, where two main plasma populations with $m_D \sim m_T$ are present. To overcome the limitations of the standard Zhdanov model an improved version of the closure coefficients, based on Grad's 21N-moment method, was recently proposed [79]. The improved model removes the hypothesis on single main species and impurity masses and allows the modelling of arbitrary plasma mixtures.
Simulations performed with different closure models, showed significant differences as far as the transport of impurities is concerned, while global electron density and temperature are only marginally affected [77–79].

Kinetic corrections to the fluid model

In the edge of tokamaks, there are regions where hypothesis (2.4) is not fully satisfied. The degree of discrepancy from the fluid approximation can be expressed by introducing the *Knudsen number* $K = \lambda_{coll}/L$. For the fluid approximation to be valid $K \ll 1$ should hold, while the *long mean-free path regime* corresponds to $K \sim 1$.
Failure of hypothesis (2.4) can lead to the computation of unphysically high fluxes while solving the fluid conservation equations. To avoid the model breakdown, upper limits can be imposed on the transport coefficients according to the method described by W. Fundamenski [80]. The flux limits are computed based on the flux predictions of different kinetic models in the long mean-free path regime.

We first discuss the validity of the fluid hypothesis when the plasma is in the sheath-limited regime introduced in section 1.3.2. Indeed, due to the low plasma density, the collisional mean free path can easily become similar or even longer than the system dimension, thus $K \gtrsim 1$. However, the fluid approximation can still be applied, as long as suitable boundary conditions accounting for the formation of an electrostatic sheath at the plasma-wall interface are implemented in the direction of the magnetic field. Both kinetic models and fluid models with sheath boundary conditions find that the sheath-limited regime is characterised by the development of convective-dominated heat transport with $T_e \approx$ constant along the parallel direction. This result is found in

spite of the fact that the classical heat conduction coefficient (2.12) diverges for $\lambda_{coll} \ll L$. The conductive heat flux is limited by the absence of electron temperature gradients. The name *sheath-limited* is indeed used to indicate that the electrostatic sheath influences the plasma within a collisional mean free path. For long λ_{coll}, thus, the sheath boundary conditions limit the properties of the plasma along the whole plasma flow without the need for artificially imposed limits [80]. This discussion is important since justifies the applicability of the fluid models to the low-density plasmas of the GyM LPD and thus the validity of the results presented in chapters 4 and 5 of this thesis. The presence of an electrostatic sheath at the plasma wall interface is discussed in more detail in section 2.3.1.

The implementation of artificial flux limits is instead important in intermediate collisionality regimes. We consider the classical Spitzer-Harm electron heat conductivity in equation (2.12). According to the classical description, the value of the conductive heat flux is determined by equation (2.11) as the product of the classical heat conductivity and the parallel electron temperature gradient. However, kinetic models show that temperature gradients are steeper than the ones predicted with this classical picture [30]. To correct the fluid model for this kinetic effect, flux limits are added to the classical heat conduction flux. In the SOLPS-ITER code, the flux limit for heat conduction flux is implemented as:

$$\kappa^{e}_{\mathrm{Lim},\parallel} = \frac{\kappa^{e}_{\parallel}}{1 + |\mathbf{q}_{e,T\parallel}|/q_{\mathrm{Lim}}} \tag{2.18}$$

where $q_{\mathrm{Lim}} = \alpha_\kappa n_e T_e^{3/2} \sqrt{m_e}$ is the limiting flux and α_κ is a free parameter.

2.1.3. Cross-field transport: diffusive and turbulent approaches

Previous sections 2.1.1 and 2.1.2 discuss the Braginkii model which describes well the plasma transport in the direction parallel to the magnetic field in the limit of laminar flow. On the contrary, cross-field transport is governed by small-scale fluctuations of the plasma parameters, usually called *micro-instabilities*. The effect of these micro-instabilities is to enhance radial cross-field transport by several orders of magnitude with respect to what can be estimated with classical collision theory. The origin of this phenomenon is presently attributed to the formation of coherent filamentary structures, elongated in the direction parallel to $\vec{\mathbf{B}}$, known as *"blobs"* [34, 81, 82].

From classical transport theory, particle diffusion coefficients can be estimated as $D_{\mathrm{class}} = (\Delta L)^2/\tau$, where ΔL is the average radial displacement resulting from binary

collisions and τ is the collisional time. In a magnetized plasma, the cross-field classical diffusion coefficient $D_\perp^{\text{class}}$ is thus:

$$D_\perp^{\text{class}} = \frac{(\Delta L)^2}{\tau} \approx \frac{r_{\text{L,i}}^2}{\tau_{ie}} \propto T^{-1/2} B^{-2} \tag{2.19}$$

where we assumed that the typical displacement is of the order of the ion gyro-radius and the collisional time is the classical Coulomb ion-electron collision time. This gives $D_\perp^{\text{class}} \approx 10^{-6} - 10^{-4}\,\text{m}^2\,\text{s}^{-1}$ for typical SOL conditions [30]. However, if we estimate the experimental cross-field diffusion as $D_\perp^{\text{exp}} \approx a^2/\tau_E \approx 1\,\text{m}^2\text{s}^{-1}$, where a is the tokamak minor radius and τ_E is the energy confinement time, it is clear that the classical treatment largely underestimates the cross-field transport.

To simulate *anomalous radial transport* in the edge of magnetically confined plasmas two main strategies have been developed:

- *"diffusive-based cross-field codes"* cross-field transport is modelled within a diffusive approximation[1]:

  $$\Gamma_{n,\perp} = -D_n \frac{\partial n_i}{\partial r} \tag{2.20}$$

  This method introduces an *anomalous transport coefficient* D_n that needs to be estimated from scaling laws or, if available, extrapolated from experimental data. Nonetheless, it is quite effective in providing a quantitative estimate of the radial flow and the consequent fluxes at the divertor targets.

- *"first principle turbulent codes"* resolve turbulent spatial and temporal scales and are capable of self-consistently describing the edge plasma turbulence responsible for the enhanced transport. The numerical implementation of this second approach, however, requires a much higher computational cost and those models present limitations in terms of the size of the system they can describe.

The diffusive and turbulent approaches are implemented in the plasma transport models of the two numerical code suits used in the development of this thesis work, SOLPS-ITER and GBS, respectively. Further information is given in section 3.2.

2.2. Plasma-neutrals interaction

Interaction between plasma and neutral atoms and molecules in the scrape-off layer and divertor of a tokamak has a crucial role in establishing the plasma and power ex-

[1] Sometimes an additional convective term $\Gamma_{n,\perp}^{\text{convect}} = -n_i u_{\text{pinch}}$ can be also added to equation (2.20).

haust. Section 1.3 introduced the phenomenology of plasma detachment and plasma recycling. In this section, we give further details on how to model these aspects and why they are strictly connected with the interaction between neutral atoms and molecules and the plasma.

2.2.1. Modelling high recycling regime

From the point of view of modelling, plasma detachment is characterized by the presence of strong dissipation mechanisms in the energy, momentum and particle balance equations (2.1), (2.2) and (2.3). These dissipation mechanisms are induced mainly by plasma-neutral interaction.
As discussed in section 1.3.2, at low gas puff the plasma is in the sheath-limited regime. This regime is characterized by relatively low plasma density, small ion flux at the target and thus small recycled neutral flux. For this reason, *low-recycling regime* is sometimes used instead of the sheath-limited regime. Since temperature is constant along a flux tube and neutral density is low, a first sound approximation to model sheath-limited plasmas can be to assume purely convective heat transport and neglect plasma-neutral interactions.

The increase in gas puffing rate raises the plasma density, the particle heat flux at the divertor target and, consequently, the recycled neutral flux. This regime is thus given the name *high recycling regime*. The concentration of the recycled neutrals and intrinsic impurities generated by the sputtering process rises and accumulates in front of the divertor. The formation of a negative density gradient forces then them to migrate within the scrape-off layer towards the X-point. To correctly model a regime for which plasma recycling becomes important, a neutral transport model should be also considered in addition to the plasma transport model. Since neutral-neutral collision frequencies are usually low, full kinetic models based on the Boltzmann equation are usually implied.
During their migration inside the plasma, neutral atoms and molecules undergo a large variety of atomic and molecular interaction processes with electrons and ions, the most important being electron impact ionization. These processes and the corresponding atomic and molecular databases in which their reaction rates are collected are discussed in detail in section 2.2.2. The plasma-neutral interaction in the divertor region is an important energy dissipation mechanism for the plasma and its effect is included in the plasma transport model by adding proper source and sink contributions to the plasma fluid equations, as discussed in section 2.1.2.
A second effect of increasing the average plasma density is the increase in plasma

collisionality. Considering the classical Spitzer-Harm expression of the electron heat conductivity (2.12) one has $\kappa_{\parallel} \propto n^2 \ln(n)$. The increased heat conductivity results in the development of negative temperature gradients along the flux tube from upstream, close to the outer midplane (OMP), to the divertor target. A regime in which collisionality and parallel heat conduction are important is called *conduction-limited regime*, in contrast to the convective-dominated sheath-limited regime.
The combination of increased heat conduction and plasma-neutral dissipation in the divertor results in a reduction of the peak temperature at the strike point and a reduction of the plasma heat flux at the targets. This is the partially-detached regime discussed in section 1.3.2.
The *full detachment* of the plasma from the divertor targets is obtained when the ion flux at the wall is suppressed by moving the ionization front upward. This is caused by two mechanisms: (i) charge-exchange reactions between ions and neutral, that act as a drag force in the ion momentum balance equation, and (ii) volumetric recombination processes, either electron-ion recombination (EIR) or molecular assisted recombination (MAR). Both mechanisms start to be effective at low electron temperature ($T_e \lesssim 5\,\mathrm{eV}$), hence after attaining a low target temperature in the high recycling partially detached regime.

For an accurate description of detachment thus one needs to include in its model an extensive database for atomic processes, including ionization, neutral radiation and charge-exchange processes [83, 84]. Several studies, moreover, highlight the importance of molecular reactions such as molecular ionization, producing H_2^+ ions, dissociation and molecular activated dissociation (MAD) and recombination (MAR). The latter, in particular, seem to be crucial in establishing detached conditions [85–87]. This is also the reason why the analysis of plasma detachment in pure He plasma is of great interest. As a noble gas, He does not form molecules and thus the analysis of He plasma detachment allows the isolation of the effects of purely atomic interactions.
Finally, detached conditions in reactor-relevant devices with a metallic wall are usually obtained through the seeding of extrinsic impurities, as discussed in section 1.3.2. The description of this aspect thus requires the use of a multi-species plasma model, able to include impurities different from the main hydrogenic species, their ionization and transport within the plasma, as discussed in section 2.1.2.

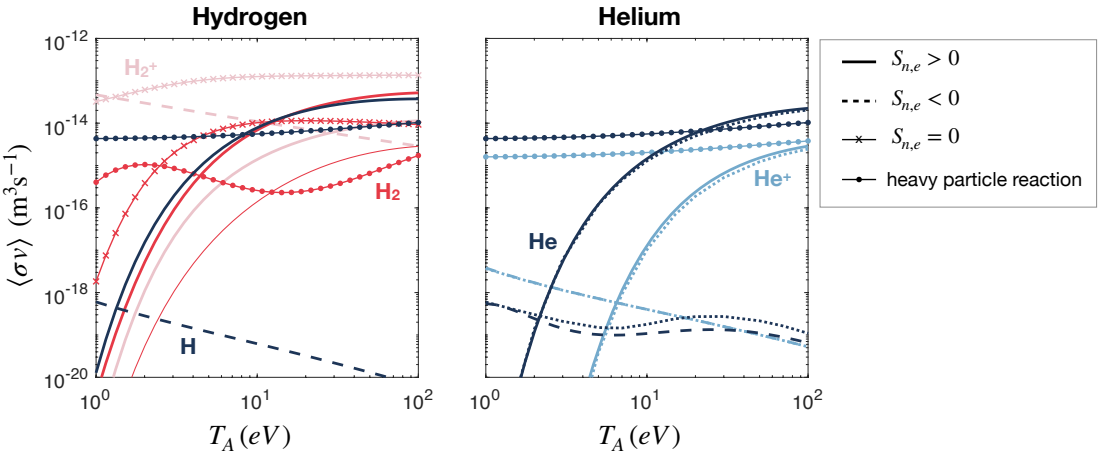

Figure 2.1: Hydrogen and helium reaction rate coefficients $\langle \sigma v \rangle$ as a function of the background temperature T_A. Colour distinguishes between atomic and molecular reactions: blu lines correspond to reactions involving only atomic ions and neutrals; red lines correspond to molecular reactions. Line style identifies the type of reaction: solid lines correspond to reactions increasing the number of electrons in the system (ionization); dashed lines to reactions reducing the number of electrons in the system (recombination); lines with an 'x' marker to reactions that do not modify the number of electrons in the system (dissociation of molecules); lines with 'dots' markers correspond to reactions between heavy species only (charge-exchange). For double parameter fits we used $n_A = 1e18\,\mathrm{m}^{-3}$ and $E_B = 10\,\mathrm{eV}$. The reaction rates plotted in this figure are obtained from fits according to AMJUEL and HYDHEL databases. A comparison of the AMJUEL (solid) and ADAS (dotted) fits is also shown in the helium plot.

2.2.2. Atomic and molecular databases

In section 2.1.2, we saw that the contribution of plasma-neutral interactions is usually included as source terms added to the Braginskii fluid model. This section addresses how these source terms are computed. Moreover, section 2.2.1, mentioned several plasma-neutral collision processes that should be considered to model high recycling regime and detachment. Each of these interactions is modelled as a binary collision process of the form:

$$A + B \rightarrow C + D \tag{2.21}$$

where B is called *probe particle* and it is usually considered mono-energetic with energy E_0 and A is the *bulk particle*, that represents the background plasma species with which the probe collides. Background species is supposed to be described by a *Maxwellian distribution functions* with a temperature equal to the plasma species temperature $T_A = T_a$ and a drifting velocity equal to the plasma fluid velocity $\vec{\mathbf{u}}_A = \vec{\mathbf{u}}_a$. With these hypotheses, plasma-neutral interaction sources are written as:

$$S_n = n_A n_B \langle \sigma v \rangle \qquad \vec{\mathbf{S}}_m = m_A n_A n_B \langle \sigma v \rangle \vec{\mathbf{u}}_A \qquad S_T = n_A n_B \langle E \sigma v \rangle \tag{2.22}$$

The sign of these source terms in the fluid equations can be positive (source) or negative (sink) depending on the specific reaction considered. The *rate coefficient* $\langle \sigma v \rangle$ and the *energy rate coefficient* $\langle E \sigma v \rangle$ are obtained by averaging the cross-section over the distribution function of the bulk specie:

$$\langle \sigma v \rangle = \int \sigma(v) v \, f_A^{Max}(v_r) dv_r \qquad \langle E \sigma v \rangle = \int E \sigma(v) v \, f_A^{Max}(v_r) dv_r \tag{2.23}$$

where v_r is the relative velocity between A and B and E is the total energy loss of the background species A per collision event.
Operationally, plasma fluid codes use fits of the rate coefficients contained in suitable databases. Different types of fits are used according to the reaction considered:

- H.2 type: single parameter fit. Reaction rates are fitted as a function of the temperature of the background species $\langle \sigma v \rangle (T_A)$.
- H.3 type: double parameter fit. Reaction rates are fitted as a function of the temperature of the background species and energy of the probe particle $\langle \sigma v \rangle (T_A, E_B)$.
- H.4 type: double parameter fit. Reaction rates are fitted as a function of temperature and density of the background species $\langle \sigma v \rangle (T_A, n_A)$.

- H.10 type double parameter fit. Energy reaction rates are fitted as a function of temperature and density of the background species $\langle E\sigma v\rangle\,(T_A, n_A)$.

The reaction rates $\langle \sigma v\rangle$ of the most relevant reactions in pure hydrogen and pure helium plasmas are shown in figure 2.1 as a function of the background species temperature. For double parameter fits we used $n_A = 1e18\,\mathrm{m}^{-3}$ and $E_B = 10\,\mathrm{eV}$. Blue lines represent the three purely atomic reactions of ionization (solid line), recombination (dashed line) and charge-exchange (dotted marked line). For hydrogen, the number of reactions is largely increased by the presence of molecular species, plotted in red.

2.3. Plasma-wall interaction

As already mentioned, any magnetic configuration is characterised by some degree of loss of plasma confinement and thus some degree of interaction between the plasma and the surrounding materials of the tokamak vessel. The divertor configuration described in section 1.3.1 was introduced to control and mitigate the effect of this interaction, both from the plasma and material points of view.
The plasma-wall interface is characterised by the development of a narrow layer of net positive charge in front of the wall surface. The *electrostatic sheath* accelerates the ions towards the wall while repelling the electrons. The magnitude of the potential drop across the sheath, the *sheath-potential*, depends on temperatures of electron and ion populations at the sheath entrance. These features determine the energy at which ions impact the solid material, an important variable in its erosion.

2.3.1. The electrostatic sheath

The lower inertia of electrons results in negative charge build-up on the solid surface in contact with the plasma. In turn, this leads to the formation of a thin layer with a positive net charge at the plasma-wall interface, called *electrostatic sheath*. The electrostatic sheath is characterized by a strong electric field repulsive for the electrons and attractive for the ions. If the magnetic field is oblique to $\vec{\mathbf{B}}$ as in figure 2.2.a, a magnetic sheath develops in front of the electrostatic one. The characteristic dimension of the electrostatic and magnetic sheaths are of the order of the Debye length λ_{Debye}

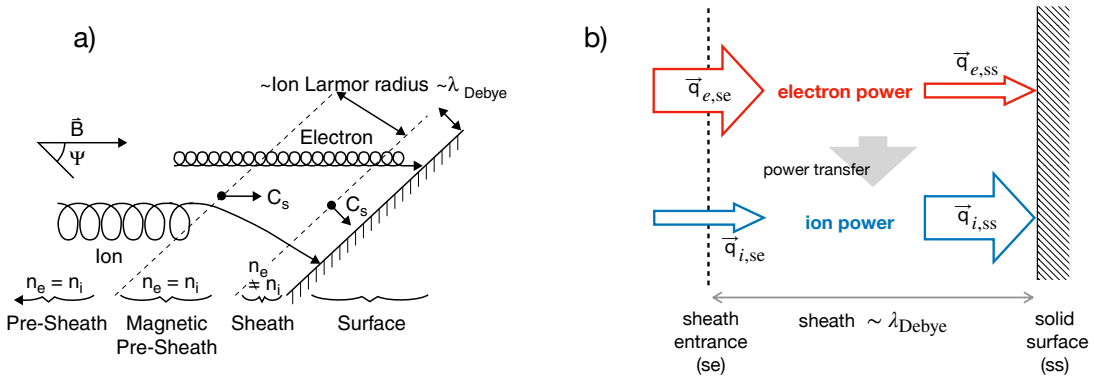

Figure 2.2: **a)** Electrostatic and magnetic sheath when $\vec{\mathbf{B}}$ is oblique to the surface from [30]. The analysis was first made by Chodura [88]. **b)** Electron-ion heat transfer mechanism in the sheath.

and ion gyro-radius r_i, respectively:

$$L_{Sh} \sim \lambda_{\text{Debye}} = \sqrt{\frac{\epsilon_0 T_e}{n_e e^2}} \qquad L_{MSh} \sim r_i \simeq \frac{m v_\perp}{ZeB} \tag{2.24}$$

A direct consequence of the existence of the sheath is *Bohm criterion* [30, 89], which prescribes the ion velocity at the sheath entrance $u_{i,\text{se}}$ to be grater or equal to the *ion acoustic speed* c_s:

$$u_{i,\text{se}} \geq c_s = \sqrt{\frac{(ZT_e + \gamma_{\text{ad}} T_i)}{m_i}} \tag{2.25}$$

where γ_{ad} is a numerical factor of order ~ 1, depending on the hypothesis on ions temperature in the sheath. Bohm criterion is often written as $M \geq 1$, where one introduces the adimensional Mach number $M = u_i / c_s$.
Bohm criterion provides thus a simple expression for particle flux at the sheath entrance:

$$\Gamma_{\text{se}} = n_{\text{se}} c_s \tag{2.26}$$

If ion momentum is conserved along the flux tube, the ion density at the sheath entrance is $n_{\text{se}} \approx 0.5 n_i$, where n_i is the upstream ion density. Assuming also that particles are conserved within the sheath, the whole flux entering the sheath reaches the solid surface $\Gamma_{\text{se}} = \Gamma_{\text{ss}}$.
The electrostatic sheath also controls the rates at which energy is removed from the plasma at the plasma-wall interface. Heat fluxes at the sheath entrance are usually

written in terms of *sheath transmission coefficients* γ_e and γ_i:

$$|\vec{\mathbf{q}}_{e,\mathrm{se}}| = \gamma_e T_e \Gamma_{\mathrm{se}} \qquad |\vec{\mathbf{q}}_{i,\mathrm{se}}| = \gamma_i T_i \Gamma_{\mathrm{se}} \tag{2.27}$$

where $\gamma_e \simeq 4.83 - 5.12$ and $\gamma_i \simeq 1.5 - 2.93$, according to the models[2] considered in [30] (Tab. 25.1).
If energy conservation in the sheath is assumed, then the total power entering the sheath also reaches the solid surface of the wall $\vec{\mathbf{q}}_{\mathrm{se}} = \vec{\mathbf{q}}_{e,\mathrm{se}} + \vec{\mathbf{q}}_{i,\mathrm{se}} = \vec{\mathbf{q}}_{\mathrm{ss}}$. However, the electron-repelling potential in the sheath acts as an *electron–ion energy-transfer mechanism*, transferring energy from electrons to ions as shown in figure 2.2.b.
The total power deposited onto the wall, in addition to $\vec{\mathbf{q}}_{\mathrm{ss}}$ should also include the power from ion recombination at the wall surface. When an ion from the plasma recombines with an electron from the material, indeed, the recombination potential energy is released as heat to the material and contributes to the deposited power.

$$|\vec{\mathbf{q}}_{tot,\mathrm{wall}}| = |\vec{\mathbf{q}}_{\mathrm{ss}}| + E_{\mathrm{iz}} \Gamma_{se} \tag{2.28}$$

This second contribution is the reason why in a detached plasma regime, we are not only interested in dissipating heat along the SOL to reduce plasma temperature at the target, but we also want to reduce the ion flux at the wall to lower the recombination contribution.

In the numerical implementation of plasma fluid models, the Bohm criterion and its consequences are crucial to set boundary conditions at the plasma-wall interfaces.

2.3.2. Plasma recycling and erosion of the plasma-facing components

Section 1.3.3 introduced the process of plasma recycling and section 2.2.1 described how the high-recycling regime impacts boundary plasma properties, introducing the need for a neutral transport model coupled to the plasma model.
From the modelling point of view, the recycling of plasma ions at the wall is modelled as a boundary condition of the neutral transport model. If an ion flux impinges at the wall, the corresponding neutral recycling flux is estimated by exploiting particle R_N and energy R_E recycling coefficients, which give the fraction of ions that are reflected into the plasma as neutrals and energy that they retain. R_N and R_E depend on ion and wall species and the impact angle and energy of the ion. Results of Monte Carlo simulations

[2] This values are obtained considering a plasma with electrons and H^+ ions.

performed with the TRIM code are collected in a database [90] of R_N and R_E values for several projectile-ot-target couples and several values of impact angles and energies and this database is part of the EIRENE neutral transport model.
In the EIRENE, moreover, the particle recycling coefficient can be rescaled on specific wall surfaces using the RECYCT parameter. If the wall and divertor surfaces can be considered saturated with hydrogen atoms, then RECYCY = 1, while on unsaturated walls 0 < RECYCT < 1 should be used. A RECYCT < 1 is also used to model the effect of turbomolecular pumps. In this case, the value of the recycling coefficient is related to the turbo-pump speed $S\,(\mathrm{L\,s^{-1}})$ by:

$$S = A \times (1 - RECYCT) \times 3.638 \times \sqrt{T/m} = A \times p_a \times 3.638 \times \sqrt{T/m} \tag{2.29}$$

where $A\,(\mathrm{cm^2})$ is the effective area of the pumping surface, T(K) is the temperature and m(aum) is the mass of the neutral species. $p_a = 1 - RECYCT$ is called *albedo* of the surface and represents the surface absorption probability.

Sputtering of the wall material is modelled in a way similar to recycling. Databases exist to provide the probability of releasing an atom from a specific surface as a function again of ion and wall species, impact angle and impact energy. The number of impurities released into the plasma is thus estimated as the product of the ion flux at the wall and the *physical sputtering yield* computer at ion impact angle and energy, $\Gamma_{\mathrm{ero,ph}} = Y_{ph}(E,\theta)\Gamma_{\mathrm{i,ss}}$. Several models exist proving analytical expression for $Y_{ph}(E,\theta)$ [91, 92].
For hydrogenic plasma discharges in carbon wall machines, chemical sputtering is also important. Its modelling is analogous to the one $\Gamma_{\mathrm{ero,ch}} = Y_{ch}\Gamma_{\mathrm{i,ss}}$. However, simple expressions for Y_{ch} as a function of impact energy and angle are not available and a global *chemical sputtering yield* $1\% < Y_{ch} < 5\%$ is usually considered.

One possibility to describe intrinsic impurities in the plasma is to use multi-species fluid models described in section 2.1.2. The main aim when following this path is to assess the effect that these impurities have on the main plasma properties, e.g. in terms of distribution of the impurities in the plasma or radiative contribution. However, for specific studies on erosion, impurity migration and redeposition on the machine wall, specific tools implementing kinetic models for impurity transport are implied. These codes do not solve the main plasma transport problem but take the results from boundary plasma models and use them as *plasma background*. Examples of erosion-impurity migration codes are WallDYN [93, 94], DIVIMP [95] and ERO2.0 [96]. The latter, in particular, is considered in the context of this thesis.

From the plasma background and the magnetic equilibrium reconstruction, ERO2.0 estimates the fluxes onto the PFCs and computes their erosion. Subsequently, the code follows the Monte Carlo trajectories and assesses the transport of the eroded impurities inside the plasma background, including the possibility for ionization. The trajectories are followed up to the wall location, where impurities are ultimately re-deposited. The code also allows for the investigation of local micro-scale morphological modification of the material surface exposed to the plasma [97, 98].
By coupling ERO2.0 with suitable boundary plasma models to provide the plasma background, several studies assessing global wall erosion and impurity migration of JET [99], WEST [100] and ITER [101] tokamaks were performed.
When performing the coupling between the main plasma model and the erosion-migration model, one should consider that plasma transport codes are usually bi-dimensional, while erosion models, like the one implemented in ERO2.0, are 3D. The plasma background is computed assuming rotational symmetry and the 2D computational mesh usually lies in the plane perpendicular to the symmetry direction (more details on this topic are given in section 3.2.3). ERO2.0, by contrast, has a computational domain that covers the full cylindrical volume of the linear device. To be used by ERO2.0, plasma backgrounds obtained with 2D plasma transport code are interpolated on a 3D domain by rotation around the symmetry axis.

This thesis presents the first global coupling of the SOLPS-ITER boundary plasma code and ERO2.0 in a linear geometry. The study, presented in section 4.5, assesses the erosion of the main chamber of the GyM LPD under helium plasma operation.
Moreover, the main goal of the analysis presented in chapter 6 is the production of a helium plasma background for PMI modelling in ASDEX-Upgrade tokamak.

3 | Thesis goals and methods

This chapter summarises the motivations, goals and methods of this PhD thesis and it is meant as a joint between the first introductory part of this thesis and the discussion of the results presented in Part II and Part III.
In particular, section 3.1 gives a brief outline of the objectives of the thesis and summarises the structure of the next chapters. Section 3.2 and 3.3 discuss the numerical tools employed to develop the work. These latter sections, besides introducing some general features of the standard numerical codes exploited in the work, also discuss several original methodological aspects developed in the context of this thesis.

3.1. Motivations, objectives and outline of the thesis

The discussion presented in chapters 1 and 2 highlighted the key role that the boundary plasma has in controlling the confinement properties in a tokamak through its interaction with the surrounding wall structures. Understanding, predicting and mitigating plasma-wall interaction and the resulting particle and heat loads on the divertor and first wall is a crucial requirement for a fusion reactor. Investigating and predicting a complex system such as the edge plasma of magnetically confined plasma requires the development of numerical tools for interpreting experimental results and for making predictions in the design phase of new machines.

To further the understanding of the theoretical framework of boundary plasma and plasma-material interaction modelling, this thesis work aims to extend the applicability of standard boundary plasma codes to non-standard, yet very relevant, conditions. In particular, the work focused on improving the available modelling tools to describe linear plasma devices, which constitute an asset for the research on material for the PFCs of future fusion reactors. In light of the ITER Pre-Fusion Operation, the investigation of helium plasma properties is crucial, especially concerning the behaviour of the edge plasma and its interaction with PFC materials, tungsten in particular. These aspects are investigated, both in linear device and tokamak geometries and plasma conditions. Finally, following the recent interest in negative triangularity as a promising

configuration for the development of reactor-relevant scenarios, this thesis presents a study of plasma detachment in negative triangularity, in comparison with standard positive triangularity scenarios.

The results of this thesis work can be divided into two parts:
Part II is entitled *"Plasma dynamics and plasma-wall interaction in LPDs"* and collects the achievements in developing an extended modelling framework to describe linear plasma devices. Although their longstanding exploitation in PMI experiments, the available modelling tools for LPDs were indeed quite limited. This thesis work aimed at filling this gap, by optimising and testing standard boundary plasma codes in cylindrical geometry. In particular, it focused on the analysis of helium plasmas in the GyM linear machine of the ISTP-CNR in Milano using the SOLPS-ITER boundary plasma package. This allowed for improving the capabilities of the SOLPS-ITER code to deal with pure helium plasmas by optimising the set of plasma-neutral interactions and developing a simplified global balance model. The coupling between plasma transport, erosion of the surrounding materials and impurities migration was investigated presenting the first global modelling in a linear device. In particular, a helium plasma background produced by the boundary code SOLPS-ITER was used as input for 3D erosion investigation by the ERO2.0 code. Due to their simple geometry, moreover, LPDs are an ideal testbed for the development and validation of modelling strategies of interest for tokamaks. The benchmark of diffusive and turbulent approaches for radial cross-field transport was carried out by comparing model equations and results from SOLPS-ITER and GBS simulations.
Part III is instead devoted to *"Modelling the edge plasma in tokamaks"*. The numerical tool exploited for these studies is the boundary code package SOLPS-ITER and the works are developed to support experimental activities in the context of the EUROfusion Work Packages Tokamak Exploitation (WP-TE) and Plasma-Wall Interaction and Exhaust (WP-PWIE). Specifically, the competencies to model helium plasmas acquired with the studies performed on LPDs were extended to the tokamak conditions with the main purpose of reconstructing the plasma background of a helium discharge in ASDEX-Upgrade to be used subsequently for erosion modelling. The plasma background, which consists in the distribution of densities, velocities and temperatures of ions and electrons was validated and benchmarked with the available experimental data. Another novel and original exploitation of the SOLPS-ITER boundary plasma package was the modelling of the different detachment behaviour observed in positive and negative triangularity plasmas in TCV. This work is the first analysis of boundary plasma transport in negative triangularity performed with SOLPS-ITER.

Specifically, chapter 4 investigates the possibility of successfully applying SOLPS-ITER to linear geometry. It presents a benchmark of the simulation results with the available experimental data of the GyM linear machine and with a newly developed global 0D model to describe He plasma in linear geometry. This simplified model helped share light on the relevant plasma-neutral interaction processes of relevance for low-temperature helium plasmas. Finally, the first global erosion and impurity migration study in a linear device is presented.
Chapter 5 discusses the benchmark of the SOLPS-ITER and GBS cross-field transport model in a linear geometry. The benchmark includes the comparison of the equations solved by SOLPS-ITER and GBS in linear geometry and a benchmark of results obtained simulating the same system with the two codes.
Chapter 6 presents our strategy to produce an L-mode helium plasma background with SOLPS-ITER to be used for the modelling of a global PMI experiment in ASDEX-Upgrade. The chapter includes the benchmark with the available AUG experimental data and a discussion of the importance of He^{+} and He^{2+} fluxes onto the PFCs.
Chapter 7 is devoted to the first numerical study of plasma detachment in a TCV negative triangularity configuration performed with SOLPS-ITER. The study includes the benchmark of the simulations with TCV experimental data of a negative triangularity discharge, the comparison with a positive triangularity discharge with similar parameters and the investigation of detachment properties through the modelling of a density ramp experiment.

3.2. Numerical tools for edge plasma modelling

This section introduces the standard numerical tools for boundary plasma modelling, which were used in this thesis work. The general features of SOLPS-ITER and GBS boundary plasma code packages are presented in sections 3.2.1 and 3.2.2, respectively. In addition, section 3.2.3 discusses the original contribution of this thesis related to the application of these two codes in linear geometry.

3.2.1. SOLPS-ITER code

The SOLPS-ITER code package is a combination of a 2D multi-fluid, mean-field plasma transport code and the 3D kinetic Monte Carlo neutral transport code.
The SOLPS code package, version 4.0, 4.2 and 4.3, was historically implied for divertor performance studies and geometry optimization of the ITER project. Since then,

SOLPS developments were performed by different research groups in Europe, focusing on separate issues of neutrals and plasma transport models. The SOLPS-ITER code package groups the latest B2.5 plasma model [102] together with the fully parallelized version of EIRENE. The results presented in this thesis work are obtained with the SOLPS-ITER code version 3.0.7.

SOLPS-ITER uses a field-aligned coordinate system to solve the plasma transport problem in the boundary of tokamaks. The computational domain is a 2D poloidal section of the tokamak chamber, with a realistic contour mimicking the vacuum vessel profile. The plasma mesh is built upon a realistic magnetic equilibrium reconstruction: it is a structured quadrangular mesh, which covers an area going from the edge of the confined region to the outer flux surface tangent to a first wall (non-divertor) structure. The lack of extension of the plasma mesh to the first wall is one of the limitations of the present version of the code. Extensive work was performed in recent years to extend the plasma grid to the vessel [103–105] and the first version of the code with an extended grid is ready to be released. The EIRENE Monte Carlo code, instead, uses an unstructured triangular grid covering the plasma domain and the outer SOL, up to the actual vessel contour. Within EIRENE geometry, it is possible to define localized surfaces for pumping and fuelling throughput.

The plasma module, B2.5, solves a multi-species extension of Braginskii equations. The multi-species model is normally used to model a hydrogenic plasma, including heavier impurities. Density and momentum conservation equations are solved for each ion species, while energy conservation relies on the single-ion temperature approximation. Temporal resolution is typically much larger than the turbulence temporal scales $\Delta t_{\mathrm{SOLPS}} \approx 10^{-5} - 10^{-7}$ s. The average effect of anomalous transport is included through a diffusive-advective approximation of the cross-field fluxes. On the neutral side, the flexibility of Monte Carlo implementation allows for the inclusion of a wide range of atomic and molecular phenomena, required for a realistic and quantitative investigation of plasma detachment and radiative power losses in the divertor.

Figure 3.1 shows a simplified workflow of the code package. Besides the two main modules, B2.5 and EIRENE, the code suite includes modules for mesh generation and input/output processing (DivGeo, Carre, Uinp, Triang). The coupled equations for particle, momentum and energy balances and the potential equation are solved implicitly in B2.5 by using an iterative procedure. The algorithm follows the SIMPLE algorithm (Semi-Implicit Method for Pressure-Linked Equations) [106]. At the beginning of each time step, the plasma-neutral sources are computed by EIRENE and then processed and rescaled by the B2.5-EIRENE interface.

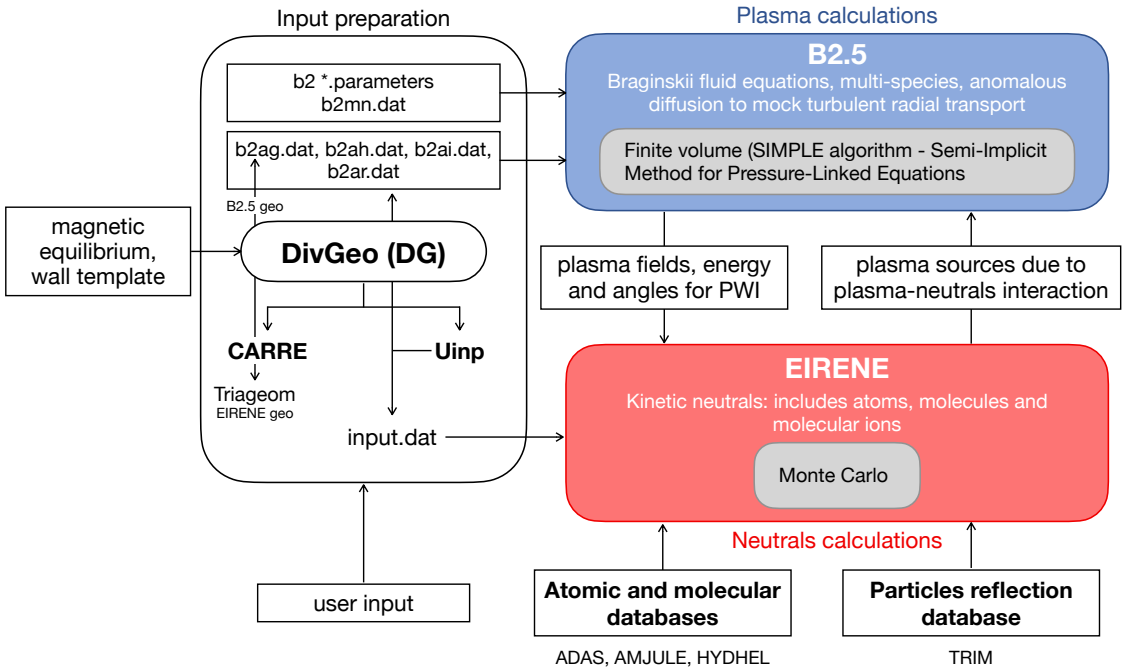

Figure 3.1: Simplified SOLPS-ITER workflow. A more detailed one is given in [107].

3.2.2. GBS: the Global Braginskii Solver

The Global Braginskii Solver (GBS) is a three-dimensional, flux-driven, first-principles turbulence code that evolves the Braginskii equations in the drift-reduced approximation [109, 110]. It implements the classical two-fluids Braginskii model coupled to a single atomic species kinetic neutral model.

The GBS code was initially developed to study plasma turbulence in basic plasma devices. Works with this first version include global simulations in simple magnetized plasma (SMT) configurations, like the TORPEX device [55, 111, 112], and linear devices, such as LAPD [113]. An electrostatic model in the cold ion limit was used and the Boussinesq approximation was applied to simplify the numerical implementation of the divergence of the polarisation current. Later, GBS development was oriented towards the tokamak geometry. In particular, the latest version of GBS [108] implements a non-field-aligned coordinate system and uses an axial-symmetric domain with a rectangular poloidal cross-section. The domain encompasses the whole plasma volume retaining the core-edge-SOL turbulence interplay. It is flexible on the choice of the magnetic configuration: single null (SN), double null (DN) and snowflake equilibrium configurations were investigated. The magnetic configuration can be loaded from the equilibrium reconstruction of experimental discharges or a Grad-Shafranov solver.

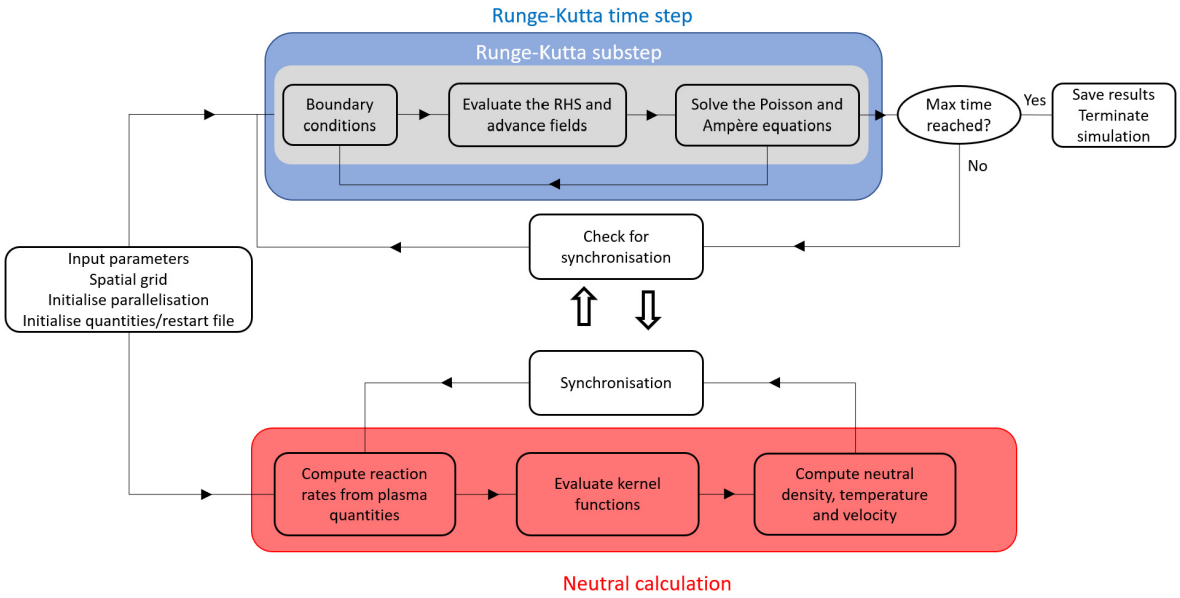

Figure 3.2: GBS workflow from [108].

The physical model has been improved including ion temperature dynamics [114] and relaxing Boussinesq approximation. Electromagnetic effects are also included [115]. The neutrals dynamic is solved by a self-consistent kinetic neutral model [116]. The model includes a single atomic species, interacting with the plasma through ionization, recombination and charge-exchange processes. Concerning the numerical implementation, a fourth-order Runge-Kutta algorithm provides the plasma time evolution and the spatial discretization by a fourth-order centred finite differences scheme. Ampere and Poisson equations are solved by an optimized iterative solver.
GBS workflow is shown in figure 3.2. Plasma and neutrals dynamics are run in parallel. After every time step, the plasma module checks if a new neutral calculation is available and updates the plasma equations' value of the plasma-neutral interaction sources. In parallel, the neutral module computes the density, temperature and velocity of the neutral population. After every neutral calculation, the plasma and neutral modules synchronize, and the values of the plasma density, electron and ion temperatures used to compute the reaction rates for plasma-neutrals interaction are updated.

3.2.3. Linear geometry

Both SOLPS-ITER and GBS numerical tools are developed and optimised to model the boundary plasma in a tokamak geometry. A consistent part of the work carried out in this thesis work was devoted to investigating the possibility to apply these codes

in cylindrical geometry and then investigating the plasma dynamic and phenomena related to PMI in the GyM linear plasma device. This section presents a summary of the main features of SOLPS-ITER and GBS when used to model a linear device. In particular, it focuses on the reference frame used to write the equations and on the differential operators in linear geometry. A detailed summary of the physical model and equations implemented in the two codes will be given in section 5.1.

SOLPS-ITER in linear geometry

The B2.5 equations and the 2D field-aligned grid onto which they are solved are tailored for tokamaks simulations. The plasma equations are written considering the two curvilinear orthogonal coordinate systems shown in figure 3.3.a. Those are the *dynamical reference frame* ($\mathbf{e}_\parallel, \mathbf{e}_\perp, \mathbf{e}_y$), aligned with the characteristic directions of the plasma motion, and the *geometrical reference frame* ($\mathbf{e}_x, \mathbf{e}_y, \mathbf{e}_z$). The full derivation of Braginskii equations in curvilinear coordinates is found in [117].
Considering a tokamak and exploiting the rotational symmetry in the toroidal direction $\mathbf{e}_z$, the plasma transport problem can be reduced to two-dimensional in the geometrical reference frame. In this frame, the metric is diagonal and entirely described by the three metric coefficients h_x, h_y, h_z. The x-coordinate varies along the flux surfaces, while the y-coordinate is perpendicular to them, as shown in the left part of figure 3.3.b.
When considering a LPD, the problem can again be reduced to 2D exploiting rotational symmetry around the cylinder axis. The $\mathbf{e}_z$ basis vector in linear geometry is along the azimuthal direction and the bi-dimensional problem is solved on the plane that contains the cylinder axis. Specifically, in this plane the x-coordinate corresponds to the axial direction and the y-coordinate is in the radial direction, as shown in the right part of figure 3.3.b..
The general transformation rules of a vector $\mathbf{v}$ from the dynamical frame to the geometrical one, derived in [117], for a linear plasma device reduce to:

$$u_x = b_x u_\parallel \qquad u_z = -b_x u_\perp \tag{3.1}$$

where $b_x = B_x/B$. The relations are obtained by setting to zero the azimuthal component of the magnetic field $b_z = B_z/B = 0$. Indeed, a major difference, when using B2.5 to simulate a LPD, is the absence of the azimuthal component of the magnetic field B_z, which is instead the dominant component in tokamaks. This eliminates several terms in SOLPS-ITER equations, mainly related to the possibility to investigate drifts.
A general comment related to drifts in SOLPS-ITER is worth mentioning. When drifts are activated in a tokamak simulation, what is accounted for is the effects that the ad-

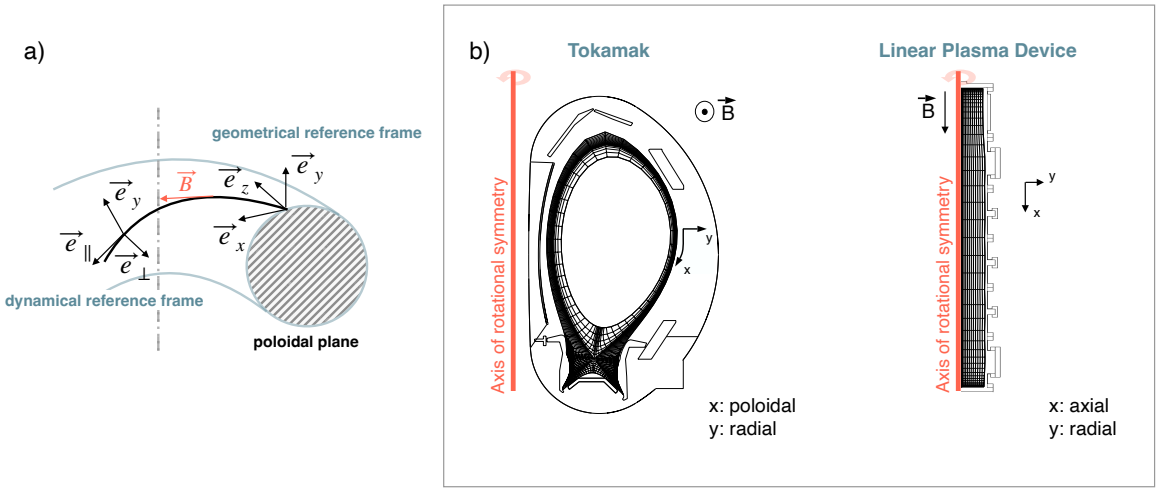

Figure 3.3: **a)** Curvilinear reference frames of B2.5. The *dynamical reference frame* ($\mathbf{e}_{\parallel}, \mathbf{e}_{\perp}, \mathbf{e}_y$) is aligned to the characteristic directions of the plasma motion: parallel to the magnetic field **B** ($\mathbf{e}_{\parallel}$) and orthogonal to **B** in the magnetic flux surface ($\mathbf{e}_{\perp}$); the third direction is orthogonal to the magnetic flux surfaces ($\mathbf{e}_y$). The *geometrical reference frame* ($\mathbf{e}_x, \mathbf{e}_y, \mathbf{e}_z$), where $\mathbf{e}_x$ is in the poloidal direction, $\mathbf{e}_y$ is orthogonal to the flux surfaces in the poloidal plane and $\mathbf{e}_z$ is in the toroidal direction. **b)** Geometrical reference frame conversion from a tokamak to a LPD. In both cases the z direction can be ignored, assuming rotational symmetry around the axis reported in red.

ditional poloidal and radial fluxes have on the projection of plasma parameters onto the poloidal plane, where the SOLPS-ITER mesh lies. In a LPD, the mesh lies in the plane containing the axial and radial directions, while the effect of drifts - the $E \times B$- *drift* is the only relevant one - is to produce a rotation of the plasma column in the azimuthal direction. This rotation has no effect on plasma parameters in the plane where the mesh is lying and the absence of drifts is consistent with the 2D axial symmetric description. SOLPS-ITER equations in liner geometry will be discussed in detail in section 5.1.1.

GBS in linear geometry

GBS is a fully 3D boundary plasma code. Since no symmetry assumption is in place, the direction of the symmetry axis is no longer a concern when moving from the tokamak to the linear geometry. The cylindrical geometry of a linear machine is regarded as an *infinite-aspect-ratio torus*: both in tokamaks and LPDs simulations, the z-direction $\mathbf{e}_z$ is set along the main magnetic field component, i.e. in the toroidal and axial direction, respectively. The transformation of the model equations from toroidal to an infinite-cylinder reference frame, schematically represented at point (1) in figure 3.4, is practically achieved by modifying the differential operators implemented in the code as

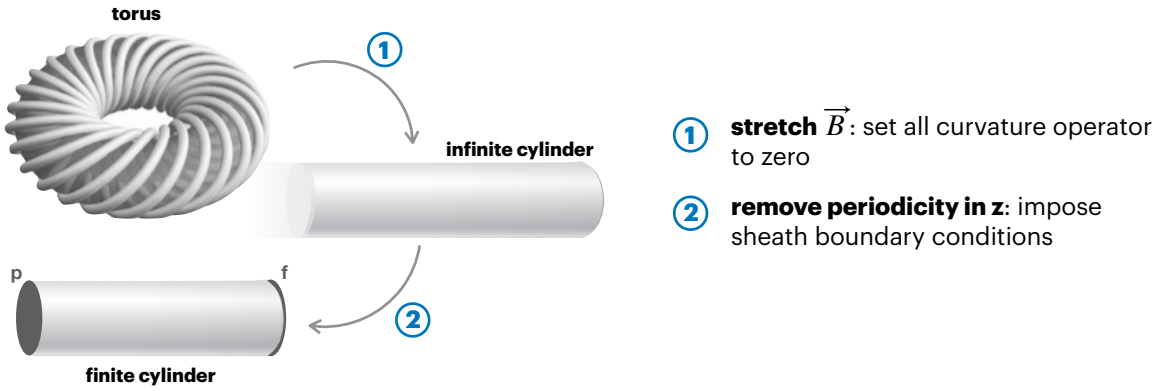

Figure 3.4: Steps required to adapt the GBS numerical tools to the linear geometry. Step ① implies moving from a torus from an infinite cylinder, by modifying the differential operators implemented in the code, and ② accounts for the finite length of the cylinder, by imposing proper boundary conditions.

follows:

$$\begin{aligned}
&\nabla_{\parallel} f = \partial_z f \\
&\nabla^2_{\parallel} f = \partial_{zz} f \\
&\nabla^2_{\perp} f = \partial_{xx} f + \partial_{yy} f \\
&C(f) = 0 \\
&[g, f] = [g, f]_{xy} = \partial_x g \partial_y f - \partial_x f \partial_y g
\end{aligned} \tag{3.2}$$

Sheath-boundary conditions are then implemented in the z-direction, in place of the periodic boundary conditions used in tokamaks simulations.

$$\begin{aligned}
&\partial_z n = \mp \frac{n}{c_s} \partial_z u_i \\
&u_i = \pm c_s \\
&u_e = \pm c_s \, e^{(\Lambda - e\phi_{Sh}/T_e)} \\
&\partial_z T_e = 0 \\
&\partial_z \omega = 0
\end{aligned} \tag{3.3}$$

The upper sign refers to the front boundary and the lower sign refers to the posterior boundary. The two boundaries are indicated in figure 3.4 with **f** and **p**, respectively. GBS equations in linear geometry, implementing operators (3.2), are given in section 5.1.2.

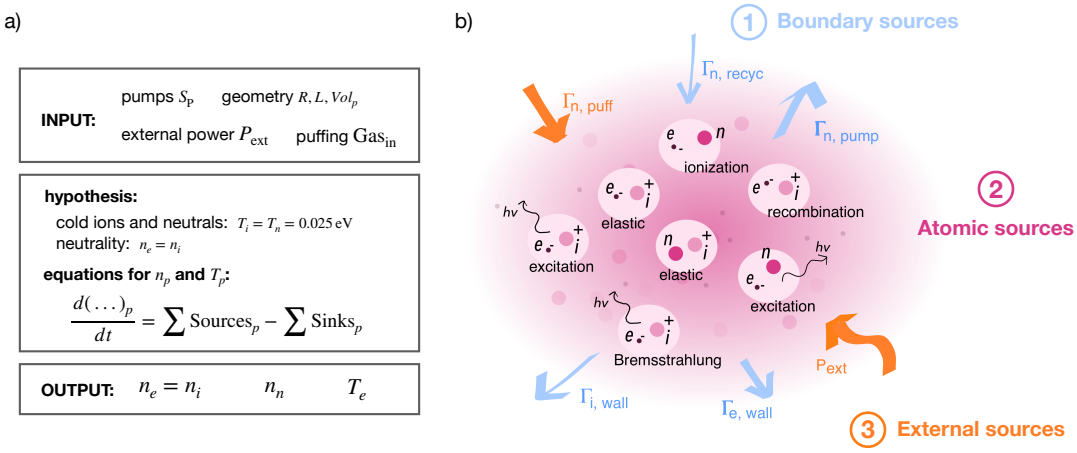

Figure 3.5: **a)** Blocks containing the basic elements of the point model: the first block contains the model inputs; the second block synthetically describes the main hypotheses and the structure of the model equations; the third block specifies the outputs of the model. **b)** The sources and sinks terms in the plasma balance equations: (1) flux towards the boundary and recycling, (2) atomic processes and (3) externally supplied particles and power.

3.3. A novel global 0D model for LPDs

In addition to the exploitation of standard edge plasma tools described in section 3.2, this thesis work also contributed to the development of an original 0D model for the investigation of helium plasma in typical LPD conditions. This section presents the general principles of this model and how its equations are derived from the volume average of a standard plasma fluid model.
In the following of this thesis, the model will be successfully benchmarked with results of SOLPS-ITER simulations, in section 4.3, and it will be used to implement plasma-neutral interaction sources in GBS simulations of linear geometry, in section 5.3. Finally, in section 4.4.2, the 0D model will be extended to explicitly include the He meta-stable populations. The equations for the meta-stable resolved model are detailed in appendix B.

3.3.1. General principles

A global point model to describe a plasma is based on a set of space-independent balance equations describing density (n_p) and temperature (T_p) for each one of the considered populations (p). Such a model has no interest in addressing the spatial variation of its variables, but rather it investigates in a simple and effective way the

relative contributions of different source/sink mechanisms in determining a stationary plasma state. Although these general ideas can be extended to an arbitrary number of populations, the basic version of this model is developed to investigate helium plasma and considers three populations: electrons (e), ions (i) and neutral atoms (n). The ionic population, moreover, only contains singly ionized atoms (Z = 1), consistently with the low ionization degree and temperature ($T_e \leq 15\,\text{eV}$). Each population is represented by its values of density and temperature and our final goal is to solve a six-unknowns problem for n_e, T_e, n_i, T_i and n_n, T_n.

In the context of the modelling of typical LPDs, an additional hypothesis can be made. First, plasma neutrality is assumed and for a single ion species simply reads $n_i = n_e$. Second, neutral and ion temperatures are assumed to be constant and equal to room temperature, $T_i = T_n = 0.025\,\text{eV}$. The hypothesis on the ion temperature is valid for the low-density plasma of GyM, for higher densities, although in LPDs usually $T_e \gtrsim T_i$, energy equipartition can heat up ions and this hypothesis should be revised.

The sources and sinks mechanisms considered are atomic processes of ionization, recombination, electron excitation of neutral and ion ground states and elastic collisions; particle and heat losses due to plasma-wall interaction and particle recycling; active pumping and gas injection; heating by an external source. With these hypotheses, the problem reduces to a system of three ordinary differential equations for the evolution in time of ion density, atom density and electron temperature:

$$\frac{dn_i}{dt} = R_{\text{iz}} n_e n_n - R_{\text{rc}} n_e n_i - \Gamma_{i,\text{wall}} n_i \tag{3.4}$$

$$\frac{dn_n}{dt} = -R_{\text{iz}} n_e n_n + R_{\text{rc}} n_e n_i + \Gamma_{n,\text{recyc}} n_i - \Gamma_{n,\text{pump}} n_n + \frac{\Gamma_{n,\text{puff}}}{\text{Vol}} \tag{3.5}$$

$$\begin{aligned}\frac{3}{2} n_e \frac{dT_e}{dt} = {} & \frac{P_{\text{ext}}}{\text{Vol}_e} - E_{\text{iz}} R_{\text{iz}} n_e n_n - E_{i,\text{rad}} R_{i,\text{rad}} n_e n_i - E_{n,\text{rad}} R_{n,\text{rad}} n_e n_n - \Gamma_{e,\text{wall}} T_e n_e \\ & - \frac{3}{2} \frac{2m_e}{m_i} R_{i,\text{el}} n_i n_e (T_e - T_i) - \frac{3}{2} \frac{2m_e}{m_n} R_{n,\text{el}} n_n n_e (T_e - T_n) \\ & - \frac{3}{2} \left(R_{\text{iz}} n_e n_n - R_{\text{rc}} n_e n_i - \Gamma_{i,\text{wall}} n_i \right) T_e\end{aligned} \tag{3.6}$$

where, m_i and m_e are the ion and electron mass respectively and P_{ext} is the external power supplied to the electrons. A summary of the terms in the equations and their physical meaning are reported in table 3.1.

Physical meaning	Formula/symbol	Units
Volume reactions		
Ionization	R_{iz}	$[\text{cm}^3\,\text{s}^{-1}]$
Recombination	R_{rc}	$[\text{cm}^3\,\text{s}^{-1}]$
Ionization energy loss	$E_{\text{iz}} R_{\text{iz}}$	$[\text{eV}\,\text{cm}^3\,\text{s}^{-1}]$
Neutral excitation	$E_{n,\text{rad}} R_{n,\text{rad}}$	$[\text{eV}\,\text{cm}^3\,\text{s}^{-1}]$
Ion excitation	$E_{i,\text{rad}} R_{i,\text{rad}}$	$[\text{eV}\,\text{cm}^3\,\text{s}^{-1}]$
Electron-ion equilibration	$R_{i,\text{el}}(T_e - T_i) = \nu_{ei}/n_i(T_e - T_i)$	$[\text{eV}\,\text{cm}^3\,\text{s}^{-1}]$
Electron-neutral equilibration	$R_{n,\text{el}}(T_e - T_n) = \sigma_{n,\text{el}} u_{e,\text{th}}(T_e - T_n)$	$[\text{eV}\,\text{cm}^3\,\text{s}^{-1}]$
Contributions at the boundary		
Ion-to-wall sink	$\Gamma_{i,\text{wall}} = \Gamma_{i,\text{wall}_\parallel} + \Gamma_{i,\text{wall}_\perp}$	$[\text{s}^{-1}]$
Neutral recycling	$\Gamma_{n,\text{recyc}} = \beta\Gamma_{i,\text{wall}}$	$[\text{s}^{-1}]$
Neutral pumping[a]	$\Gamma_{n,\text{pump}} = S_P \times 1\text{e}3/\text{Vol}_n$	$[\text{s}^{-1}]$
Neutral puffing[b]	$\Gamma_{n,\text{puff}} = \text{Gas}_{\text{in}} \times 4.48\text{e}17$	$[\text{s}^{-1}]$
Electron-to-wall energy sink	$\Gamma_{e,\text{wall}} T_e$	$[\text{eV}\,\text{s}^{-1}]$

[a] S_P is the total pumping speed, expressed in $[\text{l}\,\text{s}^{-1}]$

[b] Gas_{in} is the mass inflow due to neutral gas puffing, expressed in Standard Cubic Centimeters per Minute [sccm], where 1 sccm = 4.48×10^{17} atoms s^{-1}

Table 3.1: Summary of the different contributions to particles and energy balance equations in the global point model. Direct correspondence with the contributions shown in figure 3.5 should be seen.

3.3.2. Volume average of SOLPS-ITER equations

The ion loss contribution related to the sink action of the solid wall of the vacuum chamber $\Gamma_{i,\text{wall}}$[1] is derived directly from the volume average of the corresponding term in the SOLPS-ITER:

$$\Gamma_{i,\text{wall}}\, n_i = \frac{1}{\text{Vol}_i} \int_{\text{Vol}_i} \left[\frac{1}{\sqrt{g}} \frac{\partial}{\partial x} \left(\frac{\sqrt{g}}{h_x} n_i^\star u_{x,i}^\star \right) + \frac{1}{\sqrt{g}} \frac{\partial}{\partial y} \left(\frac{\sqrt{g}}{h_y} n_i^\star u_{y,i}^\star \right) \right] \sqrt{g}\, dx\, dy\, dz \tag{3.7}$$

here h_x, h_y and h_z are the metric coefficients and $\sqrt{g} = h_x\, h_y\, h_z$; Vol_i is the total volume occupied by the ions. Quantities indicated with $\star$ represent space-dependent variables, to distinguish them from global variables, which are the unknowns of the point model. On the RHS of equation (3.7), the first term represents transport parallel to the magnetic field $\Gamma_{i,\text{wall}_\parallel} n_i$, while the second represents cross-field transport $\Gamma_{i,\text{wall}_\perp} n_i$. Reference frame is shown in figure 3.3.a.

[1] Dimensionally, this quantity is the inverse of a time $\Gamma_{i,\text{wall}} = 1/\tau_{i,\text{wall}}$, where $\tau_{i,\text{wall}}$ can be interpreted as the particle confinement time.

Applying Gauss Theorem and assuming (i) axial velocity at the targets equal to the Bohm velocity, $u_{x,i}^{\star,T} = c_s \simeq \sqrt{T_e/m_i}$, with $T_e \gg T_i$; (ii) constant electron temperature $T_e^\star = T_e$; (iii) diffusion approximation for radial transport $u_{y,i} n_i^\star = -D_\perp \partial n_i^\star / (h_y \, \partial y)$, where $D_\perp$ is the coefficient for anomalous diffusion and λ_n is particle decay length at the boundary[2], the integration of equation (3.7) gives:

$$\begin{aligned} \Gamma_{i,\text{wall}} &= \Gamma_{i,\text{wall}_\parallel} + \Gamma_{i,\text{wall}_\perp} \\ &= \frac{\alpha u_{x,i}^{\star,T} \mathrm{A}_T}{\mathrm{Vol}_i} + \frac{u_{y,i}^{\star,Lat} \mathrm{A}_{Lat}}{\mathrm{Vol}_i} = \frac{\alpha c_s \mathrm{A}_T}{\mathrm{Vol}_i} + \frac{D_\perp \mathrm{A}_{Lat}}{\lambda_n \mathrm{Vol}_i} \end{aligned} \tag{3.8}$$

where A_T and A_{Lat} are the target and lateral wall areas, respectively.

The effective coefficient for parallel transport $\alpha = n_{\text{se}}/n_i$ is defined as the ratio of the plasma density at the sheath entrance over the point plasma density. Analytical expression for α can be found integrating the 1D total momentum equation [30] along the distance covered by ions L_{tr}:

$$\frac{d}{dx}\left(m_i n_i^\star u_{x,i}^{\star 2} + n_e^\star T_e^\star\right) = S_m \tag{3.9}$$

where we neglected electron inertia and ion pressure $p_i^\star = n_i^\star T_i^\star$, under the assumption that $T_e \gg T_i$.
Momentum conservation, i.e. $S_m = 0$, readily gives $\alpha = 0.5$ or equally, $n_{i,T} = 0.5 n_i$. To solve equation (3.9) including momentum loss due to ion-neutral friction requires additional hypotheses on $n_i^\star$, $n_n^\star$ and $u_{x,i}^\star$ profiles. The source term is written as

$$S_m = -m_i R_{in,\text{el}} n_n^\star n_i^\star (u_{x,i}^\star - u_{x,n}^\star) \tag{3.10}$$

and the model we propose assumes a constant density profile $n_n^\star = n_n$ and null velocity $u_n^\star = 0$ for the neutrals, a Heaviside profile for plasma density $n_i^\star = n_i - (1-\alpha) H(x - L_{\text{tr}}) n_i$ and a linear profile for the ion velocity $u_{x,i}^\star = c_s / L_{\text{tr}} x$. With these hypotheses α is:

$$\alpha = \frac{1/2}{1 + \sigma_{CX} n_n L_{\text{tr}}/6} \tag{3.11}$$

where σ_{CX} is the cross-section of the $\mathrm{He}^+ - \mathrm{He}$ charge exchange reaction computed at $E_i = 1/2 m_i c_s^2$. The cross-section is taken from the HYDHEL database, as indicated in

[2]The ratio $D_\perp/\lambda_n$ has the dimensions of a velocity and can be regarded as the effective radial velocity at the boundary.

table 4.1.

Electron heat flux at the boundary $\Gamma_{e,\text{wall}} T_e n_e$ is not integrated for SOLPS-ITER equations. At constant T_e, it can be conveniently estimated from sheath boundary conditions using the sheath transmission coefficients introduced in section 2.3.1:

$$\Gamma_{e,\text{wall}} T_e n_e = \left(2 + V_{sh} + eV_{ps}\right) T_e \Gamma_{i,\text{wall}} n_i \tag{3.12}$$

where the first contribution is the heat flux associated with a one-way electron Maxwellian distribution; the second one is the energy loss due to the sheath potential drop[3], $V_{sh} = 0.5 \ln(2\pi m_e/m_i)(1 + T_i/T_e) \simeq 3.5$ for He in the cold-ion limit; the third one is the pre-sheath potential drop contribution, where the pre-sheath potential drop is computed from Boltzmann relation, $V_{ps} = \ln \alpha \simeq 0.7$ for $S_m = 0$.

Additional information on the global model and its benchmark with SOLPS-ITER can be found in [118].

[3]With V_{sh} we indicate the absolute value of the potential drop normalised to eT_e, where e is the electron charge. Dimensionally V_{sh} is a pure number and $V_{sh}T_e$ is the energy associated with the potential drop in eV.

PART II:

Plasma dynamics and plasma-wall interaction in LPDs

4 | Investigation of He plasmas in GyM with SOLPS-ITER

Linear plasma devices are fundamental tools for plasma-material interaction experiments and for testing materials for the plasma-facing components of future fusion power plants. Developing and optimising numerical tools to study these machines and complement the experimental activities would benefit the research on fusion materials and PWI processes. This chapter presents and summarises the modelling activities of the GyM linear machine done within this doctoral thesis, in the framework of a collaboration between Politecnico di Milano and ISPT-CNR.

The EUROfusion Work Package on Plasma-Wall Interaction and Exhaust (WP-PWIE) promoted the activities concerning helium plasma background modelling in GyM and the integrated study of erosion performed by coupling the SOLPS-ITER and ERO2.0 codes.

4.1. Modelling as a complement to PMI experiments in GyM

As discussed in section 1.4.1, the GyM machine is a medium flux linear plasma device, originally designed to investigate basic plasma physics phenomena and more recently used to study the issue of PMI for nuclear fusion applications. In recent years, most of the PMI activities in GyM have been carried out within the framework of the EUROfusion Consortium, under the Work Packages Plasma Facing Components (WP-PFC) [119], during Horizon 2020, and WP-PWIE, in the incoming Horizon Europe.
Most experimental studies performed in GyM would greatly benefit from complementary modelling activity. In particular:

- From multi-species modelling, one can retrieve the plasma composition and the distribution of the different species within the vacuum chamber. Knowing whether multiple charge states are present in the plasma is crucial to correctly assess erosion during PMI experiments.
- From simulations, plasma fluxes and heat loads at every location within the simulated domain can be evaluated. This is an important complement to experimental

measurements since plasma diagnostics can only give information localised in space. By benchmarking simulations and experimental data at a specific location, it is possible to retrieve information on the plasma at locations where experimental data are unavailable.

- Simulation of erosion, transport and redeposition of impurities can help to optimise the experimental setup by giving information on possible impurity accumulations.
- Materials with controlled morphological properties are produced at the NanoLab of Politecnico di Milano. These samples are then exposed to the GyM plasma and characterised by post-mortem techniques. Comparison between the results of this experimental characterisation with models describing the surface evolution of material under PMI can provide a tool to validate such models.

For all the studies mentioned above, the first step is the modelling of the plasma background inside the linear device. In the context of this thesis, this is done by optimising the SOLPS-ITER boundary plasma package for this purpose.

4.2. Modelling a linear device with SOLPS-ITER

This section describes the steps to set up a SOLPS-ITER simulation of a linear plasma device and complements the general discussion on its reference frame in linear geometry, presented in section 3.2.3. The most relevant differences with respect to a standard tokamak simulation are related to the computation of the magnetic field and the plasma mesh generation. Indeed, the SOLPS module for the mesh generation, Carre, could not deal with linear geometries, until very recently. Standard boundary conditions used in tokamak simulations can instead be adapted to a linear geometry, without further developments.

4.2.1. Computation of the magnetic field and mesh reconstruction

The work presented here is based on a set of Matlab routines that were first developed within M. Sala's PhD thesis [120] and that were further developed and optimised in the context of this PhD thesis. The purpose of these scripts is to compute the magnetic field and the magnetic flux function Ψ in a linear plasma device, given the position of the azimuthal coils and the external current density value and build the B2.5 computational

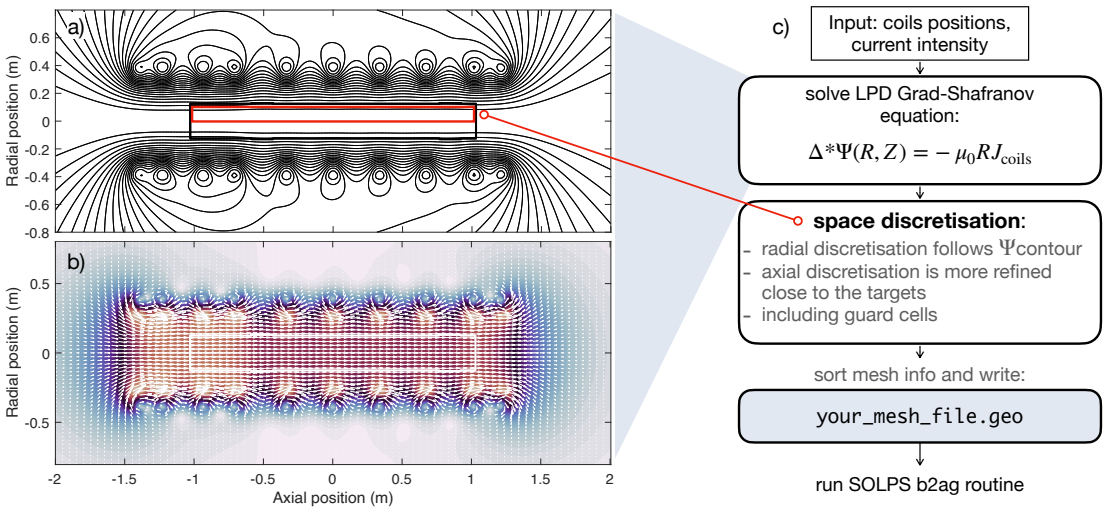

Figure 4.1: **a)** GyM flux function $\Psi(Z, R)$. **b)** GyM total magnetic field $\vec{\mathbf{B}}_{\text{tot}}(Z, R) = \vec{\mathbf{B}}_Z(Z, R) + \vec{\mathbf{B}}_R(Z, R)$ **c)** Algorithm implemented in Matlab to generate the LPD mesh for SOLPS-ITER.

mesh aligned to the Ψ surfaces. The mesh information is then written in a text file with a format that can be read by standard SOLPS-ITER routines and used to create the standard geometry inputs.

A simplified Grad-Shafranov equation is solved to retrieve the value of Ψ in the (R, Z) plane, assuming symmetry in the azimuthal direction:

$$\Delta^*\Psi(R, Z) = -\mu_0 R J_\phi \tag{4.1}$$

where $J_\phi = J_{\text{coils}}$ is the current flowing in the GyM azimuthal coils. In linear geometry J_ϕ does not include plasma current contributions, making the solution of equation (4.1) straightforward. Axial $B_Z = R^{-1}\,\partial\Psi/\partial R$ and radial $B_R = -R^{-1}\,\partial\Psi/\partial Z$ magnetic fields components can also be computed. GyM flux function and total magnetic field are shown in figure 4.1.a and 4.1.b, respectively.

As discussed in section 3.2.3, SOLPS plasma mesh extends from the symmetry axis towards the first flux surface tangent to the lateral wall. This region is contoured by a red box in figure 4.1.a. Space discretisation of the plasma domain is performed, resulting in a mesh with rectangular cells aligned with the flux surfaces in the axial direction. At the four mesh boundaries, ghost cells are added to implement B2.5 boundary conditions. Then, the mesh information, including the position of each cell centre and corner and the value of the magnetic field components in the cell centre, is formatted into a text file. This file must have the same format as the `your_mesh_file.geo` created by Uinp in the standard tokamak mesh generation procedure.

Generation of `b2fgmtry` and `fort.30` geometry files follow the usual procedure. Before running the SOLPS-ITER b2ag routine, however, one has to add the following two lines to the b2ag.dat input file:

```
'b2agsi_isymm'          '2'
'b2agfs_geometry'       'your_mesh_file.geo'
```

to set cylindrical geometry and specify the file with the mesh information.
Further details on the mesh generation procedure for a LPD are included in a tutorial entitled *"Hints on how to generate SOLPS-ITER input files for Linear Plasma Devices"*, which was made available in SOLPS-ITER documentation.

4.2.2. Simulation setup: boundary conditions, sources and transport properties in linear devices

Section 4.2.1 describe the procedure to obtain the SOLPS-ITER plasma computational mesh in a linear geometry. In figure 4.5.a, the overall simulation domain is shown. This includes the plasma mesh (with rectangular cells) superimposed on the neutral mesh (triangular cells), the vacuum chamber profile, the location of the pumping and puffing systems and the position of the Langmuir probes used to benchmark simulations and experimental data. Further details on the boundary conditions, anomalous transport coefficients and external power source implementation are discussed in the following of this section.

Plasma and neutrals boundary conditions

Plasma boundary conditions used in SOLPS-ITER simulations of GyM are:

- Basis of the cylinder: sheath boundary conditions, as implemented on divertor targets in tokamak SOLPS-ITER simulations.
- Symmetry axis: zero particles and energy fluxes, zero velocity for the parallel momentum equation and zero current for the potential equation.
- Lateral wall: zero parallel velocity and zero current. Exponentially decaying profile for temperatures, with decay length λ_{decay}. For particles fluxes we used either an exponentially decaying profile for the density, with decay length λ_{decay}, or small-leakage boundary conditions $\Gamma = -\alpha_{\text{leak}}\,\Gamma_{sh}$, where Γ_{sh} is the corresponding flux using sheath boundary conditions and $\alpha_{\text{leak}} \sim 1 \times 10^{-3} - 1 \times 10^{-2}$ is a small parameter. Figure 4.2 shows the radial electron density and temperature profiles for

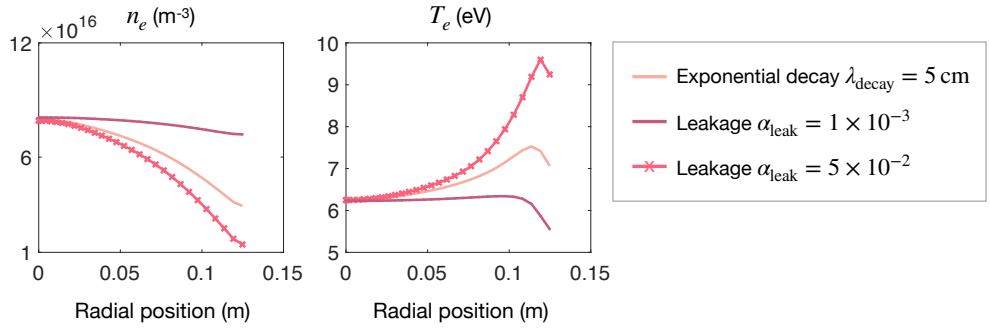

Figure 4.2: Radial profiles of electron density and temperature for different density boundary conditions at the lateral wall. Exponentially decaying profile with decay length $\lambda_{\text{decay}} = 5$ cm, leakage boundary conditions with $\Gamma_n = -1 \times 10^{-3}\,\Gamma_{n,sh}$ and $\Gamma_n = -5 \times 10^{-2}\,\Gamma_{n,sh}$.

different radial density boundary conditions. All the other simulation parameters are fixed.

The main difference with respect to tokamaks simulations is related to the heat flux boundary condition at the core. In tokamaks, this is used to set the source of power coming from the core plasma. In LPDs, a symmetry/zero-flux boundary condition is used instead and the external power source is implemented as described later.

As discussed in section 2.3.2, particle and energy recycling boundary conditions for neutral particles, imposed on the EIRENE side of the simulations, exploit coefficients from an internal TRIM database. From this database, it is possible to assess the particle and energy reflection coefficients at the wall surface, providing the ion energy and the impact angle with respect to the surface normal and the target (material) and projectile (ion) species. SOLPS-ITER simulations of GyM assumed that the full chamber wall is made of iron (Fe), that is $\approx 80\%$ of AISI 304L alloy.
The red dashed segments in figure 4.5.a show the position of turbo-molecular pumps in GyM and the corresponding absorbing surfaces (RECYCT < 1) implemented in the simulations. Since axial symmetry is assumed in EIRENE, the area of each pumping surface to be considered when computing the numerical value of the RECYCT coefficients from equation (2.29) is $A = 2\pi r_p L_p$, where r_p and L_p are the distance from the axis and the width of the pumping surfaces.
Gas throughput is also imposed as a particle flux from an EIRENE surface close to the left base and indicated in figure 4.5.a with a triangle.

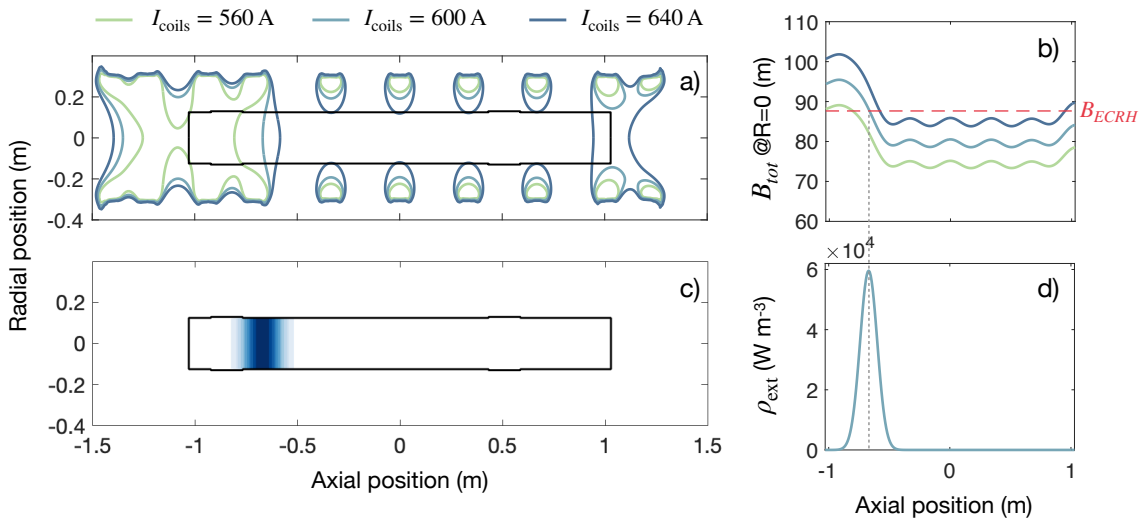

Figure 4.3: ECRH source in GyM is modelled with a Gaussian axial profile, peaked at the ECR position. **a)** ECR position on the (Z,R) plane; **b)** on axis magnetic filed: at I_{coils} = 600 A, the $\mathbf{B}_{tot}(Z,0) = B_{ECRH}$ at $z_{ECRH} \simeq -0.67$ cm. **c)** Power density distribution used to model ECRH source in GyM: **d)** a gaussian axial profile, peaked at the ECR position, constant radially within the plasma volume.

External power source

As discussed in section 1.4.1, GyM is equipped with two gyrotron sources at 2.45GHz, which heat the plasma exploiting ECRH at magnetic field B_{ECRH} = 87.5 mT. Figure 4.3.a shows the position of the resonance on the (Z, R) plane for different values of external current I_{coils} and figure 4.3.b locates the axial position where $B_{tot}(Z,0) = B_{ECRH}$. In the simulations presented in this work, we always considered I_{coils} = 600 A, so that the resonant magnetic field is well localised axially at $z_{ECRH} \simeq -0.67$ cm.
SOLPS-ITER allows adding external particles, momentum and energy sources and setting arbitrary radial and axial profiles by using the `b2.sources.profile` input namelist. GyM ECRH source is implemented as an external electron energy source contribution with the power density distribution shown in figure 4.3.c. A constant radial profile was chosen as a first approximation. Axially we used a gaussian profile peaked at the position of the electron cyclotron resonance with $\sigma \simeq 10$ cm, as shown in figure 4.3.d. The total power absorbed by electrons is given by the integral of the Gaussian power density over the plasma volume

$$P_{ext} = \int \rho_{max} e^{-\frac{(z-z_{ECRH})^2}{\sigma^2}} dV \simeq \pi\sqrt{\pi}\rho_{max}\sigma r_0^2 \tag{4.2}$$

where r_0 is the plasma radius and ρ_{max} is the peak power density.

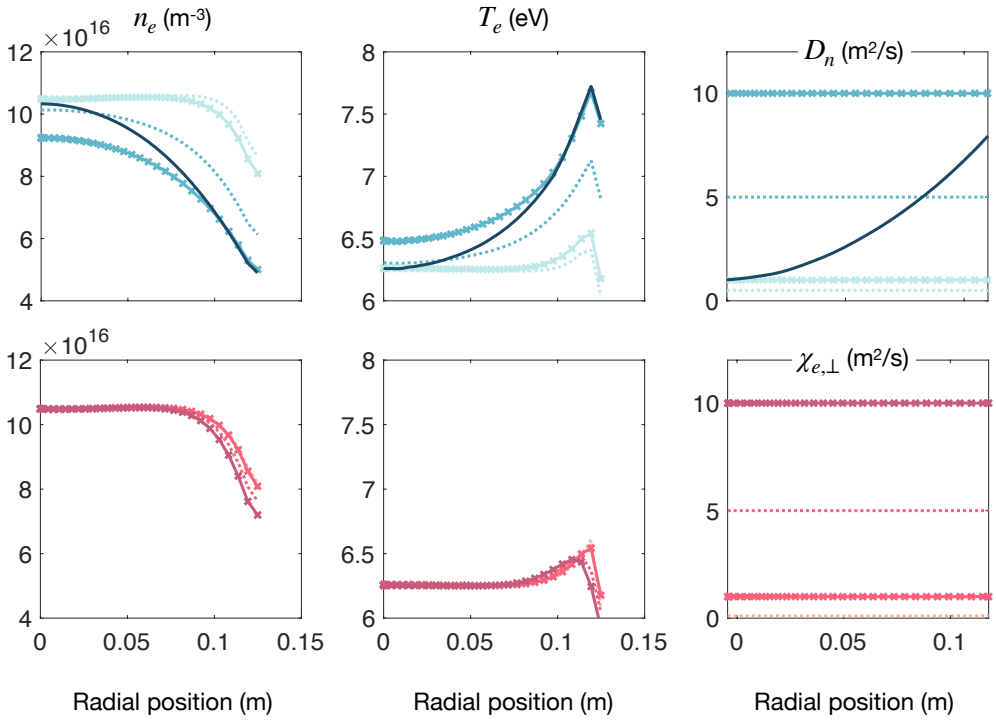

Figure 4.4: Radial profiles of electron density (left), temperature (middle) and anomalous transport coefficient (right). Profiles are taken at the axial position corresponding to LP 4U in figure 4.5. Blue lines (top) represent the scan over anomalous particle transport coefficient D_n and red lines (bottom) are the scan over anomalous electron heat transport coefficient $\chi_{e,\perp}$.

Transport coefficients

GyM plasma conditions fall into the sheath-limited regime: low density and small parallel temperature gradients. According to the discussion presented in section 2.1.2, parallel kinetic corrections in the sheath-limited regime are small if sheath boundary conditions are imposed at the plasma-wall interface. This was confirmed by simulations performed with different electron heat flux limiting factors (α_κ in equation (2.18)): this free parameter was shown to have no impact on GyM simulations and it was set to $\alpha_\kappa = 0.15$ for all the simulations presented in the following.

The effect of different anomalous particle and heat transport coefficients was also investigated. Constant and radially varying profiles were tested and optimised both in shape and value to match simulated profiles and experimental data, as presented in section 4.2.3. To understand the effect that these parameters have on SOLPS-ITER simulations we performed a parametric scan of D_n and $\chi_{e,\perp} = \kappa_{e,\perp}/n_e$ at fixed neutral pumping (2 turbo-pumps with $S = 500\,\mathrm{L/s}$ corresponding to $p_a = 0.013$ on the pumping surfaces) and puffing ($\Gamma_{n,\mathrm{puff}} = 1.88 \times 10^{19}\,\mathrm{atoms/s}$), fixed external power ($P_{\mathrm{ext}} = 520\,\mathrm{W}$)

and radial decay length boundary condition ($\lambda_{\text{decay}} = 5\,\text{cm}$). Radial profiles of electron density and temperature for different radial profiles of D_n and $\chi_{e,\perp}$ are shown in figure 4.4.

The parametric scan of anomalous particle transport is performed at constant $\chi_{e,\perp} = 1\,\text{m}^2/\text{s}$. Simulations with constant D_n radial profiles show that for $D_n \lesssim 5\,\text{m}^2/\text{s}$, an increase of the anomalous transport increases the magnitude the radial density and temperature gradients, without modifying n_e and T_e values at $r = 0$. For $D_n \gtrsim 5\,\text{m}^2/\text{s}$, instead, increasing anomalous transport does not modify the radial shape of plasma profiles but tends to translate the whole profile towards lower densities and higher temperatures. A simulation with $D_n \propto r^2$ was also performed. D_n profile was chosen such that $D_{n,r=0} = 1\,\text{m}^2/\text{s}$ and $D_{n,r=r_0} = 10\,\text{m}^2/\text{s}$. The resulting n_e and T_e show an almost perfect transition between the profiles obtained with constant $D_n = 1\,\text{m}^2/\text{s}$ for $r \simeq 0$ and the profiles at constant $D_n = 10\,\text{m}^2/\text{s}$ for $r \simeq r_0$. The parametric scan over $\chi_{e,\perp}$, performed at constant $D_n = 1\,\text{m}^2/\text{s}$, show that the effect of $\chi_{e,\perp}$ on the plasma parameters is almost negligible. This is consistent with the hypothesis of the sheath-limited regime, dominated by convection rather than conduction.

4.2.3. Benchmark of SOLPS-ITER simulations with experimental data

Finally, we present the benchmark of SOLPS-ITER simulations with GyM experimental data. These simulations are performed using the full set of plasma-neutral interaction processes listed in table 4.1.

The simulation was set up to match the puffing and pumping conditions of the experimental discharge. The two turbomolecular pumps were working at speed $S = 500\,\text{L/s}$ and the gas flow rate was set to $\Gamma_{n,\text{puff}} = 42\,\text{sccm} = 1.88 \times 10^{19}\,\text{atoms/s}$. According to the discussion of section 4.2.2, this gives a particle absorption probability at EIRENE pumping surfaces $p_a = 0.013$.

The experimental neutral pressure measured along the two ducts connecting the main chamber to the turbomolecular pumps is $p_{\text{He}}^{\text{exp}} = 0.09\,\text{Pa}$. The measured value is almost identical for both pressure gauges. The simulated pressure distribution extracted from SOLPS-ITER is shown in figure 4.5.b. The pressure distribution is peaked close to the bases of the cylinder, reproducing plasma recycling, and it is almost uniform in the central plasma region. The simulated values well reproduce the experimental ones.

Before moving to the analysis and benchmark of the radial plasma profiles, we first comment the general plasma properties in GyM. The only relevant ion population in GyM conditions He^+. In fact, from SOLPS-ITER simulations $n_{He^{2+}}/n_{He^+} \lesssim \times 10^{-3}$

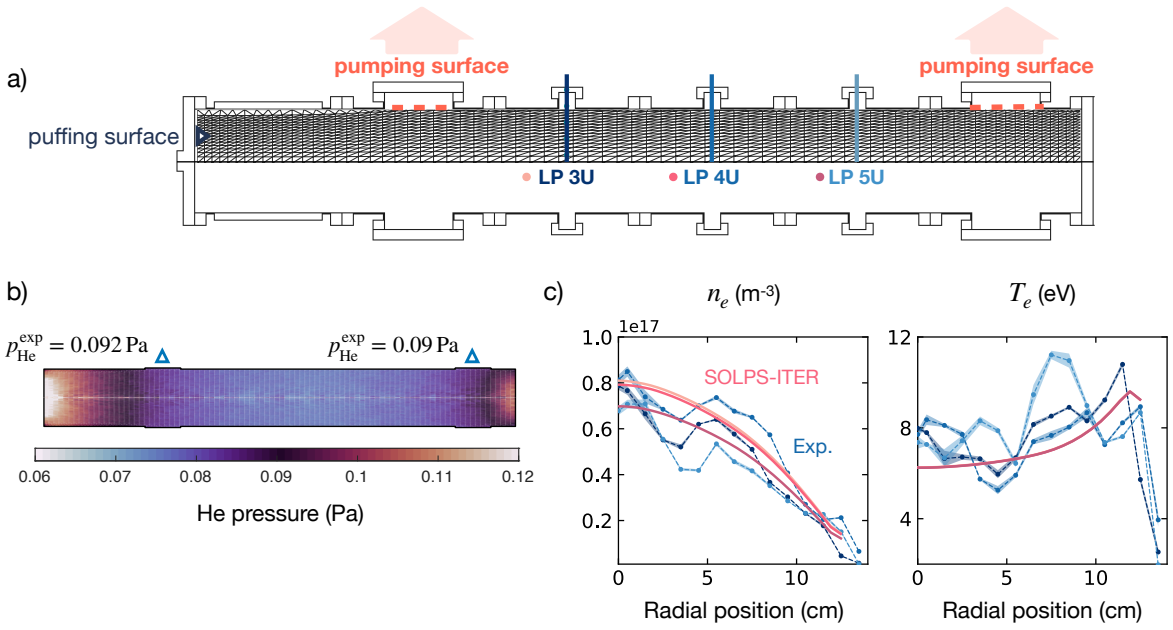

Figure 4.5: **a)** SOLPS-ITER computational domain for GyM simulations, including the plasma mesh (rectangular) superimposed on the neutral mesh (triangular), the vacuum chamber profile, the location of the pumping and puffing systems and the position of the Langmuir probes. **b)** Comparison of experimental and simulated neutral gas pressure. **c)** Comparison of electron density (left) and temperature (right) radial profiles: blue lines are the experimental LP measurements and red lines are SOLPS-ITER results. Radial profiles are shown at three axial locations, corresponding to the experimental location of the LPs.

and thus in the following we will consider $n_i = n_{He^+} = n_e$. Ion temperature is low $T_i \lesssim 0.05\,\text{eV} \ll T_e$, hence a cold ion approximation can be well justified.

The experimental profiles of electron density and electron temperature are estimated using three Langmuir probes located in sectors 3, 4, and 5 of the GyM chamber, as shown in figure 4.5.a. To match the simulated plasma profiles and the experimental ones, we acted on the optimisation of three parameters: (i) the anomalous transport coefficient D_n, (ii) the leakage boundary condition factor and (iii) the total absorbed power by electrons. The parametric scans presented in section 4.2.2 helped in understanding the effect of the different parameters on the simulation results and it was a useful guide to obtain the matching shown in figure 4.5.c. The simulation was performed using anomalous particle transport coefficient D_n with a profile $\propto r^2$, as the one shown in figure 4.4. Radial leakage boundary condition with $\alpha_{\text{leak}} = 5 \times 10^{-2}$ was used to match the experimental plasma density close to the lateral wall. A total absorbed electron power $P_{\text{ext}} = 400\,\text{W}$ was imposed. During the experiments, the microwave source@2.45 GHz delivered a total power of $P_{RF} = 1200$ W, hence the absorption efficiency of the wave in the plasma can be estimated around $\eta \sim 30\%$.

4.3. Benchmark of a 0D global model against SOLPS-ITER simulations

Complex simulations such as the one presented in section 4.2 come at the price of a high computational cost. Moreover, due to the complexity of the model, a straightforward interpretation of their results can be difficult. A simplified approach to guide the interpretation of simulation results can be particularly appealing also in connection with the simplified geometry of a linear plasma device. In the context of this thesis, we thus developed an original global 0D model, i.e. zero-dimensional and space-independent, based on the volume average of fluid equations for a magnetized plasma. The equations are obtained from the space integration of the SOLPS-ITER model as described in section 3.3. In this section, we present the results of the benchmark analysis between the 0D model and SOLPS-ITER.

Twenty-five SOLPS-ITER simulations were performed varying the total external power absorbed by the electron population ($P_{\text{ext}} = 180\,\text{W}, 360\,\text{W}, 540\,\text{W}, 720\,\text{W}, 900\,\text{W}$) and the neutral puffing intensity ($\Gamma_{n,\text{puff}} = 5\,\text{sccm}, 10\,\text{sccm}, 15\,\text{sccm}, 20\,\text{sccm}, 25\,\text{sccm}$). These simulations were performed with a single pumping surface (the one on the RHS in figure 4.5) with $p_a = 0.018$, corresponding to a pumping speed $S = 760\,\text{L}\,\text{s}^{-2}$. Anomalous transport coefficients with constant radial and axial profiles were used, $D_n = 0.5\,\text{m}^2/\text{s}$ and $\chi_{e,\perp} = 1.5\,\text{m}^2/\text{s}$. Radial decay length boundary conditions were applied to the lateral wall, with $\lambda_{\text{decay}} = 5\,\text{cm}$. In these simulations, the only atomic reactions considered in EIRENE were electron impact ionization and recombination. Charge exchange and electron impact excitations were neglected. A discussion on the implications of the assumptions on atomic reactions is given in section 4.4.
The same parameters were used to solve equations (3.4), (3.5) and (3.6). In this case, however, due to the much lower computational cost, the parametric scan spanned over 25 values of puffing strengths in the range $4-26\,\text{sccm} \simeq 1.8\times10^{18}-1.2\times10^{19}\,\text{atoms}/\text{s}$ and 25 values of electron power in the range $100-1000\,\text{W}$. $E_{n,\text{rad}}R_{n,\text{rad}}$ and $E_{i,\text{rad}}R_{i,\text{rad}}$ in equation (3.6) were set to 0 in order to neglect electron impact excitation, as done in SOLPS-ITER simulations. The effective coefficient for parallel transport was set equal to $\alpha = n_{\text{se}}/n_i = 0.5$, neglecting ion-neutral friction due to charge-exchange reactions.
To compare SOLPS-ITER and the 0D results, the volume average of SOLPS-ITER results was taken. Results of the benchmark are shown in figure 4.6. In particular, figure 4.6.a and figure 4.6.b show the global electron density and temperature, respectively, as a function of the two scan parameters P_{ext} and $\Gamma_{n,\text{puff}}$. The blue surface represents the 0D parametric scan, while the red "X"s are volume average results of SOLPS-ITER simulations. A remarkable qualitative agreement is observed between

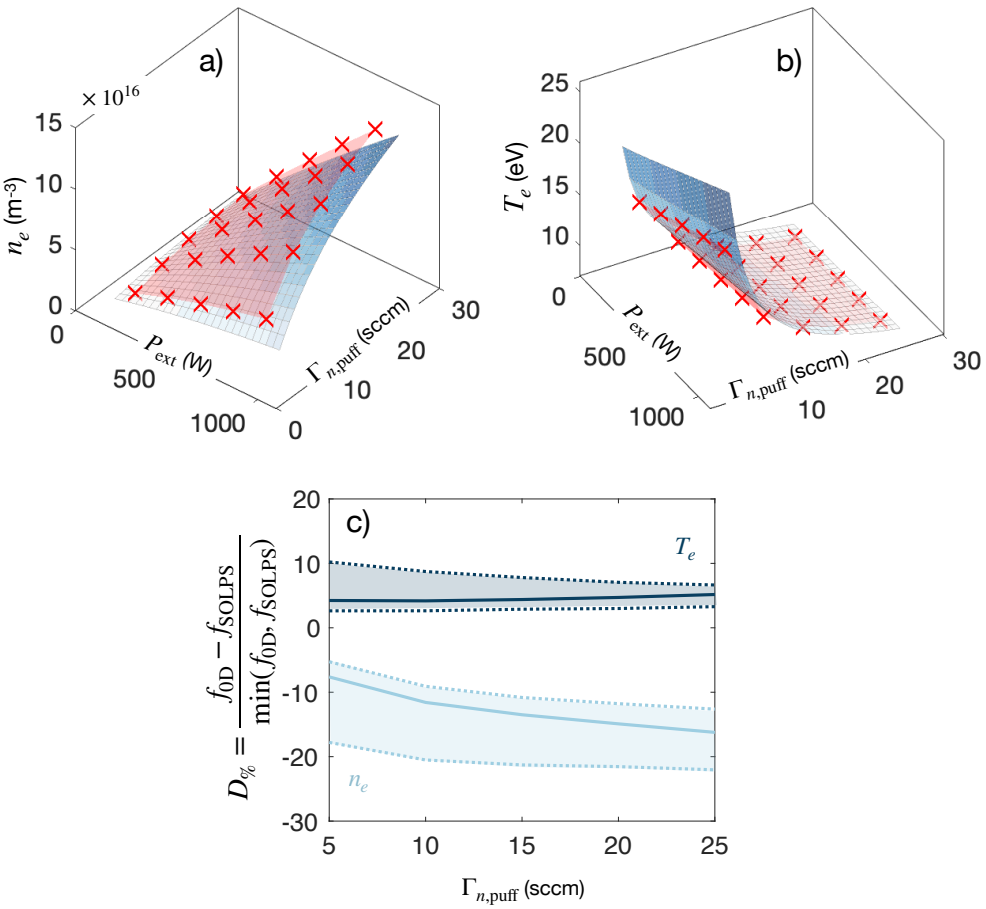

Figure 4.6: Benchmark of the 0D model for He plasma with SOLPS-ITER. **a)** Electron density and **b)** electron temperature as a function of the puffing rate ($\Gamma_{n,\text{puff}}$) and external electron power (P_{ext}). The blue surface represents 0D results and the red "X"s represent SOLPS-ITER simulations. **c)** Maximum relative difference between the two models as a function of puffing strength. The shadowed area represents the minimum and maximum variation as a function of P_{ext}.

the two models: the 0D model is capable of reproducing the trends of the plasma electron density and temperature as a function of both P_{ext} and $\Gamma_{n,\text{puff}}$. Quantitative differences are computed as:

$$D_{\%} = \frac{f_{0D} - f_{\text{SOLPS}}}{\min(f_{0D}, f_{\text{SOLPS}})} \tag{4.3}$$

where f is either n_i or T_e, and shown in figure 4.6.c as a function of the puffing strength. For each value of $\Gamma_{n,\text{puff}}$, the solid line is the median over the P_{ext} values and the shadowed area goes from the minimum to the maximum values of $D_{\%}$ in the P_{ext} range. The temperature difference is in any of the cases considered below $\lesssim 10\%$ while the density difference is between $\simeq 10\% - 20\%$ and increases increasing the puffing strength.

4.3.1. Analytical formulae

Simplified analytical formulas for n_i, n_n and the ionization degree $\theta_{\text{iz}}(T_e)$ as a function of T_e can be derived from equations (3.4), (3.5) and (3.6). The main hypotheses can be summarised as follows: (i) steady-state; (ii) only electron collision processes with neutral atoms are considered, this is a good approximation at small θ_{iz}; (iii) charge-exchange is neglected, $\alpha = n_{\text{se}}/n_i = 0.5$; (iv) electron impact excitation and ionization rate coefficients are only functions of T_e, n_e dependence is neglected.

With these assumptions, the neutral density n_n is obtained from equation (3.4):

$$n_n(T_e) = \frac{\Gamma_{i,\text{wall}}}{R_{\text{iz}}} \tag{4.4}$$

and substituting equation (4.4) into equation (3.6), one gets the expression of n_i:

$$n_i(T_e) = \frac{P_{\text{ext}}}{\text{Vol}_{\text{i}}} \left[\Gamma_{e,\text{wall}} T_e + \left(E_{\text{iz}} + \frac{E_{n,\text{rad}} R_{n,\text{rad}}}{R_{\text{iz}}} \right) \Gamma_{i,\text{wall}} \right]^{-1} \tag{4.5}$$

The analytical profiles of plasma and neutral density as a function of the electron temperature are shown in figure 4.7.a for $P_{\text{ext}} = 900\,\text{W}$ and $\Gamma_{n,\text{puff}} = 30\,\text{sccm}$. Neither equation (4.4) nor equation (4.5) explicitly depend on $\Gamma_{n,\text{puff}}$. However, the effect of the puffing strength is introduced as an upper limit to the neutral density $n_{n,\infty}$, which is set by a proper combination of puffing and pumping. For more information on the derivation of $n_{n,\infty}$ refer to section 4.3.2.

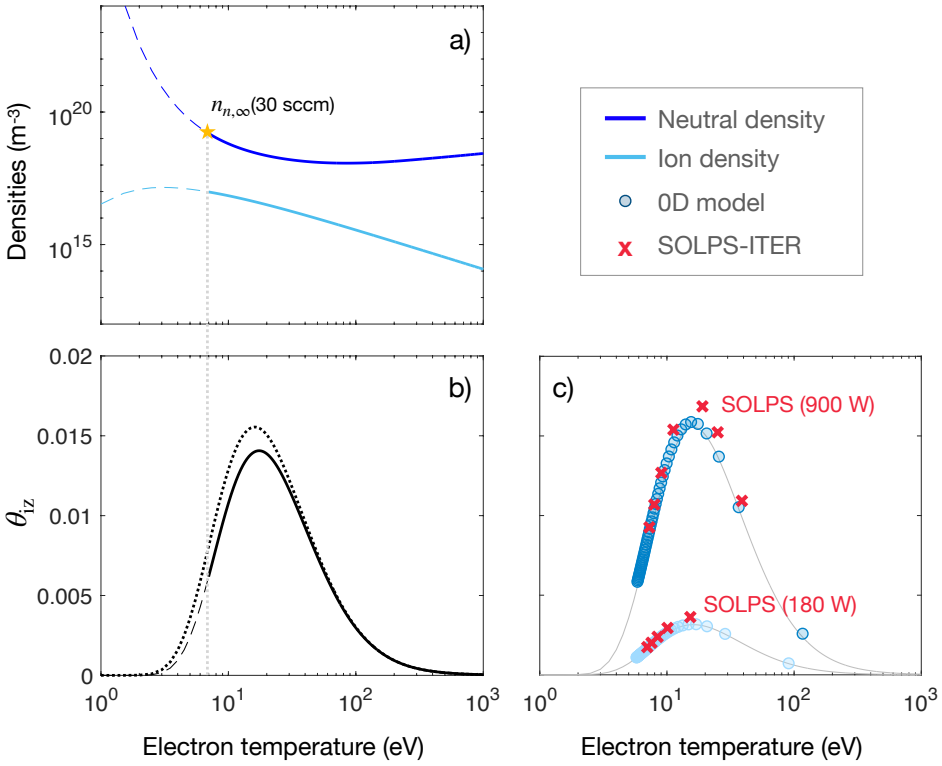

Figure 4.7: **a)** Analytical profiles for plasma and neutral densities as a function of T_e. **b)** Analytical profiles for the ionization degree θ_{iz}. Dashed lines are obtained without any limiting condition on n_n, solid is obtained limiting neutral density to $n_n < n_{n_\infty}$, with $\text{Gas}_{in} = 30\,\text{sccm}$. **c)** Comparison of θ_{iz} obtained with analytical (solid line), 0D (dots) and SOLPS-ITER (crosses) models. Data are shown for $P_{ext} = 900\,\text{W}$ $P_{ext} = 180\,\text{W}$. $E_{n,rad}R_{n,rad} = 0$ in the 0D model and in equation (4.6) to allow consistent comparison with SOLPS-ITER simulations.

Finally, combining equations (4.4) and (4.5), $\theta_{\mathrm{iz}}(T_e)$ is:

$$\theta_{\mathrm{iz}}(T_e) = P_{\mathrm{ext}} \left[\frac{\Gamma_{i,\mathrm{wall}} \mathrm{Vol}_e}{R_{\mathrm{iz}}} \left(\Gamma_{e,\mathrm{wall}} T_e + \left(E_{\mathrm{iz}} + \frac{E_{n,\mathrm{rad}} R_{n,\mathrm{rad}}}{R_{\mathrm{iz}}} \right) \Gamma_{i,\mathrm{wall}} \right) + P_{\mathrm{ext}} \right]^{-1} \tag{4.6}$$

The profile of $\theta_{\mathrm{iz}}(T_e)$ as a function of T_e is shown in figure 4.7.b (solid line). It has an asymmetric bell shape, which tends to zero at very low and very high temperatures and has a maximum for T_e around of the ionization energy, $E_{\mathrm{iz}} = 24.58\,\mathrm{eV}$ for helium. The maximum θ_{iz} for typical plasma conditions in GyM is below $\simeq 2\,\%$.
The analytical profile of θ_{iz} from equation (4.6) is compared to the results of the full 0D model and SOLPS-ITER simulations in figure 4.7.c. To be consistent with the SOLPS-ITER plasma-neutral interaction model, $E_{n,\mathrm{rad}} R_{n,\mathrm{rad}}$ is set to 0 both in the 0D model equations and in equation (4.6). The effect of switching off this term is shown in figure 4.7.b with a dotted line. The increase of the electron density (and thus the θ_{iz}) as a consequence of switching off electron impact excitation will be discussed in more detail in section 4.4.
Figure 4.7.c compares results of the θ_{iz} according to the analytical formula, the 0D model and SOLPS-ITER simulations. θ_{iz} computed using equaton (4.6) with $P_{\mathrm{ext}} = 900\,\mathrm{W}$ and $P_{\mathrm{ext}} = 180\,\mathrm{W}$ is plotted with solid lines. The 0D model is solved at the same input powers (lighter blue dots $P_{\mathrm{ext}} = 180\,\mathrm{W}$ and darker blue dots $P_{\mathrm{ext}} = 900\,\mathrm{W}$) for 50 values of $\Gamma_{n,\mathrm{puff}}$ in the range $2 - 50$ sccm. Finally, the red crosses are volume-averaged results of SOLPS-ITER simulations at different puffing strengths. For $P_{\mathrm{ext}} = 900\,\mathrm{W}$, we performed two additional simulations with lower puffing strength, $\Gamma_{n,\mathrm{puff}} = 3 - 4\,\mathrm{sccm}$ which corresponds to the two crosses at higher T_e. The trend of $\theta_{\mathrm{iz}}(T_e)$ obtained from the seven SOLPS-ITER simulations reproduce the same bell-shape peaked at ≈ 25 eV is obtained with the analytical formulas and with the point model.

4.3.2. Time dependent analysis

So far we considered the comparison of the steady-state solutions of SOLPS-ITER and the 0D model. Here, we investigate the time evolution of equations (3.4), (3.5) and (3.6).

Before moving to the full system of equations, it is convenient to solve the gas dynamics in absence of the plasma, i.e. solving equation (3.5) with $n_i = n_e = T_e = 0$. The analytical solution for the equation is:

$$n_n(t) = n_{n_0} \exp\left(-t/\tau\right) + n_{n_\infty} \left(1 - \exp\left(-t/\tau\right)\right) \tag{4.7}$$

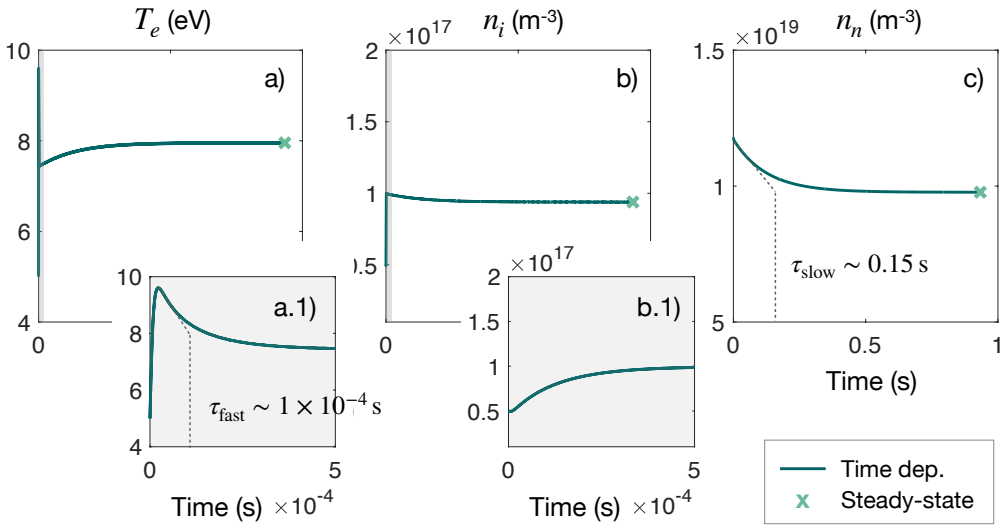

Figure 4.8: Time evolution of **a)** plasma density, **b)** electron temperature and **c)** neutral density. In the grey boxes, the fast time scale $t < 5 \times 10^{-4}$ s is shown for the plasma density and electron temperature in figures a.1) and b.1), respectively. The "X"s represent the steady-state solutions.

where n_{n_0} is the initial neutral density value, $n_{n_\infty} = \Gamma_{n,\text{puff}} / \left(\Gamma_{n,\text{pump}} \text{Vol}_n\right)$ is the steady-state value of neutral density and the time constant $\tau = \tau_{\text{pump}} = 1/\Gamma_{n,\text{pump}} \sim 0.13\,\text{s}$ depends only on the pumping speed $S_P = 760\,\text{L}\,\text{s}^{-1}$. n_{n_∞} was used as the higher limit to the neutral density in deriving equations (4.4) and (4.5) in section 4.3.1.

To solve the full plasma system, we consider the input parameters described in section 4.3 and we fix $P_{\text{ext}} = 900\,\text{W}$ and $\text{Gas}_{\text{in}} = 20\,\text{sccm}$. Solutions as a function of time are plotted in figure 4.8.

In figures 4.8.a, 4.8.b and 4.8.c, the long-term evolution of the plasma density, electron temperature and neutral density is shown, respectively. The system reaches the steady-state in a few fractions of a second and we can roughly estimate the dominant time constant of the system to be $\tau_{\text{slow}} \sim 0.15\,\text{s}$ that is very close to the gas time constant in absence of the plasma τ_{pump}.

If we compare figure 4.8.a and 4.8.b with figure 4.8.c, we can see that, while the neutral density transient can be well approximated by a simple exponential decay with a time constant τ_{slow}, the plasma dynamic (electron temperature and ion density) is characterised by two different time constants: the plasma experiences a very fast transient at τ_{fast} followed by a small and slow adjustment at τ_{slow}. The fast transients of plasma density and electron temperature are shown in figures 4.8.a.1 and 4.8.b.1, respectively. The time constant $\tau_{\text{fast}} \sim 1 \times 10^{-4}\,\text{s}$ is of the same order of magnitude as the ion confinement time $\tau_{\text{wall}} = \Gamma_{i,\text{wall}}^{-1} \sim 1 \times 10^{-4}\,\text{s}$. From the physical point of view, thus, the slow

plasma and neutral dynamics can be ascribed to the neutral pumping-puffing dynamics, while the very fast transient only experienced by the charged particles is related to the particle confinement time.

4.4. The role of atomic reactions in low-temperature helium plasmas

The SOLPS-ITER model is based on Braginkii fluid equations and as discussed in section 2.1.1 was originally developed for a two-population fluid and then extended to multi-species plasma with the hypothesis of a main hydrogenic species. In most SOLPS applications, if He is present in the plasma, it is a minor impurity. In this condition, it is legit to consider only the very basic reactions to account for the creation and destruction of plasma particles and SOLPS-ITER simulations usually only included electron impact ionization (EI) and the effective recombination (RC) of He (reactions 1, 3, and 4 in table 4.1). The simulations presented in section 4.3 only included these three processes. However, additional reactions can be important if helium is no longer a minority species as in the studies presented in this chapter.
This section aims at investigating when and how other plasma-neutral interaction processes become important. Understanding the impact of atomic processes on the overall plasma simulation and defining a more complete set of reactions for a He plasma can significantly improve our description of pure He plasmas.

4.4.1. SOLPS-ITER plasma-neutral interaction processes in helium

The effects of plasma-neutral interactions in helium were analysed with SOLPS-ITER simulations and with the simplified 0D global model described in section 4.3. One of the aims of this work has been the optimisation of the reaction database in EIRENE to improve SOLPS-ITER capabilities to describe pure helium plasmas. The full set of plasma-neutral reactions considered in this work is reported in table 4.1. In addition to ionization and recombination, we investigated the effects of electron impact excitation (reaction 2), charge exchange reactions among helium ions and neutrals (reaction 5) and elastic collisions among He atoms (reaction 6).

The effect of He elastic collisions is very small ($\lesssim$ 2%) and it won't be considered in more detail. For the analysis of the other reactions, we started with a common SOLPS-ITER simulation setup. The input parameters are the ones optimised to match the experimental data, discussed in section 4.2.3. The reference simulation, indicated with

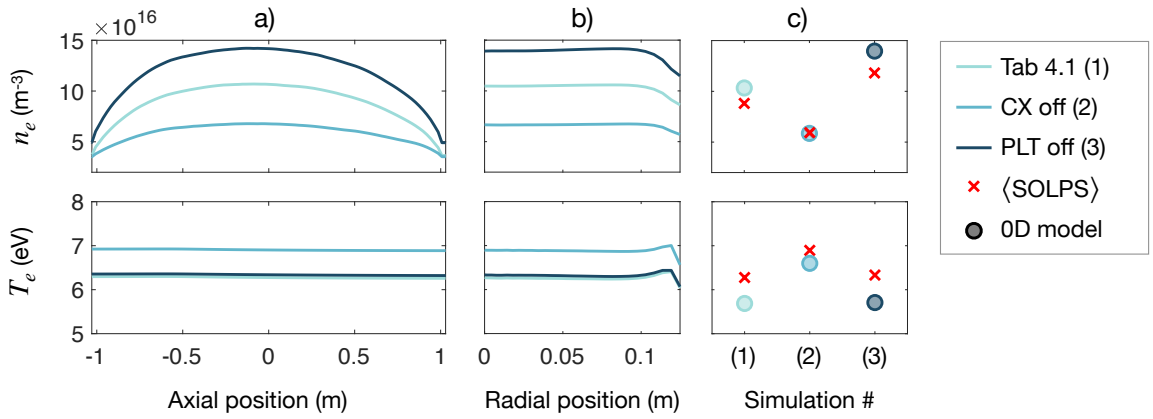

Figure 4.9: Effect of the helium plasma-neutral interaction process on the plasma parameters. **a)** Axial and **b)** radial profiles of electron density (top) and electron temperature (bottom) estimated by SOLPS-ITER with different plasma-neutral reaction databases in EIRENE. **c)** Comparison of the volume average electron density and temperature by SOLPS-ITER (X) and the 0D model (o).

(1) in the following, is the same that we compared to experimental data in figure 4.5.c and includes all the plasma-neutral reactions in table 4.1.
Simulation (2) is performed by turning off charge-exchange reactions between ions (He^+ and He^{2+}) and neutral atoms. Simulation (3) excludes the electron impact excitation process from the available electron energy loss mechanisms. When this process is included, the power lost by electrons in interactions with neutral He per unit volume is computed as

$$P^{\text{loss}}_{\text{e,He}} = (E_{\text{iz}} \langle \sigma v \rangle_{\text{iz}} + \langle E \sigma v \rangle_{\text{PLT}})\, n_e n_{\text{He}} \tag{4.8}$$

where $E_{\text{iz}} = 24.5\,\text{eV}$ is the He ionization energy, $< \sigma v >_{\text{iz}}$ is the ionization rate coefficient and $< E\sigma v >_{\text{PLT}}$ is the excitation energy rate coefficient [121].
The results of the three simulations are shown in figure 4.9.a and 4.9.b in terms of axial and radial profiles of electron density and temperature.
The same three conditions are also investigated using the global 0D model. To recover the same conditions as simulation (1), we solved equations (3.4), (3.5) and (3.6) with $\alpha = n_{\text{se}}/n_i$ computed according to equation (3.11). Conditions of simulation (2) are obtained by setting $\alpha = 0.5$. Finally, conditions of simulation (3) are obtained by setting $E_{n,\text{rad}} R_{n,\text{rad}} = 0$ and $E_{i,\text{rad}} R_{i,\text{rad}} = 0$ and α according to equation (3.11). The results, in terms of the average electron density and temperature, are shown in figure 4.9.c and compared to the volume average of SOLPS-ITER results.

Charge exchange reactions act as s sink of ion momentum. Neglecting these atomic processes, collisional drag among ions and neutrals is deactivated. The effect is to

	Reaction	Type	Database
1.a)	$He + e^- \rightarrow He^+ + 2e^-$	EI - H.4	ADAS adf11/scd96
1.b)	$He^+ + e^- \rightarrow He^{2+} + 2e^-$		
2.a)	$He + e^- \rightarrow He^{(*)} + e^-$	EI - H.10	ADAS adf11/plt96
2.b)	$He^+ + e^- \rightarrow He^{+(*)} + e^-$		
3.a)	$He^+ + e^- \rightarrow He$	RC - H.4	ADAS adf11/acd96
3.b)	$He^{2+} + e^- \rightarrow He^+$		
4.a)	$He^+ + e^- \rightarrow He + h\nu$	RC - H.10	ADAS adf11/prb96
4.b)	$He^{2+} + e^- \rightarrow He^+ + h\nu$		
5.a)	$He^+ + He \rightarrow He + He^+$	CX - H.1 - H.3	HYDHEL 5.3.1
5.b)	$He^{2+} + He \rightarrow He + He^{2+}$	CX - H.1 - H.3	HYDHEL 6.3.1
6)	$He + He \rightarrow He + He$	EL - H.2	AMMONX R-HE-HE

Table 4.1: List of He atomic reactions included in SOLPS-ITER model. For additional information of the reaction types see section 2.2.2 or refer to Eirene manual (`http://www.eirene.de/`). This is now the default set of reactions defined when helium is present among the plasma species in SOLPS-ITER.

decrease the ion-to-wall confinement time, leading to a decrease in the ion densities and an increase in the electron temperature. This behaviour is well reproduced both by SOLPS-ITER and the 0D model. The reduction of the ion confinement time $\tau_{\text{wall}} = \Gamma_{i,\text{wall}}^{-1}$ is connected with the increase of the ion flux at the wall $\Gamma_{i,\text{wall}} \times A_{\text{wall}}$. This is well described by the 0D model, where indeed the effective coefficient for parallel transport computed using eqaution (3.11) is $\alpha = n_{\text{se}}/n_i < 0.5$, which is the limit without CX.
Electron impact excitation introduces an additional energy loss mechanism for electrons, besides ionization. Unlike ionization, however, electron impact excitation does not contribute to the creation of additional charged particles. For fixed input power, the fraction which is used to create electrons is reduced leading to an overall density decrease without, however, affecting the electron temperature value. Again, this behaviour is well reproduced both by SOLPS-ITER and the 0D model.

The SOLPS-ITER default database for He plasmas has been updated, including all the reactions listed in table 4.1.

4.4.2. Metastable states in He plasma

Results presented in section 4.4.1 were obtained using the rate coefficients from the *metastable unresolved* ADAS database [121]. In low-temperature, low-density plasma conditions typical of LPDs, however, meta-stable states and their transport within the plasma could significantly affect the plasma properties. This section presents the first

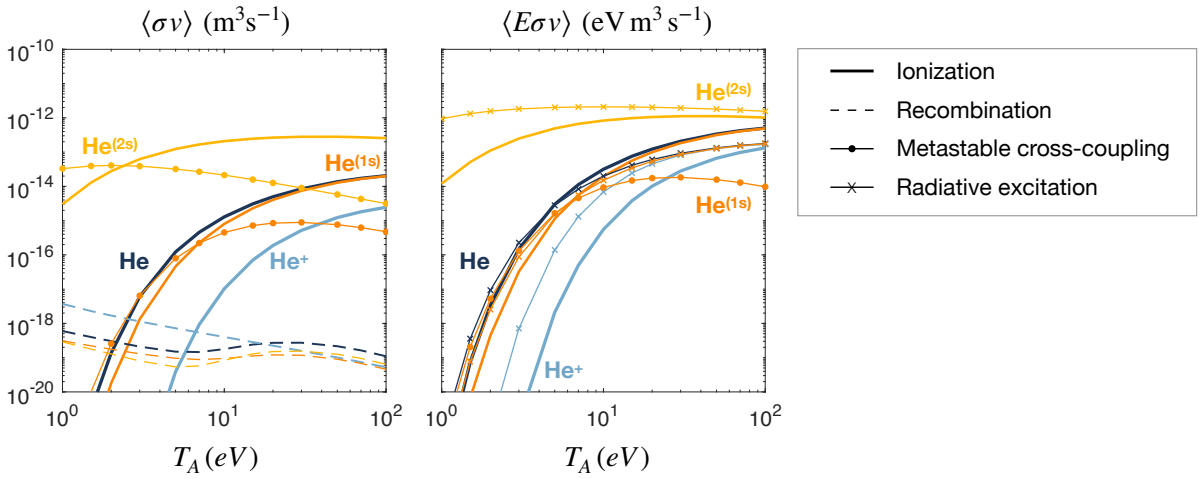

Figure 4.10: Helium reaction rates with metastable state un-resolved (blue) and resolved (orange). Two metastable states are resolved for He atoms, $He^{(1s)}$ and $He^{(2s)}$, spin separation of the (2s) level is neglected. A single metastable state (ground state) is considered for He^+ ions.

investigation of the effect of meta-stable He states through the extension of the 0D model used in the previous sections to the metastable-resolved analysis. The use of a global model is not compatible with the investigation of local meta-stable transport. However, due to the approximately uniform distribution of neutral atoms in GyM, such a model can give us preliminary insight into the effects that these additional atom populations may have on the global plasma properties.

Unresolved reaction rates are estimated by solving the ADAS radiative collisional model assuming that the excited He meta-stable states are in static equilibrium with the ground state. This means that the densities of the metastable populations are relaxed to steady-state ($dn_{n,\text{meta}}/dt \simeq 0$) and the effect of metastable states are incorporated within the expressions of the ground state reaction rates. See [121] for details. In this sense, the *metastable un-resolved rates* used for the analysis in secion 4.4.1 do not entirely neglect the excited metastable state, they just neglect their lifetime. A resolved treatment, on the contrary, explicitly solves a density evolution equation for every metastable state.
Metastable un-resolved and resolved rate coefficients and energy rate coefficients for He are shown in figure 4.10. The un-resolved rate coefficients are plotted in blue while the resolved ones are in orange. We can notice that the He un-resolved curve and the corresponding $He^{(1s)}$ curves slightly differ only for very low temperatures $T_e \simeq 1$ eV.

To explicitly include the density evolution of the metastable He states, we considered ADAS resolved rate coefficients, neglecting however the spin-level separation. A single $He^{(2s)}$ state, accounting for both the singlet $He^{1(2s)}$ and triplet $He^{3(2s)}$ states, is consid-

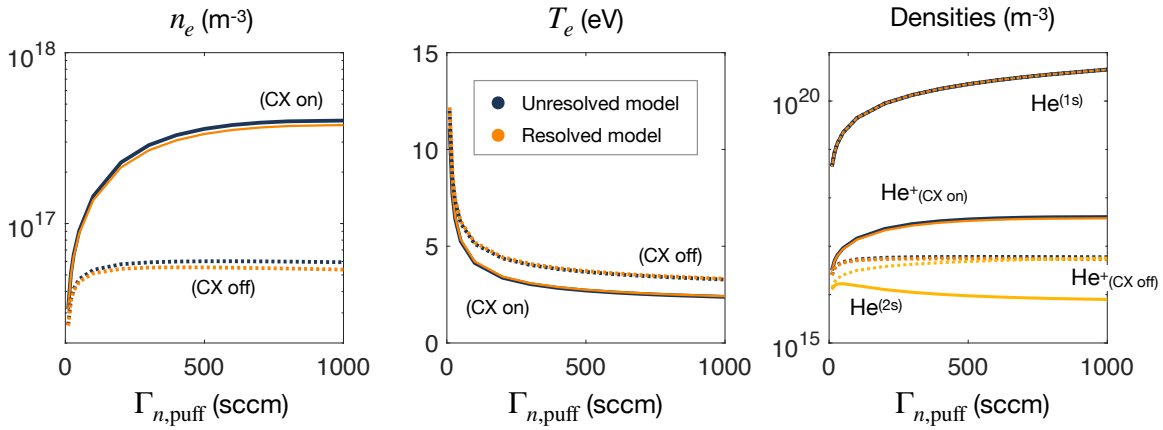

Figure 4.11: Results of the 0D model with metastable unresolved (blue) and metastable resolved (orange, yellow lines on the right density graph represents the metastable He$^{(2s)}$ population). Solid lines are simulations with CX reactions and dotted lines are simulations with CX turned off in EIRENE.

ered. With this hypothesis, to include the He$^{(2s)}$ metastable state, an additional density equation for $n_{n,(2s)}$ should be included in the 0D model. The four equations for the evolution of ion density, n_i, ground state He atoms $n_{n,(1s)}$, metastable He atoms $n_{n,(2s)}$ and electron temperature are reported in appendix B.
Solution of this set of equation with P_{ext} = 400 W, $S = 2 \times 500$ L/s and puffing strength scanning from $\Gamma_{n,\mathrm{puff}} = 10 - 1000$ sccm is shown in figure 4.11. This figure shows the comparison of the un-resolved (blue) and resolved (orange) models, with (α from equation (3.11)) and without charge exchange (α = 0.5). It can be observed that the effect of resolving the evolution of the metastable state is only appreciable ($\approx$ 7% maximum difference in n_e) for very high puffing strengths, that are not experimentally available in GyM. Moreover, the effect of switching between the resolved and the un-resolved models is much smaller than the effect related to the charge-exchange reactions considered in detail in section 4.4.1.

4.5. Global simulations of PWI in LPD

The final analysis presented in this chapter is related to the study of global wall erosion, caused by PWI in the GyM linear device. This study represents the first global simulation of PWI in a linear plasma device, including both the description of plasma and impurity transport and of plasma-facing material evolution. The integrated description of the plasma and the PWI process is obtained by coupling SOLPS-ITER and ERO2.0.

4.5.1. SOLPS-ITER and ERO2.0 coupling in linear geometry

The SOLPS-ITER and ERO2.0 coupling scheme is shown in figure 4.12. The general idea is to use the distribution of the plasma inside the device, retrieved from densities, velocities and energies computed by SOLPS-ITER, and the magnetic equilibrium as input for the erosion calculations.
ERO2.0 takes as input electron and ion quantities that are computed by the plasma solver of SOLPS-ITER, namely B2.5. As discussed in section 1.3.3, when using a 2D plasma background to feed ERO2.0, the first step is to interpolate the bidimensional plasma solutions to the 3D ERO2.0 dominion, exploiting axial symmetry. This is shown in figure 4.12.a. While performing this interpolation one has to consider two aspects: (i) the different spatial resolution and shape of the two meshes; (ii) that the B2.5 mesh does not extend radially up to the wall, hence a proper extrapolation scheme should be used [99]. In the simulations we are considering in this work, a constant extrapolation of the last B2.5 radial value is used for all quantities since the outermost flux surface used to build the SOLPS-ITER mesh is just a few mm away from the lateral wall. This is shown in the circular box in figure 4.12.b.
Finally, the 3D wall geometry of the GyM linear device is produced using standard Computer Aided Design (CAD) software (figure 4.12.c). In this work we consider three main 3D structures: (i) the two flanges at the base of the cylindrical chamber; (ii) the lateral wall, including the holes present in the different sectors for the turbomolecular pumps, magnetron sources and the diagnostics; (iii) 28 bushings, cylindrical structures (1 cm diameter, 2 cm height) protruding inside the plasma from the lateral wall, used for the positioning of a W liner inside the vacuum vessel made of steel. On top of these structures, the polygonal mesh used by ERO2.0 to compute erosion and redeposition is built.

4.5.2. Effect of plasma background and atomic reactions on wall erosion

One of the studies that were performed exploiting the global coupling between SOLPS-ITER plasma background and ERO2.0 is the evaluation of the total wall erosion in GyM. Further analysis on erosion and impurity migration modelling by ERO2.0 in GyM can be found in [122].
The first analysis discussed in this section aims to compute the total wall erosion due to helium plasma-wall interaction considering different wall materials and applying a negative bias to the bases of the cylindrical chamber of GyM to increase the ion im-

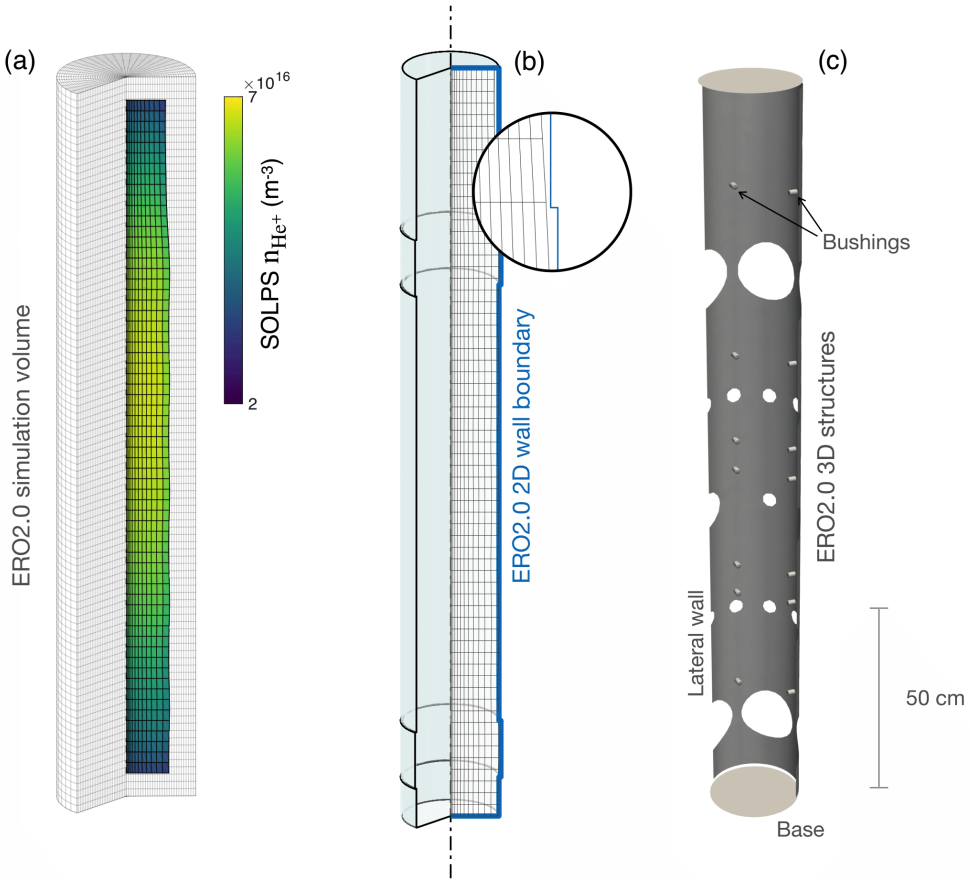

Figure 4.12: SOLPS-ITER and ERO2.0 global coupling scheme: **a)** SOLPS-ITER plasma is projected onto the 3D ERO2.0 grid. **b)** Definition of 3D domain boundary for ERO2.0 simulation, by rotation of a 2D wall contour. **c)** 3D CAD structures used by ERO2.0 to compute erosion and redeposition.

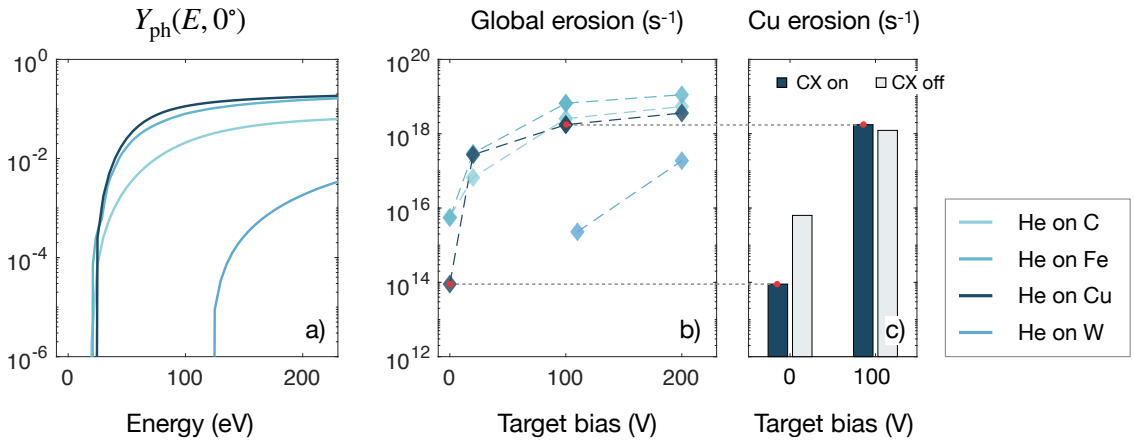

Figure 4.13: **a)** Physical sputtering yields Y_{ph} of the different materials considered in the erosion studies. The yield is plotted as a function of the impact energy for incidence normal to the surface $Y_{ph}(E, 0°)$. **b)** Global erosion of GyM PFCs for different wall materials. A negative bias was imposed on GyM bases (targets) to evaluate the effect of different impact energies. **c)** Global erosion estimated by ERO2.0 with different plasma backgrounds: including and neglecting charge-exchange reactions between He atoms and ions. For $V_{bias} = 0$ the ion impact energy $E = V_{sh}T_e \simeq 24$ eV is close to the sputtering threshold $E_{Cu,th} \simeq 20$ eV.

pact energy to the wall. The choice of materials includes C and W, which are fusion-relevant materials with low and high Z, respectively, and Fe and Cu, two materials with similar physical sputtering thresholds used as a proxy of the AISI 304L stainless steel of the GyM chamber. The physical sputtering yields of these materials are shown in figure 4.13.a as a function of impact energy and for incidence normal to the surface.

Applying the procedure described in section 4.5.1, we set up the input for the erosion simulations implying the plasma background which was previously benchmarked against GyM experimental data, as described in section 4.2.3. With this fixed plasma background, different ERO2.0 simulations were performed, changing the wall materials and the magnitude of the negative bias applied at the bases of the GyM chamber[1]. Results of this analysis are shown in figure 4.13.b.

The total erosion rate curves for the different materials as a function of the applied bias have a trend similar to the sputtering yields as a function of impact energy $Y_{ph}(E, 0°)$. In particular, it is clear that W has the highest sputtering threshold among the materials considered $E_{W,th} \simeq 130$ eV. In simulations with W wall and $V_{bias} < 110$ V, in fact, no erosion was computed. This is consistent with the fact that the energy gained by ions

[1] Established that only negative (ion accelerating) biases are considered, we report the absolute value of V_{bias}.

due to the sheath acceleration is $E_{sh} = V_{sh} T_e \simeq 24$ eV and thus with bias $V_{\text{bias}} \gtrsim 110$ V the sputtering threshold can be overcome.
A second analysis was performed investigating the effect of different plasma backgrounds on the global erosion rates computed by ERO2.0. In particular, following the discussion on plasma-neutral interactions presented in section 4.4.1, we investigated the effect of including or neglecting charge-exchange reactions in plasma modelling. We repeated ERO2.0 simulations with Cu wall and $V_{\text{bias}} = 0$ and $V_{\text{bias}} = 100$ V, using a plasma background which neglected CX reactions. Results are shown in figure 4.13.c. Simulations with $V_{\text{bias}} = 0$ correspond to a situation in which the impact energy of He ions on the material is close to the sputtering threshold. Referring to figure 4.13.a, we observe that the sputtering yield is very steep around E_{th} and, thus, even small variations in the plasma background electron temperature ($T_{e,\text{CXoff}} \simeq T_{e,\text{CXon}} + 0.5$ eV) can represent drastic differences in the outcomes of the erosion computation (up to ≈ 2 orders of magnitude). Erosion simulations are much less sensitive to small variations in the plasma background fare from the sputtering threshold of the material. At $V_{\text{bias}} = 100$ V, the small increase in the background T_e, obtained by switching off the CX, is compensated by the reduction in the ion flux at the wall due to the collisional drag and the global erosion rate is similar in the two cases.

4.6. Conclusions

This chapter presents and summarises the most recent modelling activities of the GyM linear plasma device done in collaboration with ISTP-CNR in the framework of EUROfusion WP-PWIE.

The SOLPS-ITER code was used and optimised to study helium plasmas in a linear geometry. This work improved the code capabilities to deal with non-toroidal geometries and extend the default databases for plasma-neutral interactions of non-hydrogenic plasmas, with a particular focus on helium plasma.
Despite SOLPS-ITER being developed to simulate the edge plasma in tokamaks, in this work we demonstrated that it can be also adapted to investigate the plasma behaviour in LPDs. The results of the code were benchmarked with experimental data of GyM plasma. Good agreement was obtained by tuning the cross-field particle diffusion coefficient D_n and the leakage coefficient of the radial boundary condition.

A novel and simplified plasma model for linear geometries, specifically developed for helium plasma, was presented and benchmarked with SOLPS-ITRE results. The 0D

model is based on the volume average of 2D fluid equations and provides a very simple and effective tool to describe complex systems as plasmas in LPDs. The simplified study sheds light on the importance of various plasma-neutral interaction processes in determining plasma density and temperature and thus the heat and particle fluxes on the materials. In particular, charge exchange reactions enhance the collisional drag of ions, resulting in an increased plasma density and a reduced electron temperature. Electron impact excitation, if included among the possible electron-atom impact processes, tends to reduce the electron density since part of the electron energy goes into the excitation of neutral atoms which does not result in ionization. Moreover, the analysis of a metastable-resolved model, i.e. which explicitly includes both $He^{(1s)}$ and $He^{(2s)}$ atom populations, showed negligible difference with respect to the results obtained with a metastable-unresolved model even for the low T_e conditions of GyM.

Finally, the global coupling of SOLPS-ITER plasma background with ERO2.0 Monte Carlo code was used to study erosion of the PFCs in GyM linear device. The work represents the first example of an investigation of global erosion in a LPD, through the coupling of a fluid plasma background and an erosion-impurity migration model. The analysis shows that small variations in the plasma background parameters can significantly affect the estimation of erosion if the ion impact energy is close to the sputtering threshold of the material.

5 | SOLPS-ITER and GBS transport models in linear geometry

The magnitude of particles, momentum and heat radially transported across the magnetic flux surfaces determines the scrape-off layer width and the particles and heat loads onto the PFCs. The availability of quantitatively predictive models to describe radial cross-field transport at the edge of magnetic confinement devices, however, is still an open issue of boundary plasma modelling. This chapter aims to investigate two of the available physical models to describe this problem, exploiting the simplified geometry offered by linear plasma devices. Consistently with the work presented in the chapter 4 of this thesis, the analysis is performed considering helium plasmas and geometry consistent with the GyM linear machine. The investigation presents a detailed comparison of the equations implemented in the plasma transport solver of SOLPS-ITER and GBS numerical packages for linear geometry and a benchmark of the results obtained with the two codes.

The work presented is the outcome of a four-month visiting period at the École Polytechnique Fédérale de Lausanne (EPFL) where the GBS code is developed.

5.1. Diffusive and turbulent transport models for LPDs

In section 2.1.3, we introduced two approaches that are currently the most adopted for the modelling of turbulent cross-field transport in tokamaks, namely the *mean-field diffusive approximation* and the modelling of *first-principle turbulence*. This section will analyse these two plasma transport models in detail by comparing the equations implemented by SOLPS-ITER and GBS boundary transport codes.

5.1.1. SOLPS-ITER equations in linear geometry

From the outcomes of the discussion presented in section 4.2.3, we can assume that the conditions of a helium plasma in GyM are well described within the single and

cold ion approximation. Although SOLPS-ITER solves multi-ion Braginskii equations, including separate density and momentum equations for He^+ and He^{2+} and a single ion energy equation, in this section we only report the density and momentum equation for He^+ ions and we neglect ion energy equation, assuming $T_i \approx 0$. This is done in order to allow a simpler comparison with the GBS model.

With these hypotheses, the SOLPS-ITER plasma transport model reduces to six equations for the six unknown variables: $n_i = n_e$, $u_{i\parallel}$, $u_{e\parallel}$, $j_\parallel$, ϕ and T_e:

$$\partial_t n_i + \partial_z(n_i u_{i\parallel}) - \partial_r(D_n \partial_r n_i) = S_n \tag{5.1}$$

$$\begin{aligned} m_i \left[\partial_t(n_i u_{i\parallel}) + \partial_z(n_i u_{i\parallel}^2) - \partial_r((D_n \partial_r n_i) u_{i\parallel})\right] &= -e n_i \partial_z \phi \\ &+ \partial_z\left(\frac{4}{3}\eta_{i\parallel}\partial_z u_{i\parallel}\right) + \partial_r(\eta_{i\perp}\partial_r u_{i\parallel}) - \frac{e n_i}{\sigma_\parallel} j_\parallel + 0.71 n_i \partial_z T_e + S_m \end{aligned} \tag{5.2}$$

$$u_{e\parallel} = u_{i\parallel} - \frac{j_\parallel}{e n_e} \tag{5.3}$$

$$j_\parallel = \sigma_\parallel \left[\frac{1}{e n_e}\partial_z(n_e T_e) - \partial_z \phi\right] - \alpha_\parallel \partial_z T_e \tag{5.4}$$

$$\partial_z\left(\sigma_\parallel \partial_z \phi\right) = \partial_z\left[\frac{\sigma_\parallel}{e n_e}\partial_z(n_e T_e) + \alpha_\parallel \partial_z T_e\right] \tag{5.5}$$

$$\begin{aligned} \frac{3}{2}\partial_t(n_e T_e) + \partial_z\left[\frac{3}{2} n_e T_e u_{e\parallel} - 0.71 T_e j_\parallel / e - \kappa_\parallel \partial_z T_e\right] - \partial_r\left[\frac{5}{2}(D_n \partial_r n_i) T_e + \kappa_\perp \partial_r T_e\right] \\ + n_e T_e \partial_z u_{e\parallel} = u_{e\parallel}\left[-\frac{e n_i}{\sigma_\parallel} j_\parallel + 0.71 n_i \partial_z T_e\right] + S_{T,e} \end{aligned} \tag{5.6}$$

The parallel transport coefficients are computed according to Braginskii's formulation, discussed in section 2.1.1, while the cross-field ones are anomalous. In particular, the parallel thermo-electric coefficient is $\alpha_\parallel = 0.71\sigma_\parallel/e$. S_n, S_m and S_T include both the plasma-neutral interaction sources and the external sources if present.

5.1.2. GBS equations in linear geometry

The GBS plasma transport model is based on the drift-reduced approximation of two-fluids Braginskii equations. The linear geometry equations are derived from the original GBS model [108] by applying the differential operators (3.2), as discussed in section 3.2.3.
The cold ion approximation is used $T_i \simeq 0$, together with the Boussinesq approximation of Poisson equation $\nabla \cdot (n_e \nabla_\perp \phi) \simeq n_e \nabla_\perp^2 \phi$. We also neglect electromagnetic effects by neglecting the magnetic flux function $\Psi = 0$.

With these hypotheses, the GBS plasma transport model is based on seven equations for the seven unknown $n_i = n_e$, $u_{i\parallel}$, $u_{e\parallel}$, $j_\parallel$, ϕ, T_e and the plasma vorticity ω:

$$\partial_t n_e = -\frac{1}{B}(\partial_x \phi \partial_y n_e - \partial_x n_e \partial_y \phi) - \partial_z (n_e u_{e\parallel}) + S_n \tag{5.7}$$

$$\begin{aligned} n_i m_i \partial_t u_{i\parallel} = &- \frac{n_i m_i}{B}(\partial_x \phi \partial_y u_{i\parallel} - \partial_x u_{i\parallel} \partial_y \phi) - n_i m_i u_{i\parallel} \partial_z u_{i\parallel} \\ &- \partial_z (n_e T_e) + \frac{4}{3}\eta_{i\parallel} \partial_z{}^2 u_{i\parallel} + S_m - S_n m_i u_{i\parallel} \end{aligned} \tag{5.8}$$

$$\begin{aligned} n_e m_e \partial_t u_{e\parallel} = &- \frac{n_e m_e}{B}(\partial_x \phi \partial_y u_{e\parallel} - \partial_x u_{e\parallel} \partial_y \phi) - n_e m_e u_{e\parallel} \partial_z u_{e\parallel} - \partial_z (n_e T_e) \\ &+ e n_e \partial_z \phi - 0.71 n_e \partial_z T_e + \frac{e n_e}{\sigma_\parallel} j_\parallel + \frac{4}{3}\eta_{e\parallel} \partial_z{}^2 u_{e\parallel} - S_n m_e u_{e\parallel} \end{aligned} \tag{5.9}$$

$$j_\parallel = e n_i u_{i\parallel} - e n_e u_{e\parallel} \tag{5.10}$$

$$\partial_t \omega = -(\partial_x \phi \partial_y \omega - \partial_x \omega \partial_y \phi) - u_{i\parallel} \partial_z \omega + \frac{B \omega_{ci}}{e n} \partial_z j_\parallel \tag{5.11}$$

$$\partial_x^2 \phi + \partial_y^2 \phi = \omega \tag{5.12}$$

$$\begin{aligned} \frac{3}{2} n_e \partial_t T_e = &- \frac{3}{2}\frac{n_e}{B}(\partial_x \phi \partial_y T_e - \partial_x T_e \partial_y \phi) - \frac{3}{2} n_e u_{e\parallel} \partial_z T_e \\ &+ 0.71 T_e \partial_z j_\parallel / e + \partial_z \left(\kappa_{\parallel e} \partial_z T_e\right) - n_e T_e \partial_z u_{e\parallel} + S_T - S_n \left(\frac{3}{2} T_e - \frac{1}{2} m_e u_e^2\right) \end{aligned} \tag{5.13}$$

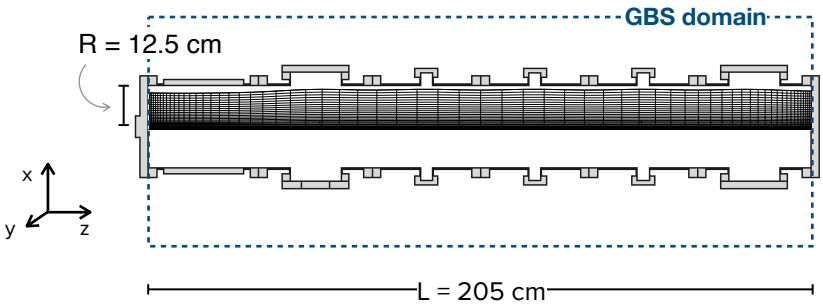

Figure 5.1: Geometry used to perform the benchmark simulations between SOLPS-ITER and GBS plasma transport model.

where the parallel transport coefficients are based on the Braginskii model described in section 2.1.1. In addition to the source terms S_m and S_T in the momentum and energy equations, there are also terms including the particle source S_n. This is the consequence of writing GBS equations in the advective form, rather than the conservative form used by SOLPS-ITER. See the discussion in appendix A.

5.1.3. Analysis of the equations and discussion of the main differences between the two models

The derivation of both SOLPS-ITER and GBS physical models starts from the original Braginkii equations (2.1), (2.2) and (2.3), presented in section 2.1.1. The final equations, however, present some differences which will be highlighted in this section.

We start recalling some general aspects of the two codes already mentioned in section 3.2.3. First, SOLPS-ITER implements a 2D model, while GBS is a full 3D model. The SOLPS equations are solved on the (z, r) plane exploiting axial symmetry, while GBS equations use a tridimensional (x, y, z) coordinate system. To write the equations presented in sections 5.1.1 and 5.1.2 we used the reference frame indicated in figure 5.1, where the z direction is parallel to the magnetic field, i.e. along the axial direction of the cylinder, $r = \sqrt{x^2 + y^2}$ is the radial direction and the plane (x, y) is orthogonal to the magnetic field. Further information on specific geometry setup for this study is given in section 5.2.
The mean-field and turbulent natures of the two codes usually require very different time and spatial scales for the solutions of equations (5.1) - (5.6) and (5.7) - (5.13), respectively. In particular, the turbulent spatial scales should be of the order of the ion gyro-radius. In GyM, however, $r_i \approx$ cm due to the low magnetic field and the two codes

used similar spatial resolutions, as discussed more in detail in section 5.2.

Comparing equations (5.1) - (5.6) to equations (5.7) - (5.13), it is clear that GBS physical model has one unknown more than the SOLPS model. The plasma vorticity ω is related to the curl of the $E \times B$-drift velocity. An expression of the vorticity is obtained by subtracting ion and electron density equations. The difference is related to the divergence of the polarisation velocity $\vec{u}_{\text{pol}}$ [110]:

$$\nabla \cdot \left(n\vec{u}_{\text{pol}}\right) \propto \nabla_{\perp} \cdot \frac{d}{dt}\vec{E}_{\perp} \propto \vec{b} \cdot \nabla \times \vec{u}_{E} \propto \omega \tag{5.14}$$

In both models, we assumed $n_i = n_e$, thus a single density equation is required. However, the density conservation equation is written for ions in SOLPS - equation (5.1) - and for electrons in GBS - equation (5.7). The cross-field contributions to the divergence of the particle flux are written, respectively:

$$\begin{aligned} \nabla \cdot (n_i \vec{u}_{i\perp})\big|_{\text{SOLPS}} &= -\partial_r(D_n \partial_r n_i) \\ \nabla \cdot (n_e \vec{u}_{e\perp})\big|_{\text{GBS}} &= \frac{1}{B}(\partial_x \phi \partial_y n_e - \partial_x n_e \partial_y \phi) \end{aligned} \tag{5.15}$$

where we introduced the anomalous-diffusive approximation $\vec{u}_{i,\perp}\big|_{\text{SOLPS}} = -D_n \partial_r n_i / n_i$, while for GBS the cross-field velocity is $\vec{u}_{e\perp}\big|_{\text{GBS}} = \vec{u}_{\text{E}\times\text{B}} = -(\nabla_{\perp}\phi \times \vec{b})/B$. Neglecting radial currents, however, we can write $\vec{u}_{e\perp}\big|_{\text{GBS}} = \vec{u}_{i\perp}\big|_{\text{GBS}}$ and thus directly compare SOLPS and GBS $\vec{u}_{i\perp}$ terms.
Substituting the parallel current equation (5.4) into the SOLPS ion momentum equation (5.2) and neglecting ion perpendicular viscosity $\eta_{i,\perp} \simeq 0$, one gets:

$$m_i \left[\partial_t(n_i u_{i\parallel}) + \partial_z(n_i u_{i\parallel}^2) - \partial_r((D_n \partial_r n_i) u_{i\parallel})\right] = -\partial_z(n_e T_e) + \partial_z\left(\frac{4}{3}\eta_{i\parallel}\partial_z u_{i\parallel}\right) + S_m \tag{5.16}$$

This equation is the conservative form of equation (5.8), assuming again the radial cross-field particle flux to be $(\Gamma_{n,\perp})_{\text{SOLPS}} = -D_n \partial_r n_i$ and $(\Gamma_{n,\perp})_{\text{GBS}} = n_i \vec{u}_{E\times B}$, respectively. The cross-field component of the non-linear term in the momentum equation is thus:

$$\begin{aligned} \nabla \cdot (n_i \vec{u}_{n,\perp} u_{i\parallel})\big|_{\text{SOLPS}} &= -\partial_r(D_n \partial_r n_i u_{i\parallel}) \\ n_i \vec{u}_{n,\perp} \cdot \nabla u_{i\parallel}\big|_{\text{GBS}} &= \frac{n_i m_i}{B}(\partial_x \phi \partial_y u_{i\parallel} - \partial_x u_{i\parallel} \partial_y \phi) \end{aligned} \tag{5.17}$$

SOLPS model keeps the dependence of $\eta_{i\parallel}(r, z)$, while in GBS constant $\eta_{i\parallel}$ is assumed. In GBS, the electron velocity is obtained by solving the drift-reduced electron momentum equation (5.9). The plasma current density is then obtained by applying the stan-

dard definition (5.10). The generalised Ohm's Law for the parallel current density is instead implemented in SOLPS through equation 5.4, obtained by neglecting the electron inertia and viscosity in the electron momentum equation. Electron velocity is thus obtained from equation (5.3) corresponding to equation (5.10), i.e. the standard definition of plasma current density. If we write equation (5.9) in conservative form neglecting electron inertia and viscosity, we obtain an expression analogous to equation (5.4).
In SOLPS-ITER the potential equation (5.5) is obtained by substituting the expression of the parallel current density (5.4) into the current continuity equation $\nabla \cdot \vec{j} = 0$. While in GBS, current continuity is used to obtain the vorticity equation (5.11), by setting to zero the difference between the electron and ion density equations, one gets:

$$\nabla \cdot \left(n\vec{u}_{\text{pol}}\right) = -\nabla_{\parallel}\frac{j_{\parallel}}{e} \qquad \xrightarrow{\nabla^2_{\perp}\phi=\omega} \qquad \frac{en_i}{B\omega_{ci}}\frac{d}{dt}\omega = -\nabla_{\parallel}j_{\parallel} \tag{5.18}$$

where Poisson equation (5.12) is also used. It is noticeable that the potential equation in SOLPS - equation (5.5) - results purely parallel, while in GBS - equation (5.12) - purely orthogonal to $\vec{B}$.
The electron energy equations (5.6) and (5.13) model heat transport in the parallel direction with analogous expressions, except that they use the conservative and advective forms of the equations, respectively.

$$\begin{aligned}\nabla \cdot (\frac{3}{2}n_e T_e u_{e\parallel} + \vec{q}_{e\parallel}) + n_e T_e \nabla \cdot u_{e\parallel}\Big|_{\text{SOLPS}} = \\ \partial_z\left(\frac{3}{2}n_e T_e u_{e\parallel} - 0.71\, T_e j_{\parallel}/e - \kappa_{\parallel}\partial_z T_e\right) + n_e T_e \partial_z u_{e\parallel}\end{aligned} \tag{5.19}$$

$$\begin{aligned}\frac{3}{2}n_e u_{e\parallel}\cdot\nabla T_e \;+\; \nabla\cdot\vec{q}_{e\parallel} + n_e T_e\nabla\cdot u_{e\parallel}\Big|_{\text{GBS}} = \\ \frac{3}{2}n_e u_{e\parallel}\partial_z T_e - 0.71\, T_e\partial_z j_{\parallel}/e - \kappa_{\parallel e}\partial_z\left(\partial_z T_e\right) + n_e T_e\partial_z u_{e\parallel}\end{aligned}$$

Again, GBS approximates the transport coefficients to their constant values: $\partial_z(0.71\, T_e j_{\parallel}/e) \simeq 0.71\, T_e\partial_z j_{\parallel}/e$ and $\kappa_{e\parallel} \simeq$ constant. Cross-field electron heat transport is given by:

$$\nabla \cdot (\frac{3}{2}n_e T_e \vec{u}_{e\perp} + \vec{q}_{e\perp}) + n_e T_e \nabla \cdot \vec{u}_{e\perp}\Big|_{\text{SOLPS}} = -\partial_r\left(\frac{5}{2}T_e(D_n\partial_r n_i) + \kappa_{e\perp}\partial_r T_e\right) \tag{5.20}$$

$$\frac{3}{2}n_e\vec{u}_{e\perp}\cdot\nabla T_e \;+\; \nabla\cdot\vec{q}_{e\perp} + n_e T_e\nabla\cdot\vec{u}_{e\perp}\Big|_{\text{GBS}} = \frac{3}{2}\frac{n_e}{B}(\partial_x\phi\partial_y T_e - \partial_x T_e\partial_y\phi)$$

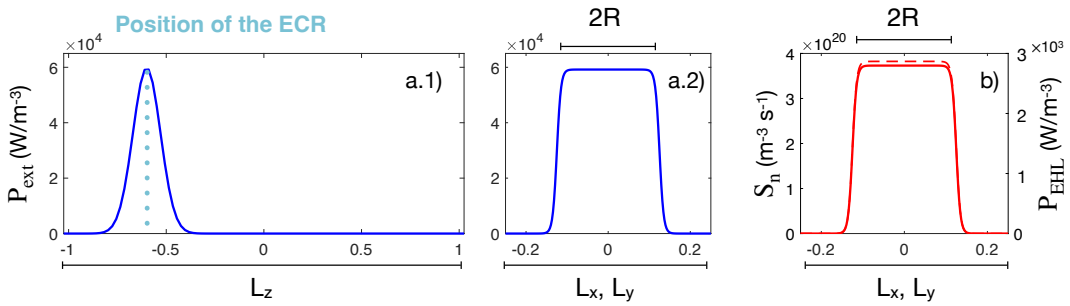

Figure 5.2: Setup of the benchmark simulation between SOLPS-ITER and GBS. **a)** GBS external electron energy source and **b)** plasma-neutral interaction sources of particles and energy estimated using the 0D global model developed in the context of this thesis.

SOLPS-ITER introduces the anomalous thermal conductivity $\kappa_{e\perp}$ to model cross-field thermal conduction and makes other two approximations: (i) $\vec{u}_{e\perp} \cdot \nabla(n_e T_e) \approx 0$, and thus $n_e T_e \nabla \cdot \vec{u}_{e\perp} \approx \nabla \cdot (n_e T_e \vec{u}_{e\perp})$, and (ii) $\vec{u}_{e\perp} \approx \vec{u}_{i\perp} = -D_n \partial_r n_i / n_i$.
As for the other equations, in the GBS model, cross-field advection is driven by $E \times B$ advection $n_e \vec{u}_{E\times B} \cdot \nabla T_e$. This, however, is specific to linear geometry since all the other terms involve the curvature operator $C(f) = B/2(\nabla \times \vec{b}/B) \cdot \nabla f \approx 0$.

5.2. Simulation setup: geometries and sources

The setup of SOLPS-ITER and GBS simulations had the aim of producing results that could be qualitative and quantitative benchmarked. Although the GyM linear device is again the reference machine for this study, a direct comparison with GyM experimental data is not intended here. For these reasons, to perform SOLPS-ITER simulation we did not use the optimised setup described in section 4.2. Instead, we choose the simpler set of inputs, e.g. constant profiles for the transport coefficients and a reduced set of plasma-neutral interactions. In particular, this simulation used $D_n = 0.5\,\mathrm{m}^2/\mathrm{s}$ and $\chi_{e,\perp} = 1\,\mathrm{m}^2/\mathrm{s}$; pumping speed of $S = 500\,\mathrm{L/s}$ corresponding to $p_a = 0.013$ on EIRENE pumping surfaces; puffing strength $\Gamma_{n,\mathrm{puff}} = 1.88 \times 10^{19}\,\mathrm{atoms/s}$; external power $P_{\mathrm{ext}} = 520\,\mathrm{W}$; radial decay length boundary condition $\lambda_{\mathrm{decay}} = 5\,\mathrm{cm}$. To simplify the implementation in GBS, we also neglected the ion momentum sink due to $\mathrm{He} - \mathrm{He}^+$ charge-exchange reactions, i.e. $S_m \approx 0$ in equations (5.2) and (5.8).

The (x,z) plain of the computational domains is shown in figure 5.1. As discussed in section 3.2.3, the GBS domain is a 3D parallelepiped, thus with a squared cross-section in the (x,y) plane. To avoid distortion of the plasma solution near the edges of the domain, we decided to extend the GBS domain radially such that $L_x, L_y \gtrsim 2r_0$,

where L_x, L_y are GBS mesh dimensions and $r_0 = 0.125$ m is GyM plasma radius.
The external electron power source, reproducing GyM ECRH source, was modelled as done in SOLPS, with a constant radial profile extending from $-r_0$ to r_0 and Gaussian axial profile peaked at the position of the ECR. The axial and radial profiles of the external power source are shown in figure 5.2.a.1 and 5.2.a.2, respectively.
Since the focus of the present analysis is the benchmark of the diffusive and turbulent plasma transport models, GBS neutral transport model was not used in this study. Plasma-neutral interaction sources were implemented as external contributions and estimated using the 0D global model, previously benchmarked against SOLPS-ITER. See section 4.3. A constant radial profile from $-r_0$ to r_0 was used also for the plasma-neutral interaction sources and the flat-top values for the ionization particle source S_n and the electron heat loss (EHL) sink P_{EHL} are computed as:

$$S_n = R_{\text{iz}}(T_e, n_e) n_e n_n \qquad P_{\text{EHL}} = (E_{\text{iz}} R_{\text{iz}}(T_e, n_e) + E_{\text{n,rad}} R_{\text{n,rad}}(T_e, n_e)) n_e n_n \tag{5.21}$$

where $n_i = n_e$, n_n and T_e are computed solving equations (3.4), (3.5) and (3.6). Differently from P_{ext}, the plasma-neutral interaction sources are axially constant. Their profile is shown in figure 5.2.c.

The numerical solution of equations (5.1) - (5.6) and equations (5.7) - (5.13) used a similar space discretisation but requires very different time discretisation. SOLPS-ITER mesh has dimensions $n_z \times n_r = 94 \times 28$, corresponding to average space discretisations $\Delta z\big|_{\text{SOLPS}} = 2$ cm and $\Delta r\big|_{\text{SOLPS}} = 0.4$ cm. In GBS, we used instead a rectangular grid $n_x \times n_y \times n_z = 200 \times 200 \times 100$, corresponding to $\Delta x\big|_{\text{GBS}} = \Delta y\big|_{\text{GBS}} = 0.25$ cm and $\Delta z\big|_{\text{GBS}} = 2$ cm[1]. The time steps used to evolve in time the two models differed by several orders of magnitude. SOLPS-ITER equations were solved using $\Delta t\big|_{\text{SOLPS}} = 1 \times 10^{-5}$ s. GBS simulations started with a $\Delta t\big|_{\text{GBS}} = 2 \times 10^{-11}$ s, successively relaxed to $\Delta t\big|_{\text{GBS}} = 2 \times 10^{-10}$ s, but still $\Delta t\big|_{\text{GBS}} \ll \Delta t\big|_{\text{SOLPS}}$.

5.3. Comparison of SOLPS and GBS results

SOLPS-ITER and GBS simulations were performed using the setup described in section 5.2. This section analyses and compares the results.
To adequately compare the results of the two codes, it is first convenient to make a

[1] We recall that SOLPS-ITER mesh extends from the cylinder axis to the lateral wall (total width $\simeq r_0$), while GBS mesh extends all across the plasma diameter plus the additional space added to avoid edges problems (total width $\simeq 4r_0$). See the meshes in figure 5.2.a.

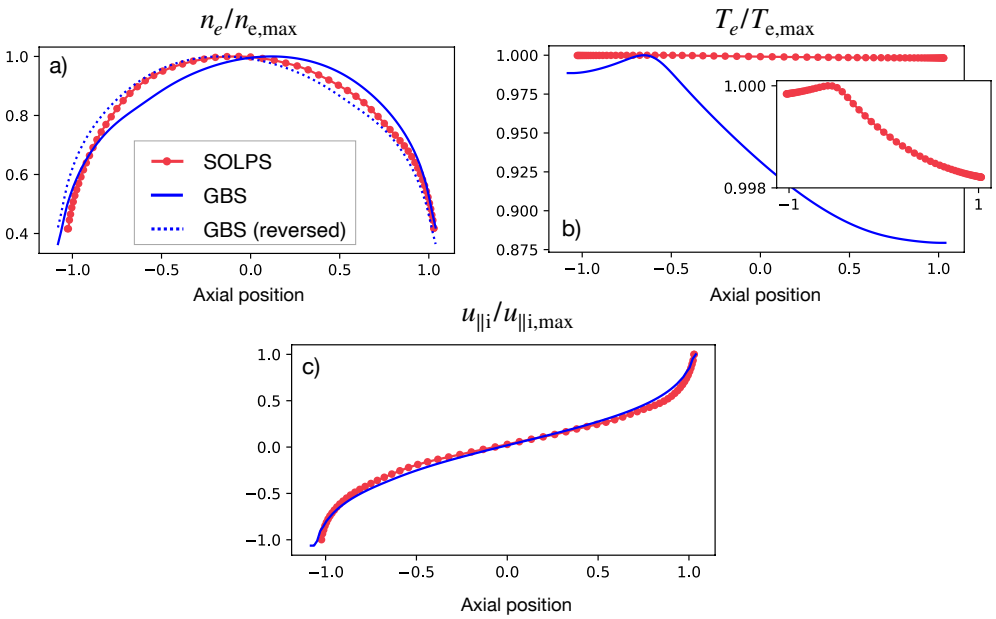

Figure 5.3: Benchmark of SOLPS-ITER and GBS (time-averaged) axial profiles of **a)** n_e, **b)** T_e and **c)** u_i. The profiles are normalised to the respective maximum value, to better appreciate the qualitative behaviour.

time average of GBS results.
To compare the SOLPS and GBS results, thus, we perpetuated the GBS simulation until the volume average of the seven unknowns reaches a steady state value. This guarantee that the level of convergence of the two simulations is comparable. The quantities to be compared with SOLPS variables were then computed by taking the average over the last 10 time steps.

5.3.1. Axial plasma profiles

This section analyses the axial and radial profiles of electron density and temperature and ion parallel velocity computed by SOLPS-ITER and GBS simulations.
Before comparing the qualitative behaviour, we shell notice that quantitative differences in the results are found. GBS results, on average, underestimate n_e and overestimate T_e by $\approx$ a factor of 2. The difference in u_i is smaller, due to Bohm boundary condition $u_i \sim \sqrt{T_e}$.
To compare the qualitative features of the profiles, we thus normalised SOLPS and GBS results to their maximum values. The normalised axial profiles at $r = 0$ extracted from SOLPS (red) and GBS (blue) simulations of n_e, T_e and u_i are shown in figure 5.3. Qualitatively, the two codes produce results that are in good agreement. This is an

important confirmation of the correct implementation of the new sheath boundary condition model in the z-direction, developed to simulate the linear geometry with GBS.

Figure 5.3.a shows that both models predict $n_{se} \approx 0.5 n_{up}$, where n_{se} is the density at the z-boundaries and n_{up} is the density at $z = 0$. This is in agreement with having neglected ion momentum loss due to charge exchange. It is also interesting to analyse the effect on n_e of the non-symmetric (concerning the z-direction) P_{ext} profile (figure 5.2.a). The density profile is not perfectly symmetric for $z = 0$: this feature is reproduced by both codes but, while SOLPS predicts a slightly higher density near the P_{ext} peak ($z < 0$), GBS does the opposite. This can be appreciated by comparing SOLPS results (red curve) with the GBS results plotted with a reversed x-axis (blue dotted curve), in figure 5.3.a. A possible explanation can be related to the fact that in GBS the external source in the temperature equation is implemented as $\partial_t T_e \propto P_{\text{ext}}/n_0$, where $n_0 = n_i$ is the ion density computed by the 0D model.
Temperature profiles are shown in figure 5.3.b. SOLPS predicts an almost perfectly flat profile for $T_e(z)$, while $\partial_z T_e$ estimated by GBS is non-negligible. If we zoom the T_e axis very close to ≈ 1, as shown in the box in figure 5.3.b, however, we observe that the non-symmetric profile of T_e is well captured by both codes. The T_e is located in correspondence of the P_{ext} peak $z \approx -0.6$ m. The difference, in this case, can be related to the fact that GBS uses a constant value for $\kappa_{e\|}$.
To conclude the discussion on axial profiles, figure 5.3.c shows an almost perfect qualitative match of the ion velocity profiles computed by the two codes.

5.3.2. Turbulent driven transport in linear devices

Lastly, we investigate the origin of turbulent transport in a linear device, further analysing the results of the GBS simulation and the differences between the SOLPS and GBS cross-field transport models.

Figure 5.4 shows successive snap-shots of the instantaneous electron density computed by GBS on the cross-field (x,y) plane. The time evolution of $n_e(x, y)$ clearly indicates that the plasma column is subject to a rotation in the counter-clockwise direction. From the quantitative point of view, however, the main question that a cross-field transport model wants to answer is not whether the plasma rotates in the azimuthal θ direction, but rather if this rotation is associated with the presence of radially outward fluxes directed towards the walls.
According to the cross-field model implemented in GBS - see equation (5.15) - the pres-

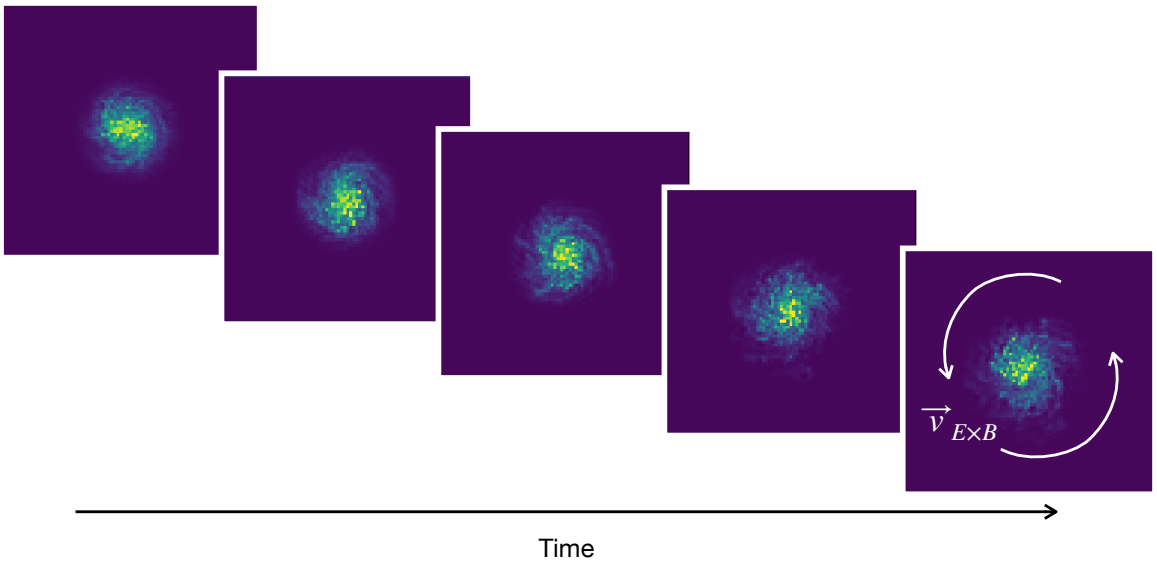

Figure 5.4: 2D map of the instantaneous GBS electron density on the (x,y) plane.

ence of non-parallel to $\vec{B}$ fluxes is associated with $E \times B$ advection. Considering e.g. particle conservation, cross-field particle fluxes are given by $\nabla \cdot (n_e \vec{u}_{E\times B}) \neq 0$. From the definition of $\vec{u}_{\mathrm{E\times B}} = -(\nabla_\perp \phi \times \vec{b})/(n_e eB)$ and assuming $\vec{B} = B\vec{z}$, one finds that a necessary condition to have a radial flux associated with $\nabla \cdot (n_e \vec{u}_{E\times B})$ is that $\partial_\theta \phi \neq 0$. To better see this, we write GBS cross-field flux contribution in cylindrical coordinates instead of the Cartesian one used in equation (5.15). We find:

$$\nabla \cdot (n_e \vec{u}_{E\times B})\big|_{\mathrm{GBS,cyl}} = \frac{\vec{b}}{B} \cdot \{\phi, n_e\}_{\mathrm{cyl}} = \frac{r}{B}(\partial_r \phi \partial_\theta n_e - \partial_r n_e \partial_\theta \phi) \tag{5.22}$$

In general, thus we can conclude that whenever cross-field fluxes are described according to equation (5.22), the existence of azimuthal fluctuations is a necessary condition to allow the existence of non-parallel to $\vec{B}$ contributions. Equation (5.22) considers particle flux, but the same conclusion can be drawn for all the quantities for which cross-field transport is described by the Poisson brackets $\vec{b} \cdot \{\phi, \cdot\} = 1/B(\partial_x \phi \partial_y(\cdot) - \partial_y(\cdot)\partial_x \phi)$.

The above discussion highlights also why the physical model implemented in SOLPS-ITER does not include self-consistently radial cross-field transport and needs to artificially introduce the hypothesis of anomalous diffusivity. As discussed in section 3.2.3, the SOLPS model is bi-dimensional and assumes axial symmetry, i.e. by definition, it neglects contributions related to the azimuthal variations of the plasma quantities. According to equation (5.22), thus, no cross-field flux can be self-consistently described. Note, however, that axial symmetry does not prevent the plasma column to rotate in

the θ-direction, as long as this rotation does not produce the variation of the plasma profiles in θ.

The results presented in this section concern specifically linear geometry, however, extending the discussion to toroidal geometries is clearly of interest. Indeed, also for tokamaks, 2D mean-field codes assume symmetry with respect to the toroidal direction, i.e. $\partial_\phi(\cdot) = 0$. Investigating the effect of relaxing the toroidal approximation moving to full 3D description may lead to the appearance of additional cross-field contributions even in the mean-field non-turbulent regime. A 3D but still mean-field description, in turn, would allow reducing the computational cost connected to the resolution of the turbulent temporal time scales $\Delta t\big|_{\text{turb}} \ll \Delta t\big|_{\text{mean-field}}$.

5.4. Conclusions

This chapter presented a detailed analysis and comparison of the plasma transport models implemented in SOLPS-ITER and GBS boundary plasma codes in a linear geometry and discussed the results obtained by performing a benchmark simulation of helium plasma in the geometry of the GyM linear machine.
Assuming a single ion species and quansineutrality, the SOLPS-ITER model solves 6 equations for the unknown n_i, $u_{i\parallel}$, $u_{e\parallel}$, $j_\parallel$, ϕ and T_e. Besides the 6 equations implemented in SOLPS, the GBS model also includes one equation for the plasma vorticity $\omega \propto \nabla \times (\vec{u}_{E\times B})$.
The numerical methods to implement the solution of the equations are respectively finite volume and finite difference methods. In terms of space and time discretisation, a difference of several orders of magnitude exists between SOLPS and GBS time discretisation $\Delta t\big|_{\text{GBS}} \simeq 1 \times 10^{-10}\,\text{s} \ll \Delta t\big|_{\text{SOLPS}} \simeq 1 \times 10^{5}\,\text{s}$.
As concerns about the classical transport coefficients, both models implement classical Braginkii expressions. SOLPS can also implement more complex Balescu or Zdhanov expressions for non-hydrogenic multi-species plasmas. GBS additionally simplify Braginkii expressions by using constant averaged values allowing for simplification in the spatial integration of fluxes.
By performing a benchmark simulation of the GyM linear device with the two codes, we conclude that qualitatively similar results can be obtained. However, quantitative discrepancies of $\approx$ a factor 2 are observed and should be better investigated.

A one-to-one comparison of each equation also allows identifying the different treat-

ments the two codes imply to model cross-field transport. On the one hand, in absence of drifts, the SOLPS-ITER model does not include any cross-field fluxes, except for the anomalous-diffusive ones. In GBS, on the other hand, cross-field fluxes are driven by advection due to ($E \times B$)-velocity. A key finding of this work is that even though the ($E \times B$)-drift was activated in the SOLPS model, no radial cross-field flux would result. The absence of the radial fluxes in the SOLPS transport model is a consequence of the axial symmetry approximation, i.e. the hypothesis on null gradients of the plasma quantities in the azimuthal direction.

PART III:

Modelling edge plasma in tokamaks

6 | Investigation of helium plasmas in ASDEX-Upgrade with SOLPS-ITER

The operation of a tokamak in helium plasma has a role of primary importance in the ITER Research Plan. ITER plans to use He, alternatively to H and D, during Pre-Fusion Operation Phases and He ash will be present in the plasma mixture during the D-T active phase, as discussed in section 1.2.2.
For these reasons, the investigation of the properties of helium plasma discharges in present-day tokamaks is one of the priorities of the EUROfusion Program in preparation and support of ITER operation. The Work Package Tokamak Exploitation (WP-TE), in particular, has several Research Topics dedicated to helium plasmas, e.g. aimed at investigating the L-H transition threshold, PWI and plasma detachment in He. Moreover, PWI of helium plasma in W-wall tokamaks is further investigated within the WP Plasma-Wall Interaction and Exhaust.

The results presented in this chapter were developed to support and interpret PWI experiments in He in the context of EUROfusion WP-TE and WP-PWIE.

6.1. ASDEX-Upgrade and PWI experiments in helium plasmas

One of the materials considered for the PFCs in a fusion reactor is tungsten (W). ITER divertor will be made of W due to its very good power handling properties: W has a high melting temperature, high sputtering threshold and low probability to retain hydrogenic species. A relevant concern when dealing with helium plasma in a W environment, however, is the formation and evolution of nanostructures on the tungsten surface denominated *tungsten fuzz (W fuzz)*. Studies on PMI in linear plasma devices showed that W microstructure undergoes structural modifications under energetic He ion or atom bombardment. Experiments performed in the NAGDIS-I linear device [123] allow identifying surface and plasma conditions under which the W fuzz is formed. These conditions are related to the impact energy of He ions ($E_i \gtrsim 20$ eV), the surface temperature of the material ($T_{surf} \gtrsim 1000$ K) and the plasma fluence ($\Phi \gtrsim 1 \times 10^{24}\,m^{-2}$).
Some critical questions to which present-day He plasma experiments in W-wall toka-

maks want to answer are whether W fuzz can be observed in present-day tokamaks, whether it is expected under ITER operational conditions and if and how its presence compromises the plasma operation.

ASEDX-Upgrade is a full W-wall tokamak well-suited to perform PWI experiments. It is equipped with a divertor manipulator (DIM-II) [19] which allows retracting 2 of the 128 divertor tiles without breaking the vacuum inside the vessel. These tiles can accommodate samples of materials to test their erosion properties and "markers", samples with a different composition used to assess properties related to impurities migration and redeposition. Before being exposed to the plasma in the divertor region, the surface properties of the samples can be modified, e.g. by pre-exposing them to plasmas in LPDs to obtain W fuzz. Samples are placed at the position of the plasma outer strike point for the entire duration of the experiments and they can be easily extracted for analysis with post-mortem techniques. Several PWI experiments were performed exploiting the DIM-II manipulator in hydrogenic plasmas and a few experimental campaigns were performed with He plasma. In particular, during 2019 He campaign, the formation and destruction of W fuzz were investigated in L-mode and H-mode discharges in AUG. During this campaign, two slightly different lower-single null magnetic equilibria were used in L and H-mode experiments. This allowed for a poloidal shift of the OSP of $\approx$ 6 cm to locate the peak plasma loads onto different samples, as shown in figure 6.1. In H-mode discharges (red line), the OSP coincides with sample J1 with W fuzz on the plasma-facing surface, pre-formed in the PSI2 linear plasma device. In these experiments, the aim was the investigation of W fuzz erosion during H-mode operation. L-mode OSP is instead located onto sample J2 with a rough plasma-facing surface, to investigate the possibility of fuzz growth.

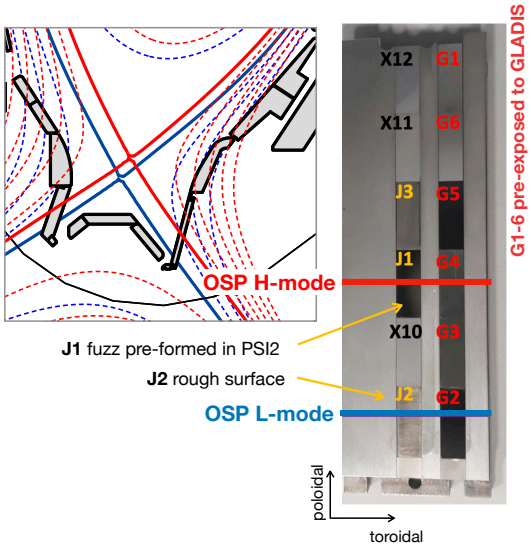

Figure 6.1: Setup of the He PMI experiments in ASDEX-Upgrade.

These experiments made available an extensive database of samples, exposed to different plasma conditions and subsequently analysed with post-mortem techniques to assess the plasma-induced modification to the materials. Comparison of the data retrieved by the analysis of these experiments to the results of simulations can be an

excellent means to benchmark and validate the available models for PMI. The general strategy of PMI simulations is similar to the one used to study the erosion of the GyM wall, as described in section 4.5. A plasma background produced by a boundary plasma transport code (e.g. SOLPS-ITER) is used by erosion/impurity transport codes (e.g. ERO2.0) to assess gross and net erosion of the tokamak wall, migration of wall materials across the tokamak volume and the formation of co-deposited layers onto the PFCs.
The following sections of this chapter focus on the production and optimisation of the plasma background to reproduce the properties of helium discharges in AUG.

6.2. Modelling AUG L-mode helium discharge with SOLPS-ITER

In this work, SOLPS-ITER is used to model steady-state plasma conditions. When performing simulations aimed at benchmarking a tokamak experimental discharge, one has to first identify a time window within the discharge flattop t_{ref} at which the experimental conditions can be considered steady-state. The choice of t_{ref} can also be driven by the availability of the different diagnostic data.
In tokamak toroidal geometry, the full SOLPS-ITER capabilities can be exploited to build a filed-aligned computational mesh based on the reconstruction of the experimental magnetic equilibrium.
As discussed in section 5.3.2, the SOLPS-ITER transport model assumes toroidal symmetry $\partial_\phi(\cdot) \simeq 0$ of the plasma quantities. Modelling tokamaks, the code offers the possibility to include the effects of $E \times B$ and diamagnetic drift contributions and ion viscosity, considering a toroidal magnetic field. These additional transport mechanisms give rise to cross-field and poloidal contributions to particle, momentum and energy fluxes. All the simulations considered in this chapter, however, were performed with a simplified transport model which neglected the drift contributions. The cross-field transport is purely anomalous and it is modelled as a diffusive process. By tuning the radial profile of the anomalous transport coefficients it is possible to tune the magnitude of the radial transport, thus affecting the simulation results. The anomalous transport coefficients for particles and energy were used as free parameters, to benchmark the experimental plasma profiles both at the outer midplane and at the outer divertor target. Since the purpose of this work is to obtain a plasma background which reproduces the conditions of plasma loads on the PMI samples exposed at the plasma OSP, we started our analysis by focusing on the low-field side conditions and assuming purely diffusive cross-field transport. To reproduce the asymmetries of plasma transport between high

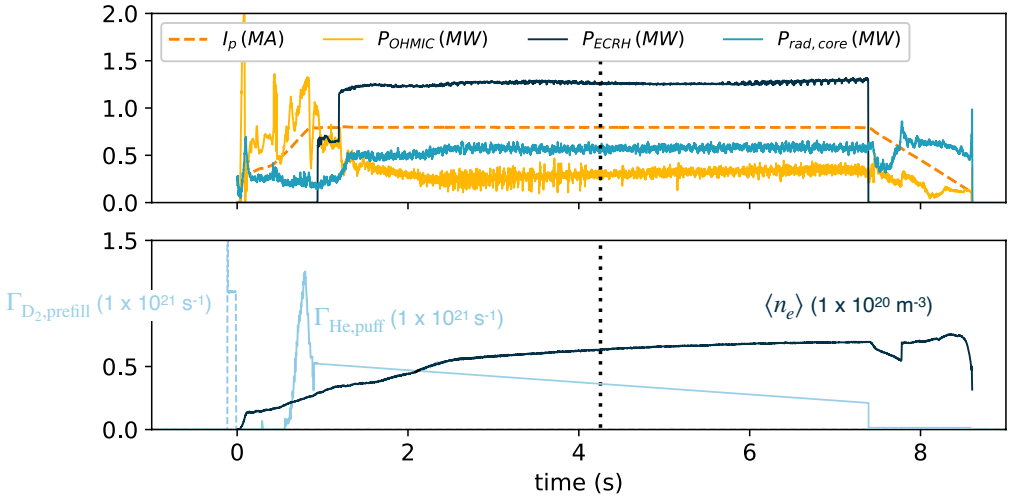

Figure 6.2: Time traces of the global parameters of the reference AUG discharge (#36687). The top figure shows the Ohmic, ECRH and radiated power (the dashed line is the plasma current I_p). The bottom figure shows the gas throughput and the average density $\langle n_e \rangle$. The vertical dotted line highlights the reference time of SOLPS-ITER simulations $t = t_{ref}$.

and low-field sides and simultaneously benchmark the plasma profiles at the inner and outer divertor targets, however, the effect of drifts should be accounted for.

As discussed in section 3.2.1, SOLPS-ITER is mostly used to model hydrogenic plasmas, possibly including heavier impurities. The modelling of pure helium can thus be considered a non-standard application of the code and requires some care in the input preparation. Many of the relevant comments on the setup of He plasma-neutral interaction databases, discussed in section 4.4 for GyM, remain valid. Differently from what was observed for the low-temperature plasma of the GyM LPD, in a tokamak, the temperature close to the separatrix is in the range of $\approx 50 - 100$ eV and the main plasma species in the confined region is He^{2+}. The simulations presented in this chapter include three heavy-particle populations: He atoms and He^{+} and He^{2+} ions. The set of atomic reactions included in the EIRENE model is reported in table 4.1. Intrinsic impurities, i.e. tungsten eroded from the wall, are not considered in these simulations, since they will be considered in detail by the coupling with ERO2.0, and D prefill impurities are neglected at this stage.

6.2.1. Global parameters, magnetic equilibrium and mesh reconstruction of the reference AUG discharge

The ASDEX-Upgrade discharge used as a reference for the SOLPS-ITER simulations (#36687) is a lower single null (LSN) magnetic configuration with forward magnetic field[1] $B_\phi = 2.5\,\mathrm{T}$ and ECRH additional heating. The time evolution of the main discharge parameters is reported in figure 6.2. The flattop is between $\sim 1.3 - 7.5$ s and the reference time for SOLPS simulations is chosen around $t_{\mathrm{ref}} \simeq 4.2$s. The flattop value of the plasma current $I_p = 0.795\,\mathrm{MA}$ corresponds to a Ohomic heating power $P_{\mathrm{Ohm}} \simeq 0.3\,\mathrm{MW}$. Additional plasma heating is provided to the plasma by $P_{\mathrm{ECRH}} \simeq 1.33\,\mathrm{MW}$ of ECRH power. This value of P_{ECRH} brings the system very close to the L-H transition threshold and transient fluctuations attributable to ELMs are observed. However, the proximity to the L-H threshold makes it difficult to clearly define a confinement regime and the ELMs type.
The line average plasma density $\langle n_e \rangle$ and gas throughput are shown in the bottom box of figure 6.2. In helium plasma experiments in AUG, the only effective pumping system is turbo-molecular pumps, while cryo-pumps are not effective for helium pumping. The average plasma density is thus set by the gas throughput during the plasma ramp-up. This is shown in figure 6.2 by the peak of Γ_{He} around ≈ 1 s, just before the ECRH power is activated. During the plasma flattop, the gas injection is low and decreases in time in order to keep $\langle n_e \rangle \approx$ constant.

The magnetic equilibrium reconstruction at $t = t_{\mathrm{ref}}$ is shown in figure 6.3.a. The position of the X-point is moved downward with respect to standard LSN configurations in AUG in order to position the outer strike point on the samples placed on the divertor manipulator. The equilibrium magnetic configuration of figure 6.3.a is used to build the computational mesh, shown in figure 6.3.b. The plasma mesh has dimensions $n_x \times n_y = 96 \times 36$ and it is represented with black lines. As discussed in section 3.2.1, B2.5 mesh radially extends only to the first open magnetic flux surface tangent to a non-divertor wall structure. EIRENE triangular mesh is shown in grey. This mesh covers the plasma region, below the B2.5 quadrangular mesh, and extends up to the machine wall.

[1] We defined a forward magnetic field discharge one in which the $\nabla\vec{B}$-drift points downward. If the sign of the magnetic field is reversed and the $\nabla\vec{B}$-drift points upward, the discharge is said to be a reversed field discharge.

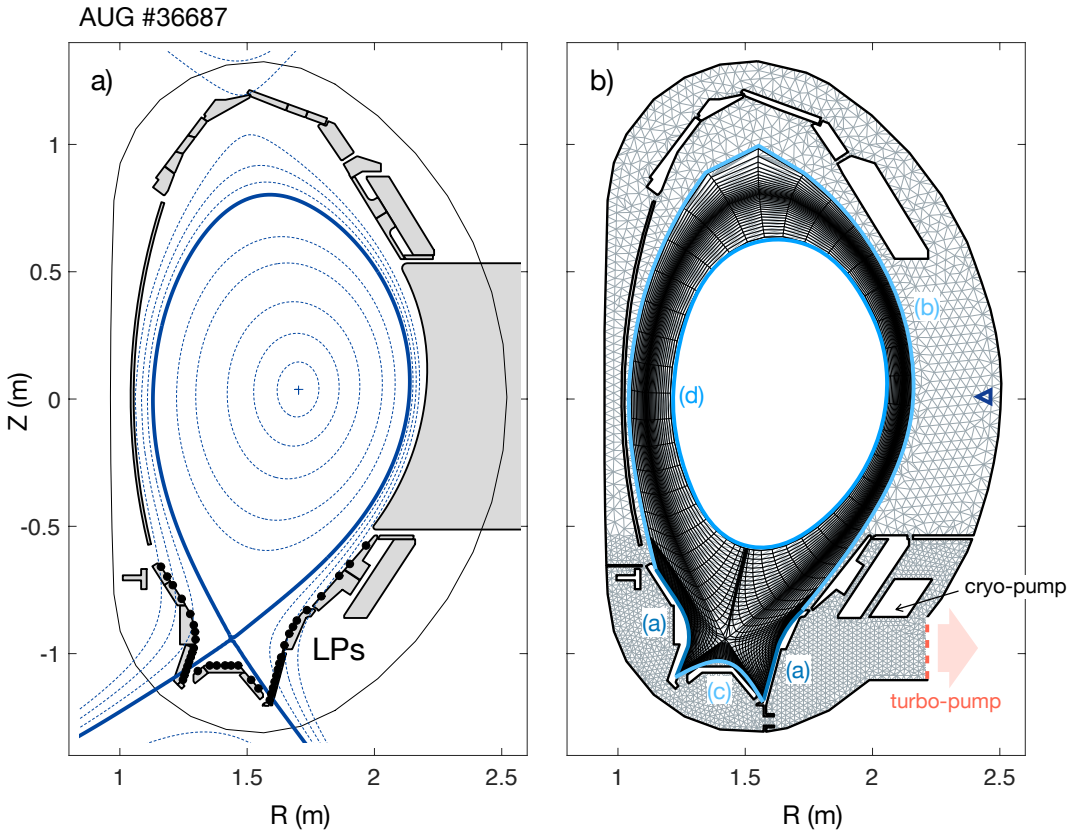

Figure 6.3: **a)** Experimental magnetic equilibrium reconstruction AUG reference discharge (#36687). The figure shows the magnetic axis (+) and the shape of the magnetic flux surfaces (dashed blue lines, solid blue line for the separatrix). **b)** SOLPS-ITER mesh for ASDEX-Upgrade simulations. Black lines represent the B2.5 plasma mesh and the grey ones the EIRENE neutral mesh.

6.2.2. Boundary conditions

B2.5 density, momentum and energy conservation equations are solved according to the following boundary conditions. The letters in the following list correspond to the different plasma boundaries, as shown in figure 6.3.b.

(a) Divertor targets: sheath boundary conditions, for densities, temperatures, velocities and electrostatic potential.

(b) Far SOL: zero gradients of the parallel velocities, zero current for the potential equation and decay boundary condition for n_a, T_e and T_i with $\lambda_{\text{decay}} = 1\,\text{cm}$.

(c) PFR: zero gradients of the parallel velocities, zero current for the potential equation and decay boundary condition for n_a, T_e and T_i with $\lambda_{\text{decay}} = 1\,\text{cm}$.

(d) Core: at the core boundary, we used zero parallel velocity gradient and zero current boundary conditions. For electron and ion energy equations, we imposed the total power entering the edge region from the core. This value is estimated from experiments as $P_{\text{e+i,core}} = P_{\text{Ohm}} + P_{\text{ECRH}} - P_{\text{rad}} \simeq 1.13\,\text{MW}$ and it is assumed that it is shared equally between electrons and ions. Two density boundary conditions are used: (i) Dirichlet boundary condition (BCCON = 1) with $n_{\text{He}^{2+}} = 5 \times 10^{19}\,\text{m}^{-3} = n_{e,\text{exp}}/2$ and $n_{\text{He}^{+}} = 0$; (ii) a feedback boundary condition that imposes a null total (ion + neutrals) flux at the core boundary (BCCON = 27 for $n_{\text{He}^{2+}}$ and BCCON = 26 for $n_{\text{He}^{2+}}$). The condition $\Gamma_{\text{core,B2.5,He}^{2+}} + \Gamma_{\text{core,B2.5,He}^{+}} + \Gamma_{\text{core,EIRENE,He}} = 0$ is set at each iteration, combining B2.5 (for ions) and EIRENE results (for neutrals).

The wall recycling coefficients at the EIRENE mesh boundary are estimated from the TRIM database for He helium on W materials. The EIRENE pumping surface corresponding to the turbo-molecular pump is shown in red in figure 6.3.b. The surface albedo is set to $p_a = 0.007$. The pumping surface, which corresponds to the cryogenic pump (indicated with the black arrow in figure 6.3.b), is deactivated $p_a = 0$ since cryopumps are not effective in pumping helium species. Helium gas puff is done from a surface located at the OMP, as indicated by the blue triangle in figure 6.3.b. The location corresponds to the experimental gas valve. The He puffing strength is regulated by a feedback condition which imposes the value of the electron temperature at the outer midplane separatrix.

6.2.3. Anomalous transport coefficients

The optimisation of the anomalous transport coefficients to produce results in agreement with the experimental profiles at the OMP and at the OSP required extensive work to characterise the influence of the value and the radial shape of D_n and $\kappa_{i/e,\perp}$. In this section, we present the preliminary analyses performed to understand these effects.

The first study was a scan of D_n and $\kappa_{i/e,\perp}$, assuming constant values all over the computational domain and equal electron and ions thermal conductivities $\kappa_{i,\perp} = \kappa_{e,\perp}$. The particle diffusivity D_n was scanned in the range $0.15 - 0.3\,\mathrm{m}^2/\mathrm{s}$, while the thermal diffusivity $\chi_{i/e,\perp} = \kappa_{i/e,\perp}/n_{i/e}$ was varied in the range $0.2 - 0.5\,\mathrm{m}^2/\mathrm{s}$. All the simulations were performed with Dirichlet density boundary conditions at the core. The electron density at the separatrix is fixed at $n_{e,\mathrm{sep}} = 1 \times 10^{19}\,\mathrm{m}^{-3}$ due to the feedback He puffing strength condition. The results in terms of radial profiles of n_e and T_e at the OMP (left) and OSP (right) are shown in figure 6.4.
The top line presents the results of the D_n parametric study. The results show that an increase of the D_n value results in a decrease in the core and OPS peak T_e and an increase of the peak n_e at the OSP. It should be noted, however, that the upstream density profiles are also determined by the choice of the core density boundary condition. Indeed, this analysis should be compared with the analogous parametric scan of D_n presented in section 7.3.2 in the context of the investigation of negative triangularity transport. In those simulations, a null total core particle flux is imposed; hence, the density value is not constrained at the core boundary and the OMP density profile is free to vary. Despite the differences upstream, however, the choice of the core BC does not influence the general T_e and n_e trends at the divertor.
The bottom line in figure 6.4 shows the $\chi_{i,\perp} = \chi_{e,\perp}$ scan. A variation in the anomalous thermal diffusivity mostly affects the T_e profiles at the OMP. In particular, by increasing the thermal diffusivity the core electron temperature decreases consistently with increased cross-field heat removal. At the outer divertor, however, almost no differences are observed both in n_e and T_e profiles.

A second analysis was performed investigating the effect of the radial shape of the D_n and $\chi_{e/i,\perp}$ profiles. To remove the constraint on the density value, all the simulations were performed by imposing a null total particle flux at the core boundary. The electron density at the separatrix $n_{e,\mathrm{sep}}$ was again fixed by applying the feedback condition on the He puffing strength. The results of these analyses are shown in figure 6.5.
Figures 6.5.a and 6.5.b display the effects of a variation in the radial shape of D_n and of an increase of the D_n value in the SOL region, respectively. These analyses are

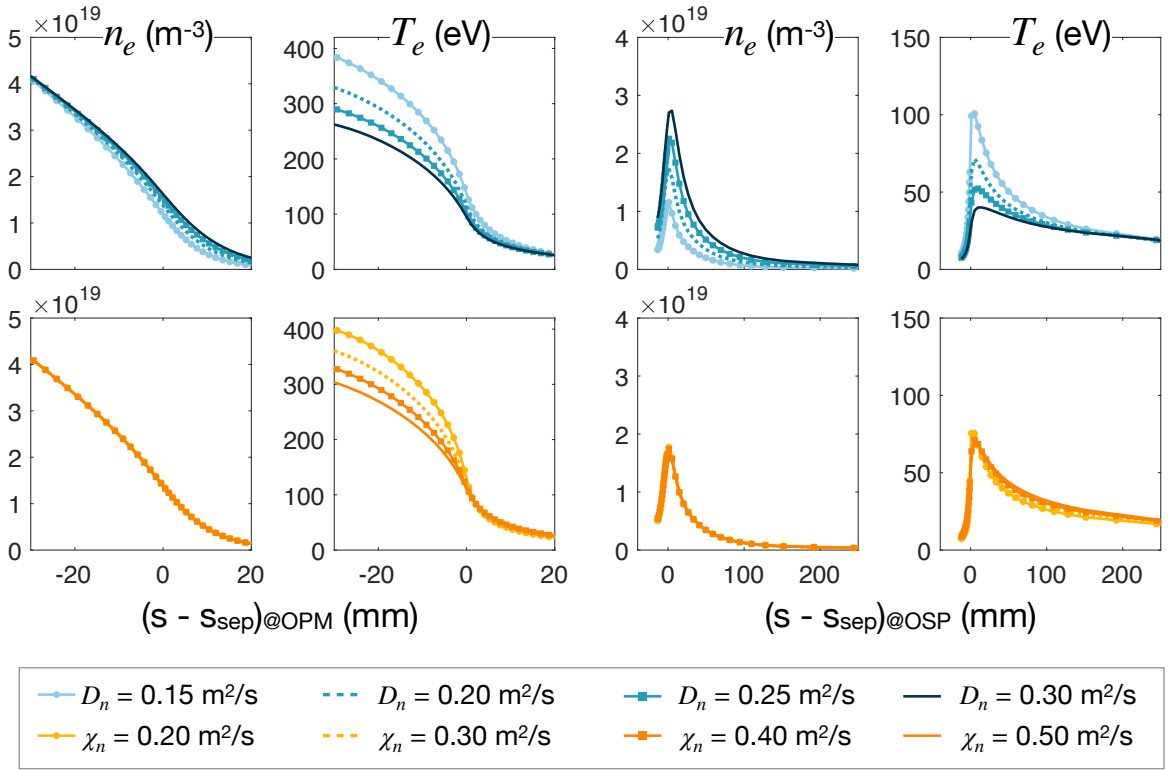

Figure 6.4: Parametric scan of the anomalous transport coefficients D_n (top, blue lines) and χ_e (bottom, orange lines). Radial profiles of the electron density and temperature are shown at the outer midplane (OMP) and close to the outer strike point (OSP). These simulations used Dirichlet boundary conditions for the ion density equations at the core boundary (BCCON = 1).

performed at constant heat diffusivity $\chi_{e,\perp} = \chi_{e,\perp} = 0.8\,\mathrm{m}^2/\mathrm{s}$ and $n_{e,\mathrm{sep}} = 1 \times 10^{19}\,\mathrm{m}^{-3}$. The first panel on the left shows the D_n profiles used in the analysis. This analysis investigates a D_n step profile, lower in the core region and higher in the SOL. The radial n_e and T_e profiles at the OMP and outer divertor which resulted from the simulations are shown in the two central and right panels, respectively.
In figure 6.5.a, all profiles have $D_n^{\mathrm{low}} = 0.07\,\mathrm{m}^2/\mathrm{s}$ at the core side and $D_n^{\mathrm{high}} = 0.8\,\mathrm{m}^2/\mathrm{s}$ in the far SOL, while the shape of the transition from low to high D_n is varied between simulations. Among the five simulations, one (dotted line) has qualitatively different n_e and T_e profiles at the divertor. In this simulation the low to high D_n transition starts for $s > s_{\mathrm{sep}}$. If the anomalous diffusion coefficient remains low across the whole core region and only increases outside the separatrix, cross-field transport is strongly suppressed. This results in energy accumulation in the core region resulting in $T_{e,sep} \approx 150$ eV. The low particle diffusion out of the core region suppresses the density in the SOL and produces a sheath-limited plasma regime with very high OSP peak temperatures $T_{e,\mathrm{max@OSP}} \approx 150$ eV. For the other four simulations, the increase of D_n begins for $s < s_{\mathrm{sep}}$ and the different D_n profiles produce differences in the shape of the radial n_e profiles at the OMP. Although the upstream differences, however, the profiles at the outer divertor are similar both concerning n_e and T_e.
Figure 6.5.b shows the second analysis on the D_n profile, performed by modifying the height of the step. Here $D_n^{\mathrm{low}} = 0.07\,\mathrm{m}^2/\mathrm{s}$ and $D_n^{\mathrm{high}} = 0.8 - 1.6 - 2.4\,\mathrm{m}^2/\mathrm{s}$, according to the different simulations. The increase of the anomalous diffusion in the SOL produces an increase of the n_e at the core boundary and a consequent reduction of T_e. Indeed, if more ions are removed radially in the far-SOL, a higher He puffing strength is needed to obtain the same electron density at the separatrix. A higher radially inward atom flux is compensated by higher to satisfy the condition of null total particle flux at the core boundary. At the divertor, however, the increased core density does not result in higher $n_{e,\mathrm{max@OSP}}$. On the contrary, lower T_e close to the separatrix at the OMP produces a reduction of the $T_{e,\mathrm{max@OSP}}$.

An analysis similar to the one performed on D_n was also performed on the thermal diffusivities $\chi_{e/i,\perp}$, under the assumption $\chi_{i,\perp} = \chi_{e,\perp}$. Similar boundary conditions were used, i.e. null total particle flux at the core boundary and constant $n_{e,\mathrm{sep}} = 1.25 \times 10^{19}\,\mathrm{m}^{-3}$. The results of the analysis are shown in figure 6.5.c and 6.5.d. D_n has a fixed profile for all the simulations, corresponding to the solid dark blue line in figure 6.5.a. Both in figure 6.5.c and 6.5.d, the solid red line refers to simulations with constant $\chi_{i,\perp} = \chi_{e,\perp} = 0.6\,\mathrm{m}^2/\mathrm{s}$, while the other simulations used a step profile for $\chi_{e/i,\perp}$.
As for D_n, figure 6.5.c shows the effect of a radial shift in the step $\chi_{e/i,\perp}$ profile, while

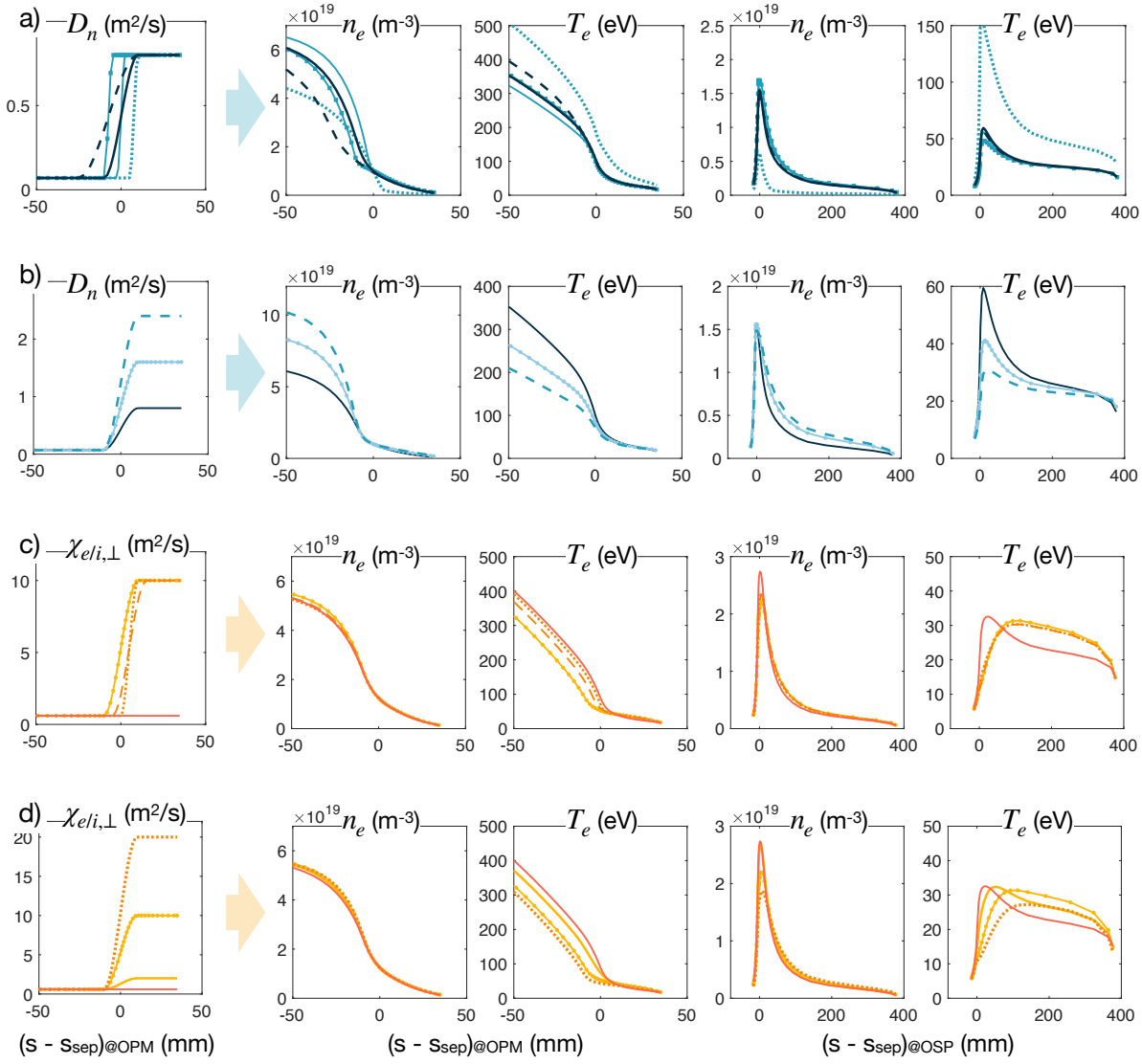

Figure 6.5: Parametric scan of the D_n and $\chi_{i/e,\perp}$ radial profiles. In each figure, from left to right, the figure shows the D_n radial profile, the simulated n_e and T_e radial profiles at the OMP and OSP.

figure 6.5.d presents the effect of an increase in the step height. In general terms, we can observe that the effect of changes in $\chi_{e/i,\perp}$ is lower with respect to similar changes in D_n. The most noticeable effect is on the core temperature profiles, shown at the OMP: a higher $\chi_{e/i,\perp}$ value in the core region, either because of shifting of the profile or because of a steeper gradient, results in a lower core temperature. An increase of the value of $\chi_{e/i,\perp}$ in the SOL has as its main effect the flattening of the outer diverter temperature profile away from the OSP. This, however, does not result in a strong reduction of the average electron temperature at the outer divertor, even for very high thermal diffusivities $\chi_{e/i,\perp} \approx 10\,\mathrm{m}^2/\mathrm{s}$. At high $\chi_{e/i,\perp} \approx 10\,\mathrm{m}^2/\mathrm{s}$, however, the peak n_e at the OSP is reduced.

6.2.4. Separatrix density and core input power

The analysis presented in section 6.2.3 on the parametric scan of the anomalous diffusivities is motivated by the lack of a theoretical or experimental method to estimate those parameters. However, even parameters which can in principle be more easily estimated from experimental data, such as the electron density at the separatrix or the total input power at the core boundary, are affected by uncertainties. These uncertainties can, in turn, impact the simulation results.
In this section, we thus performed a parametric scan on $n_{e,\mathrm{sep}}$ and $P_{\mathrm{e+i,core}}$ within the range of values compatible with the experimental uncertainties.

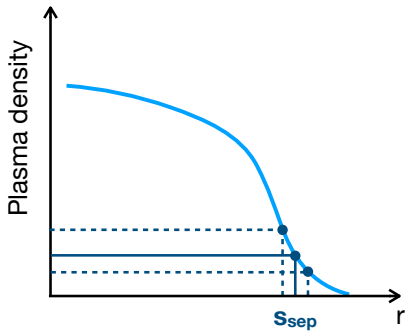

Figure 6.6: Effect of the experimental uncertainty on the separatrix position.

The magnetic equilibrium of an experimental discharge is reconstructed by solving the Grad-shafranov equation. In this way, the position of the separatrix on the poloidal plane is obtained and then used to visualise the experimental plasma density and temperature profiles as a function of the distance from the separatrix $s - s_{\mathrm{sep}}$. The separatrix position, however, can be affected by uncertainties of a few millimetres. Considering the density profile at the OMP, a radial shift of the separatrix modifies the estimated value of the electron density at the separatrix, as displayed in figure 6.6. The following analysis assesses the impact of varying the density value at the separatrix $n_{e,\mathrm{sep}}$ in the range $1 - 1.3 \times 10^{19}\,\mathrm{m}^{-3}$, corresponding to a maximum shift in the separatrix position of 2 mm. The results of the seven simula-

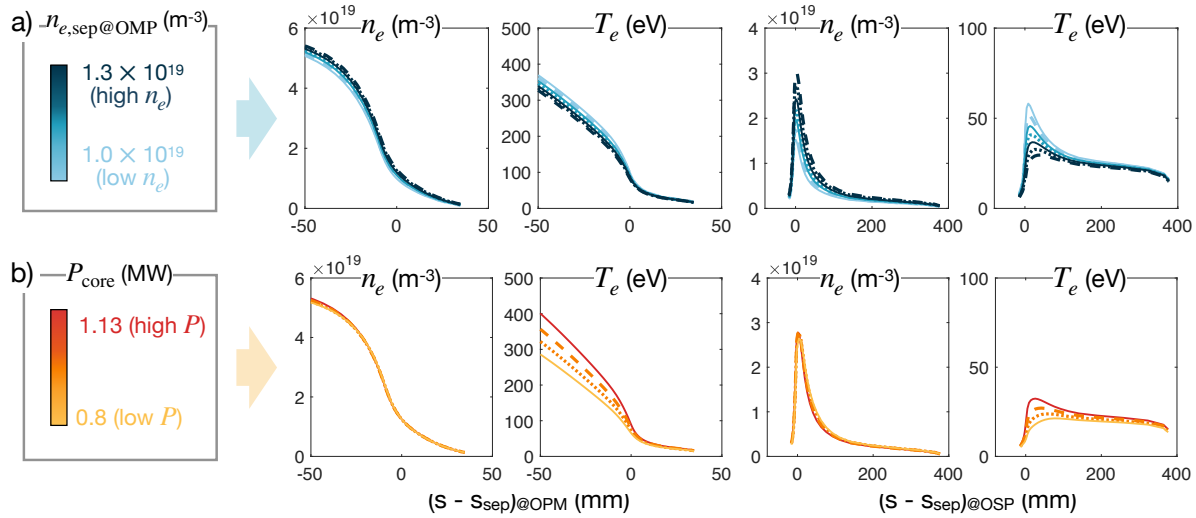

Figure 6.7: Parametric scan of the **a)** electron density value at the separatrix $n_{e,sep}$ and **b)** core input power $P_{e+i,core}$. The scans are performed at fixed anomalous transport coefficients. The figure shows the simulated n_e and T_e radial profiles at the OMP and OSP.

tions performed are shown in figure 6.7.a. At the OMP, for increasing $n_{e,sep}$ the density and temperature profiles are slightly shifted (upward and downward, respectively) but in any case stay within the experimental error. At the divertor, on the contrary, variation of $\approx$ a factor of 2 in the peak values of n_e and T_e at the outer strike point is observed, proving the electron density at the separatrix to be a very sensitive parameter to control the outer divertor properties.

The second parameter that is analysed in this section is the value of the core input power $P_{e+i,core} = P_{e,core} + P_{i,core}$, with $P_{e,core} = P_{i,core}$. As discussed in section 6.2.2, this parameter is set up as the core boundary condition for the ion and electron energy equations. Experimentally, $P_{e+i,core}$ is given by the ECRH and Ohmic input power, reduced by the fraction of power radiated from the main plasma. In this work, we considered a maximum input power of 1.135 MW corresponding to the whole $P_{Ohm} + P_{ECRH} - P_{rad}$ and we assumed a reduction of this value up to 30%. The results of simulations performing a parametric scan of $P_{e+i,core}$ in the range $0.8 - 1.135$ MW, are shown in figure 6.7.b. The analysis shows that the n_e profiles are unaffected, while a reduction of $P_{e+i,core}$ results in a reduction of the plasma temperature, both upstream and at the divertor targets.

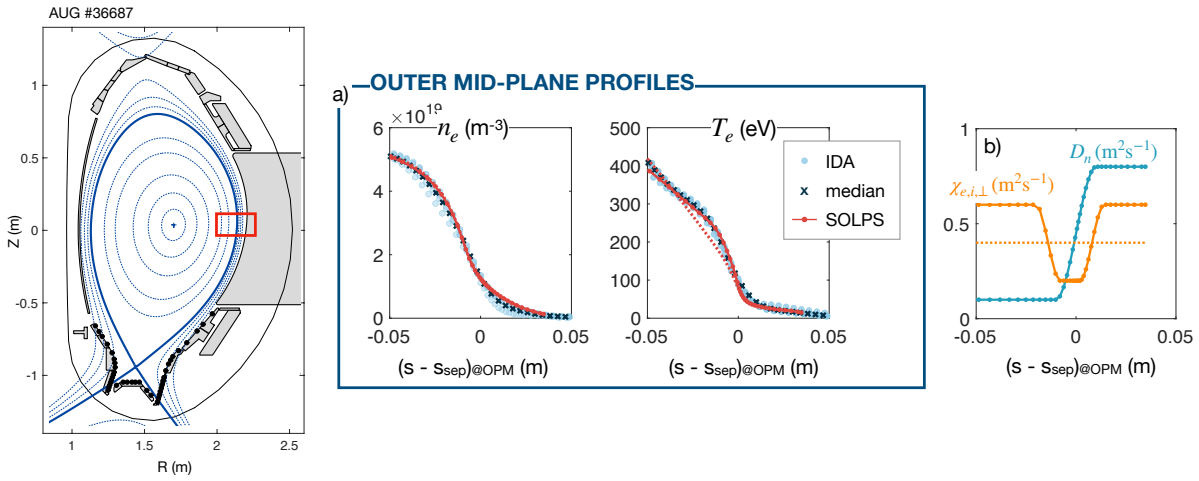

Figure 6.8: Benchmark between SOLPS-ITER simulations and ASDEX-Upgrade data at the outer mid-plane. The dotted lines in figure **a)** correspond to the simulation done with constant $\chi_{e/i,\perp}$ (dotted line in **b)**). Solid red lines in **a)** correspond to the well-shaped $\chi_{e/i,\perp}$ profile (solid orange line in **b)**).

6.2.5. Benchmark with experimental data

The preliminary studies presented in sections 6.2.3 and 6.2.4 allowed us to understand how the different input parameters modify the simulation results. Those analyses were crucial to optimise SOLPS-ITER setup and obtain a good agreement with AUG experimental plasma profiles at the outer midplane and divertor. At the OMP, the experimental profiles of electron density and temperature are estimated by the Integrated Data Analysis (IDA) tool of AUG [124]. Data acquired between t = 4.1 and t = 4.3 s (dots in figure 6.8) were used for comparison with SOLPS-ITER simulations. Their median values over the time interval are also displayed (crosses in figure 6.8). At the divertor targets, the ion saturation current is measured by fixed Langmuir probes and used to estimate plasma temperature and the plasma heat flux. The divertor LP data are taken again between t = 4.1 and t = 4.3, as the IDA.

The results discussed in section 6.2.3 highlight that the shape of the outer mid-plane plasma profiles can be controlled by the shape of the D_n profile. A step radial profile symmetric with respect to the separatrix was used, with $D_n^{\text{low}} = 0.1\,\text{m}^2/\text{s}$ and $D_n^{\text{high}} = 0.8\,\text{m}^2/\text{s}$. Among the shape of the $\chi_{i,\perp}$ and $\chi_{e,\perp}$ considered in section 6.2.3, we used a constant radial profile with $\chi_{i,\perp} = \chi_{e,\perp} = 0.4\,\text{m}^2/\text{s}$, where the value was adjusted so that simulations match the experimental T_e at the core boundary. The separatrix electron density was imposed to $n_{e,\text{sep}}$ in the range $1.25 \times 10^{19}\,\text{m}^{-3}$ and the total electron and ion power at the core boundary $P_{\text{e+i,core}} = 0.9$ MW. The results of SOLPS-ITER simulations with these parameters as input are shown in figure 6.8 with dotted lines.

We observe a good agreement between the simulated and the experimental density profiles and between the T_e values at the core boundary and in the SOL. However, in the region around $s - s_{sep} \approx -2$ cm, the simulated profile with constant $\chi_{i/e,\perp}$ underestimates the experimental temperature and does not reproduce the shape of the profile. The agreement can be improved by implying the well-shaped heat diffusivity profile shown with a solid orange line in figure 6.8.b. Figure 6.8.a displays the corresponding simulation results with solid red lines. It should be noted that well-shaped profiles for the anomalous diffusivities are commonly used to model H-mode discharges with numerical codes like SOLPS-ITER. The need for such a shape for $\chi_{e,\perp}$ to model this AUG discharge could be due to the proximity to the L-H transition. Further investigation is however needed.

The simulation results at the outer divertor are plotted in figure 6.9. Different shapes of $\chi_{e/i,\perp}$ produce no differences in the outer divertor profiles and thus we reported only the one corresponding to the well-shaped profile.
In helium plasma discharges, estimating the electron density from the ion saturation current collected by the divertor LPs is not straightforward. Indeed, each He^{2+} ion collected contributes twice to the electrical current density as each He^{+} and knowing the plasma composition is thus crucial. To benchmark simulations and experiments, we compared the experimental ion saturation current[2] $j_{sat}^{exp} = I/(q_e \times A_{probe})$ to the one estimated by SOLPS as $j_{sat}^{SOLPS} = \Gamma_{He^+} + 2 \times \Gamma_{He^{2+}}$, where Γ_{He^+} and $\Gamma_{He^{2+}}$ are the particle fluxes of the two species. This comparison is shown in the top graph of figure 6.9; the middle graph shows the comparison of simulated and experimental electron temperature and at the bottom the comparison of the plasma power fluxes. The experimental plasma power flux is estimated from Langmuir probe data, assuming a total heat transmission coefficient at the plasma sheath $\gamma \simeq 7$, i.e. $P_{plasma}^{exp} = \gamma q_e T_e j_{sat} \approx 7 q_e T_e j_{sat}$. Using the optimised parameter setup, good agreement is found between the experimental and simulated profiles. The experimental ion saturation current peak is slightly broader and shifted towards the SOL if compared to the simulated one. Drift contributions to the poloidal and radial fluxes should be included in the model in order to have a more complete description of plasma transport and investigate the possibility of better reproducing the j_{sat} experimental profile. The flat and constant electron temperature profile is well reproduced by SOLPS modelling. The dotted line in the bottom figure corresponds to the total power flux at the divertor target $P_{tot} = P_{plasma} + P_{rec} + P_{neut} + P_{rad}$, which includes besides the power flux transported by the plasma, also the one due

[2] In the following we will always use the ion saturation current normalised to the unit charge q_e. For a plasma with $Z_{eff} = 1$, this corresponds to the ion flux. This is not the case for He plasmas since He^{2+} is also present.

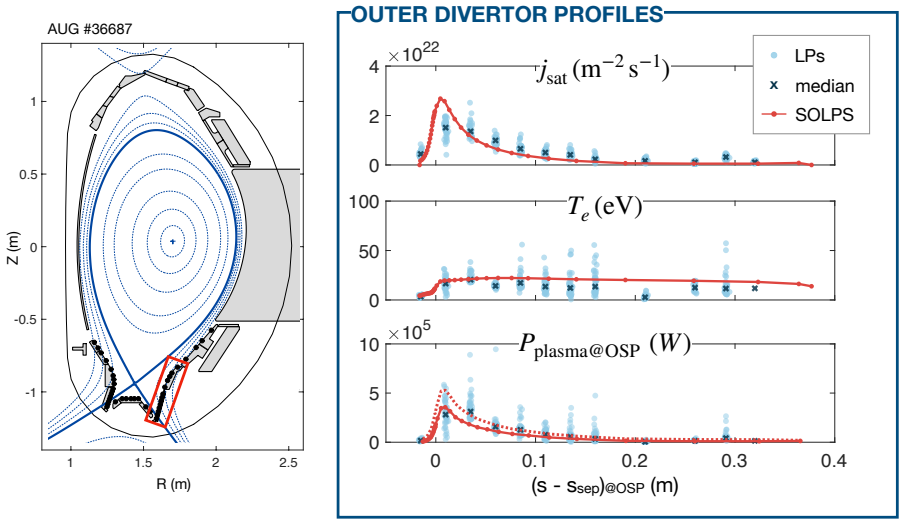

Figure 6.9: Benchmark between SOLPS-ITER simulations and ASDEX-Upgrade data at the outer divertor. The ion saturation current measured by the divertor LPs is compared with the total unit-charge flux at the divertor $j_{sat}^{SOLPS} = \Gamma_{He^+} + 2 \times \Gamma_{He^{2+}}$. The experimental plasma power flux is estimated by assuming a total heat transmission coefficient at the sheath $\gamma \simeq 7$, i.e. $P_{plasma} = \gamma q_e T_e j_{sat} \approx 7 q_e T_e j_{sat}$. The dotted line in the bottom figure corresponds to the total power flux at the divertor target $P_{tot} = P_{plasma} + P_{rec} + P_{neut} + P_{rad}$, which includes besides the power flux transported by the plasma, also the one due to recombination of ions at the divertor, neutral power flux and power flux due to core radiation.

to recombination of ions at the divertor, neutral power flux and power flux due to core radiation. The total plasma heat loads can be computed by summing the total power transported by the plasma and the power associated with the ion recombination at the wall. This quantity can be used as an estimate of the degree of detachment of the plasma. Close to the outer strike point, $P_{plasma} + P_{rec}$ contributes to $\gtrsim 90\%$ of the total OSP power, thus identifying a clearly attached condition.

6.3. Analysis of the ion fluxes

As mentioned in section 6.1, the final aim of this work will be the modelling of a full PMI experiment performed in AUG. The SOLPS-ITER plasma background, described in section 6.2.5, is used as input for erosion and impurity transport modelling with ERO2.0. Knowing the distribution of plasma density, velocity and temperature of the different ion and electron populations, ERO2.0 evaluated the fluxes onto the divertor and PFCs, computes the sputtered fluxes and traces the impurities within the plasma

up to the position where they are re-deposited.
In He plasmas, two ion populations exist in the boundary and divertor region. He^+ and He^{2+} have different charges and they are thus accelerated to different energies within the electrostatic sheath in front of the wall surface. As mentioned in section 1.3.3, the plasma recycling process and the physical sputtering yield Y_{ph} strongly depend on the ion impact energy. Thus, knowing the flux composition in terms of different ion species is crucial to correctly estimating erosion. Discriminate between He^+ and He^{2+} from experimental data alone is however difficult since the spectroscopic techniques can only detect the presence of singly ionised He and electrostatic probes measures the total charge collected.
This section aims thus to further analyse the results of SOLPS-ITER simulations retrieving, in particular, the composition of the ion flux onto the PFCs and outer divertor.

Figures 6.10.a-c presents the analysis of poloidal fluxes at the outer divertor. The profile of the total ion saturation current as a function of the distance from the OSP, already shown in figure 6.9, is plotted in the top box of figure 6.10.b. The analysis of the flux composition is then shown in the middle and bottom boxes of figure 6.10.b. In particular, the middle box shows the He^+ (dotted) and He^{2+} (solid) fluxes onto the outer divertor and the bottom figure shows their relative fractions $\Gamma_{He^+/He_{tot}}$ (dotted) and $\Gamma_{He^{2+}/He_{tot}}$ (solid).
A similar analysis is shown in figures 6.10.d and 6.10.e for the radial ion fluxes onto the non-divertor PFCs. As discussed in section 3.2.1, the present version of SOLPS-ITER can not exactly assess the fluxes onto non-divertor wall surfaces, since the plasma computational mesh is limited radially. In our analysis, thus, we considered the fluxes crossing the last radial cell of the plasma mesh. For a more realistic description, one should use a model with an extended grid [105, 125].
From the analysis presented in figure 6.10, we can first infer that radial fluxes onto the non-divertor PFCs are more than two orders of magnitude lower than poloidal fluxes at the OSP. This conclusion, however, could not be quantitatively benchmarked due to the lack of experimental data for the discharge of interest. Nonetheless, AUG is provided with fixed Langmuir probes on several non-divertor components, such as the inner heat shield and the upper wall. In the future, these signals may be also used to expand the experimental benchmark. In case the experimental measurements showed significant differences with the simulation results, the parameter optimisation described in sections 6.2.3 and 6.2.4 should be repeated to find a different set of parameters that reproduce simultaneously the experimental divertor and radial fluxes. In particular, if simulations underestimated the radial experimental fluxes, anomalous particle diffusiv-

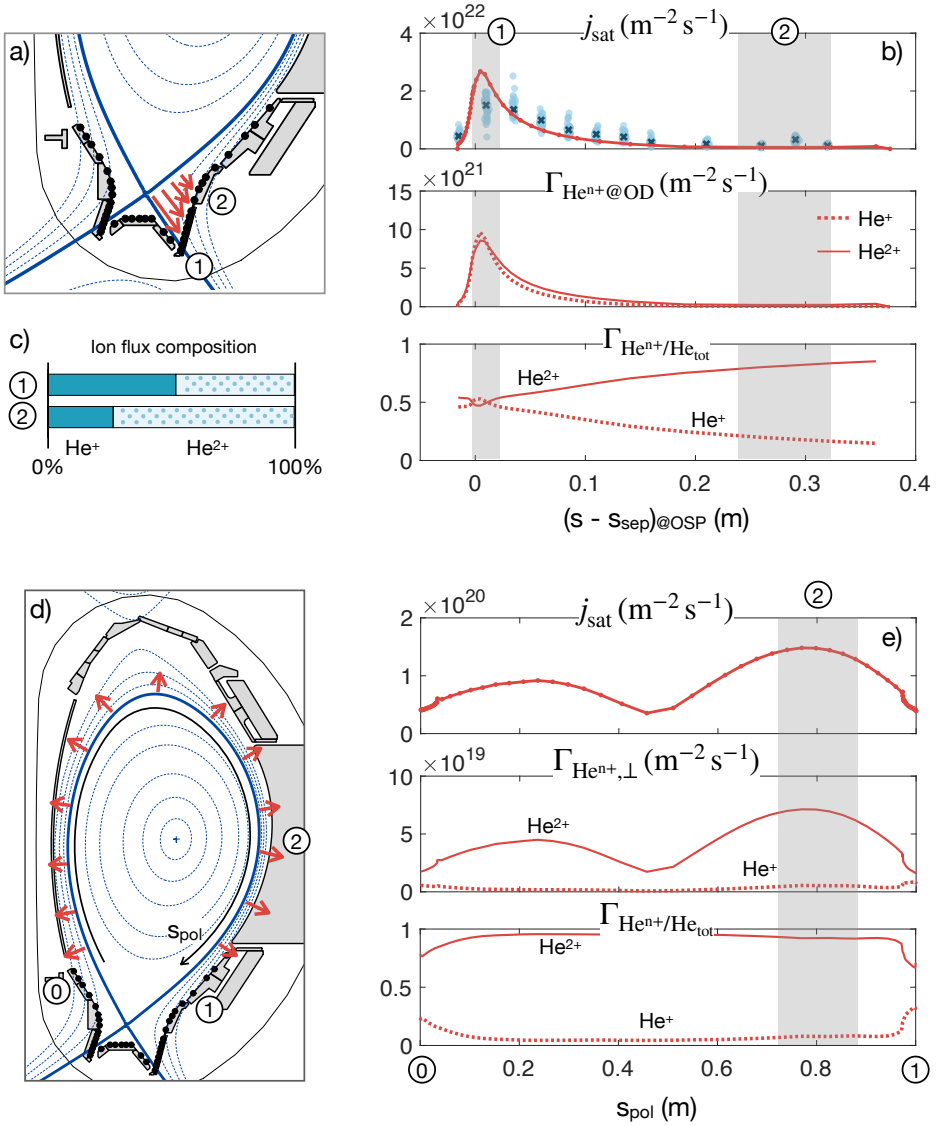

Figure 6.10: Analysis of the poloidal ion fluxes onto the outer divertor target (a, b and c) and radial ion fluxes onto the main chamber (d and e). **a)** Poloidal flux onto the outer divertor. **b)** Profiles of the ion saturation current j_{sat} (top), the poloidal ion fluxes j_{sat} and j_{sat} (middle) and their relative fraction (bottom) as a function of the distance from the OSP. **c)** Flux composition at the outer divertor ① close to the OSP and ② further in the SOL. **d)** Radial ion fluxes onto the PFCs, computed as the radial fluxes crossing the last radial cell of the B2.5 mesh. **e)** Profiles of the ion saturation current j_{sat} (top), the poloidal ion fluxes j_{sat} and j_{sat} (middle) and their relative fraction (bottom) as a function of the distance along the poloidal distance s_{pol} between inner and outer divertor: ⓪ corresponds to the inner divertor limit, ① to the outer divertor limit and ② is the gas puffing region.

ities need to be increased and $n_{e,\mathrm{sep}}$ is likely to need adjustment in order to match the OSP peak density (or ion saturation current).
The radial fluxes are almost entirely due to He^{2+} ions and the He^{+} contributions only increase to $\approx 25-30\%$ close to the divertor targets. A slight increase of the He^{+} ion flux fraction is also observed for $s_{\mathrm{pol}} \approx 0.8$, i.e. close to the He puffing valve. On the outer divertor, which corresponds to the location of the PMI experiment, He^{+} fluxes become more important. Across the OSP, in particular, it is found that He^{+} is the most abundant species and $\Gamma_{He^{+}/He_{\mathrm{tot}}} \gtrsim 50\%$. Moving further in the SOL, the $\Gamma_{He^{+}/He_{\mathrm{tot}}}$ fraction decreases. This trend is shown in figure 6.10.c, where the percentage flux composition is displayed. These values are computed as the mean value of $\Gamma_{He^{n+}/He_{\mathrm{tot}}}$ in regions ① and ②, highlighted in figure 6.10.a and 6.10.b.
The fractional abundance of He^{+} and He^{2+} in the particle flux onto the wall strongly affects the erosion of the PFCs. Indeed, the sheath acceleration of the ions, and thus their impact energy on the wall, depends on the ion charge Z according to the formula:

$$E_{\mathrm{wall}} = 0.5 Z T_e \ln\left[(2\pi m_e/m_i)(1 + T_i/T_e)\right] \simeq 3.5 Z T_e \tag{6.1}$$

thus He^{2+} ions ($Z = 2$) are subjected to a sheath acceleration that is twice the one for He^{+} ($Z = 1$). The physical sputtering yield of helium ions on tungsten $Y_{\mathrm{ph,W}}(E_{\mathrm{wall}}, \theta)$, shown in figure 4.13.a, has a sputtering threshold $E_{\mathrm{W,th}} \simeq 130\,\mathrm{eV}$. Considering the condition at the outer divertor shown in figure 6.9, since $T_e \simeq T_i \simeq 20$ eV, according to equation (6.1), only He^{2+} ions reach the divertor with sufficient energy to sputter the tungsten tiles.
More in general, if the plasma temperature at the sheath entrance is high enough for the He^{+} ions to overcome the sputtering threshold ($T_e \simeq T_i \gtrsim 40$ eV), the erosion flux can be computed as:

$$\Gamma_{\mathrm{ero,ph}} = \left[\frac{f}{1+f} Y_{\mathrm{ph,W}}(E_{\mathrm{wall,He^{2+}}}, \theta) + \frac{1-f}{1+f} Y_{\mathrm{ph,W}}(E_{\mathrm{wall,He^{+}}}, \theta)\right] j_{\mathrm{sat}} \tag{6.2}$$

where $f = \Gamma_{He^{2+}/He_{\mathrm{tot}}}$ and $1 - f = \Gamma_{He^{+}/He_{\mathrm{tot}}}$. E_{wall} depends on T_e and T_i as described in equation (6.1) and $Y_{\mathrm{ph,W}} = 0$ if $E_{\mathrm{wall}} < E_{\mathrm{W,th}}$.

To further investigate the origin of the He^{+} flux distribution, we analysed the spatial distribution of the ionization particle sources. This is plotted on the left of figure 6.11. Due to the high plasma temperatures, the large majority of particles escaping radially from the confined region are He^{2+}. This explains why the radial flux is mostly from He^{2+} ions. Additionally, since for high electron temperatures $T_e \gtrsim 20$ eV, the electron impact recombination of He^{2+} is negligible, He^{+} are only generated by the ionization of

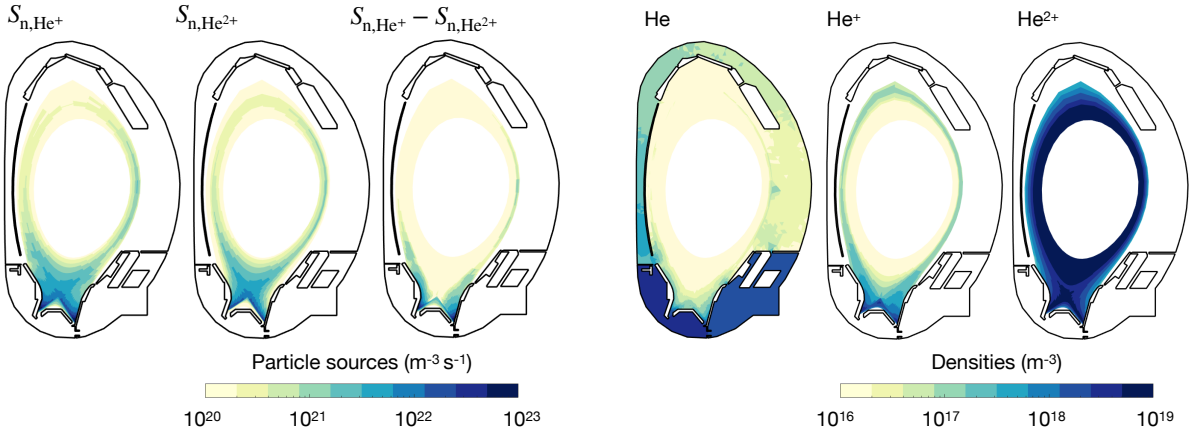

Figure 6.11: 2D maps of the ionization particle sources ($m^{-3}\,s^{-1}$) and density (m^{-3}) distributions. From left to right, the figure shows the total ionization rate of He $\rightarrow$ He^+, the total ionization rate of He^+ $\rightarrow$ He^{2+}, corresponding to the effective He^{2+} particle source, and the effective He^+ particle source given by the difference of $S_{n,He^+} - S_{n,He^{2+}}$. The three 2D maps on the right represent the density distributions of He, He^+ and He^{2+}, respectively.

He atoms produced by the plasma recycling at the divertor or at the other PFCs. From left to right, the first three plots in figure 6.11 show the total ionization rate of He atoms into He^+, the total ionization rate of He^+ into He^{2+} and the effective He^+ particle source, computed as the difference of the previous two.

The effective production of He^+ ions is mostly localised very close to the outer strike point and decreases moving away from it, both in the poloidal and cross-field directions. This explains the behaviour observed in figure 6.10, for which $\Gamma_{He^+/He_{tot}}$ becomes comparable to $\Gamma_{He^{2+}/He_{tot}}$ only close to the OSP, while the second is the dominant contribution everywhere else. In the far-SOL at the outer midplane, close to the gas injection location, we observed a lower but still significant effective production of He^+, which is responsible for the slight increase of $\Gamma_{He^+/He_{tot}}$ around $s_{pol} \approx 0.8$, as observed in figure 6.10.e. As soon as we move closer to the separatrix, however, the production rate of He^{2+} dominates and the produced He^+ are ionised to He^{2+}. The effective production of He^+ is thus completely negligible inside the confined region.

The three 2D maps on the right of figure 6.11 show the densities of He atoms and He^+ and He^{2+} ions. These density distributions result from the balance of particle production via ionization and transport processes, described by the SOLPS-ITER model. This information, together with the corresponding velocities and temperature distributions, is ready to be used as the plasma background for erosion and impurity migration studies.

6.4. Conclusions

This chapter presented a summary of the modelling effort devoted to the production of a pure helium plasma background for the investigation of erosion and impurity transport, migration and re-deposition in a full-W tokamak. The work is part of a joint effort of the EUROfusion TE and PWIE Work Packages to investigate plasma-wall interactions in He plasmas in view of the non-active phase of ITER.

The integrated PMI modelling requires the knowledge of the full distributions of density, velocities and temperatures of each ion population and electrons throughout the entire plasma volume. Since most of the data that can be received from the experiments are only available at very specific locations, typically the outer midplane and the divertor targets, the reconstruction of the full plasma background through modelling is crucial. The SOLPS-ITER code package allows the investigation of how the different ion populations in the plasma are transported and interact with neutrals and the surrounding wall in the boundary of a tokamak. Exploiting this numerical tool, we reproduced the conditions of a pure helium plasma experiment performed in ASDEX-Upgrade.
SOLPS-ITER is the state-of-the-art numerical code for boundary plasma modelling. Its standard applications usually imply the presence of a main hydrogenic species, H, D or T, possibly mixed with a lower concentration of heavier impurities, originating from PWI or seeded to attain plasma detachment. These results show the possibility of successfully implying SOLPS-ITER also to investigate pure helium plasma considering only He^{+} and He^{2+} ion populations and He atoms. The choice to use the SOLPS-ITER code package to produce the plasma He background for the PMI studies in AUG tokamak follows naturally from the work presented in chapter 4 on the investigation of low-temperature He plasmas in the GyM linea plasma device.

A field-aligned computational mesh was produced exploiting the experimental magnetic reconstruction of the discharge of interest to perform the simulations. After the simulation setup, the first part of the work was devoted to an extensive analysis of the free parameters of the code. These include the cross-field anomalous transport coefficients for particles and energy and other parameters, such as the separatrix electron density and the core input power, which were varied within their experimental uncertainty. These preliminary studies allowed us to identify an optimised set of parameters with which it was possible to obtain a satisfactory agreement with the available experimental data. However, evaluating the electron density from the ion saturation current collected from the divertor Langmuir probes is not straightforward for He plasma. Indeed, both He^{+} and He^{2+} ions are present in the divertor region and the latter contributes twice the

former to the total collected charge. The LP ion saturation current was thus compared with the sum of the ion fluxes, weighted to the ion charge.
Finally, the composition of the ion flux was analysed in detail. The relative fractions of $\Gamma_{He^+/He_{tot}}$ and $\Gamma_{He^{2+}/He_{tot}}$ were evaluated in the radial cross-field fluxes onto the non-divertor PFCs and in the poloidal fluxes onto the outer divertor. The results show that non-divertor fluxes are almost entirely ($\gtrsim$ 90%) due to He^{2+}, while the total ion flux onto the divertor is made approximately half by He^+ and half by He^{2+}. The reason for the increased He^+ ion fraction is found by analysing the effective production rate of He^+ ions, which is given by the difference between the ionization rates of He^+ and He^{2+} and it is localised in front of the strike points. The He^{2+}/He^+ flux fraction, moreover, influences the erosion of the PFCs. In the conditions of the considered experiment, where $T_e \simeq T_i \simeq 20$ eV in front of the outer divertor, the tungsten tiles can only be eroded by He^{2+} ions and the magnitude of the eroded flux is given by $f/(f+1)\,Y_{ph,W}(E_{wall,He^{2+}}, \theta) j_{sat}$, where f is the He^{2+} flux fraction $f = \Gamma_{He^{2+}/He_{tot}}$.

The results presented in this chapter represent a successful first step towards an integrated investigation of PMI experiments involving helium plasmas in W-wall tokamaks. After benchmarking at the locations where experimental data are available, density, temperature and velocity distributions are ready to be used as background plasma for erosion and impurity migration studies with the Monte Carlo code ERO2.0.

7 | Investigation of negative triangularity plasmas in TCV with SOLPS-ITER

Magnetic confinement equilibria with negative triangularity are considered an alternative for the operation of future power reactors since they may exhibit H-mode grade confinement in L-mode operation. Operation in L-mode is preferable since it would avoid the challenges related to the presence of edge localised modes (ELMs), the narrowing of the scrape-off layer widths and the requirement of density control.
The EUROfusion consortium is making efforts to study negative triangularity scenarios and to compare their properties to standard positive triangularity ones. In particular, understanding if and how the triangularity shape influences the development of plasma detachment is crucial for implementing this configuration in reactor-relevant conditions.

The work described in this chapter is thus devoted to extending the application of the SOLPS-ITER boundary plasma code to negative triangularity scenarios to investigate their detachment properties. The study aims at comparing how plasma detachment is reached in negative and positive triangularity discharges in TCV. Differently from the previous chapters of this thesis, this analysis considered a deuterium plasma, possibly including C impurities from the wall erosion. The work is supported by the EUROfusion WP-TE, within the research topic on negative triangularity as an alternative for the European DEMO.

7.1. Negative triangularity and detachment studies in TCV

The term triangularity in a tokamak refers to the shape of the separatrix on a poloidal plane. Considering a poloidal cross-section, distortions from symmetry with respect to a vertical plane passing through the magnetic axis define a non-null triangularity. If the distortion results in a triangular shape that points to the low field, the triangularity is conventionally defined as positive. If it points to the high-field side, the triangularity is negative. Examples of negative and positive triangularity configurations are shown in the right panels of figures 7.1 and 7.6, respectively. Today, most tokamaks operate in positive triangularity and so will do ITER. However, experimental observations on

TCV [126, 127] and DIII-D tokamaks [128, 129] showed that negative triangularity (NT) discharges may exhibit increased plasma confinement properties with respect to analogous positive triangularity (PT) discharges.
As discussed in section 1.3.2, fully detached conditions are required to ensure safe power exhaust and a steady state operation of a fusion reactor. If negative triangularity is to be considered as an alternative to the standard positive configurations for future power reactors, the investigation of the detachment in this configuration is crucial. Recent experimental studies in the TCV were thus performed in this direction. The outcomes seem to indicate that detachment is generally harder to reach in negative triangularity with respect to positive. In particular, the experiments on TCV have shown a lower outer target cooling and lower heat flux mitigation in density ramp experiments in NT with respect to PT. The analysis also indicates that for similar upstream conditions the outer divertor heat flux channel may be narrower and the divertor neutral pressure lower in NT [130, 131].

7.2. Modelling negative triangularity discharge with SOLPS-ITER

The simulations presented in this chapter aim to support the interpretation of the experimental observations discussed in section 7.1. In particular, we focused on understanding whether the observed differences are related to the shapes of the magnetic flux surfaces or if different cross-field transport properties should be assumed for the two configurations. The investigation exploits the SOLPS-ITER boundary plasma package to simulate plasma transport and detachment in two TCV discharges with positive and negative triangularity configurations. Extending the use of SOLSP-ITER to negative triangularity equilibria is an original outcome of this work. As done for AUG modelling presented in chapter 6, the simulations were performed using the simplified transport model which neglects drifts.

7.2.1. Global parameters, magnetic equilibrium and mesh reconstruction of the negative triangularity discharge

The TCV discharge used as a reference for the SOLSP-ITER simulations in negative triangularity (#67465) is an Ohmic discharge with a LSN configuration and forward magnetic field, with $B_\Phi = 1.4\,\mathrm{T}$. The triangularity is fixed around $\delta = -0.27$ and the plasma current is $I_p = -220\,\mathrm{kA}$. Figure 7.1 shows the time evolution of the line averaged electron density on the top-left of the figure, the poloidal cross-section of the

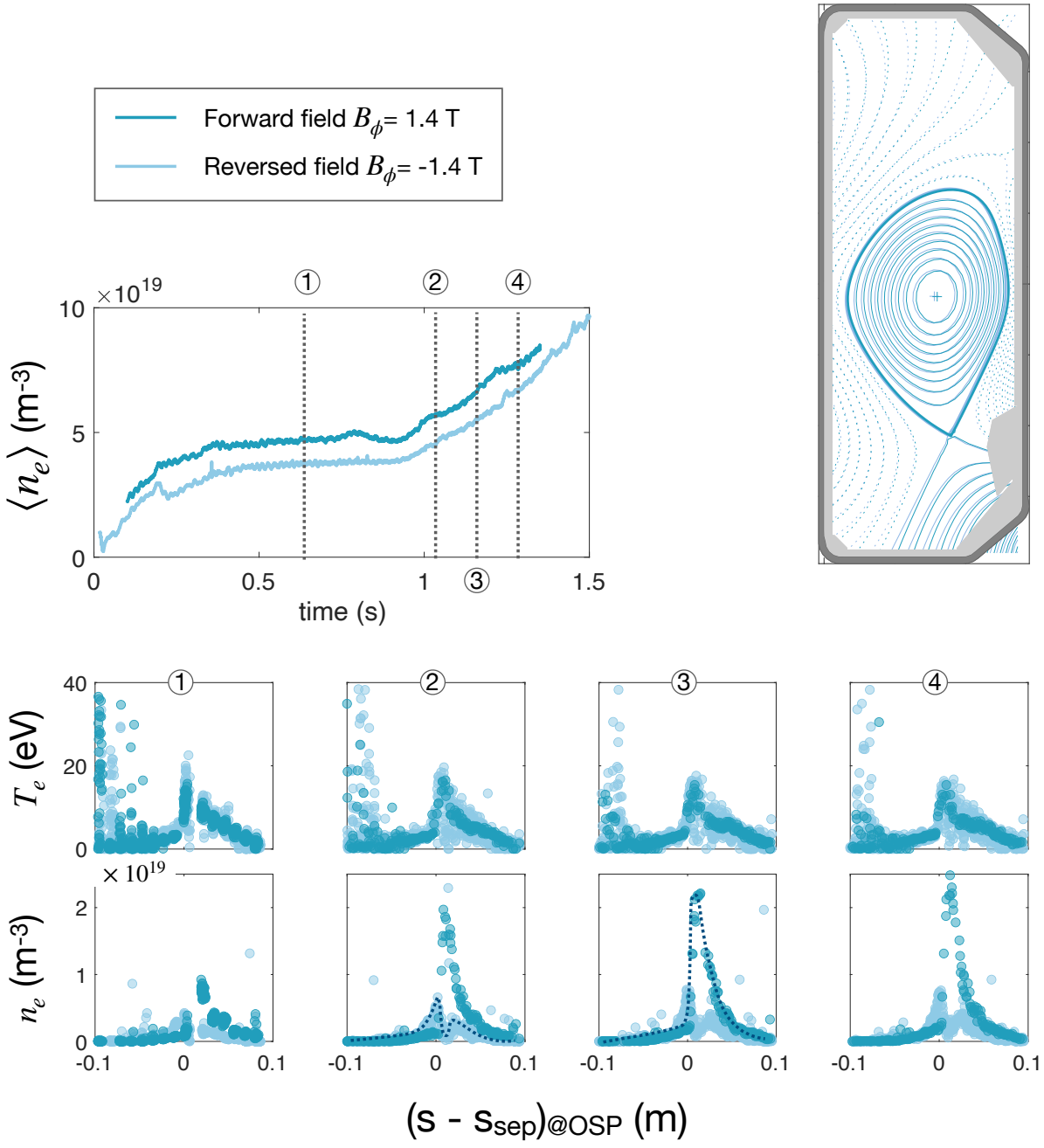

Figure 7.1: Line averaged electron density (top-left), magnetic equilibrium reconstruction (top-right) and electron temperature and density profiles at the OSP (bottom) of the reference TCV discharges in negative triangularity. The figure shows a comparison of a forward (B_ϕ = 1.4 T) and reversed magnetic field (B_ϕ = −1.4 T) discharges with the same global parameters.

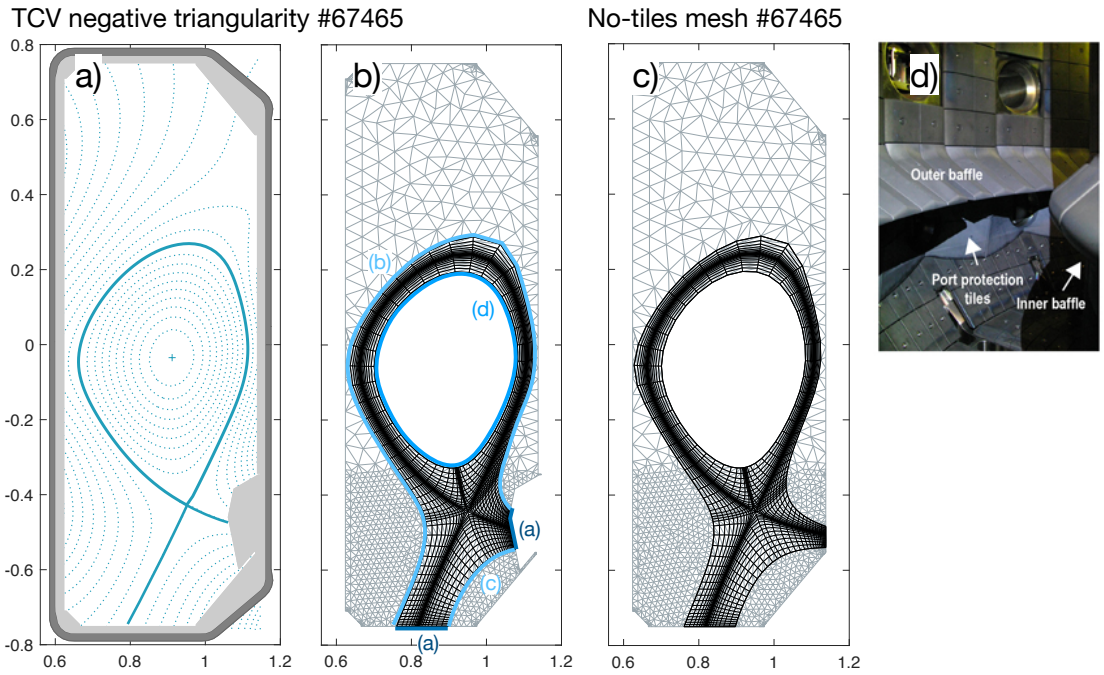

Figure 7.2: **a)** Magnetic equilibrium reconstruction of reference discharge #67465. **b)** SOLPS-ITER mash for the negative triangularity discharge, including axisymmetric port protection tile element. **c)** SOLPS-ITER mash for the negative triangularity discharge without port protection tile element. **d)** Picture of the lower part of TCV vessel showing TCV baffled configuration and the real shape of the port protection tile elements from [21].

magnetic equilibrium on the top-right and the electron temperature and density at the outer strike point, estimated by the in-vessel Langmuir probes on the bottom panels. Figure 7.1 also compares the forward field discharge with a reversed field discharge (#67070) with analogous global parameters. In particular, we should notice the difference in terms of the shape of the electron density profiles at the outer strike point. An approximated fit of the experimental data is shown with a dashed line in the two central figures. The different shapes of the n_e profiles for forward and reversed fields are related to the opposite direction of the ∇B-drift velocity in the two configurations, pointing upward and downward respectively. In section 7.2.3, we will discuss the origin of this difference in shape and the consequences of the choice of a simplified transport model, which neglects drifts, on the capabilities to discriminate this difference. Despite the difference in the n_e profile, however, the T_e profile at the OSP and its trend as a function of the increased $\langle n_e \rangle$ are very similar for both forward and reversed field configurations.

SOLPS-ITER has no particular limitations in building meshes with unconventional values of triangularity, as long as the equilibrium configuration belongs to the set of al-

lowed magnetic topologies (and the single-null surely does).
Providing the code with the magnetic reconstruction of the experimental equilibrium, shown in figure 7.2.a, the computational mesh displayed in figure 7.2.b was produced: B2.5 mesh is shown in black and has a resolution $n_x \times n_y = 84 \times 24$, while EIRENE neutral mesh is shown in grey.
In 2019, TCV underwent a major upgrade of the first wall structure. Modular and removable gas baffles were installed in the lower part of the chamber to increase the separation between the divertor and the plasma core [21]. In the low-field side (LFS) region, the installation was accompanied by additional port protection tiles that shadow the lower lateral ports from direct plasma exposure. Even in the configuration without baffles, which was used in the discharges of reference for these simulations, the port protection tiles are present on the LFS of the chamber. This modifies the cross-section of the first wall contour by including the grey structure shown figure 7.2.a in the region of the outer strike point. SOLPS-ITER mesh is built accordingly (figure 7.2.b). As shown in the picture in figure 7.2.d, however, the port protection tiles are not toroidally symmetric. EIRENE on the other hand assumes toroidal symmetry of the 2D poloidal profile of the vessel, provided as input to generate the mesh. To investigate the effects of the toroidal symmetry approximation done on the port protection tiles a simulation was performed with the mesh shown in figure 7.2.c, which neglects the presence of these structures and the OSP is located on a flat surface. Taking into account the full toroidal shape of these tiles can be particularly relevant for NT configurations since the OSP impacts on top of these structures.

7.2.2. Simulation setup and optimisation

After the geometry definition, the following steps were the simulation setup and the optimisation of boundary conditions and anomalous transport coefficients.
Pure deuterium plasma was considered for most of these studies, allowing for the minimum computational cost in terms of the number of species. Plasma-neutral interactions among D^+ ions, D atoms, D_2 molecules and D_2^+ molecular ions were considered in EIRENE database. The reaction rate coefficients of all the considered interaction processes are shown in figure 2.1. The impact of impurities sputtered from the graphite first wall of TCV and their transport within the plasma were considered performing two multispecies plasma simulations (D + C) at low ($n_{e,\mathrm{sep}} = 1 \times 10^{19}\,\mathrm{m}^{-3}$) and high ($n_{e,\mathrm{sep}} = 2 \times 10^{19}\,\mathrm{m}^{-3}$) density, respectively.
Figures 7.3.a, 7.3.b and 7.3.c show the results of the preliminary simulations aiming

at optimising boundary conditions and understanding the impact of carbon impurities. They represent the electron density and temperature profiles as a function of the radial distance from the separatrix at the outer midplane (OMP) and at the inner (ISP) and outer strike points (OSP).

Boundary conditions

Concerning EIRENE boundary conditions, particle and energy recycling coefficients are computed according to the TRIM database for deuterium ions and atoms on the carbon surface. These coefficients are then multiplied by a RECYCT = 0.99 to take into account unsaturated carbon surfaces and pumping. Differently from what was done for GyM (section 4.2.2) and AUG (section 6.2.2) simulations, where the pumping surfaces were localised, here RECYCT < 1 on the entire vessel surface.
In simulations including C impurities, physical sputtering yield Y_{ph} is calculated according to the Roth-Bohdansky formula [132] and a constant chemical sputtering yield equal to Y_{chem} = 3.5% is used, as done in previous simulations of TCV with SOLPS-ITER [133].
A feedback condition on the D_2 gas injection is also used. The puffing strength $\Gamma_{D_2,\text{puff}}$ is adjusted iteratively to match the separatrix electron density value at the OMP selected by the user. Most simulations described in this section used $n_{e,\text{sep@OMP}} = 1 \times 10^{19}\,\text{m}^{-3}$.

Referring to the different boundaries shown in figure 7.2.b, the BCs used to solve B2.5 equations in TCV simulations are the following:

(a) Divertor targets: sheath boundary conditions, for densities, temperatures, velocities and electrostatic potential.

(b) Far SOL: zero gradients of the parallel velocities, zero current for the potential equation and decay boundary condition for n_a, T_e and T_i with $\lambda_{\text{decay}} = 1$ cm.

(c) PFR: zero gradients of the parallel velocities, zero current for the potential equation and decay boundary condition for n_a, T_e and T_i with $\alpha_{\text{leak}} = 1 \times 10^{-3}$.

(d) Core: at the core boundary, we used zero parallel velocity gradient and zero current boundary conditions. Different density boundary conditions were analysed as discussed in the following. For electron and ion energy equations, we imposed the total power entering the edge region from the core. However, since the total power absorbed by the plasma is a quantity subjected to uncertainty, we evaluated the effect of a 20% error in $P_{\text{e/i,core}}$.

Dirichlet boundary condition (BCCON = 1) at the core mesh boundary is the easiest

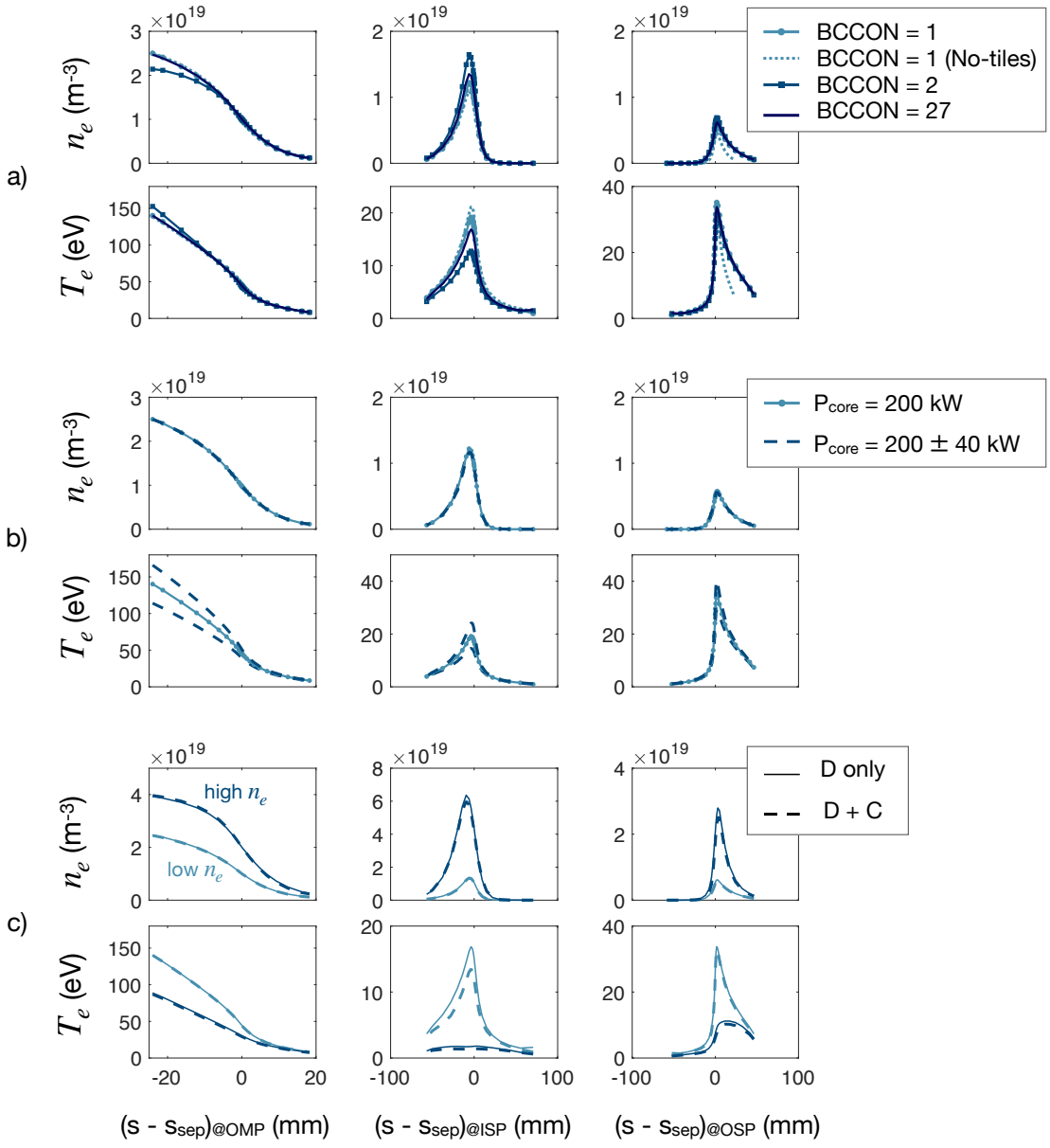

Figure 7.3: **a)** Effect of different core density boundary conditions. The dotted line shows the profiles obtained with BCCON = 1 and the mesh which neglects the port protection tiles (figure 7.2.c). **b)** Effect of different core temperature boundary conditions in terms of total power entering the edge plasma from the core. **c)** Effect of including carbon ions eroded from the wall into the simulations. n_e and T_e profiles as a function of the distance from the separatrix are shown at the outer-mid plane @OMP (left), inner strike point @ISP (centre) and outer-strike point @OSP (right) are shown.

choice to match the experimental radial profiles at the OMP. By comparison with the Thompson Scattering (TS) measurements, we set $(n_{D^+})_{core} = 2.5 \times 10^{19}\,m^{-3}$. This strategy, however, is not optimal to perform the modelling of the density ramp which will be described in section 7.3. For this reason, we also tried a Neumann boundary condition (BCCON = 2) imposing $(\partial_r n_e)_{core} = -1 \times 10^{20}\,m^{-4}$ and the feedback boundary condition on the total isonuclear species particle flux (BCCON = 27). As discussed in section 6.2.2, this latter BC imposes the value of the total (ion + neutrals) particle flux crossing the core boundary. For a deuterium plasma the condition reads $\Gamma_{core,B2.5,D^+} + \Gamma_{core,EIRENE,D_2} + \Gamma_{core,EIRENE,D} + \Gamma_{core,EIRENE,D_2^+} = 0$

Figure 7.3.a presents the B2.5 density boundary conditions analysis. The comparison of results obtained with different BCs shows that the three boundary conditions produce similar results. The value of $(\partial_r n_e)_{core}$, however, underestimates the magnitude of the density gradient at the core boundary. In the following, we will consider only Dirichlet and feedback boundary condition for density, thus the $(\partial_r n_e)_{core}$ was not further optimised.

Figure 7.3.a also shows (dotted line) the result of the simulation performed with the mesh that neglects the port protection tiles in the vessel structure (figure 7.2.c). The simulation was performed with Dirichlet density BC at the core boundary, i.e. $(n_{D^+})_{core} = 2.5 \times 10^{19}\,m^{-3}$. As one expects, the main difference with respect to the analogous simulation with the standard mesh is at the OSP. In particular, a sharper decrease in the density and temperature profiles is obtained. This is related to the fact that the SOL flux tube at the OSP is more narrow in the mesh of figure 7.2.c than the one of figure 7.2.b. If one plots the profiles at the OSP as a function of the mesh cell number, instead of the physical distance from the separatrix $s - s_{sep}$, then the two profiles are superimposed.

Results of the analysis of the electron and ion energy core boundary conditions are shown in figure 7.3.b. The experimental core power is computed as the difference between the Ohmic power and the power radiated from the core $P_{Ohm} - P_{rad} \approx 200\,kW$. To understand the impact that the experimental uncertainty of this value has on the simulation results, we performed three simulations with $P_{core} = 160 - 200 - 240$ kW. We also assumed that the effective core power is equally shared between electron and ion populations. Simulations are performed with Dirichlet BC at the core boundary, i.e. $(n_{D^+})_{core} = 2.5 \times 10^{19}\,m^{-3}$. The main differences in the three simulations are related to the temperature profiles, while n_e profiles are almost identical due to the Dirichlet boundary condition at the core. The temperature at the core boundary and its peak value at the strike points are directly proportional to the core power.

Anomalus transport coefficients

Differently from the analysis presented in section 6.2.2 for ASDEX-Upgrade simulations, for TCV it was possible to obtain good qualitative and quantitative agreement with the experimental data implying constant radial and poloidal profiles of D_n and $\chi_{e,i}$. A parametric scan similar to the one presented in section 6.2.2 was performed and eventually $D_n = 0.2\,\mathrm{m}^2/\mathrm{s}$ and $\chi_{e,i} = 1.0\,\mathrm{m}^2/\mathrm{s}$ were chosen. These values agree with anomalous transport coefficients used in other positive triangularity TCV simulations [133–135].

Carbon impurities

Finally, we evaluated the effect of carbon impurities eroded from TCV graphite first wall. To do so, we activated physical and chemical sputtering of the PFCs and we added carbon atoms (C) and ions (C^+, C^{2+}, C^{3+}, C^{4+}, C^{5+} and C^{6+}) to the plasma species. The carbon impurity effect was evaluated under two scenarios: low-density and high-density. Both used feedback density boundary condition at the core (BCCON = 27 and BCCON = 26 for the carbon ions), total power at the core boundary $P_{\mathrm{core}} = 200$ kW, $D_n = 0.2\,\mathrm{m}^2/\mathrm{s}$ and $\chi_{e,i} = 1.0\,\mathrm{m}^2/\mathrm{s}$. They differed on the feedback condition on gas puffing strength: the low-density case set the target electron density value at the separatrix@OMP to $n_{e,\mathrm{sep@OMP}} = 1 \times 10^{19}\,\mathrm{m}^{-3}$, while the high-density case used $n_{e,\mathrm{sep@OMP}} = 2 \times 10^{19}\,\mathrm{m}^{-3}$.
Figure 7.3.c compares the results of the four simulations: low and high-density scenarios with only deuterium (solid line) and activating sputtering and including carbon (dashed line). In general, the results including C impurities are very similar to the ones obtained including only D species, in terms of n_e and T_e profiles at the OMP and strike points. Slight differences in the T_e can be observed at the inner strike point for the low-density simulation: including C results in a reduction of the peak electron temperature of ≈ 3 eV.

Simulations including carbon, however, provide additional information related to impurities concentration and distribution. Figure 7.4 shows the density of the different carbon ion populations inside the plasma domain. Data refers to the high-density scenario. The comparison of the impurity concentration with spectroscopic diagnostic can provide an additional benchmark between the simulations and the experimental data. The total concentration of carbon ions (summed over all the charge states) is $\approx 2\%$ of the total ion ($D^+ + C^{n+}$) concentration in the SOL and reaches $\approx 5 - 7\%$ in the PFR. In the core plasma, the impurity concentration is $\lesssim 0.5\%$. Low-charge states (C^+, C^{2+} and C^{3+}) are mostly localised outside the separatrix in the lower part of the SOL (below the

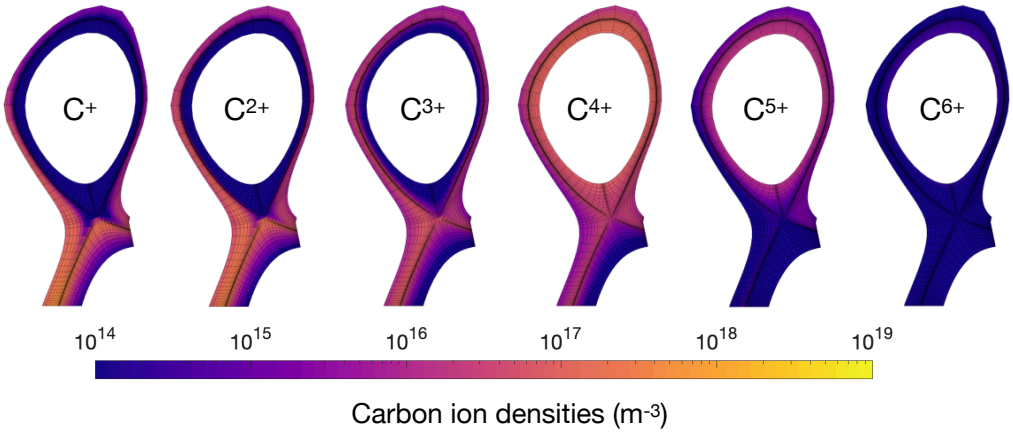

Figure 7.4: Density distribution of the carbon ion impurities in the plasma.

midplane), around the inner divertor leg and in the PFR. C^{+} and C^{2+} are the most abundant states. In the lower SOL, their concentration is $\approx$ 1% of the total ion concentration and in the PFR it is close to $\approx$ 5%. Higher charge states are present in the core region and in the upper SOL. The dominant high-charge impurity is C^{4+}. Its concentration is $\approx$ 1% in the upper SOL and $\approx$ 0.5% in the upper core region. C^{5+} is mostly localised in the upper SOL (above the outer mid-plane) and in the upper core and in these regions has a concentration $\lesssim$ 0.1%. C^{6+} has a concentration below $\lesssim 1 \times 10^{-5}$.

7.2.3. Benchmark with experimental data

The analysis presented in section 7.2.2 allowed us to understand the effects of the different code parameters and optimise the simulations to benchmark the experimental data. The experimental data for the benchmark are selected around $t_{\text{ref}} \simeq 0.7$ s, which corresponds to ① in figure 7.1. T_e and n_e profiles at the mid-plane are retrieved from the Thompson Scattering measurements, while the target profiles are estimated from the vessel Langmuir Probes.

The optimised simulation implied the plasma mesh including the port protection tiles (figure 7.2.b) and consider a pure D plasma without carbon impurities. Concerning BCs, it used the feedback boundary condition on the core particle flux (BCCON = 27) and a total core power P_{core} = 200 kW equally divided between electron and ion populations (BCENE = 8 and BCENI = 27). Constant anomalous transport coefficients were used, $D_n = 0.2\,\text{m}^2/\text{s}$ and $\chi_{e,i} = 1.0\,\text{m}^2/\text{s}$. The feedback condition on the gas puffing strength is also used, setting a target value for $n_{e,\text{sep@OMP}} = 1 \times 10^{19}\,\text{m}^{-3}$.

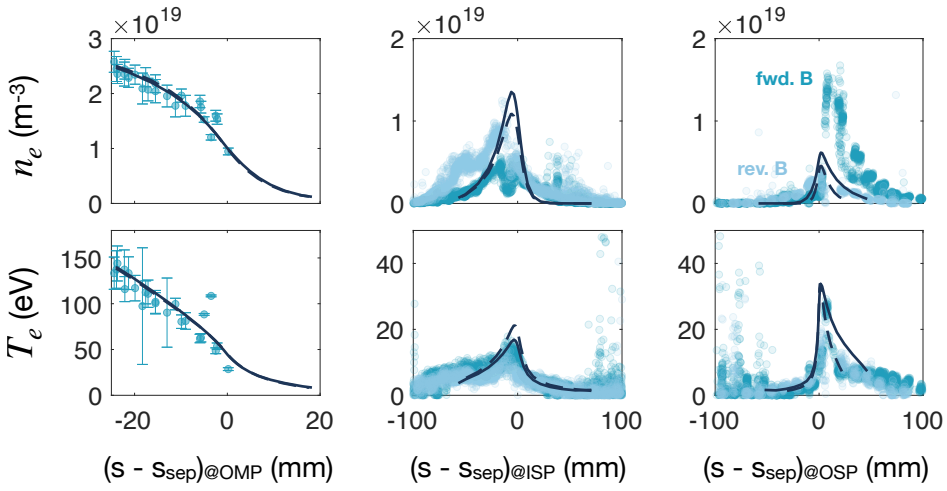

Figure 7.5: Benchmark between the experimental n_e and T_e radial profiles and SOLPS-ITER simulations of negative triangularity configurations. The dashed line shows the results obtained with the No-tile mesh (figure 7.2.c). The benchmark is done with Thompson Scattering data at the OMP (left), and Langmuir probes data at the ISP (centre) and OSP (right).

The simulated electron density and temperature profiles at the OMP and strike points are shown in figure 7.5 (solid lines) and compared with experimental data (dots). Globally, a qualitative and quantitative agreement can be observed. In particular, at the OMP, the selected combination of boundary conditions and anomalous diffusion coefficients is able to quantitatively and qualitatively recover many of the experimental features, such as the shape of density and temperature profiles, the n_e and T_e values at the core boundary. Only the electron temperature at the separatrix is slightly overestimated if compared to TS data.

The electron density profile at the strike points is the quantity for which the simulations are less close to the experimental data. The discrepancy between simulations and experiments is largely due to the absence of the effect of the drift in the SOLPS-ITER transport model implied to perform these simulations. As highlighted in section 6.2.2, the direction of the ∇B-drift velocity affects the shape of the strike points n_e profiles, as showed by the comparison of forward and reversed field data in figure 7.1. For further interpretation of the density profiles and to improve the agreement with the experimental profiles, thus, SOLPS-ITER simulations including drifts should be performed. For this reason, most of the conclusions that will be drawn in the following will be based on the T_e profile at the OSP. Temperature profiles, indeed, match well the LP estimate at both strike points.

As discussed in section 7.2.1 the port protection tiles in correspondence with the OSP are not toroidally symmetric and the LPs used to estimate n_e and T_e profiles are installed on top of those tiles. To further investigate the impact of the hypothesis of toroidal symmetry of the PFCs implied by SOLPS, the dashed line in figure 7.5 shows the profiles obtained with the mesh which excludes the port protection tiles (figure 7.2.c). This simulation is performed with the same setup used for the reference simulation (solid line), except for the density boundary condition at the core which is a Dirichlet condition (BCCON=1) with $(n_{D^+})_{core} = 2.5 \times 10^{19}\,m^{-3}$. The differences between solid and dashed lines at the ISP are only related to the different choices for the density boundary conditions at the core boundary. At the OSP, instead, the comparison highlights that the longer outer divertor leg, corresponding to the mesh without the target protection tiles, results in a narrower T_e peak. This simulated profile seems to better reproduce the experimental one. The peak value of T_e at the strike point, on the contrary, is not affected by the different meshes.

7.2.4. Comparison with a positive triangularity discharge

Once the NT simulation was benchmarked with experimental data, we investigated the differences with respect to a similar discharge with positive triangularity. The strategy adopted to perform the PT simulation was to keep the same setup parameters used for the benchmark of the NT simulation with experimental data and only exchange the NT plasma mesh with the one built on the PT equilibrium, as discussed in section 7.2.3. By keeping the same boundary conditions and anomalous transport coefficients, the aim of this study is to isolate the differences related to a different shape of the magnetic topology.

As a reference for the positive triangularity analysis, we used a TCV discharge (#67467) with very similar parameters as the negative triangularity one. Again it is an Ohmic LSN discharge with forward field $B_\phi = 1.4$ T and plasma current $I_p = -220$ kA. The triangularity is now positive but with a similar absolute value $\delta = 0.27$. Figure 7.6 shows the time evolution of the line averaged electron density $\langle n_e \rangle$ (top-left), the magnetic equilibrium plotted on a poloidal cross-section (top-right) and the outer strike point T_e and n_e estimated once more by the in-vessel Langmuir probes (bottom). In this case, we consider only the forward $\vec{B}$ field configuration.
The plasma mesh is built on the magnetic equilibrium reconstruction at $t_{ref} = 0.8$ s. The shape of the PT equilibrium on the poloidal plane is shown in figure 7.7.a and the SOLPS-ITER mesh is shown in figure 7.7.b. The resolution of the B2.5 mesh (black) is

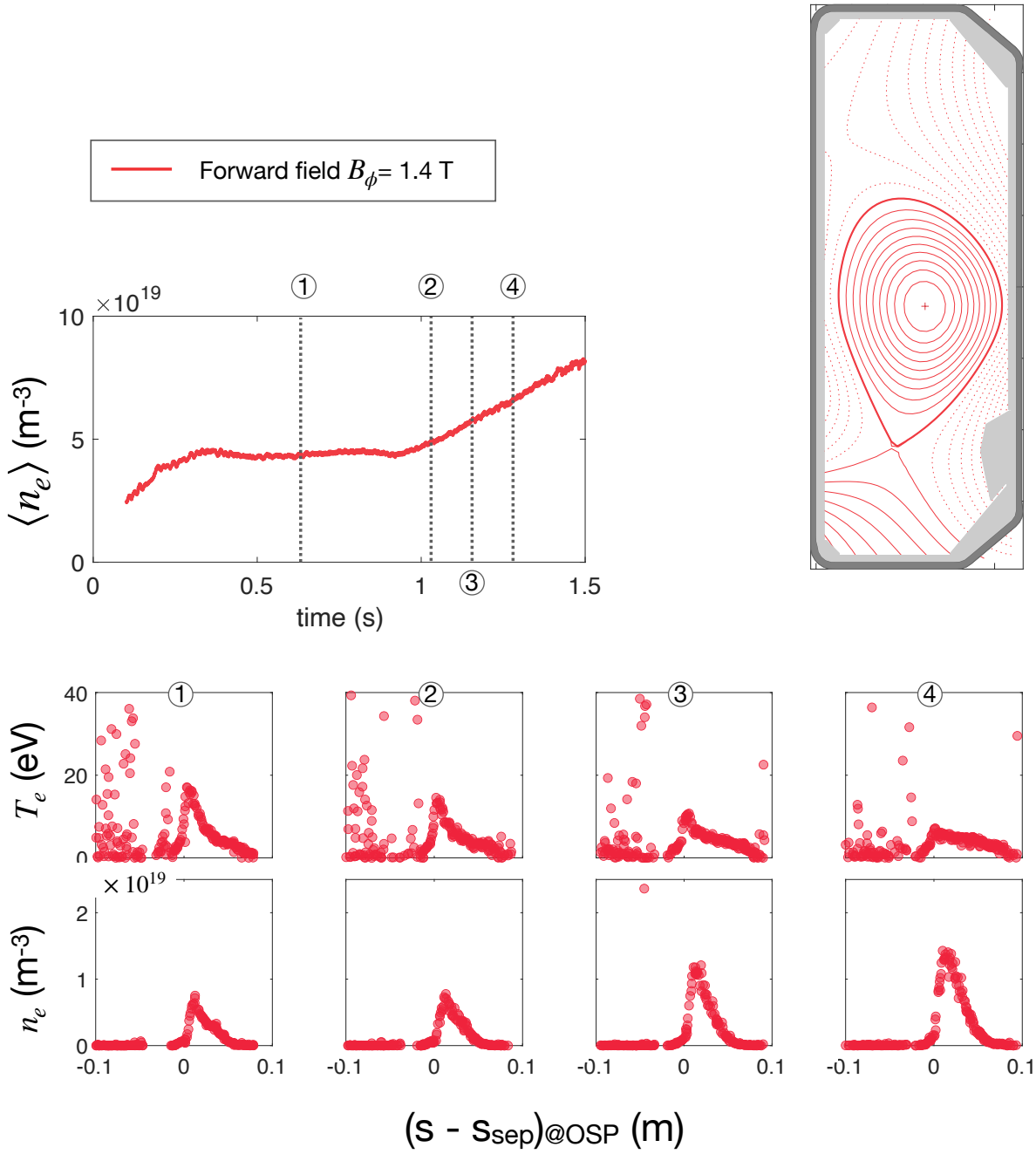

Figure 7.6: Line averaged electron density (top), electron temperature and density profiles at the OSP (bottom) and magnetic equilibrium reconstruction (right) of the reference TCV discharges in positive triangularity. The figure shows a comparison of forward (B_ϕ = 1.4 T) and reversed magnetic field (B_ϕ = −1.4 T) discharges with the same global parameters.

the same which was used for the NT simulations, $n_x \times n_y = 84 \times 24$. EIRENE triangular mesh is plotted in grey.

The results of the SOLPS-ITER simulation with PT are shown in figure 7.8 and compared with the corresponding experimental data. As for the NT benchmark, we reported the electron density and temperature profiles at the OMP and strike points and we used experimental data from TS and LPs, respectively. Despite the simulation setup being optimised for negative triangularity, the comparison of the simulated profiles shows remarkably good agreement with the experimental data for PT. In particular, the simulated density profiles at the strike points, which showed discrepancies with respect to LP measurements for NT configuration, almost perfectly match the experiments in PT. This could be a sign of a lower influence of drift velocities in positive triangularity with respect to the negative one. Unfortunately, the reversed $\vec{B}$ field discharge has no vessel LP data available to compare. SOLPS-ITER simulations with drifts activated could provide more information on the density profiles at the strike points.

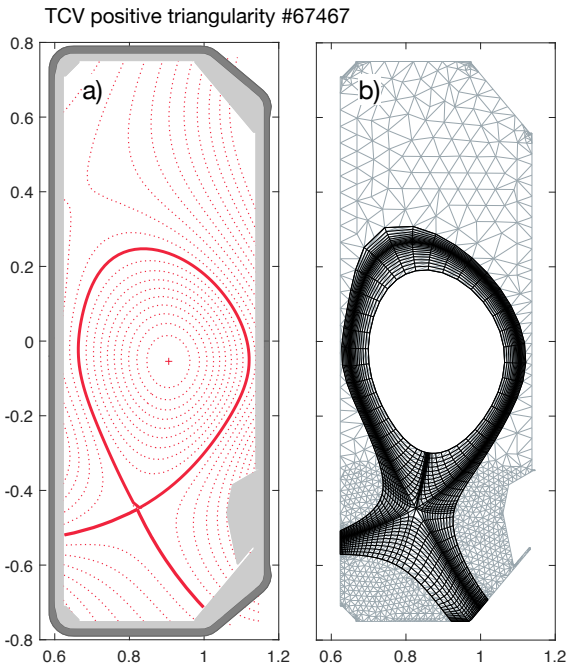

Figure 7.7: **a)** Magnetic configuration and **b)** SOLPS-ITER mash for the positive triangularity discharge.

The second aspect that can be noted is that assuming the same density and heat anomalous transport as of NT, in PT electron temperature is globally overestimated by SOLPS. At the core boundary and at the strike points the difference between simulation and experiments is $\approx 10 - 15$ eV. By increasing the anomalous heat conductivities $\kappa_{e,\perp}$ and $\kappa_{i,\perp}$ the benchmark is improved at the core boundary but the overestimation is maintained at the strike points.

Finally, we compare NT and PT simulations. The outer midplane profiles in NT and PT are similar. However, although both simulations use $D_n = 0.2\,\mathrm{m}^2/\mathrm{s}$ the density profile in PT is slightly less steep and results in lower radial particle flux. This can be observed in the lower red and blue curves in figure 7.9, where the density and radial particle flux profiles at the OMP are shown for $n_{e,\mathrm{sep@OMP}} = 1 \times 10^{19}\,\mathrm{m}^{-3}$.

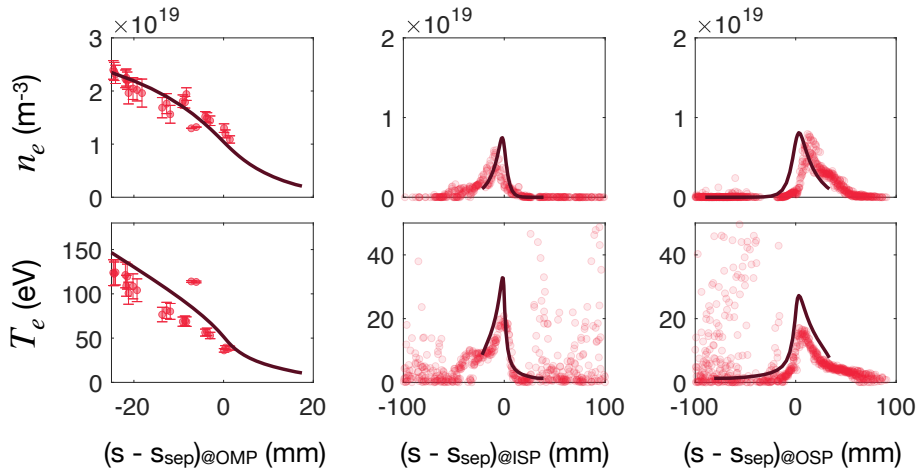

Figure 7.8: Benchmark between the experimental n_e and T_e radial profiles and SOLPS-ITER simulations of positive triangularity configurations. The benchmark is done with Thompson Scattering data at the OSP (left), and Langmuir probes data at the ISP (centre) and OSP (right).

Concerning electron temperature at the strike points, we observe that SOLPS-ITER simulations predict that at the ISP the peak electron temperature is higher for the PT simulation $T_{e,\text{max@ISP,PT}} > T_{e,\text{max@ISP,NT}}$ while at the OSP it is higher for NT one $T_{e,\text{max@OSP,PT}} < T_{e,\text{max@OSP,NT}}$. This trend is also observed experimentally, although $T_{e,\text{max,PT}}$ is overestimated by simulations both at the ISP and OSP, as discussed previously in this section. As already discussed, for further analysis of the electron density profiles at the strike points drifts fluxes should be included in the SOLPS-ITER model. Another interesting comment can be done regarding the width of the electron temperature peak at the OSP. If we consider simulation with the plasma mesh without port protection tiles (figure 7.2.c), simulations reproduce the experimental observation of a narrower heat flux tube in NT, which results in a narrower T_e peak at the OSP with respect to PT. On the contrary, a wider T_e peak in NT is obtained using the mesh with toroidally symmetric tiles. As discussed in section 7.2.3, this once again highlights that the toroidal symmetry approximation can have a role in determining the correct plasma profiles at the OSP for the NT simulation.

In conclusion, both simulations and experiments seem to indicate that in discharges with NT equilibrium, plasma is more detached at the ISP and more attached at the OSP if compared to PT discharges with similar upstream conditions. Concerning PFC erosion and comparing NT and PT discharges, a higher sputtering yield is expected for NT at the OSP and for PT at the ISP. However, the eroded flux also depends on the incident ion flux, thus on the ion density in front of the divertor. A more detailed analysis should be hence performed with drifts activated.

7.3. Density ramp simulations

All the simulations presented in section 7.2 aimed at reproducing the reference experimental conditions during the low-density flattop indicated with ① in figures 7.1 and 7.6 for negative and positive triangularities, respectively. With the work presented in this section, instead, we aimed at investigating the plasma conditions during the density ramp, corresponding to points ②, ③ and ④ in the same figures. The aim of this analysis was the examination of how positive and negative triangularity scenarios with similar parameters evolve towards the outer strike point detachment.

In this work, the density ramp was modelled with SOLPS-ITER following two different strategies: (i) by increasing electron density at the separatrix $n_{e,\text{sep@OMP}}$ through the feedback condition on D_2 puffing at constant anomalous diffusion coefficients (section 7.3.1) and (ii) by reducing the anomalous particle diffusion coefficient D_n at constant $n_{e,\text{sep@OMP}}$ (section 7.3.2). The analysis (i) at increasing $n_{e,\text{sep@OMP}}$ is performed for both positive and negative triangularity.

7.3.1. Density ramp modelling by increasing $n_{e,\text{sep@OMP}}$

This section describes modelling a density ramp with SOLPS-ITER at constant anomalous diffusion. Starting from the reference setup for NT and PT configurations described in section 7.2.3 and 7.2.4, we repeated the simulation only varying $n_{e,\text{sep@OMP}}$ in the range $0.75-2.0\times10^{19}\,\text{m}^{-3}$. All the other parameters related to anomalous transport and boundary conditions were kept fixed. This method allows isolating the effects of the density increase in negative and positive triangularity if the only difference between the two configurations is a different shape of the magnetic flux surfaces. In doing so, we assumed that the density ramp, i.e. the increase in $\langle n_e \rangle$, is directly related to the increase of the density at the separatrix $n_{e,\text{sep@OMP}}$. We compared SOLPS-ITER simulation results at increasing $n_{e,\text{sep@OMP}}$ with experimental data referring to subsequent instants during the density ramp. In this way, we investigated whether the different magnetic shapes alone can be responsible for the differences between PT and NT discussed in section 7.1 or if additional assumptions of a different behaviour with respect to cross-field transport should be considered.

Figure 7.10 shows the simulated radial profiles (solid lines) of electron density and temperature at the OMP and OSP for $1.0-1.25-1.5-1.75-2.0\times10^{19}\,\text{m}^{-3}$ compared to experimental profiles (dots) taken at different times along the density ramp. Darker

colours mean higher density. The global agreement between simulations and experiments is good for both NT and PT density scan simulations. In particular, the simulated values of $(n_e)_{@\mathrm{OMP}}$ at the core boundary are within the experimental error both in NT and PT. For higher $n_{e,\mathrm{sep@OMP}}$, the simulated profiles in the core region ($s - s_{\mathrm{sep}} < 0$), however, overestimate n_e in PT.

The density profiles at the OMP for NT and PT are compared in a single graph in figure 7.9 (top). The bottom panel of figure 7.9, instead, compares the radial cross-field ion fluxes[1]. In absence of drifts, cross-field fluxes are only due to anomalous diffusion, as shown by equation (5.17) in section 5.1.3. Despite all simulations having the same diffusion coefficient $D_\perp = 0.2\,\mathrm{m}^2/\mathrm{s}^{-1}$, negative triangularity simulations produce systematically higher cross-field fluxes close to the separatrix and thus higher (in modulus) electron density gradients. The presence of steeper density gradients in the edge plasma seems to be confirmed by experimental data. Figure 7.11.a shows the line averaged electron density $\langle n_e \rangle$ as a function of the separatrix electron density $n_{e,\mathrm{sep@OMP}}$ in the negative (both forward and reversed field discharges) and positive triangularities (forward field). We can observe that $\langle n_e \rangle$ is generally higher in NT and it is higher for lower $n_{e,\mathrm{sep@OMP}}$, which means that stronger gradients in the plasma edge should exist so that higher core densities can be reached. We also observe that the maximum $n_{e,\mathrm{sep@OMP}}$ in NT is limited to lower values with respect to PT.

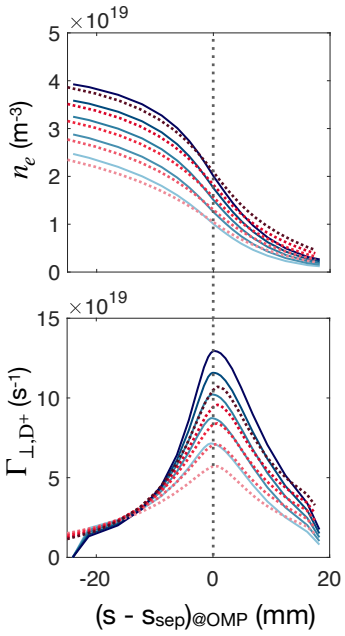

Figure 7.9: Comparison of OMP electron density (top) and D^+ cross-field flux profiles (bottom) in density scan NT (solid blue) and PT (dotted red).

Moving to the analysis of T_e profiles at the OMP, from figure 7.10 we can observe that NT simulations tend to underestimate T_e at higher densities, while PT simulations overestimate T_e at lower densities. Both NT and PT simulations, moreover, overestimate the electron temperature at the separatrix with respect to experiments.

At the outer strike point, both NT and PT simulations predict an increase in the n_e peak value and a reduction of the T_e peak at increasing density. Experimentally, however,

[1] In absence of radial currents, $\Gamma_{\perp,D^+} = \Gamma_{\perp,e}$

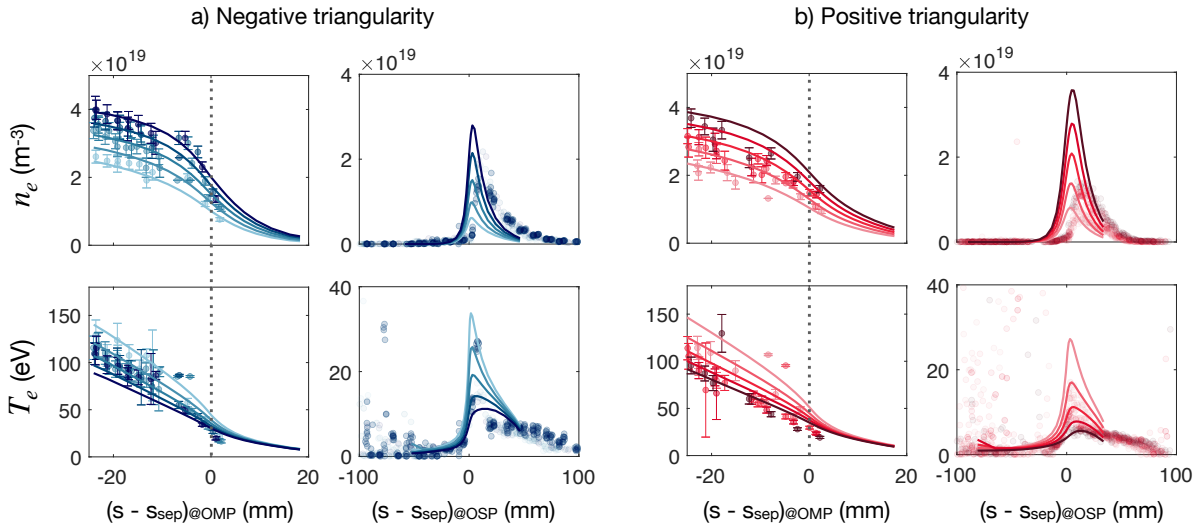

Figure 7.10: Density ramp simulations with **a)** negative and **b)** positive triangularity configurations and benchmark with experimental data collected at different times during the density ramp. Outer midplane (first column) and outer strike-point (second column) profiles are reported.

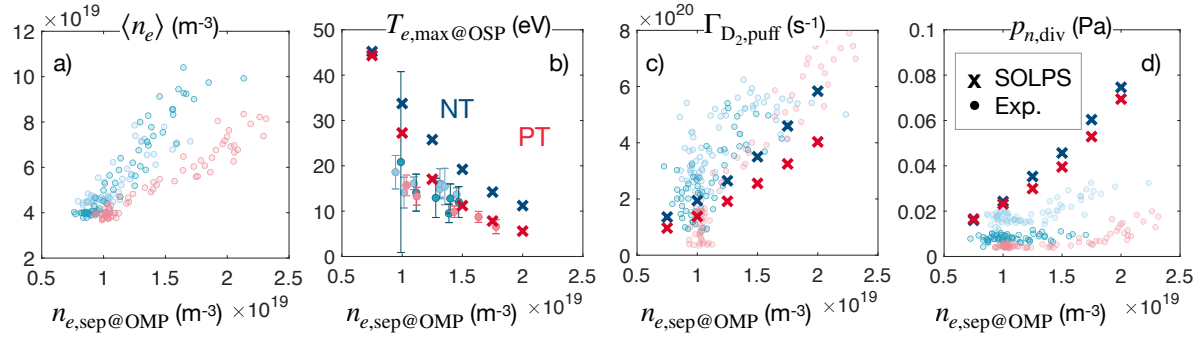

Figure 7.11: Analysis of detachment from density ramp simulations with negative and positive triangularity configurations. **a)** Line averaged electron density, **b)** peak electron temperature at the OMP, **c)** D_2 gas puffing strength and **d)** divertor gas pressure as a function of the separatrix electron density.

this is only observed for positive triangularity. For NT, both n_e and T_e peaks remain almost constant through the density ramp. Quantitatively, simulations tend to underestimate the experimental n_e at the OSP for low density and overestimate it at high density. The T_e peak value at the OSP as a function of $n_{e,\text{sep@OMP}}$ is shown in figure 7.11.b. The general experimental trend for which the peak temperature at the outer strike point is higher in NT with respect to PT is reproduced by simulations. However, NT simulations overestimate a factor of ≈ 2 the peak temperature value and of a factor ≈ 4 its decrease as a function of the separatrix density, with respect to experiments. We also notice that, as observed earlier, the experimental $n_{e,\text{sep@OMP}}$ in NT is limited to $\approx 1.5 \times 10^{19}\,\text{m}^{-3}$, despite a globally higher $\langle n_e \rangle$ (with respect to PT). In PT, instead, despite the overestimation of $T_{e,\text{max@OSP}}$ for the lowest densities, at $n_{e,\text{sep@OMP}} \gtrsim 1.25 \times 10^{19}\,\text{m}^{-3}$ simulations match well the temperature detachment trend: both the decreasing trend and the absolute value of $T_{e,\text{max@OSP}}$.
Figures 7.11.c and 7.11.d show the trends of D_2 gas puffing strength and the divertor gas pressure as a function of $n_{e,\text{sep@OMP}}$. Simulations recover the correct ordering between negative and positive triangularity results: both puffing and pressure are higher for NT. The puffing strength is quantitatively well estimated by the simulations[2], while the divertor pressure is overestimated with respect to experimental one of a factor $\approx 2-3$. This discrepancy was observed in previous SOLPS-ITER simulations of TCV [134, 135]. We observed, however, that including C impurities can reduce the discrepancy. In the simulation with $n_{e,\text{sep@OMP}} = 2 \times 10^{19}\,\text{m}^{-3}$ including C impurities estimates $p_{n,\text{div}} \approx 0.06$ Pa.

7.3.2. Density ramp modelling by decreasing D_n

As discussed in section 7.3.1, the density ramp simulations at increasing $n_{e,\text{sep@OMP}}$ and constant anomalous particle diffusion D_n overestimate the temperature detachment at the OSP for NT, while producing a good agreement with the experimental findings for PT. To further investigate this different detachment behaviour a second modelling approach for the density ramp was also implemented for the negative triangularity case.
This section thus discusses the modelling of the density ramp in NT by reducing the value anomalous ion diffusion coefficient D_n at constant $n_{e,\text{sep@OMP}}$. This preliminary study assesses the effect of a constant reduction of the anomalous diffusion coefficients. The global value of D_n varied, but its profiles (poloidal and radial) are kept

[2]We recall that the simulations were performed with the feedback scheme for the gas puffing, thus making this quantity an outcome of the simulation rather than an input.

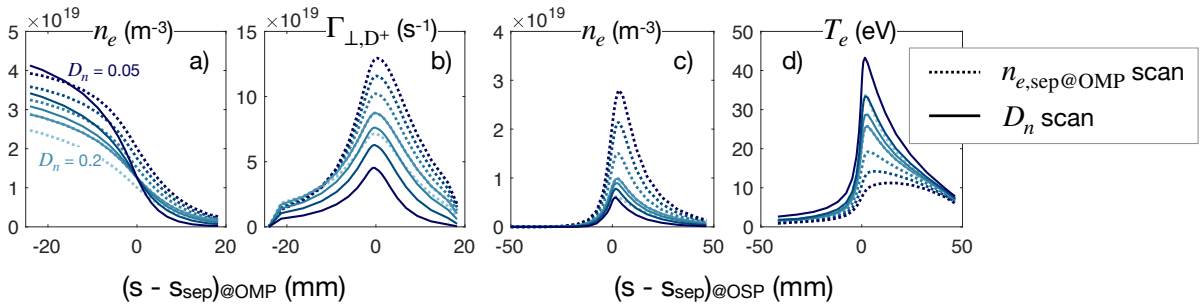

Figure 7.12: Density ramp modelling strategies at increasing $n_{e,\text{sep@OMP}}$ (dotted) and at decreasing D_n (solid). **a)** Electron density and **b)** ion cross-field flux at the outer midplane and **c)** electron density and **d)** temperature at the outer strike point.

constant. The simulations are performed with the reference inputs described in section 7.2.3 in terms of mesh and boundary conditions. The feedback condition on the D_2 puffing strength fixed the value of $n_{e,\text{sep@OMP}} = 1.25 \times 10^{19}\,\text{m}^{-3}$. This value is chosen to be in the range of the experimentally obtained values for $n_{e,\text{sep@OMP}}$. The particle diffusion coefficient is decreased in the range $0.2 - 0.05\,\text{m}^2/\text{s}^{-1}$.

Results of the simulations at decreasing D_n are shown in figure 7.12 with solid lines and compared to the simulations at constant D_n and increasing $n_{e,\text{sep@OMP}}$ (dotted lines). The darker the solid line, the lower the corresponding D_n. We observe that by decreasing D_n at constant $n_{e,\text{sep@OMP}}$, we were able to reproduce the foreseen density-ramp behaviour, i.e. an increase in the core electron density at the outer midplane. Moreover, this second modelling strategy of the density ramp suppresses detachment at the OSP, producing behaviour that is more similar to what is observed experimentally for NT discharges. Indeed, by decreasing D_n we obtained higher core density and higher peak temperature at the OSP. The opposite trend was instead found by increasing, i.e. higher core density corresponded to lower $T_{e,\text{sep@OSP}}$.

7.4. Conclusions

In this chapter, we presented the first analysis of boundary plasma transport in negative triangularity performed with SOLPS-ITER. The study was done in the context of the EUROfusion WP-TE research topic on the investigation of negative triangularity as an alternative configuration for the European DEMO power plant. The main focus of this work has been the support of experimental detachment investigation in negative triangularity L-mode Ohmic TCV discharges, performing interpretative modelling with the SOLPS-ITER boundary plasma code package.

This work showed that the SOLPS-ITER code is able to perform simulations of negative triangularity single null configurations producing results that are in good agreement with the experimental data. Even though we used a simplified transport model which neglects drifts, outer midplane n_e and T_e profiles and T_e profiles at the strike points quantitatively and qualitatively match the experimental data from TS and LPs. Comparing experimental plasma profiles of forward and reversed field discharges, we concluded that to have a better understanding and interpretation of the strike points n_e profiles the model including drift velocities contributions is required. The effect of carbon impurities sputtered from the PFCs was also evaluated and since only marginally modified the results of interest, it was neglected in the subsequent analyses.
The NT magnetic equilibrium of the reference discharge is such that the outer strike point is located on the recently installed TCV port protection tiles. These elements are not toroidally symmetric and thus their correct 3D geometry can not be simulated with the standard toroidal-symmetry approximation implied in SOLPS-ITER. To evaluate the consequence of SOLPS approximation, we performed simulations with toroidally-symmetric tiles and with a straight wall boundary without the tiles. The two geometries differ from each other in the length and flux expansion of the outer divertor leg. The increase of the leg length resulted in a narrowing of the SOL flux tubes at the plasma-wall interface and a consequent reduction of the OSP electron temperature peak width. The reduction in width was not accompanied, however, by an increase in the peak value.

The NT discharge was then compared to a PT one with similar parameters. The NT-PT comparative simulation was performed by using two different plasma meshes, with the same resolution but built on the NT and PT magnetic equilibrium reconstructions, respectively. All the others code parameters (boundary conditions, plasma-neutral interaction model and anomalous transport coefficients) were kept fixed. Results of the comparative simulations show that some of the differences between NT and PT discharges which were observed in experiments can be recovered only by assuming different shapes of the magnetic flux surfaces. In particular, we find that T_e at the OSP is higher in NT with respect to PT and the heat flux channel between OMP and OSP is wider in PT.

Preliminary studies of plasma detachment were performed both in negative and positive triangularity configurations. Density ramp experiments were first simulated assuming that the increase of the line averaged plasma density $\langle n_e \rangle$ corresponds to an increase of the density at the separatrix $n_{e,\text{sep@OMP}}$. We perform a series of SOLPS-ITER simulations (in NT and PT) by increasing $n_{e,\text{sep@OMP}}$ in the range $0.75 - 2.0 \times 10^{19}\,\text{m}^{-3}$. This study keeps anomalous diffusion constant and thus isolates the effects of the

$n_{e,\text{sep@OMP}}$ increase with different magnetic flux surface shapes. Results of the simulations show that some of the features observed experimentally are reproduced. In particular, NT OSP electron temperature is higher than the PT one, for every value of $n_{e,\text{sep@OMP}}$. The experimental trend of temperature detachment in PT is also well reproduced. However, NT simulations overestimate the decrease of $T_{e,\text{max@OMP}}$ at increasing $n_{e,\text{sep@OMP}}$. This results in an overestimation of plasma detachment in NT.
The second strategy used to model the density ramp was to fix $n_{e,\text{sep@OMP}}$ and artificially decrease the cross-field diffusion of particles by reducing the D_n coefficient. With this method, OSP detachment is completely suppressed for NT the configuration according to SOLPS-ITER results.
In conclusion, the experimental observations on NT reduced detachment made in TCV are compatible with the assumption of a limitation of the $n_{e,\text{sep@OMP,NT}} \lesssim 1.5 \times 10^{19}\,\text{m}^{-3}$ (lower with respect to analogous PT conditions). The increase of the line averaged plasma density at fixed edge density could be achieved by suppression of cross-field transport.

Conclusions and perspectives

This doctoral thesis is well-integrated into the international context of the research on nuclear fusion and touches on several topics among the current priorities of edge plasma investigation. In particular: (i) it focused on the modelling of linear plasma devices, which are largely used for plasma-material interaction studies and as material-testing facilities for plasma-facing components; (ii) improved the numerical investigation of helium plasmas, focusing on plasma-neutral interaction databases and the reconstruction of helium plasma background for the modelling of PMI experiments in tokamaks and LPDs; (iii) it presents the first analysis on plasma detachment modelling in negative triangularity tokamaks.

The main conclusions of the work can be summarised as follows, together with the perspectives for future developments.

Advance and improve the available modelling tools for linear plasma devices: SOLPS-ITER is the state-of-the-art code package used to investigate edge plasma in tokamaks and that was implied to design the ITER divertor. The physical model includes the transport of the plasma ions and electrons along and across the magnetic flux surfaces, the physics of plasma-neutrals interaction and plasma recycling. Within the thesis work, we proved the possibility to exploit this code to describe the plasma inside a linear plasma device and then use the plasma background for global and local PMI modelling in LPDs.
We developed a set of Matlab-based scripts to produce the field-aligned plasma mesh, consistent with the geometry and the magnetic field of the GyM linear plasma device of ISTP-CNR. We performed a benchmark of the SOLPS-ITER modelling with GyM experimental data and we used the plasma background to perform the first global modelling of the erosion of the GyM vacuum chamber during plasma operation. This study was performed for a helium plasma background, investigating the erosion of different wall materials and the effect of negative bias applied to the wall.
An interesting development of this work would be to perform more realistic simulations of a PMI experiment in GyM LPD by implying the new extended grid version of the

SOLPS-ITER package. This would allow for the possibility to include the sample-holder geometry within the plasma column. An analysis of how the sample holder influences the plasma background could be performed and compared with experiments. Moreover, erosion and impurity migration modelling would then allow for the description of the realistic experimental geometry in which PMI experiments are performed in GyM.

The simple cylindrical geometry of a LPD was also used as a testbed for the benchmark of the mean-field diffusive and turbulent cross-field transport models. A detailed comparison of the equations implemented in the 2D SOLPS-ITER and 3D GBS numerical codes was performed and the two codes were used to model the plasma transport in the GyM linear device.
This work highlighted the role of gradients in the symmetry direction $\partial_\phi(\cdot)$ in producing additional radial fluxes. These gradients are neglected because of the symmetry hypothesis made by 2D models and, although derived for the linear geometry, this conclusion is valid also for tokamaks.
A possible further development could be the investigation of the magnitude of the additional cross-field contributions related to $\partial_\phi(\cdot)$ in typical tokamak conditions, to understand if they are compatible with typical anomalous contributions. Additionally, one could then assess if an improved description of radial cross-field transport could be obtained by including the 3D contributions within the mean-field approximation, thus still avoiding the computational cost connected to the resolution of the turbulent temporal time scales.

Improve and develop modelling tools for helium plasmas in LPDs and tokamaks: Tokamak operation in helium plasma and the consequent interaction between helium ions and the wall materials are crucial aspects to be further investigated in preparation for the ITER Pre-Fusion Operation Phases. This thesis work contributed to advancing the modelling activities in this direction, focusing both on the PMI modelling in LPDs and boundary plasma tokamaks.
The SOLPS-ITER database of plasma-neutral interaction processes for helium was expanded, including charge exchange and excitation of He atoms. These processes were proven to be particularly important in a low-temperature mildly ionized plasma as the one produced in the GyM machine. Moreover, the influence of these processes on the plasma background also had consequences in determining the global erosion of the device chamber.
The role of atomic processes in low-temperature plasma was also examined thanks to the development of an original 0D global model. This tool was benchmarked against

SOLPS-ITER simulations showing a remarkably good agreement in both reproducing the qualitative trends and the quantitative results. Moreover, with the 0D model, it was possible to investigate the global effect of metastable helium atoms, explicitly considering the additional particle population. A direct development of this work would be the inclusion of $He^{1(2s)}$ and $He^{3(2s)}$ populations in the EIRENE model to address the possibility of local effects connected to the transport of the metastables.

SOLPS-ITER was also implied to reconstruct the helium plasma background of an ASDEX-Upgrade discharge. The work presented in this thesis focused on the investigation of an attached L-mode discharge. The outcomes of our modelling allow retrieving the relative fraction of He^{+} and He^{2+} ions in the total ion flux collected by the divertor probes. This parameter is crucial to correctly assess the erosion properties since the ion impact energy at the wall depends on the ion charge, however, it is not easily estimated from experimental measurements.
In the future, the database of helium simulations should be further expanded by investigating different operational conditions. Experimental discharges in helium, in fact, were performed in ASDEX-Upgrade under L and H-mode conditions with attached and detached plasmas. In the context of analysing the PFC erosion, it could be interesting to investigate how the He^{+}/He^{2+} relative fraction varies with varying discharge parameters. The investigation of the plasma detachment mechanism in helium, moreover, is important since it allows studying this phenomenon in purely atomic plasma and comparing it to molecular species like hydrogen or deuterium.

Identification of different detachment behaviour in negative and positive triangularity: Alternative magnetic configurations with improved confinement and reduced PWI are of great interest for future fusion reactors. In this thesis, the SOLPS-ITER boundary plasma package was used for the first time to compare the detachment behaviour of negative and positive triangularity configurations. Recent experimental observation in TCV seems to indicate a reduced detachment of the outer strike point in NT discharges if compared to similar PT ones.
The outcomes of the SOLPS-ITER modelling described in this thesis indicated that the experimental observations are compatible with different behaviour of negative and positive triangularity configurations with respect to cross-field transport at increasing average plasma density. Indeed, the experimental trend of positive triangularity detachment during a density ramp experiment is well captured by simulations at increasing separatrix electron density with constant cross-field diffusion. If the same analysis is performed for the negative triangularity equilibrium, detachment is overestimated with

respect to the experiment. To reproduce the detachment suppression observed experimentally, cross-field transport must be reduced in the NT simulations by decreasing the anomalous particle diffusion coefficient D_n.
Due to the promising role that negative triangularity tokamaks may have as an alternative configuration for the European DEMO reactor, this first and preliminary outcome deserves to be further investigated. In particular, the SOLPS-ITER model should include fluxes related to drift velocities, which were neglected in this preliminary analysis. This would allow for better comparison with forward and reversed field experiments. Moreover, this first negative triangularity simulation database should be extended. The first possibility is to repeat the D_n density-ramp simulations for different $n_{e,\text{sep@OMP}}$, seeking for correlations between the radial cross field flux, the separatrix density and the OSP electron temperature. A second possibility could be to focus on lower and upper triangularities separately, by performing simulations based on different equilibria reconstruction to build the plasma mash. Finally, a comparative study with turbulent codes should be performed in order to understand the role of triangularity in determining the physical origin of the different cross-field behaviours.

A | Conservative and advective form of Braginskii equations

Density conservation equation:

$$\frac{\partial n}{\partial t} + \nabla \cdot \left(n\vec{\mathbf{v}}\right) = S_n \tag{A.1}$$

Momentum conservation equation:

Conservative form:

$$\begin{aligned}\frac{\partial(nm\vec{\mathbf{v}})}{\partial t} + \nabla \cdot (nm\vec{\mathbf{v}}\vec{\mathbf{v}}) + \nabla p + \nabla \cdot \underline{\underline{\Pi}} \\ = Zne(\vec{\mathbf{E}} + \vec{\mathbf{v}} \times \vec{\mathbf{B}}) + \sum_{a \neq a'} \vec{\mathbf{R}}_{aa'} + S_m\end{aligned} \tag{A.2}$$

Advective form:

$$\begin{aligned}nm\frac{\partial \vec{\mathbf{v}}}{\partial t} + \left(nm\vec{\mathbf{v}} \cdot \nabla\right)\vec{\mathbf{v}} + \nabla p + \nabla \cdot \underline{\underline{\Pi}} \\ = Zne(\vec{\mathbf{E}} + \vec{\mathbf{v}} \times \vec{\mathbf{B}}) + \sum_{a \neq a'} \vec{\mathbf{R}}_{aa'} + S_m - m\vec{\mathbf{v}}S_n\end{aligned} \tag{A.3}$$

Total energy conservation equation:

Conservative form:

$$\begin{aligned}\frac{\partial}{\partial t}\left(\frac{3}{2}nT + \frac{1}{2}nmv^2\right) + \nabla \cdot \left[\vec{\mathbf{q}}_s + \left(\frac{5}{2}nT + \frac{1}{2}nmv^2\right)\vec{\mathbf{v}} + \underline{\underline{\Pi}} \cdot \vec{\mathbf{v}}\right] \\ = Zne\vec{\mathbf{E}} \cdot \vec{\mathbf{v}} + \sum_{a \neq a'} Q_{aa'} + S_T\end{aligned} \tag{A.4}$$

Advective form:

$$n\left(\frac{\partial}{\partial t}+\vec{\mathbf{v}}\cdot\nabla\right)\left(\frac{3}{2}T+\frac{1}{2}mv^2\right)+\nabla\cdot\left[\vec{\mathbf{q}}_s+nT\vec{\mathbf{v}}+\underline{\underline{\Pi}}\cdot\vec{\mathbf{v}}\right] = Zne\vec{\mathbf{E}}\cdot\vec{\mathbf{v}}+\sum_{a\neq a'}Q_{aa'}+S_T-S_n\left(\frac{3}{2}T+\frac{1}{2}mv^2\right) \tag{A.5}$$

Internal energy conservation equation:

Conservative form:

$$\frac{\partial}{\partial t}\left(\frac{3}{2}nT\right)+\nabla\cdot\left[\vec{\mathbf{q}}_s+\frac{3}{2}nT\vec{\mathbf{v}}\right]+nT\nabla\cdot\vec{\mathbf{v}}+\underline{\underline{\Pi}}:\nabla\vec{\mathbf{v}} = \sum_{a\neq a'}\left(Q_{aa'}-\vec{\mathbf{R}}_{aa'}\cdot\vec{\mathbf{v}}\right)+S_T+\frac{1}{2}mv^2S_n \tag{A.6}$$

Advective form:

$$\frac{3}{2}n\left(\frac{\partial T}{\partial t}+\vec{\mathbf{v}}\cdot\nabla T\right)+\nabla\cdot\vec{\mathbf{q}}_s+nT\nabla\cdot\vec{\mathbf{v}}+\underline{\underline{\Pi}}:\nabla\vec{\mathbf{v}} = \sum_{a\neq a'}\left(Q_{aa'}-\vec{\mathbf{R}}_{aa'}\cdot\vec{\mathbf{v}}\right)+S_T-S_n\left(\frac{3}{2}T-\frac{1}{2}mv^2\right) \tag{A.7}$$

B | Equations of the 0D global model including He metastable state

This appendix reports the global 0D equations, used to perform the studies presented in section 4.4.2, including the effects of He metastable states. These equations are the metastable-resolved form of equations (3.4), (3.5) and (3.6).

$$\frac{dn_i}{dt} = R_{\mathrm{iz},(1\mathrm{s})} n_e n_{n,(1\mathrm{s})} + R_{\mathrm{iz},(2\mathrm{s})} n_e n_{n,(2\mathrm{s})} - R_{\mathrm{rc},(1\mathrm{s})} n_e n_i - R_{\mathrm{iz},(2\mathrm{s})} n_e n_i - \Gamma_{i,\mathrm{wall}} n_i \tag{B.1}$$

$$\begin{aligned}\frac{dn_{n,(1\mathrm{s})}}{dt} = &-R_{\mathrm{iz},(1\mathrm{s})} n_e n_{n,(1\mathrm{s})} + R_{\mathrm{rc},(1\mathrm{s})} n_e n_i + X_{(2\mathrm{s})\to(1\mathrm{s})} n_e n_{n,(2\mathrm{s})} \\ &- X_{(1\mathrm{s})\to(2\mathrm{s})} n_e n_{n,(1\mathrm{s})} + \Gamma_{n,\mathrm{recyc}} n_i - \Gamma_{n,\mathrm{pump}} n_{n,(1\mathrm{s})} + \frac{\Gamma_{n,\mathrm{puff}}}{\mathrm{Vol}}\end{aligned} \tag{B.2}$$

$$\begin{aligned}\frac{dn_{n,(2\mathrm{s})}}{dt} = &-R_{\mathrm{iz},(2\mathrm{s})} n_e n_{n,(2\mathrm{s})} + R_{\mathrm{rc},(2\mathrm{s})} n_e n_i + X_{(1\mathrm{s})\to(2\mathrm{s})} n_e n_{n,(1\mathrm{s})} \\ &- X_{(2\mathrm{s})\to(1\mathrm{s})} n_e n_{n,(2\mathrm{s})} - \Gamma_{n,\mathrm{pump}} n_{n,(2\mathrm{s})}\end{aligned} \tag{B.3}$$

$$\begin{aligned}\frac{3}{2} n_e \frac{dT_e}{dt} = &\frac{P_{\mathrm{ext}}}{\mathrm{Vol}_e} - E_{\mathrm{iz},(1\mathrm{s})} R_{\mathrm{iz},(1\mathrm{s})} n_e n_{n,(1\mathrm{s})} - (E_{\mathrm{iz},(1\mathrm{s})} - E_{(2\mathrm{s})}) R_{\mathrm{iz},(2\mathrm{s})} n_e n_{n,(2\mathrm{s})} \\ &- E_{n,\mathrm{rad},(1\mathrm{s})} R_{n,\mathrm{rad},(1\mathrm{s})} n_e n_{n,(1\mathrm{s})} - E_{n,\mathrm{rad},(2\mathrm{s})} R_{n,\mathrm{rad},(2\mathrm{s})} n_e n_{n,(2\mathrm{s})} \\ &- E_{(2\mathrm{s})} X_{(1\mathrm{s})\to(2\mathrm{s})} n_e n_{n,(1\mathrm{s})} - E_{i,\mathrm{rad}} R_{i,\mathrm{rad}} n_e n_i - \Gamma_{e,\mathrm{wall}} T_e n_e \\ &- \frac{3}{2} \frac{2m_e}{m_i} R_{i,\mathrm{el}} n_i n_e (T_e - T_i) \\ &- \frac{3}{2} \frac{2m_e}{m_n} R_{n,\mathrm{el}} (n_{n,(1\mathrm{s})} + n_{n,(2\mathrm{s})}) n_e (T_e - T_n) - \frac{3}{2} \frac{dn_i}{dt} T_e\end{aligned} \tag{B.4}$$

where $X_{(1\mathrm{s})\to(2\mathrm{s})}$ and $X_{(2\mathrm{s})\to(1\mathrm{s})}$ are the metastables cross-coupling coefficients, $E_{\mathrm{iz},(1\mathrm{s})}$ = 24.5 eV is the ionization energy of the ground state and $E_{(2\mathrm{s})}$ = 19.8 eV is the energy of the triplet state He $^3(2s)$.
We assumed that puffing and plasma recycling only produce gound-state He atoms, while turbo-pumps act as sink also for metastable He (2s) states.

List of Figures

List of Tables

Bibliography

[1] I. E. Agency, *Key World Energy Statistics 2021*. IEA Publications, 2021.

[2] I. E. Agency, *Net Zero by 2050 - A Roadmap for the Global Energy Sector*. IEA Publications, 2021.

[3] *ITER Research Plan within the Staged Approach (Level III – Provisional Version)*. No. ITR-18-003, ITER Organization, 2018.

[4] J. Wesson, *Tokamaks; 4th ed.* International series of monographs on physics, Oxford: Oxford Univ. Press, 2011.

[5] S. Li, H. Jiang, Z. Ren, and C. Xu, "Optimal tracking for a divergent-type parabolic PDE system in current profile control," *Abstract and Applied Analysis*, vol. 2014, pp. 1–8, 2014.

[6] F. Wagner *et al.*, "Regime of improved confinement and high beta in neutral-beam-heated divertor discharges of the ASDEX tokamak," *Physical Review Letters*, vol. 49, pp. 1408–1412, Nov. 1982.

[7] J. W. Connor and H. R. Wilson, "A review of theories of the l-h transition," *Plasma Physics and Controlled Fusion*, vol. 42, pp. R1–R74, Dec. 1999.

[8] H. Zohm, "Edge localized modes (ELMs)," *Plasma Physics and Controlled Fusion*, vol. 38, pp. 105–128, Feb. 1996.

[9] A. W. Leonard, "Edge-localized-modes in tokamaks," *Physics of Plasmas*, vol. 21, p. 090501, Sept. 2014.

[10] N. Oyama *et al.*, "Pedestal conditions for small ELM regimes in tokamaks," *Plasma Physics and Controlled Fusion*, vol. 48, pp. A171–A181, Apr. 2006.

[11] J. Garcia *et al.*, "New h-mode regimes with small ELMs and high thermal confinement in the joint european torus," *Physics of Plasmas*, vol. 29, p. 032505, Mar. 2022.

[12] A. Marinoni, O. Sauter, and S. Coda, "A brief history of negative triangularity tokamak plasmas," *Reviews of Modern Plasma Physics*, vol. 5, Oct. 2021.

[13] F. R. and, "Overview of the JET results with the ITER-like wall," *Nuclear Fusion*, vol. 53, p. 104002, Sept. 2013.

[14] A. Huber *et al.*, "Impact of the ITER-like wall on divertor detachment and on the density limit in the JET tokamak," *Journal of Nuclear Materials*, vol. 438, pp. S139–S147, July 2013.

[15] A. Widdowson *et al.*, "Overview of the JET ITER-like wall divertor," *Nuclear Materials and Energy*, vol. 12, pp. 499–505, Aug. 2017.

[16] J. Mailloux *et al.*, "Overview of JET results for optimising ITER operation," *Nuclear Fusion*, vol. 62, p. 042026, Apr. 2022.

[17] E. Gibney, "Nuclear-fusion reactor smashes energy record," *Nature*, vol. 602, pp. 371–371, Feb. 2022.

[18] U. Stroth *et al.*, "Progress from ASDEX upgrade experiments in preparing the physics basis of ITER operation and DEMO scenario development," *Nuclear Fusion*, vol. 62, p. 042006, Mar. 2022.

[19] A. Herrmann *et al.*, "A large divertor manipulator for ASDEX upgrade," *Fusion Engineering and Design*, vol. 98-99, pp. 1496–1499, Oct. 2015.

[20] O. Février *et al.*, "Divertor closure effects on the TCV boundary plasma," *Nuclear Materials and Energy*, vol. 27, p. 100977, June 2021.

[21] H. Reimerdes *et al.*, "Initial TCV operation with a baffled divertor," *Nuclear Fusion*, vol. 61, p. 024002, Jan. 2021.

[22] H. Meyer *et al.*, "Overview of physics results from MAST," *Nuclear Fusion*, vol. 49, p. 104017, Sept. 2009.

[23] E. Havlíčková, M. Wischmeier, B. Lipschultz, and G. Fishpool, "The effect of the super-x divertor of MAST upgrade on impurity radiation as modelled by SOLPS," *Journal of Nuclear Materials*, vol. 463, pp. 1209–1213, Aug. 2015.

[24] J. Harrison *et al.*, "Overview of new MAST physics in anticipation of first results from MAST upgrade," *Nuclear Fusion*, vol. 59, p. 112011, June 2019.

[25] *World Survey of Fusion Devices 2022*. Non-serial Publications, Vienna: INTERNATIONAL ATOMIC ENERGY AGENCY, 2022.

[26] B. Saoutic, M. Chatelier, and C. D. Michelis, "Tore supra: Toward steady state in a superconducting tokamak," *Fusion Science and Technology*, vol. 56, pp. 1079–1091, Oct. 2009.

[27] J. Bucalossi *et al.*, "Operating a full tungsten actively cooled tokamak: overview of WEST first phase of operation," *Nuclear Fusion*, vol. 62, p. 042007, Feb. 2022.

[28] R. Albanese *et al.*, "DTT: a divertor tokamak test facility for the study of the power exhaust issues in view of DEMO," *Nuclear Fusion*, vol. 57, p. 016010, Oct. 2016.

[29] R. Ambrosino, "DTT - divertor tokamak test facility: A testbed for DEMO," *Fusion Engineering and Design*, vol. 167, p. 112330, June 2021.

[30] P. Stangeby, *The Plasma Boundary of Magnetic Fusion Devices*. Series in Plasma Physics and Fluid Dynamics, Taylor & Francis, 2000.

[31] G. Federici, W. Biel, M. Gilbert, R. Kemp, N. Taylor, and R. Wenninger, "European DEMO design strategy and consequences for materials," *Nuclear Fusion*, vol. 57, p. 092002, June 2017.

[32] H. R. others, "Assessment of alternative divertor configurations as an exhaust solution for DEMO," *Nuclear Fusion*, vol. 60, p. 066030, May 2020.

[33] G. Matthews, "Plasma detachment from divertor targets and limiters," *Journal of Nuclear Materials*, vol. 220-222, pp. 104–116, Apr. 1995.

[34] S. I. Krasheninnikov, A. S. Kukushkin, and A. A. Pshenov, "Divertor plasma detachment," *Physics of Plasmas*, vol. 23, p. 055602, May 2016.

[35] S. Krasheninnikov, A. Kukushkin, W. Lee, A. Phsenov, R. Smirnov, A. Smolyakov, A. Stepanenko, and Y. Zhang, "Edge and divertor plasma: detachment, stability, and plasma-wall interactions," *Nuclear Fusion*, vol. 57, p. 102010, June 2017.

[36] H. Wang, H. Guo, T. Petrie, A. Leonard, D. Thomas, and J. Watkins, "Effects of low-z and high-z impurities on divertor detachment and plasma confinement," *Nuclear Materials and Energy*, vol. 12, pp. 942–947, Aug. 2017.

[37] J. Linke *et al.*, "Challenges for plasma-facing components in nuclear fusion," *Matter and Radiation at Extremes*, vol. 4, p. 056201, Sept. 2019.

[38] W. Eckstein, "Physical sputtering and reflection processes in plasma-wall interactions," *Journal of Nuclear Materials*, vol. 248, pp. 1–8, Sept. 1997.

[39] P. S. Krstic, S. J. Stuart, and C. O. Reinhold, "Chemical sputtering of fusion plasma-facing carbon surfaces," in *AIP Conference Proceedings*, AIP, 2006.

[40] S. Brezinsek *et al.*, "Fuel retention studies with the ITER-like wall in JET," *Nuclear Fusion*, vol. 53, p. 083023, July 2013.

[41] J. Roth *et al.*, "Recent analysis of key plasma wall interactions issues for ITER," *Journal of Nuclear Materials*, vol. 390-391, pp. 1–9, June 2009.

[42] A. K. Suri, N. Krishnamurthy, and I. S. Batra, "Materials issues in fusion reactors," *Journal of Physics: Conference Series*, vol. 208, p. 012001, Feb. 2010.

[43] M. Kaufmann and R. Neu, "Tungsten as first wall material in fusion devices," *Fusion Engineering and Design*, vol. 82, pp. 521–527, Oct. 2007.

[44] C. Linsmeier, B. Unterberg, J. Coenen, R. Doerner, H. Greuner, A. Kreter, J. Linke, and H. Maier, "Material testing facilities and programs for plasma-facing component testing," *Nuclear Fusion*, vol. 57, p. 092012, June 2017.

[45] M. J. Baldwin, R. P. Doerner, D. Nishijima, M. Patino, M. J. Simmonds, G. Tynan, J. H. Yu, and A. Založnik, "Plasma-material-interaction research using PISCES linear plasma devices," *Fusion Science and Technology*, vol. 75, pp. 664–673, Oct. 2019.

[46] J. Rapp *et al.*, "The material plasma exposure eXperiment: Mission and conceptual design," *Fusion Engineering and Design*, vol. 156, p. 111586, July 2020.

[47] I. J. K. others, "Simulations of fusion edge plasmas by linear plasma devices: physics and plasma–material interactions," *Journal of the Korean Physical Society*, vol. 80, pp. 717–734, Feb. 2022.

[48] T. W. Morgan, P. Rindt, G. G. van Eden, V. Kvon, M. A. Jaworksi, and N. J. L. Cardozo, "Liquid metals as a divertor plasma-facing material explored using the pilot-PSI and magnum-PSI linear devices," *Plasma Physics and Controlled Fusion*, vol. 60, p. 014025, Oct. 2017.

[49] P. Rindt, J. van den Eijnden, T. Morgan, and N. L. Cardozo, "Conceptual design of a liquid-metal divertor for the european DEMO," *Fusion Engineering and Design*, vol. 173, p. 112812, Dec. 2021.

[50] J. Scholten, P. Z. van Emmichoven, H. van Eck, P. Smeets, G. D. Temmerman, S. Brons, M. van den Berg, H. van der Meiden, M. van de Pol, M. Graswinckel, P. Groen, A. Poelman, and J. Genuit, "Operational status of the magnum-PSI linear plasma device," *Fusion Engineering and Design*, vol. 88, pp. 1785–1788, Oct. 2013.

[51] G. D. Temmerman, M. van den Berg, J. Scholten, A. Lof, H. van der Meiden, H. van Eck, T. Morgan, T. de Kruijf, P. Z. van Emmichoven, and J. Zielinski,

"High heat flux capabilities of the magnum-PSI linear plasma device," *Fusion Engineering and Design*, vol. 88, pp. 483–487, Oct. 2013.

[52] A. Kreter *et al.*, "Linear plasma device PSI-2 for plasma-material interaction studies," *Fusion Science and Technology*, vol. 68, pp. 8–14, July 2015.

[53] B. Unterberg *et al.*, "New linear plasma devices in the trilateral euregio cluster for an integrated approach to plasma surface interactions in fusion reactors," *Fusion Engineering and Design*, vol. 86, pp. 1797–1800, Oct. 2011.

[54] G. Granucci *et al.*, "The new linear plasma device GyM at IFP-CNR," *36th EPS Conference on Plasma Physics 2009, EPS 2009 - Europhysics Conference Abstracts*, vol. 33 E2, pp. 1107–1110, 2009.

[55] P. Ricci *et al.*, "Simulation of plasma turbulence in scrape-off layer conditions: the GBS code, simulation results and code validation," *Plasma Physics and Controlled Fusion*, vol. 54, p. 124047, Nov. 2012.

[56] D. Iraji *et al.*, "Imaging of Turbulent Structures and Tomographic Reconstruction of GyM Plasma Emissivity," *Fusion Science and Technology*, vol. 62, no. 3, pp. 428–435, 2012.

[57] E. Vassallo *et al.*, "Retention of nanocrystalline WN_x layers exposed to high-fluence deuterium plasmas," *Journal of Nuclear Materials*, vol. 466, pp. 621 – 626, 2015.

[58] L. Laguardia *et al.*, "Ammonia formation and W coatings interaction with deuterium/nitrogen plasmas in the linear device GyM," *Journal of Nuclear Materials*, vol. 463, pp. 680 – 683, 2015. Proceedings of the 21st International Conference on Plasma Surface Interactions 2014, 21st PSI.

[59] L. Laguardia *et al.*, "Influence of He and Ar injection on ammonia production in N_2/D_2 plasma in the medium flux GyM device," *Nuclear Materials and Energy*, vol. 12, pp. 261–266, 2017. Proceedings of the 22nd International Conference on Plasma Surface Interactions 2016, 22nd PSI.

[60] R. Caniello *et al.*, "Erosion yield and W surface enrichment of Fe-W model system exposed to low flux deuterium plasma in the linear device GyM," *Nuclear Materials and Energy*, vol. 10, pp. 9 – 16, 2017.

[61] A. Cremona *et al.*, "Experimental determination of S/XB values of Sn I emission lines in GyM device," *44th EPS Conference on Plasma Physics, EPS 2017*, 2017.

[62] A. Cremona *et al.*, “Deuterium retention and erosion in liquid Sn samples exposed to D_2 and Ar plasmas in GyM device,” *Nuclear Materials and Energy*, vol. 17, pp. 253–258, 2018.

[63] L. Laguardia and j. y. v. p. others, title=Impact of He admixture on the ammonia formation in N_2 seeded D_2 plasmas in the GyM facility

[64] P. Tolias *et al.*, “The adhesion of tungsten dust on plasma-exposed tungsten surfaces,” *Nuclear Materials and Energy*, vol. 18, pp. 18–22, 2019.

[65] P. Tolias *et al.*, “Diffusion bonding effects on the adhesion of tungsten dust on tungsten surfaces,” *Nuclear Materials and Energy*, vol. 24, p. 100765, 2020.

[66] M. Sala *et al.*, “Simulations of argon plasmas in the linear plasma device GyM with the SOLPS-ITER code,” *Plasma Physics and Controlled Fusion*, vol. 62, p. 055005, Mar. 2020.

[67] M. Sala *et al.*, “Exposures of bulk W and nanostructured W coatings to medium flux D plasmas,” *Nuclear Materials and Energy*, vol. 24, p. 100779, 2020.

[68] A. Uccello *et al.*, “Effects of a nitrogen seeded plasma on nanostructured tungsten films having fusion-relevant features,” *Nuclear Materials and Energy*, vol. 25, p. 100808, Dec. 2020.

[69] S. Pope, *Turbulent Flows*. Cambridge University Press, 2000.

[70] S. Braginskii, “Transport processes in a plasma,” *Reviews of Plasma Physics*, vol. 1, pp. 205–311, 1965.

[71] D. P. Stotler, C. F. F. Karney, A. Y. Pigarov, and I. V. Kurchatov, “Degas 2 neutral transport modeling of high density, low temperature plasmas,”

[72] D. Reiter, M. Baelmans, and P. Börner, “The EIRENE and b2-EIRENE codes,” *Fusion Science and Technology*, vol. 47, pp. 172–186, Feb. 2005.

[73] T. N. Bernard *et al.*, “Kinetic modeling of neutral transport for a continuum gyrokinetic code,” *Physics of Plasmas*, vol. 29, p. 052501, May 2022.

[74] N. Horsten *et al.*, “A hybrid fluid-kinetic neutral model based on a micro-macro decomposition in the SOLPS-ITER plasma edge code suite,” *Contributions to Plasma Physics*, vol. 60, p. e201900132, Feb. 2020.

[75] V. M. Zhdanov, “Transport processes in multicomponent plasma,” *Plasma Physics and Controlled Fusion*, vol. 44, pp. 2283–2283, Sept. 2002.

[76] V. Zhdanov, *Transport Processes in Multicomponent Plasma*. CRC Press, Apr. 2002.

[77] V. Rozhansky, E. Sytova, I. Senichenkov, I. Veselova, S. Voskoboynikov, and D. Coster, "Momentum balance for impurities in SOLPS transport code," *Journal of Nuclear Materials*, vol. 463, pp. 477–479, Aug. 2015.

[78] E. Sytova *et al.*, "Derivation of the friction and thermal force for SOLPS-ITER multicomponent plasma modeling," *Physics of Plasmas*, vol. 27, p. 082507, Aug. 2020.

[79] S. O. Makarov *et al.*, "Equations and improved coefficients for parallel transport in multicomponent collisional plasmas: Method and application for tokamak modeling," *Physics of Plasmas*, vol. 28, p. 062308, June 2021.

[80] W. Fundamenski, "Parallel heat flux limits in the tokamak scrape-off layer," *Plasma Physics and Controlled Fusion*, vol. 47, pp. R163–R208, Oct. 2005.

[81] S. Krasheninnikov, "On scrape off layer plasma transport," *Physics Letters A*, vol. 283, pp. 368–370, May 2001.

[82] D. A. D'Ippolito, J. R. Myra, and S. J. Zweben, "Convective transport by intermittent blob-filaments: Comparison of theory and experiment," *Physics of Plasmas*, vol. 18, p. 060501, June 2011.

[83] N. Ohno, "Plasma detachment in linear devices," *Plasma Physics and Controlled Fusion*, vol. 59, p. 034007, Feb. 2017.

[84] P. C. Stangeby, "Basic physical processes and reduced models for plasma detachment," *Plasma Physics and Controlled Fusion*, vol. 60, p. 044022, Mar. 2018.

[85] Y. Zhou, B. Dudson, F. Militello, K. Verhaegh, and O. Myatra, "Investigation of the role of hydrogen molecules in 1d simulation of divertor detachment," *Plasma Physics and Controlled Fusion*, vol. 64, p. 065006, May 2022.

[86] K. Verhaegh *et al.*, "The role of plasma-molecule interactions on power and particle balance during detachment on the TCV tokamak," *Nuclear Fusion*, vol. 61, p. 106014, Sept. 2021.

[87] K. Verhaegh and j. . N. others, title = A study of the influence of plasma–molecule interactions on particle balance during detachment vol. 26, p. 100922, Mar. 2021.

[88] R. Chodura, "Plasma–wall transition in an oblique magnetic field," *Physics of Fluids*, vol. 25, no. 9, p. 1628, 1982.

[89] D. Bohm, *The Characteristics of Electrical Discharges in Magnetic Fields*, ch. Minimum ionic kinetic energy for a stable sheath. McGraw-Hill, 1949.

[90] W. Eckstein and D. Heifetz, "Data sets for hydrogen reflection and their use in neutral transport calculations," *Journal of Nuclear Materials*, vol. 145-147, pp. 332–338, Feb. 1987.

[91] J. P. Biersack and W. Eckstein, "Sputtering studies with the monte carlo program TRIM.SP," *Applied Physics A Solids and Surfaces*, vol. 34, pp. 73–94, June 1984.

[92] W. Eckstein, "Sputtering yields," in *Topics in Applied Physics*, pp. 33–187, Springer Berlin Heidelberg.

[93] K. Schmid, M. Reinelt, and K. Krieger, "An integrated model of impurity migration and wall composition dynamics for tokamaks," *Journal of Nuclear Materials*, vol. 415, pp. S284–S288, Aug. 2011.

[94] K. Schmid, K. Krieger, S. Lisgo, G. Meisl, and S. Brezinsek, "Quantitative modeling of fuel retention in the JET-c and JET-ILW wall configurations by WallDYN and predictions for ITER," *Journal of Nuclear Materials*, vol. 463, pp. 66–72, Aug. 2015.

[95] P. Stangeby, C. Farrell, S. Hoskins, and L. Wood, "Monte carlo modelling of impurity ion transport for a limiter source/sink," *Nuclear Fusion*, vol. 28, pp. 1945–1962, Nov. 1988.

[96] J. Romazanov *et al.*, "First ERO2.0 modeling of be erosion and non-local transport in JET ITER-like wall," *Physica Scripta*, vol. T170, p. 014018, Sept. 2017.

[97] A. Eksaeva *et al.*, "The impact of surface morphology on the erosion of metallic surfaces – modelling with the 3d monte-carlo code ERO2.0," *Nuclear Materials and Energy*, vol. 27, p. 100987, June 2021.

[98] G. Alberti *et al.*, "ERO2.0 modelling of nanoscale surface morphology evolution," *Nuclear Fusion*, vol. 61, p. 066039, May 2021.

[99] J. Romazanov *et al.*, "Beryllium global erosion and deposition at JET-ILW simulated with ERO2.0," *Nuclear Materials and Energy*, vol. 18, pp. 331–338, Jan. 2019.

[100] S. D. Genova *et al.*, "Modelling of tungsten contamination and screening in WEST plasma discharges," *Nuclear Fusion*, vol. 61, p. 106019, Sept. 2021.

[101] J. Romazanov *et al.*, "Beryllium erosion and redeposition in ITER h, he and d–t discharges," *Nuclear Fusion*, vol. 62, p. 036011, Jan. 2022.

[102] V. Rozhansky *et al.*, "New b2solps5.2 transport code for h-mode regimes in tokamaks," *Nuclear Fusion*, vol. 49, p. 025007, Jan. 2009.

[103] S. Wiesen *et al.*, "On the role of finite grid extent in SOLPS-ITER edge plasma simulations for JET h-mode discharges with metallic wall," *Nuclear Materials and Energy*, vol. 17, pp. 174–181, Dec. 2018.

[104] W. Dekeyser *et al.*, "Implementation of a 9-point stencil in SOLPS-ITER and implications for alcator c-mod divertor plasma simulations," *Nuclear Materials and Energy*, vol. 18, pp. 125–130, Jan. 2019.

[105] W. Dekeyser *et al.*, "Plasma edge simulations including realistic wall geometry with SOLPS-ITER," *Nuclear Materials and Energy*, vol. 27, p. 100999, June 2021.

[106] S. V. Patankar, *Numerical heat transfer and fluid flow*. Series on Computational Methods in Mechanics and Thermal Science, Hemisphere Publishing Corporation (CRC Press, Taylor & Francis Group), 1980.

[107] X. Bonnin *et al.*, "Presentation of the new SOLPS-ITER code package for tokamak plasma edge modelling," *Plasma and Fusion Research*, vol. 11, no. 0, pp. 1403102–1403102, 2016.

[108] M. Giacomin *et al.*, "The gbs code for the self-consistent simulation of plasma turbulence and kinetic neutral dynamics in the tokamak boundary," *Journal of Computational Physics*, vol. 463, p. 111294, 2022.

[109] A. Zeiler, J. F. Drake, and B. Rogers, "Nonlinear reduced braginskii equations with ion thermal dynamics in toroidal plasma," *Physics of Plasmas*, vol. 4, pp. 2134–2138, June 1997.

[110] A. Zeiler, *Tokamak Edge Turbulence*. Max-Planck-Institut für Plasmaphysik, 1999.

[111] F. Riva *et al.*, "Blob dynamics in the TORPEX experiment: a multi-code validation," *Plasma Physics and Controlled Fusion*, vol. 58, p. 044005, Jan. 2016.

[112] D. Galassi *et al.*, "Validation of edge turbulence codes in a magnetic x-point scenario in TORPEX," *Physics of Plasmas*, vol. 29, p. 012501, Jan. 2022.

[113] B. N. Rogers and P. Ricci, "Low-frequency turbulence in a linear magnetized plasma," *Phys. Rev. Lett.*, vol. 104, p. 225002, Jun 2010.

[114] A. Mosetto *et al.*, "Finite ion temperature effects on scrape-off layer turbulence," *Physics of Plasmas*, vol. 22, p. 012308, jan 2015.

[115] F. D. Halpern *et al.*, "Ideal ballooning modes in the tokamak scrape-off layer," *Physics of Plasmas*, vol. 20, p. 052306, may 2013.

[116] C. Wersal and P. Ricci, "A first-principles self-consistent model of plasma turbulence and kinetic neutral dynamics in the tokamak scrape-off layer," *Nuclear Fusion*, vol. 55, p. 123014, nov 2015.

[117] M. Baelmans, *Code improvements and applications of a two-dimensional edge plasma model for toroidal fusion devices*. PhD thesis, Katholieke Universiteit Leuven, 1993.

[118] E. Tonello *et al.*, "A point plasma model for linear plasma devices based on SOLPS-ITER equations: application to helium plasma," *Nuclear Fusion*, vol. 61, p. 066036, May 2021.

[119] S. Brezinsek *et al.*, "Plasma–wall interaction studies within the EUROfusion consortium: progress on plasma-facing components development and qualification," *Nuclear Fusion*, vol. 57, p. 116041, aug 2017.

[120] M. Sala, *Numerical and experimental studies of plasma-material interaction in linear plasma devices*. PhD thesis, Politecnico di Milano, 2021.

[121] H. P. Summers *et al.*, "Ionization state, excited populations and emission of impurities in dynamic finite density plasmas: I. the generalized collisional–radiative model for light elements," *Plasma Physics and Controlled Fusion*, vol. 48, pp. 263–293, Jan. 2006.

[122] G. Alberti *et al.*, "Global SOLPS-ITER and ERO2.0 coupling in a linear device for the study of plasma–wall interaction in helium plasma," *Nuclear Fusion*, vol. 63, p. 026020, Jan. 2023.

[123] S. Kajita *et al.*, "Formation process of tungsten nanostructure by the exposure to helium plasma under fusion relevant plasma conditions," *Nuclear Fusion*, vol. 49, p. 095005, Aug. 2009.

[124] R. Fischer, C. J. Fuchs, B. Kurzan, W. Suttrop, and E. W. and, "Integrated data analysis of profile diagnostics at ASDEX upgrade," *Fusion Science and Technology*, vol. 58, pp. 675–684, Oct. 2010.

[125] H. Bufferand *et al.*, "Near wall plasma simulation using penalization tech-

nique with the transport code SolEdge2d-eirene," *Journal of Nuclear Materials*, vol. 438, pp. S445–S448, July 2013.

[126] A. P. others, "Energy confinement and MHD activity in shaped TCV plasmas with localized electron cyclotron heating," *Nuclear Fusion*, vol. 39, pp. 1807–1818, Nov. 1999.

[127] Y. Camenen *et al.*, "Electron heat transport in shaped TCV l-mode plasmas," *Plasma Physics and Controlled Fusion*, vol. 47, pp. 1971–1987, Oct. 2005.

[128] M. E. Austin *et al.*, "Achievement of reactor-relevant performance in negative triangularity shape in the diii-d tokamak," *Phys. Rev. Lett.*, vol. 122, p. 115001, Mar 2019.

[129] A. Marinoni *et al.*, "H-mode grade confinement in l-mode edge plasmas at negative triangularity on DIII-d," *Physics of Plasmas*, vol. 26, p. 042515, Apr. 2019.

[130] O. Février *et al.*, "Divertor detachment in negative-delta configurations in the TCV tokamak ." Contribution presented at the American Physics Society - Division of Plasma Physics Meeting, APS.

[131] O. Février *et al.*, "Divertor Detachment In Negative-Triangularity Configurations In The TCV Tokamak." Contribution presented at the 25th International Conference on Plasma Surface Interaction in Controlled Fusion Devices - PSI25, Jeju, Korea, 2022.

[132] J. Bohdansky, J. Roth, and H. L. Bay, "An analytical formula and important parameters for low-energy ion sputtering," *Journal of Applied Physics*, vol. 51, no. 5, p. 2861, 1980.

[133] M. Wensing, *Drift-related transport and plasma-neutral interaction in the TCV divertor*. PhD thesis, Ecole Polytechnique Fédérale de Lausanne, 2021.

[134] M. Wensing *et al.*, "SOLPS-ITER simulations of the TCV divertor upgrade," *Plasma Physics and Controlled Fusion*, vol. 61, p. 085029, July 2019.

[135] M. Wensing *et al.*, "SOLPS-ITER validation with TCV l-mode discharges," *Physics of Plasmas*, vol. 28, p. 082508, Aug. 2021.